Few-neutron systems and WIMP-nucleus interactions from chiral effective field theory

Wenig-Neutronen-Systeme und WIMP-Nukleus-Wechselwirkungen basierend auf chiraler effektiver Feldtheorie

Zur Erlangung des Grades eines Doktors der Naturwissenschaften (Dr. rer. nat.)
genehmigte Dissertation von Philipp Klos aus Darmstadt
Tag der Einreichung: 09.07.2018, Tag der Prüfung: 15.10.2018
Darmstadt 2018 — D 17

1. Gutachten: Prof. Ph.D. Achim Schwenk
2. Gutachten: Prof. Dr. Hans-Werner Hammer

TECHNISCHE UNIVERSITÄT DARMSTADT

Fachbereich Physik
Institut für Kernphysik
Theory Center

Few-neutron systems and WIMP-nucleus interactions from chiral effective field theory
Wenig-Neutronen-Systeme und WIMP-Nukleus-Wechselwirkungen basierend auf chiraler effektiver Feldtheorie

Genehmigte Dissertation von Philipp Klos aus Darmstadt

1. Gutachten: Prof. Ph.D. Achim Schwenk
2. Gutachten: Prof. Dr. Hans-Werner Hammer

Tag der Einreichung: 09.07.2018
Tag der Prüfung: 15.10.2018

Darmstadt 2018 — D 17

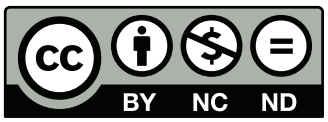

Abstract

The building blocks of atomic nuclei, protons and neutrons, interact via the strong force. The fundamental theory of the strong interaction, quantum chromodynamics (QCD), is non-perturbative at the energy scales relevant for nuclear physics. Calculations of low-energy observables based directly on QCD thus present a challenge. Effective field theories (EFTs) of QCD, such as chiral EFT, provide an alternative pathway to describe the nuclear force and the interaction of nuclei with external particles. In this thesis, chiral EFT is applied to studies of few-neutron systems as well as in calculations of nuclear structure factors relevant for dark matter searches.

Currently, only lattice QCD calculations in finite volume allow for direct solutions of QCD at low energies. Matching results obtained in chiral EFT to lattice QCD calculations thus presents a promising avenue for the construction of nuclear forces directly based on QCD. This becomes especially relevant in the few-neutron sector, which is challenging to access experimentally so that input for effective field theories is scarce. In this thesis, we take first steps in this direction by performing quantum Monte Carlo (QMC) calculations of the ground and first excited states of two neutrons in finite volume. We analyze the finite-volume effects that are crucial for the determination of infinite-volume observables from finite-volume data.

The interest in few-neutron states also stems from a recent measurement of a possible tetraneutron resonance. We present QMC calculations of three and four neutrons interacting via chiral EFT forces confined in an external potential well. By extrapolating to the physical case of vanishing external-potential strength, we obtain a quantitative estimate of possible three- and four neutron resonance energies. Our results suggest that a three-neutron resonance, if it exists, may be lower in energy than a tetraneutron resonance. Furthermore, we present an alternative approach to the extraction of resonance properties based on the volume dependence of the calculated discrete energy spectra in finite volume. Using a discrete variable representation based on plane waves, we show for both bosonic and fermionic systems of up to four particles that multi-body resonances appear as avoided level crossings in the energy spectra. Our results establish few-body finite-volume calculations as a new tool to study few-body resonances.

The analysis of dark matter direct detection experiments depends crucially on nuclear structure factors that describe the coupling of proposed dark matter particles (WIMPs) to the target nuclei used in such searches. We present a chiral power counting scheme for operators describing various types of WIMP-nucleon interactions including both nuclear one- and two-body currents. In a second step, we evaluate the corresponding structure factors for different target nuclei and determine the dominant corrections to the standard spin-independent channel. Based on chiral EFT and nuclear structure effects, we propose an extension of the standard analysis applied in experimental searches. In addition, we find that two-body contributions help improve limits on the WIMP-nucleon cross section based on collider searches of Higgs-mediated dark-matter interactions. Finally, we investigate to what extent current and planned experiments are able to distinguish the subdominant WIMP-nucleon interaction channels from the standard spin-independent interaction based on their momentum dependence.

Zusammenfassung

Atomkerne sind aus Protonen und Neutronen aufgebaut, welche durch die starke Kernkraft wechselwirken. Die fundamentale Theorie der starken Wechselwirkung ist die Quantenchromodynamik (QCD). Diese ist im für die Kernphysik relevanten Energiebereich nicht perturbativ, weshalb die Berechnung von kernphysikalischen Größen bei niedrigen Energien basierend auf der QCD eine große Herausforderung darstellt. Effektive Feldtheorien (EFT) der QCD, wie beispielsweise die chirale EFT, bieten eine Alternative zur Beschreibung der Kernkräfte und der Wechselwirkung von Kernen mit externen Teilchen. In dieser Dissertation wird die chirale EFT zur Beschreibung von Systemen aus wenigen Neutronen sowie für Berechnungen von Kernstrukturfaktoren, die für die Suche nach dunkler Materie relevant sind, eingesetzt.

Aktuell sind direkte Lösungen der QCD nur durch Gitter-Rechnungen im endlichen Volumen möglich. Durch das Anpassen von Rechnungen in chiraler EFT an Ergebnisse aus der Gitter-QCD lassen sich Kernkräfte auf Basis der QCD konstruieren. Diese Vorgehensweise ist besonders relevant für Systeme aus wenigen Neutronen, für welche experimentelle Daten rar sind. In dieser Arbeit präsentieren wir erste Schritte in diese Richtung, indem wir Quanten-Monte-Carlo-Rechnungen (QMC-Rechnungen) des Grund- und ersten angeregten Zustands des Zwei-Neutronen-Systems im endlichen Volumen durchführen. Wir analysieren die durch das endliche Volumen induzierten Effekte, welche einen Einfluss auf die Extraktion von Streuparametern haben.

Das Interesse an Zuständen aus wenigen Neutronen ist auch durch eine aktuelle Messung einer möglichen Vier-Neutronen-Resonanz begründet. In dieser Arbeit untersuchen wir mittels QMC-Rechnungen Drei- und Vier-Neutronen-Systeme, die in externen Potentialen gefangen sind. Durch Extrapolation zu verschwindender Potentialstärke der Falle können im nächsten Schritt mögliche Drei- und Vier-Neutronen-Resonanzenergien berechnet werden. Die Ergebnisse weisen darauf hin, dass eine Drei-Neutronen-Resonanz, falls diese existiert, eine niedrigere Energie aufweisen könnte als eine Vier-Neutronen-Resonanz. Ein alternativer Weg zur Berechnung von Mehrteilchenresonanzen basiert auf der Volumenabhängigkeit von diskreten Energiespektren im endlichen Volumen. Unter Verwendung der Diskrete-Variablen-Darstellung zeigen wir für bosonische wie fermionische Systeme, dass Resonanzen aus mehr als zwei Teilchen als vermiedene Kreuzungen von Energieniveaus im endlichen Volumen erscheinen. Unsere Ergebnisse etablieren Rechnungen im endlichen Volumen als neue Methode zur Untersuchung von Mehrteilchenresonanzen.

Die Auswertung von Experimenten zur direkten Detektion von dunkler Materie hängt maßgeblich von Kernstrukturfaktoren ab, welche die Wechselwirkung von postulierten Dunkle-Materie-Teilchen (WIMPs) mit den verwendeten Target-Kernen beschreiben. Wir präsentieren ein chirales Ordnungsschema für Operatoren, welche die Wechselwirkung zwischen WIMPs und Nukleonen beschreiben, wobei wir Ein- und Zweiteilchenoperatoren konsistent berücksichtigen. Im zweiten Schritt berechnen wir die zugehörigen Strukturfaktoren für verschiedene Target-Kerne und bestimmen die führenden Korrekturen zum üblicherweise angenommenen Spin-unabhängigen Kanal. Basierend auf unseren Ergebnissen schlagen wir eine erweiterte Operatorbasis für zukünftige Analysen experimenteller Ergebnisse vor. Des Weiteren zeigen wir, wie Zweiteilchenoperatoren

auch dazu beitragen, Grenzwerte des WIMP-Nukleon-Wirkungsquerschnittes aus Beschleunigerexperimenten zu via Higgs-Austausch wechselwirkender dunkler Materie zu verbessern. Schlussendlich untersuchen wir, inwiefern aktuelle und geplante Experimente in der Lage sind, verschiedene WIMP-Nukleon-Wechselwirkungen zu unterscheiden.

Contents

1 Introduction

1.1 Challenges of modern low-energy nuclear physics

A major goal of physics is to describe the large diversity of physical phenomena we observe based upon a single theory, a theory of everything. Human's closest attempt is the Standard Model of particle physics. Developed already in the 1970s, the Standard Model has had remarkable success describing the interactions of 17 fundamental particles via three out of the four fundamental forces: electromagnetism, the weak, and the strong force (and not including gravity). The Standard Model was able to predict the existence of eight of its constituents including the Higgs boson, which was only observed experimentally recently [1, 2]. Quarks and gluons, the elementary particles subject to the strong force, do not exist in isolation but only as composite states, called hadrons. Among the hadrons there are states of three quarks, the so-called baryons. The most abundant baryons are protons and neutrons, which account for almost all of the visible mass in the universe as they are the building blocks of atomic nuclei.

Modern nuclear physics aims at the description of the diverse properties of atomic nuclei and nuclear matter based on the interaction between nucleons, i.e., protons and neutrons. In addition, atomic nuclei serve as "laboratories" for new physics beyond the Standard Model. As a result, nuclear physics impacts areas well beyond its scope such as astro- and particle physics. This thesis contributes to both the study of nuclear systems as well as to leading research at the very frontier of physics.

The interaction between nucleons is described within quantum chromodynamics (QCD), the quantum field theory of the strong interaction. Calculations of nuclei and dense nuclear matter remain, however, extremely challenging as QCD is non-perturbative in the low-energy regime relevant for nuclear physics. A modern approach consists of performing lattice QCD calculations on a finite grid of discrete points in spacetime [3]. Scattering parameters in the two-particle sector can be extracted from those finite-volume calculations via the formalism derived by Lüscher [4, 5], who showed that the infinite-volume properties of interacting particles are encoded in the volume dependence of their discrete energy levels in finite volume. Due to computational limitations, lattice QCD calculations are, for the time being, constrained to systems of only a few particles. Simulating even very light nuclei will remain challenging for lattice QCD at least in the near future while medium-mass to high-mass nuclei are well beyond its current reach.

At low energies, the nuclear interaction can be described approximately by effective theories, which treat neutrons and protons as fundamental degrees of freedom. A very early theoretical description of the nucleon-nucleon (NN) potential was provided by Yukawa [6]. In his simple picture the NN force is mediated via pions. More sophisticated effective theories have been developed since. In particular, phenomenological potentials have provided a relatively accurate description of nuclear properties lacking, however, a direct connection to the underlying theory of QCD. A more systematic approach was established by Weinberg who laid the foundation for an effective field

theory (EFT) describing the interaction of nucleons and pions directly based on the symmetries of QCD [7]. Based on Weinberg's ideas, chiral EFT was developed, which borrows its name from one of the most important symmetries of QCD. Chiral EFT allows for the construction of nuclear many-body forces and currents in a systematic scheme that yields access to uncertainty estimates. Unresolved short-distance physics, going back to the fundamental interaction between quarks and gluons, is encoded as contact interactions, the coupling coefficients of which are called low-energy constants (LECs). QCD's non-perturbativeness at low energy makes a direct calculation of LECs a very difficult task, although in principle it can be done in lattice QCD. At the moment, however, the LECs are fitted to experimental data. This strategy fails for systems where experimental data are scarce or even nonexistent, which is in particular the case for few-neutron systems. An alternative consists of matching chiral EFT calculations to results obtained within lattice QCD, thus extracting the LECs of chiral EFT directly based on QCD. This thesis takes first steps in this direction by studying few-neutron systems in finite volume, thus generalizing the Lüscher formalism.

The large variety of nuclei on the nuclear chart is a consequence of the nuclear interaction. Departing from the valley of stability towards more neutron-rich nuclei one approaches the neutron drip line, beyond which nuclei are no longer bound as the attraction due to the strong force becomes too weak. From a theoretical point of view, neutron-rich nuclei serve as an unique testing ground of the nuclear force. For example, the importance of chiral three-body forces has been demonstrated recently in calculations of neutron-rich calcium isotopes [8]. Tests of the nuclear force are not constrained to systems of medium- to high-mass nuclei. Few-neutron systems at the low end of the nuclear chart are largely unknown as they are challenging to access experimentally. While a bound tetraneutron has largely been excluded theoretically [9–11], experimental evidence found recently at the RIKEN Radioactive Ion Beam Factory (RIBF) in the double-charge exchange reaction ^{4}He(^{8}He,^{8}Be) indicates that the four-neutron system might exhibit a short-lived resonance [12]. Given the relatively large error of the measured resonance energy of $(0.83 \pm 0.65 \pm 1.25)\,\mathrm{MeV}$, other experiments are currently underway to verify this result [13–15]. While further experimental data will appear in the near future, the initial result has revived much theoretical interest in a possible tetraneutron resonance. Such short-lived systems may be sensitive to details of the nuclear interaction. On the other hand, a significant challenge stems from the fact that, as unbound systems, resonances are difficult to tackle theoretically, in particular for systems comprised of more than two particles. Existing calculations to date [16, 17] mutually disagree on the energy and width of such a state, while other works [18–20] seem to exclude the possibility of such a state altogether. For a possible three-neutron resonance the situation is similar, as both older and recent publications [21–23] judge the existence of such a state to be unlikely. This thesis contributes to this controversial topic by studying the possibility of few-neutron resonances based on interactions from chiral EFT.

Motivated by the wide disparity of theoretical results on possible few-neutron resonances, we also investigate an alternative approach to extract properties of few-particle resonances based on calculations in finite volume. In the two-particle sector, it has been shown that a resonance state shows up as an avoided crossing of energy levels as the size of the finite volume is varied [24]. This technique has been used successfully to extract hadron resonances [25]. The question arises if few-body resonances can also be extracted from finite-volume calculations. Presently, there are no formal derivations for this case. In this thesis, we investigate whether few-particle resonances again show up as avoided crossings in the finite-volume, few-body energy spectrum. Aiming at

establishing this method as a tool for identifying resonance states, empirical results in this direction are also relevant to help and test formal advances regarding the derivation of three-body finite-volume quantization conditions pursued very actively [26–29].

While the Standard Model accounts for the particles that make up the luminous matter, it fails to explain the origin of the large majority of mass in the universe. A wide range of observations from astrophysics and cosmology has led to the conclusion that ordinary, baryonic matter accounts for only about 20% of the mass in the universe. The remaining 80% of the mass consists of some nonluminous form of matter therefore referred to as dark matter.

It is mostly gravitational effects on very large astronomical scales that are accounted for by the concept of dark matter. Evidence is manifold [30]: most prominent are rotation curves of galaxies that show significant deviation from the expectations based on the amount of luminous matter. However, there is also convincing evidence for the necessity of dark matter in the early stages of the universe coming from measurements of the cosmic microwave background as well as studies of Big Bang nucleosynthesis. While there is no doubt about its gravitational influence on luminous matter, the nature of dark matter remains unkown. Particle candidates, many of which have been suggested by extensions of the Standard Model [31], have so far eluded observation. Nevertheless, great effort is being put into dark matter detection experiments. Today, most searches focus on weakly interacting massive particles (WIMPs), which might interact, though weakly, with ordinary matter. Direct detection experiments search for signals of WIMPs scattering off atomic nuclei. WIMPs are expected to interact so weakly with ordinary matter that they are extremely hard to distinguish from other background radiation. These direct detection experiments therefore consist of large amounts of sensitive detector material placed deep underground to shield against background influences. In recent years, active detector masses have reached the ton scale leading to an impressive increase in detector sensitivity. Recently, the highest sensitivity has been reached by the XENON1T experiment at the Italian Laboratori Nazionali del Gran Sasso [32]. The next generation of direct dark matter detectors will cover all the experimentally accessible parameter space until the background from neutrino-nucleus scattering will start to dominate [33]. Thus, we are living in a very exciting phase of the search for dark matter.

While a dark matter signal still remains absent, direct detection experiments provide constraints on the WIMP-nucleon coupling. In order to interpret experimental data correctly, it is mandatory to incorporate nuclear effects stemming from the nucleus as a compound many-body object. While the nature of the interaction between WIMPs and the Standard Model particles, such as quarks and gluons, is of course unknown, the coupling to composite objects such as nucleons should include constraints from QCD. In a second step, one is then able to calculate nucleon form factors describing the coupling of WIMPs to nucleons and consequently to calculate nuclear structure factors describing the response of the whole nucleus. The operators describing the coupling of the WIMP to the nucleon are usually derived in non-relativistic effective theories of nucleons and WIMPs. This approach lacks fundamental properties of the underlying QCD dynamics. In this thesis instead a consistent description of the operators describing the coupling of WIMPs and nucleons including QCD effects in the framework of chiral EFT is presented.

Traditionally, the analysis of dark matter direct detection searches is limited to two different interaction types. This limitation presents a significant constraint on the parameter space of the new physics model studied. As the number of possible operators describing the WIMP-nucleon interaction is very large, a useful extension of the standard analysis should take into account only the

dominant corrections. Therefore, the corresponding nuclear responses need to be ordered according to their strength when assuming the same WIMP-nucleon coupling strengths in all channels. This thesis investigates nuclear structure effects leading to enhancements of the nuclear responses of particular operators. Based on this, an extension of the standard analysis is proposed, which allows for a more systematic analysis of direct detection experiments in the future.

This thesis is organized as follows: In the remainder of this chapter, the basics of chiral EFT will be summarized before the focus of this thesis will be discussed in more detail. This chapter ends with an introduction of the different numerical methods used throughout this thesis. In Chapter 2, we study two-neutron systems confined in a cubic box with periodic boundary conditions. We compare to results obtained with both a toy contact potential and local chiral potentials to predictions from the Lüscher formalism. In Chapter 3, possible three- and four-neutron resonance energies are extracted from quantum Monte Carlo calculations based on chiral potentials. The extraction of resonance parameters is also the subject of Chapter 4 where we return to finite volume systems. We provide evidence that the resonance energy can be obtained from avoided level crossings in the discrete energy spectrum of three and four particles.

In the second part of this thesis, we turn to the study of nuclear response functions for WIMP-nucleus scattering. We collect the relevant operator structures in Chapter 5, before we continue and analyze nuclear structure effects in Chapter 6. We propose an extension of the traditional operator basis used in the analysis of dark matter direct detection experiments. Applications of our formalism are presented in Chapter 7. We show how two-body operators from chiral EFT can contribute to improvements of limits of the WIMP-nucleon coupling obtained in collider searches. In addition, we study to what extent current and future detectors are able to distinguish between different interaction types provided a dark matter signal is found. Finally, we conclude in Chapter 8 and provide an outlook.

1.2 Chiral effective field theory

From the early days to the present advances in nuclear physics, the description of the nuclear force has been one of the main challenges in the field. Performing calculations of nuclear physics observables at low energies is highly non-trivial even though the fundamental theory of the strong interaction, quantum chromodynamics (QCD), is known. In this section, we explain that a direct application of QCD to problems of nuclear physics is in most cases not feasible and we discuss the modern approach of using effective field theories (EFTs). In particular, we focus on chiral EFT, which allows for a systematic construction of nuclear forces and currents. This section outlines a local representation of the chiral forces in coordinate space and presents an introduction to chiral currents. The local chiral forces are used throughout this thesis for different applications ranging from the finite-volume calculations in Chapter 2 to the study of few-neutron resonances in Chapter 3. Nucleon currents derived in chiral EFT will be the starting point of our extended analysis of WIMP-nucleus scattering in Chapters 5, 6, and 7.

This section is based on the extensive reviews provided in Refs. [34, 35], which we refer the reader to for a more detailed discussion.

1.2.1 Quantum chromodynamics

There are four known fundamental forces in nature: Gravity, electromagnetism, the weak force and the strong force. All of these, except for gravity, have been unified in the Standard Model of particle physics, which has been extremely successful in the description of a wide range of phenomena. For nuclear physics the most relevant interaction is the strong force because it explains the formation of nucleons and their binding in nuclei.

The gauge theory of the strong interaction, QCD, describes the interaction of the fundamental degrees of freedom, quarks (spin-1/2 fermions) and gluons (vector bosons). There are six different quark flavors (up u, down d, strange s, charm c, bottom b, top t). These quark fields have an additional degree of freedom called "color", which was introduced after the discovery of the Δ^{++} particle, which without the color degree of freedom would be forbidden by the Pauli principle. There are three color states, red (r), green (g), and blue (b), which give rise to the underlying $SU(3)$ gauge group. The antiparticles carry the corresponding "anti-color", i.e., $\bar{\text{r}}$ (antired), $\bar{\text{g}}$, and $\bar{\text{b}}$. In order for the Lagrangian of the theory to be locally gauge invariant, the gauge fields of QCD, called gluons, are introduced. With these ingredients, the QCD Lagrangian is given by

$$\mathcal{L}_{\text{QCD}} = \sum_{f=u,d,s,c,b,t} \bar{q}_f (i\not{D} - m_f) q_f - \frac{1}{2} \mathcal{G}^a_{\mu\nu} \mathcal{G}^{a\mu\nu}, \tag{1.1}$$

where q_f and m_f denote the quark fields and their respective masses. The covariant derivative reads $D_\mu = \partial_\mu + i g_s \mathcal{A}_\mu$ with the gluon field $\mathcal{A}_\mu$ and the strong coupling constant g_s. The field-strength tensor used above is defined as

$$\mathcal{G}^a_{\mu\nu} = \partial_\mu \mathcal{A}_{a\nu} - \partial_\nu \mathcal{A}_{a\mu} - g_s f_{abc} \mathcal{A}_{b\mu} \mathcal{A}_{c\nu}, \tag{1.2}$$

with f_{abc} denoting the totally antisymmetric real structure constants of $SU(3)$. The implicit sums run over the color indices $a, b, c = 1, ..., 8$ of the adjoint representation.

In nature, only composite systems of at least two quarks that are confined to color-singlet states, called hadrons, are found. These color-singlets can either be formed by systems of quarks and antiquarks that cancel their respective colors (such as an $r\bar{r}$ state) or states consisting of all three colors such as rgb. Naturally, this implies two-quark states, called mesons and three-quark states called baryons. However, there has been experimental evidence of a five quark state, which consists of four quarks and a single antiquark [36], and a four-quark state is currently under investigation [37].

The coupling strength α_s of the strong interaction is momentum dependent [38, 39]

$$\alpha_s = \frac{g_s^2}{4\pi} = \frac{4\pi}{b_0} \log^{-1} \frac{Q}{\Lambda_{\text{QCD}}}, \tag{1.3}$$

with $b_0 = (33 - 2N_f)/(12\pi)$, the number of flavors N_f, the characteristic scale of QCD $\Lambda_{\text{QCD}} \approx (200 - 400)\,\text{MeV}$ and the momentum Q. At very high energies $\alpha_s \ll 1$ and the quarks become approximately free particles, an effect also known as asymptotic freedom. However, at low momenta $Q \lesssim 1\,\text{GeV}$ the coupling strength $\alpha_s \gg 1$ causes QCD to be highly non-perturbative. As a consequence, calculations of nuclear observables directly from QCD are extremely challenging. Presently, solving QCD on a lattice of discretized Euclidian space-time presents the only available *ab initio* technique to approach this problem. This method is referred to as lattice QCD (see also Sec. 1.3.1). Extensive reviews on the subject can be found in Refs. [3, 25]. Lattice QCD not only discretizes space-time but also constrains space and time to finite extends in order to limit the required computational resources. Hence, the results need to be extrapolated to continuous space-time and infinite volumes. Furthermore, lattice QCD calculations are often performed with non-physical quark masses, making direct comparisons to experimental data impossible. In addition, calculations rely on huge computational resources, which constrains the accessible number of particles significantly. Nevertheless, lattice QCD has been able to predict masses of the lightest hadrons [40]. Very light nuclei at unphysical quark masses have been calculated in lattice QCD in Refs. [41–43].

We continue and discuss some important features of QCD, which will become relevant later when we focus on effective descriptions of the nuclear force. The six quark flavors can be grouped into three light quarks, u, d, and s with masses of roughly 2 MeV, 5 MeV, and 100 MeV, respectively, and three heavy quarks c, b, and t with masses greater than 1 GeV. Typical momenta and binding energies in the regime of low-energy nuclear physics are of the order of a few MeV per nucleon. Therefore, in order to describe the interaction between nucleons it is sufficient to only include the lightest quarks u, d, and s. We neglect the light quark masses and study the QCD Lagrangian in this so-called chiral limit, i.e., $m_u, m_d, m_s \to 0$:

$$\mathcal{L}^0_{\text{QCD}} = \sum_{l=u,d,s} \bar{q}_l i \not{D} q_l - \frac{1}{2} \mathcal{G}^a_{\mu\nu} \mathcal{G}^{a\mu\nu}. \tag{1.4}$$

Next, we define the projection operators

$$P_R = \frac{1}{2}(1+\gamma_5), \qquad P_L = \frac{1}{2}(1-\gamma_5), \tag{1.5}$$

$$q_R = P_R q\,, \qquad q_L = P_L q\,, \tag{1.6}$$

which project onto right-handed and left-handed fields. With this, we can rewrite the QCD Lagrangian in the chiral limit as

$$\mathcal{L}^0_{\text{QCD}} = \sum_{l=u,d,s} (\bar{q}_{R,l} i \not{D} q_{R,l} + \bar{q}_{L,l} i \not{D} q_{L,l}) - \frac{1}{2} \mathcal{G}^a_{\mu\nu} \mathcal{G}^{a\mu\nu}\,. \tag{1.7}$$

This Lagrangian is invariant under separate transformations of the left- and right-handed fields, i.e., under the so-called chiral symmetry $SU(3)_L \times SU(3)_R$ transformations. If this symmetry was exact, the hadron spectrum would be organized in degenerate multiplets of irreducible representations of the group $SU(3)_L \times SU(3)_R$. As a consequence parity partners, i.e., partners with the same quantum numbers but opposite parity, would be degenerate in mass, also known as parity doubling. However, the parity partners we observe in nature have very different masses. This is a consequence of the spontaneous symmetry breaking of the QCD Lagrangian. As an additional consequence, Goldstone's theorem predicts for every symmetry that is spontaneously broken a massless excitations of the vacuum, the so-called Goldstone bosons [44]. In addition to the spontaneous breaking, the $SU(3)_L \times SU(3)_R$ symmetry is also explicitly broken due to the finite quark masses. This breaking is weaker when we constrain the QCD Lagrangian to the two lightest quark flavors u and d, which have very small masses, reducing the flavor symmetry to the $SU(2)$ isospin symmetry.

The explicit symmetry breaking in the low-energy QCD Lagrangian causes the Goldstone bosons to be massive. The latter are therefore called pseudo-Goldstone bosons, which can be identified with the pions, kaons and the eta. The pion is the lightest with a mass of $m_\pi \approx 138\,\text{MeV}$ significantly lower than the naive expectation of two thirds of the nucleon mass based on the quark content of the pion.

1.2.2 Effective field theories for low-energy nuclear physics

As an alternative to direct solutions of QCD, EFTs of QCD have been developed that are valid in the regime of low-energy nuclear physics. An EFT describes the degrees of freedom relevant below some scale Λ_b based on the most general Lagrangian consistent with the symmetries of the underlying theory. In nuclear EFTs, multi-body forces appear that describe the coupling of three or more nucleons. This is a consequence of the fact that the nucleons are composite objects of quarks and gluons. Naturally, the Lagrangian of an EFT will contain infinitely many terms. In order to perform calculations an ordering scheme is required that limits the number of terms that need to be included. Therefore, the different contributions in the Lagrangian are ordered in terms of powers of a low-momentum scale, i.e., typical momenta or masses in the energy regime of the EFT. Thus, in order to reach a specific accuracy, only a finite number of terms of the EFT Lagrangian needs to be included.

The EFT Lagrangian comes with a set of so-called low-energy constant (LEC) that account for heavy degrees of freedom not described by the EFT. In principle, the LECs can be derived from the underlying theory of QCD. As this requires direct solutions of QCD, one usually resorts to fitting the LECs to experimental data.

At very low energies, the interaction between nucleons is governed by the large S-wave scattering lengths, e.g., for the proton-neutron system $a(^1S_0) = -23.8\,\text{fm}$, $a(^3S_1) = 5.4\,\text{fm}$ and for the neutron-neutron system $a(^1S_0) = -18.9\,\text{fm}$ [45]. These exceed the Compton wave length of the pion, which is $1/m_\pi \approx 1.4\,\text{fm}$. As a result, a pionless EFT, where the only relevant degrees of freedom are the nucleon momenta, is sufficient in this regime. The corresponding Lagrangian is given by a series of contact interactions between nucleons N,

$$\mathcal{L} = N^\dagger \left(i\partial_t + \frac{\nabla^2}{2M} \right) N - C_{0t}(N^\dagger P_t N)^2 - C_{0s}(N^\dagger P_s N)^2 + \dots , \tag{1.8}$$

where P_s and P_t are the projectors on $S = 0$ and $S = 1$ states, respectively, and M is the nucleon mass [46, 47]. The LECs are denotes as C_i.

For nucleons in nuclei or nuclear matter, typical momentum scales are of the order of the pion mass and, as a result, pion exchanges between nucleons need to be taken into account. Already in the 1930s, Yukawa suggested that the strong force is mediated by a massive field, which was later identified with the pion [6]. From the perspective of low-energy QCD, it is natural to include the lightest meson as the exchange particle. In the 1990s Weinberg introduced such a theory constructed as an expansion around the chiral limit. The theory is therefore referred to as chiral EFT [7, 48, 49]. The low-momentum scale of chiral EFT is of the order of the pion mass, i.e., $Q \sim m_\pi$, while the breakdown scale Λ_b is set roughly by the mass of heavier degrees of freedom that are not incorporated in the theory. The lightest mesons without a strange quark beyond the pseudo-Goldstone bosons of the broken symmetry are the ρ ($m_\rho = 775\,\text{MeV}$) and the ω ($m_\omega = 780\,\text{MeV}$). While the exact value of the breakdown scale of chiral EFT is still investigated, usually one assumes $\Lambda_\text{b} \approx 500\,\text{MeV}$, leading to an expansion parameter of $Q/\Lambda_\text{b} \approx 1/3$. Excitations of the nucleon such as the Δ isobar ($m_\Delta = 1232$) are not explicitly included in chiral EFT even though the mass difference to the nucleon is only about 300 MeV. As a consequence, some of the LECs in chiral EFT are unnaturally large. We will use Δ-less chiral EFT throughout this thesis, however, there are efforts to develop a Δ-full chiral EFT [50].

The different terms of the Lagrangian can be organized according to their power in the expansion parameter Q/Λ_b, where the low-momentum scale Q is given by $Q = \max(p, m_\pi)$ with the typical momentum p. In chiral EFT, the order λ of every term in the chiral Lagrangian is given by

$$\lambda = d + e + \frac{n}{2} - 2 , \tag{1.9}$$

where d counts derivatives or pion masses, e external fields, and n is the number of nucleon fields. The lowest order ($\lambda = 0$) Lagrangian is labeled as leading-order (LO) while higher-order terms

belong to the next-to-leading (NLO) order ($\lambda = 1$) Lagrangian, the next-to-next-to-leading (N^2LO) order ($\lambda = 2$) Lagrangian and so on. The lowest orders of the chiral Lagrangian read [51]

$$\begin{aligned}
\mathcal{L}^{(0)} =& \frac{1}{2}\partial_\mu \boldsymbol{\pi}\cdot\partial^\mu\boldsymbol{\pi} - \frac{1}{2}m_\pi^2\boldsymbol{\pi}^2 + N^\dagger\left[i\partial_0 + \frac{g_A}{2F_\pi}\boldsymbol{\tau}\boldsymbol{\sigma}\cdot\nabla\boldsymbol{\pi} - \frac{1}{4F_\pi^2}\boldsymbol{\tau}\cdot(\boldsymbol{\pi}\times\dot{\boldsymbol{\pi}})\right]N \\
& - \frac{1}{2}C_S(N^\dagger N)(N^\dagger N)\frac{1}{2} - C_T(N^\dagger\boldsymbol{\sigma}N)(N^\dagger\boldsymbol{\sigma}N) + \ldots, \\
\mathcal{L}^{(1)} =& N^\dagger\left[4c_1 m_\pi^2 - \frac{2c_1}{F_\pi^2}m_\pi^2\boldsymbol{\pi}^2 + \frac{c_2}{F_\pi^2}\dot{\boldsymbol{\pi}}^2 + \frac{c_3}{F_\pi^2}(\partial_\mu\boldsymbol{\pi}\cdot\partial^\mu\boldsymbol{\pi}) - \frac{c_4}{2F_\pi^2}\epsilon_{ijk}\epsilon_{abc}\sigma_i\tau_a(\nabla_j\pi_b)(\nabla_k\pi_c)\right]N \\
& - \frac{D}{4F_\pi}(N^\dagger N)(N^\dagger\boldsymbol{\sigma}\boldsymbol{\tau}N)\cdot\nabla\boldsymbol{\pi} - \frac{1}{2}E(N^\dagger N)(N^\dagger\boldsymbol{\tau}N)\cdot(N^\dagger\boldsymbol{\tau}N) + \ldots,
\end{aligned} \tag{1.10}$$

where N and π are nucleon and pion fields, respectively, and we denote the axial coupling as g_A and the pion decay constant as F_π. The superscripts denote $\lambda = 0, 1$, the LECs are denoted by c_i, C_S, C_T, D, and E, and the ellipses refer to terms with more pion fields and/or derivatives.

1.2.3 Chiral EFT interactions

Given the chiral Lagrangians, one can proceed and derive the scattering amplitude for a given process by constructing all contributing Feynman diagrams from the fundamental vertices given in the Lagrangian and the connecting propagators. The chiral order of a diagram discribing the interaction of nucleons with each other and/or with external fields is given by [7, 35]

$$\nu = 2(N - C) + 2L - 2 + \sum_i \lambda_i\,, \tag{1.11}$$

with the nucleon number N, C the number of disconnected parts, L the number of loops and λ_i the chiral order of the vertices that appear in the diagram. This procedure gives rise to both the nuclear forces describing the coupling of two or more nucleons to each other and the nuclear currents describing the coupling of an external field to one or more nucleons. In Figure 1.1, the hierarchy of nuclear forces according to Eq. (1.11) is shown. At LO and NLO, there are only nucleon-nucleon forces present while at N^2LO, three-body forces appear for the first time. The predictive power of an effective theory such as chiral EFT is based on the fact that once the LECs that appear up to a particular order have been determined, calculations of observables with the same accuracy are possible. In particular, the LECs can be fitted in systems that are easier to access experimentally. For example, for the leading $3N$ forces at N^2LO three out of five LECs are predicted by the NN sector. Hence, the three LECs that appear in the NN forces can be fitted to pion-nucleon and nucleon-nucleon scattering data and only two LECs need to be adjusted in three-body systems.

Starting from the chiral Lagrangians in Eq. (1.10), the nuclear forces and currents are typically derived in momentum space by performing a nonrelativistic expansion of the amplitudes. The leading order contact interaction arises from $\mathcal{L}^{(0)}$ (see also diagram in Fig. 1.1) and has two terms

$$V_{\text{cont}}^{(0)} = C_S + C_T\boldsymbol{\sigma}_1\cdot\boldsymbol{\sigma}_2\,, \tag{1.12}$$

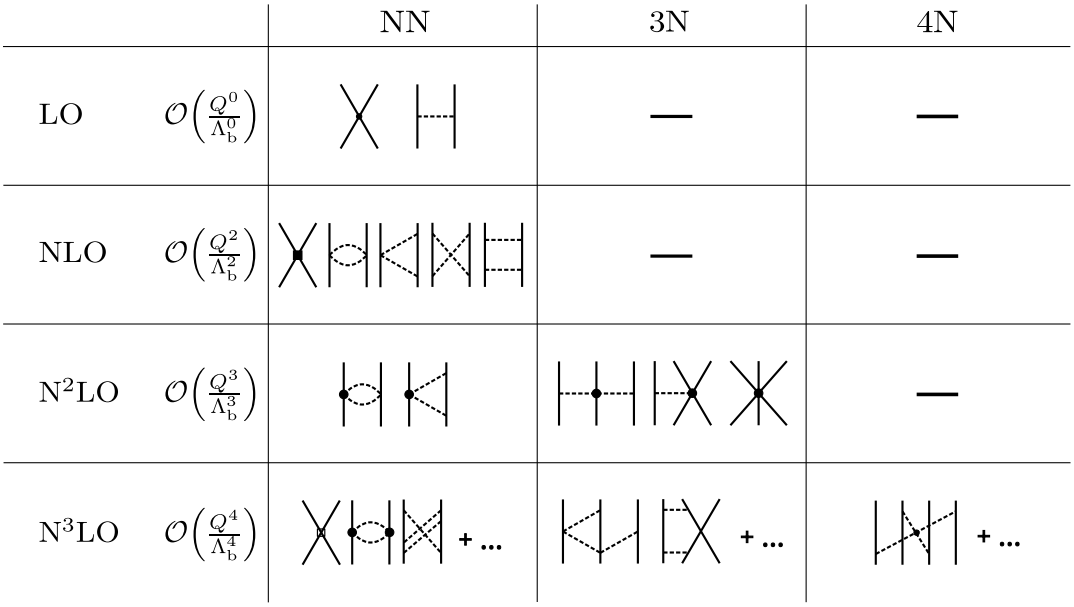

Figure 1.1: Nuclear forces from chiral EFT up to next-to-next-to-next-to leading order (N^{3}LO). Solid lines represent nucleons while pions are shown as dashed lines. The low-energy constants are shown as the different symbols at the vertices.

which describe the two S-wave channels allowed for nucleons, i.e., ${}^3S_1$ and ${}^1S_0$, and are therefore obtained by fitting to the corresponding phase shifts. The one-pion-exchange (OPE) potential

$$V_{\text{OPE}}^{(0)} = -\frac{g_A^2}{4F_\pi^2}\frac{\boldsymbol{\sigma}_1\cdot\mathbf{q}\,\boldsymbol{\sigma}_2\cdot\mathbf{q}}{q^2+m_\pi^2}\boldsymbol{\tau}_1\cdot\boldsymbol{\tau}_2\,, \tag{1.13}$$

where $\mathbf{q} = \mathbf{p}' - \mathbf{p}$ with the initial and final relative momenta of the two nucleons $\mathbf{p}$ and $\mathbf{p}'$, respectively, is entirely predicted by the pion decay constant such that there are no LECs that would have to be fitted. At higher orders, the number of diagrams increases since apart from new contact interactions, pion-loop diagrams as well as two- and more pion exchanges need to be taken into account. For a comprehensive summary of all expressions for the chiral interactions, we refer to Refs. [52, 53].

In non-perturbative summations of the chiral interactions, such as in the Lippmann-Schwinger equation, divergences occur. The usual approach to this issue is to apply a cutoff Λ to the integrals in form of regulating functions multiplied to the expressions of the forces and currents. These functions remove the high-momentum parts of the interactions. When applying the Weinberg power counting as in Eq. (1.11), not all positive powers of Λ are absorbed. Therefore, current calculations use regulating functions with a relatively small range of cutoffs roughly of the order of the breakdown scale Λ_b, e.g., $\Lambda \sim 500\,\text{MeV}$.

Several few- and many-body techniques, among which there are QMC methods employed in Chapters 2 and 3 as well as the DVR method in Chapter 4, require a local formulation of the inter-particle potentials in coordinate space, i.e., potentials that satisfy

$$V(\mathbf{r},\mathbf{r}') = \langle \mathbf{r}'|\hat{V}|\mathbf{r}\rangle = V(\mathbf{r})\delta^{(3)}(\mathbf{r}-\mathbf{r}'), \tag{1.14}$$

where $\mathbf{r}$ is the inter-particle separation. The coordinate-space expressions are obtained by Fourier transforming the momentum-space expressions of a given potential. Terms that only depend on the momentum transfer $\mathbf{q}$ between two particles are local. However, the chiral potentials are in general nonlocal as the contact interactions and parts of the pion-exchange terms that appear at N^{3}LO and beyond depend on $\mathbf{k} = (\mathbf{p}+\mathbf{p}')/2$, which does not transform into the delta-function in Eq. (1.14). Another source of nonlocality are the momentum-space regulating functions usually of the form $f(p) = \exp\big(-(p/\Lambda)^{2n}\big)$. It is, however, possible to construct a local form of the chiral potentials in coordinate space. In Refs. [54, 55], such a local potential has been presented and applied in Quantum Monte Carlo calculations. For the intrinsic nonlocalities of the chiral forces, this was achieved by replacing $\mathbf{k}$-dependent terms by using a different basis of short-range operators than the one usually used in the chiral potentials in momentum space. This approach is, however, constrained to the chiral forces up to N^{2}LO. For contributions at higher orders, it is not possible to construct a local representation. A local version of the three-nucleon forces at N^{2}LO has been derived recently in Ref. [56]. Local chiral potentials have been applied in calculations of neutron matter, light nuclei, and neutron-alpha scattering [54–58].

In order to avoid the nonlocalities attributed to the regulating functions, the momentum-space expressions of the nuclear forces are Fourier transformed without regulating function. In coordinate space, the expression of the LO contact terms in Eq. (1.12) is then given by

$$V_{\text{cont}}(\mathbf{r}) = (C_S + C_T \boldsymbol{\sigma}_1\cdot\boldsymbol{\sigma}_2)\delta(\mathbf{r}), \tag{1.15}$$

while we obtain for the LO term in Eq. (1.13)

$$V_{\text{long}}(r) = \frac{m_\pi^3}{12\pi}\left(\frac{g_A}{2F_\pi}\right)^2 \frac{e^{-m_\pi r}}{m_\pi r}\boldsymbol{\tau}_1\cdot\boldsymbol{\tau}_2\left[\boldsymbol{\sigma}_1\cdot\boldsymbol{\sigma}_2 + \left(1+\frac{3}{m_\pi r}+\frac{3}{(m_\pi r)^2}\right)S_{12}\right], \tag{1.16}$$

where $S_{12} = (3\boldsymbol{\sigma}_1\cdot\hat{\mathbf{r}}\boldsymbol{\sigma}_2\cdot\hat{\mathbf{r}} - \boldsymbol{\sigma}_1\cdot\boldsymbol{\sigma}_2)$. Both parts need to be regularized. The δ-function in the contact terms is replaced by a smeared one

$$\delta(\mathbf{r}) \to \delta_{R_0}(\mathbf{r}) = \frac{1}{\pi\Gamma(3/4)R_0^3} e^{-(r/R_0)^4}, \tag{1.17}$$

and the long-range parts, i.e., the one- and two-pion-exchange terms, are multiplied by regulator function

$$V_{\text{long}}(r) \to V_{\text{long}}(r)\Big(1 - e^{-(r/R_0)^4}\Big), \tag{1.18}$$

where R_0 is the coordinate-space cutoff. In Refs. [54, 55], the cutoff was varied between $R_0 = (0.8-1.2)\,\text{fm}$, which corresponds roughly to momentum-space cutoffs between 600 MeV and 400 MeV. The corresponding low-energy constants were obtained by fitting to nucleon-nucleon phase shifts. The two-pion exchange terms contain additional divergences which are taken care of by a spectral-function regularization [59].

Currents from chiral EFT

Similar to the nuclear forces, the nuclear currents describing the coupling of nucleons and pions to external fields can be derived from the chiral Lagrangian. For the chiral currents, the counting scheme in Eq. (1.11) is slightly modified to avoid negative powers of Q/Λ_b in the counting:

$$\nu = 2(N-C) + 2L + \sum_i \lambda_i \,. \tag{1.19}$$

The currents involved in the electroweak interaction are of vector [60–62] and axial-vector [63–65] type. A detailed derivation of the tree level amplitudes can be found in Ref. [66]. The leading order one-body vector current in momentum space reads

$$V_{\text{1b}}^{a\mu} = \bar{u}(p')\gamma^\mu \frac{\tau^a}{2} u(p)\,, \tag{1.20}$$

and corresponds to a direct coupling of the external field to the nucleon as shown in Fig. 1.2 (a). Expansion of the Dirac bilinears yields the non-relativistic limit of the time and space components of the vector current

$$V_{\text{1b}}^{a0} = \frac{\tau^a}{2}\,, \tag{1.21}$$

$$\mathbf{V}_{\text{1b}}^{a} = \frac{1}{2M}\frac{\tau^a}{2}\left(\mathbf{P} - i\boldsymbol{\sigma}\times\mathbf{q}\right), \tag{1.22}$$

where $\mathbf{P} = \mathbf{p} + \mathbf{p}'$ and $\mathbf{q} = \mathbf{p} - \mathbf{p}'$ and M is the nucleon mass. The chiral order of the temporal component is $\nu = 0$. In contrast, the spatial part is suppressed by $1/M$ in the non-relativistic limit, which we count as an additional suppression of two powers, so that its chiral order is $\nu = 2$. An

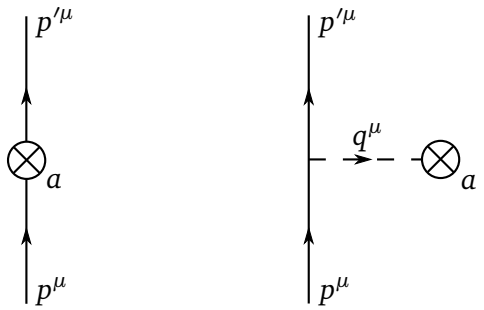

(a) (b)

Figure 1.2: Leading order one-body currents. Solid lines are nucleons, dashed lines correspond to pions and the crossed circles indicate the external particle.

additional contribution at $\nu = 1$ comes from the chiral NLO Lagrangian, which depends on the LECs c_6 and c_7:

$$V_{1\mathrm{b}\ c_6,c_7} = -\frac{1}{M}\left(\frac{c_6}{8}\tau^a + \frac{c_7}{4}\right)(\mathbf{q} + i(\mathbf{P}\times\boldsymbol{\sigma}))\cdot\mathbf{q}\,, \tag{1.23}$$

$$\mathbf{V}_{1\mathrm{b}\ c_6,c_7} = -i\left(\frac{c_6}{4}\tau^a + \frac{c_7}{2}\right)(\boldsymbol{\sigma}\times\mathbf{q})\,. \tag{1.24}$$

Both diagrams in Fig. 1.2 contribute to the leading axial one-body current. The non-relativistic limit up to $1/M$ of the temporal and spatial parts of the axial one-body current read

$$A^{0a}_{1\mathrm{b}} = \frac{\tau^a}{2} g_A(\mathbf{q}^2)\frac{\boldsymbol{\sigma}\cdot\mathbf{P}}{2M}\,, \tag{1.25}$$

$$\mathbf{A}^{a}_{1\mathrm{b}} = \frac{\tau^a}{2}\left(g_A(\mathbf{q}^2)\boldsymbol{\sigma} - \frac{g_P(\mathbf{q}^2)}{2M}(\mathbf{q}\cdot\boldsymbol{\sigma})\mathbf{q}\right), \tag{1.26}$$

with the axial and pseudoscalar form factors g_A and g_P [67]. The chiral order of Eq. (1.25) is $\nu = 2$, whereas we have for Eq. (1.26) that $\nu = 0$, regardless of the factor $1/M$ in the second term since $\frac{g_P}{M} \sim 1$.

In addition to one-body currents, the chiral Lagrangian gives rise to many-body currents describing the coupling of the external source to more than one nucleon line. The expressions can be obtained by multiplying all factors associated to vertices and propagators stemming from the chiral Lagrangian. One can distinguish between two kinds of tree-level two-body current diagrams. First, there are pion-exchange currents, where the two nucleons interact via pion exchange, shown in Fig. 1.3 (a) and (b). A special case is diagram (c) where the external particle couple to the pion "in flight". Second, a direct coupling of the two-nucleons is also possible as depicted in Fig. 1.3 (d) and (e). In both cases, the external source can couple to the nucleons either directly, see diagrams (a) and (d), or via the exchange of an additional pion, see (b) and (e). Not all diagrams contribute to all types of currents. For example, the leading axial-vector two-body currents correspond to diagrams (a), (b), (d), and (e), while the leading two-body vector currents correspond to diagrams (a) and (c) only.

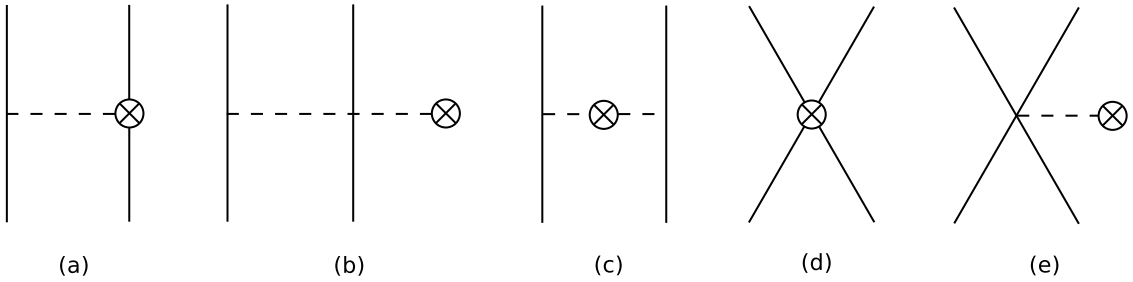

Figure 1.3: Chiral two-body currents at tree level. Solid lines are nucleons, dashed lines correspond to pions and the crossed circles indicate the external particle.

The scalar and pseudoscalar one- and two-body currents and the chiral power counting of various different types of currents will be discussed in Chapter 5.

1.3 Focus of this thesis

In the following, we set the stage by providing an introduction to the three research areas to which this thesis contributes. We start with a motivation for studies of few-nucleon systems in finite volume in Sec. 1.3.1. Next, we turn to the search for few-neutron resonances that has a long history in nuclear physics as we discuss in Sec. 1.3.2. Finally, in Sec. 1.3.3 we provide a broad introduction to the physics of dark matter and discuss why nuclear physics is important for experimental efforts searching for dark matter particles.

1.3.1 Few nucleons in finite volume from chiral EFT

The fundamental theory describing the interactions between quarks and gluons is quantum chromodynamics (QCD). Nucleons and pions, the effective degrees of freedom in nuclear physics, are composite particles of quarks and gluons and the nuclear force is a result of the interaction among the latter at a fundamental level. One of the central goals of nuclear physics is the calculation of nuclear observables directly from the underlying theory of QCD. We have discussed in Sec. 1.2 that due to the non-perturbative nature of QCD at low energies the only presently available technique to reach this goal is lattice QCD. We outline here the basics of lattice QCD. For a more comprehensive picture we refer the reader to the reviews in Refs. [3, 25]. In lattice QCD, in order to perform non-perturbative calculations, quark and gluon fields are quantized on a discrete grid of space-time points. In practical numerical calculations, the size of this grid is necessarily finite in all four space-time directions. The Euclidean partition function of QCD in the path integral formulation is

$$\mathcal{Z} = \int \mathcal{D}A_\mu \mathcal{D}\bar{\psi}\mathcal{D}\psi \, e^{-S[A_\mu]}, \tag{1.27}$$

where $S = \int d^4x \, \mathcal{L}_{\text{QCD}}$ is the QCD action with the QCD Lagrangian $\mathcal{L}_{\text{QCD}}$ defined in Eq. (1.1) with the quark fields ψ and the gluon gauge field A_μ. The integral $\int \mathcal{D}A_\mu \mathcal{D}\bar{\psi}\mathcal{D}\psi$ is over all possible configurations of the gauge and quark fields. Physical observables can be calculated from the correlation functions of operators $\mathcal{O}$ that depend on the quark and gluon fields:

$$\langle \mathcal{O} \rangle = \frac{1}{\mathcal{Z}} \int \mathcal{D}A_\mu \mathcal{D}\bar{\psi}\mathcal{D}\psi \, \mathcal{O} \, e^{-S[A_\mu]}. \tag{1.28}$$

In lattice QCD, this path integral is discretized on a grid of discrete space-time points by using an appropriate formulation of the QCD action. It is possible to evaluate the fermionic part of the path integral giving a determinant, which can be incorporated in a modified action $\tilde{S}$, leaving only the integral over the gauge field

$$\mathcal{Z} = \int \mathcal{D}A_\mu \, e^{-\tilde{S}(A_\mu)}. \tag{1.29}$$

The exponential $e^{-\tilde{S}(A_\mu)}$ is positive definite and can be interpreted as a probability density function of gluon field configurations sampled via Monte Carlo techniques similar to the Quantum Monte

Carlo methods, which will be discussed in Sec. 1.4.2. Now, it is possible to use these configurations to calculate the correlation function and obtain a statistical estimate by averaging over the set of configurations. The distance between adjacent lattice sites, called lattice spacing a, being finite introduces an ultraviolet cutoff. Furthermore, the lattice spacing needs to be smaller than the characteristic hadronic length scale of the system. There are techniques to systematically remove the effect of a finite lattice spacing.

On the other hand, the finite size of the spatial volume, which is usually taken as a cube of edge length L, introduces an infrared cutoff. As the boundary conditions are usually periodic for the spatial directions, the free-particle momenta are given by $\mathbf{p} = \frac{2\pi}{L}(n_x, n_y, n_z)$ with integer numbers n_i. In the time direction, the boundary conditions are anti-periodic for fermion fields and periodic for gauge fields. The finite size in the time direction effectively puts the system at a finite temperature. Therefore, the extend of the lattice in the time direction is usually larger than for the spatial directions as one tries to approach the zero-temperature limit. Lattice QCD calculations recover the full QCD result in the limit $L \to \infty$ and $a \to 0$.

Due to computational limitations, lattice QCD simulations of systems of more than one nucleon are restricted to unphysical masses of the lightest quarks (up and down) as the required computational resources increase with decreasing quark mass. As a result, the calculated masses of hadrons become significantly larger than the physical values. Typically, this effect is quantified by stating the pion mass of a given lattice QCD calculation. Today, calculations usually operate with a pion mass of $m_\pi \sim 200\,\text{MeV}$, while some calculations have reached the physical point. For example, calculations of the light hadron spectrum were performed with the physical quark masses in Ref. [40]. Systems of more than one nucleon are more complex and therefore require larger lattice sizes and a better accuracy to account for the fine-tuned nuclear force. Only very recently has lattice QCD been able to calculate properties of very light nuclei, however, at $m_\pi = 805\,\text{MeV}$ [42, 43] and $m_\pi = 510\,\text{MeV}$ [41]. A selection of the calculated binding energies of light nuclei together with the corresponding pion and nucleon masses obtained in these studies is shown in Table 1.1.

The restriction to finite volumes has significant consequences for the description of scattering processes. The asymptotic states, the states of the system where the particles are at very large relative distances, cannot be described by confined states as they will be affected by the boundary conditions. In addition, the finite-volume spectrum is discrete while in the real world there are continuum states that can have any continuous value of momentum. Nevertheless, it is possible to get access to the two-particle scattering amplitude from finite-volume calculations. Lüscher [4, 5] extended previous results obtained in non-relativistic quantum mechanics [68, 69] to quantum field theory. The volume dependence of the two-particle energy levels in the finite volume can be used to extract the scattering phase shift in the infinite volume by means of the Lüscher formula

$$p \cot \delta_0(p) = \frac{1}{\pi L} S\left(\left(\frac{Lp}{2\pi}\right)^2\right), \tag{1.30}$$

where p denote the discrete momenta of the finite volume states, L is the box size and δ_0 is the S-wave phase shift. The function $S(\eta)$ together with a more detailed discussion and a brief derivation of the Lüscher formula is provided in Chapter 2. There are similar formulas describing the mass shift of bound states in a finite volume [70–73] including the extension to more than two particles [74, 75]. For scattering states, however, the situation is more complicated and the

m_π	140	510	805	805
Nucleus	[Nature]	[41]	[42]	[79]
n	939.6	1320.0	1634.0	1634.0
p	938.3	1320.0	1634.0	1634.0
nn	-	7.4 ± 1.4	15.9 ± 3.8	15.9 ± 3.8 *
D	2.224	11.5 ± 1.3	19.5 ± 4.8	19.5 ± 4.8 *
^{3}n	-			-
^{3}H	8.482	20.3 ± 4.5	53.9 ± 10.7	53.9 ± 10.7 *
^{3}He	7.718	20.3 ± 4.5	53.9 ± 10.7	53.9 ± 10.7
^{4}He	28.30	43.0 ± 14.4	107.0 ± 24.2	89 ± 36
^{5}He	27.50			98 ± 39
^{5}Li	26.61			98 ± 39
^{6}Li	32.00			122 ± 50

Table 1.1: Experimental and lattice QCD data of the neutron and proton masses and binding energies of the lightest nuclei in MeV taken from Refs. [41, 42] at various values of the pion mass. The last column shows results obtained by fitting a pionless theory to the lattice QCD results marked with * and predictions for a range of Helium and Lithium isotopes. Table taken from Ref. [79] where a more detailed discussion is provided.

extension to the three-particle sector is subject of very active research [26–29]. For two particles, the Lüscher approach is commonly used to extract the scattering parameters of light hadrons such as the pion-pion scattering length [76]. In the regime of nuclear physics, where the nonanalyticities from pion exchange become important, the Lüscher result is not applicable as it corresponds to an EFT in which particles interact only via contact interactions [77]. Exponential corrections to the Lüscher formula scale as $\exp(-m_\pi L)$ and become relevant at small box sizes [78]. Lattice QCD calculations are typically constrained to box sizes of $L \sim 2.5\,\text{fm}$. A possible generalization of Lüscher's result is given by matching lattice QCD results to results obtained by calculations in effective theories including pion degrees of freedom such as chiral effective field theory (EFT). The matching would consist of adjusting the low-energy constant (LECs) of chiral EFT, such that lattice QCD results are reproduced. Once the LECs are determined it is possible to calculate phase shifts in the infinite volume using few- and many-body methods to solve the Schrödinger equation. This allows the extraction of scattering parameters in the infinite volume from lattice QCD calculations at box sizes where pion exchanges become relevant.

From the point of view of the effective field theory community this approach is appealing, too. The common approach to determine the LECs in chiral EFT is through fitting observables to experimental data. This strategy fails in channels where experimental data are scarce or nonexisitent. Of particular interest are few-neutron systems as they are difficult to access experimentally. Even the present limitation of lattice QCD calculations to unphysical quark masses could be overcome as long as the quark masses are within the range of applicability of the chiral expansion. It is then possible to extrapolate to the physical quark masses and obtain the LECs relevant for realistic calculations. Similar studies on how to exploit lattice QCD result to determine LECs in effective theories have been performed in the past. In Refs. [79, 80] the binding energies of light nuclei and neutron-deuteron scattering lengths are calculated within a pionless theory with LECs fitted to

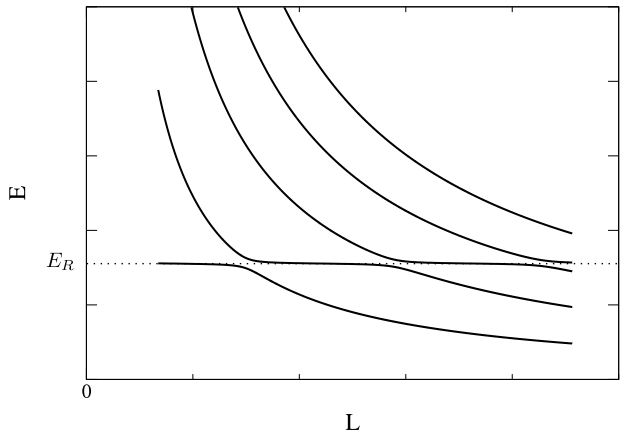

Figure 1.4: Schematic representation of the relative energy E of two particles in cubic volume with periodic boundary conditions as a function of the box size L. At the resonance energy E_R the levels exhibit an avoided level crossings.

lattice QCD results for the deuteron, dineutron and triton at unphysical quark masses. In Table 1.1 results are shown including predictions for the masses of ^{5}He, ^{5}Li, and ^{6}Li.

In Chapter 2 of this thesis we present first steps in the direction of matching chiral EFT results to lattice QCD data by performing finite-volume calculations of two neutrons interacting with chiral potentials. The neutron-neutron scattering length cannot be measured directly leading to conflicting results [81, 82]. Therefore, a direct extraction of the *nn* scattering length from lattice QCD would be particularly valuable. In the long term the goal of this project is to establish a technique to match chiral nuclear interactions to data from lattice QCD. This would allow for calculations of nuclear observables based entirely on the fundamental theory of QCD without requiring input from experimental data.

In addition to the extraction of bound-state and scattering properties from finite-volume calculations, the Lüscher results also establish a connection to resonance properties. The difference between the energy E_n of a system of two interacting particles and the energy E of the g-fold degenerate non-interacting system both confined in box of size L with periodic boundary conditions is given by

$$E_n - E = -\frac{4\pi g \tan(\delta_0(p))}{mpL^3}, \tag{1.31}$$

where m is the mass of the particles, δ_0 denotes the S-wave phase shift and $E = 2m + \frac{p^2}{m}$ is the energy of the non-interacting particles with discrete momenta $\mathbf{p} = \frac{2\pi}{L}\mathbf{n}$ where $\mathbf{n}$ is a vector of integers. This equation is still valid for two resonant particles when E is sufficiently different from the resonance energy E_R. A resonance of Breit-Wigner type, i.e., without background phase shift, corresponds to a phase shift which increases suddenly from 0 to π passing through $\delta = \frac{\pi}{2}$. In this case Eq. (1.31) breaks down as the right-hand side diverges. Wiese [24] derived a generalization of Eq. (1.31) and showed that close to the resonance energy two quasi degenerate states $E_n = E_\pm$ emerge

$$\frac{(E_+ - E)(E_- - E)}{E_+ + E_- - 2E} = -\frac{4\pi g \tan(\delta_0(p))}{mpL^3}. \tag{1.32}$$

This equation no longer breaks down at $\delta_0 = \frac{\pi}{2}$ as the left-hand side of the equation also diverges when $E_+ + E_- = 2E$. When plotting the finite volume spectrum as a function of the box size this effect manifests itself by the appearance of so-called avoided level crossings. This is two states coming so close that they almost intersect. In Fig. 1.4 we present a schematic representation of such an avoided level crossing. The horizontal plateaus correspond to the resonance energy E_R. Even though the original derivation by Wiese is limited to S-wave scattering the results can be generalized to resonances in any partial wave. This technique has been used successfully to extract hadron resonance energies [83, 84]. In Chapter 4, we study the extension of this method to few-body resonances, working off the assumption that such states again show up as avoided crossings in the finite-volume few-body energy spectrum, and that the properties of the resonance state can be inferred from the position and shape of these avoided crossings.

1.3.2 Trineutron and tetraneutron resonances

The spectrum of few-nucleon systems exhibits several bound states such as the deuteron (np), triton (nnp), ^{3}He (npp) and ^{4}He ($nnpp$). The latter is the alpha particle, which is strongly bound despite the additional repulsion stemming from the positive charges of the protons. In addition, the nuclear force is to a large degree independent of the isospin states of the interacting nucleons, meaning that the interaction depends very little on whether the particles are protons or neutrons. Therefore, it might seem natural that also pure neutron systems such as the dineutron (nn), trineutron (nnn), or tetraneutron ($nnnn$) could be bound. In case of the dineutron, there is a very low lying virtual state at about $E = 100\,\text{keV}$, highlighting that only a small increase in the attraction would leave this system bound. However, what concerns tri- and tetraneutron states, this picture is too naive as it lacks one of the most fundamental principles of quantum mechanics – the Pauli principle. If we think of the mean-field potential created by a collection of nucleons as a harmonic oscillator, only two neutrons can occupy the lowest energy S-wave state. While up to two additional protons can occupy the same state, additional neutrons need to populate the next level, i.e., the P-wave states. The existence of bound tri- and tetraneutron states is therefore unlikely. Nevertheless, in the past much effort has been invested in both experimental and theoretical investigations of such systems. Already in the 1960s the first experimental efforts rejected the possibility of a bound tetraneutron [85]. Also the assertion on the theoretical side was negative in general [86, 87]. Due to pairing effects, which usually cause a stronger binding of a system, the tetraneutron is favored over the trineutron, when judging on its potential to be bound. Accordingly, the trineutron has been found to be unbound in a range of studies [88]. Despite the negative prospect, the subject was never completely dropped and in 2002 an experimental claim spiked renewed interest in the possibility of bound tetraneutron states. A few events in the ^{14}Be break-up reaction ($^{14}\text{Be} \to {}^{10}\text{Be} + {}^4n$) allowed the conclusion that bound tetraneutrons had been formed [89]. Within a year, several theoretical studies were published that tried to answer the question if modern theoretical approaches could support a bound tetraneutron. In Ref. [88] it was found that the NN force by itself cannot bind four neutrons. A strong modifications of the NN force or adding a four-nucleon force would be required to bind the system.

Other models describe the tetraneutron as a composite dineutron-dineutron molecular system. In this model the two dineutrons are assumed to be bound due to the presence of the respective second dineutron. Evidence that neutrons form clusters within larger systems is provided by Halo

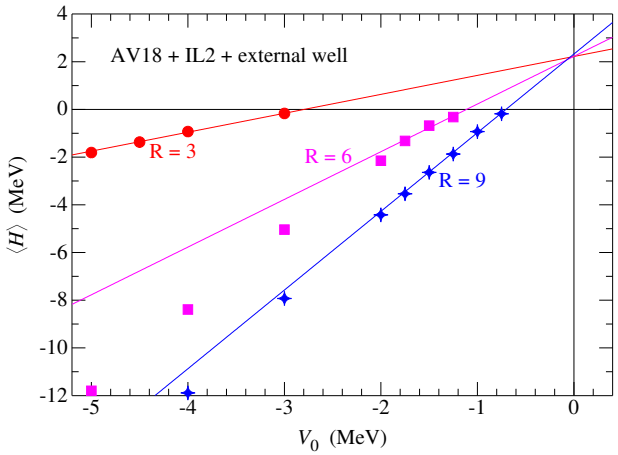

Figure 1.5: The energy of four neutrons in external Woods-Saxon potentials for varying radius R as a function of the well depth V_0. In each case, a linear fit to the GFMC results was obtained and used to extrapolate to the zero-well-depth limit. Figure taken from Ref. [93].

nuclei like ^{6}He and ^{11}Li [90]. These systems are bound despite the fact that both the two-neutron system as well as the nuclei ^{5}He or ^{10}Li are unbound. Similarly it was suggested that ^{8}He exhibits a $^{4}\mathrm{He} + {}^{4}\mathrm{n}$ structure [91]. A theoretical investigation of the dineutron-dineutron model, however, found that it is not able to explain a bound tetraneutron [9].

The most conclusive study was finally undertaken in Ref. [11] where four neutrons interacting via the Argonne v_{18} NN potential (AV18) [92] plus three-nucleon forces ($3N$) from the Illinois models [93] were studied. These advanced phenomenological potentials had been shown to describe light nuclei accurately. Performing Green's function Monte Carlo (GFMC) calculations (see also Sec. 1.4.2) it was not possible to find four-neutron systems with negative energy. In addition, a set of different modifications of the nuclear potential were studied that allow for a bound tetraneutron. It was found that in all cases the dineutron becomes bound while additional $3N$ and $4N$ forces lead to bound systems of more than four neutrons.

While the case of the bound tetraneutron had been settled, Ref. [93] also pointed to the possibility of a four-neutron resonance. The author performed calculations of four neutrons trapped in an external well such that the system becomes bound. By decreasing the potential strength of the trap, it was possible to extrapolate to the realistic case of zero external potential strength as shown in Fig. 1.5. It was suggested that the extrapolated energy of roughly 2 MeV might be an indication of a resonance, which must, however, be very broad due to a lack of evidence in the GFMC simulation. Few-neutron resonances had been investigated earlier in parallel to their bound state correspondents, however, with a less clear outcome [94]. Furthermore, the authors of the study of the ^{14}Be breakup experiment [89] admitted in a second publication the possibility that the observed signal could also stem from a near-threshold four-neutron resonance [95].

For two particles, a resonance is usually introduced via the scattering phase shift, which exhibits sudden jumps at the energy of a resonance. Due to the lack of an analog of the phase shift for more than two particles, defining many-body resonances is more cumbersome. Mostly, a resonance is defined as a pole in the S-matrix on the unphysical sheet of the complex energy plane. For physical resonances the real part of the pole $E = E_R - i\Gamma/2$ is positive, $E_R > 0$. The extraction of the

pole positions is in particular advantageous as both the resonance energy E_R and the width of the resonance Γ are obtained. However, as most numerical methods are constructed to extract bound state properties, calculations of the S-matrix for resonant states of more than two particles are challenging and have only been performed for simplified nuclear potentials [96]. In an early study of poles of the S-matrix based on the NN S-wave interaction MT I-III no observable three- or four-neutron resonances were found [94].

On the other hand, solving the Schrödinger equation $H\Psi = E\Psi$ directly is challenging as due to the positive real part of the eigenvalue E the resonance eigenfunctions are not square integrable [22]. By applying a similarity transformation to the Hamiltonian $H \rightarrow SHS^{-1}$ it is, however, possible to map the resonance wave functions onto normalizable states. In particular, the complex-scaling method (CSM) is defined by a similarity operator of the form $S = \exp\left(i\theta r \frac{\partial}{\partial r}\right)$ [97, 98]. For many potentials the energy spectra are not affected by this transformation, which would allow for an extraction of resonance properties via methods normally applied to bound states [22]. An alternative pathway to extract resonances is the method of analytic continuation in the coupling constant (ACCC) [99]. The idea is to scale the attractive part of the potential such that resonant states become bound. When the strength of the attraction is now decreased towards the physical point, the energy eigenstate will eventually reach the threshold, i.e., $E = 0$. It is now possible to construct an analytic continuation into the unphysical sheet to the point where the potential reaches its original form. The two methods described were used to study three- [22] and four-neutron resonances [18]. The Faddeev-Yakubovsky equations were solved for three and four particles interacting via the phenomenological Reid 93 NN interaction plus an additional attraction for either enhanced interactions in particular partial waves or additional three- or four-body interactions to bind the systems. It was found that the final pole positions of three- and four-neutron states have negative real parts, i.e., $E_R < 0$ and are therefore not physically observable.

Again the case seemed to be settled for about ten years until there was another possible experimental claim. A study performed at the RIKEN Radioactive Ion Beam Factory (RIBF) found candidate tetraneutron states in the double-charge-exchange reaction ^{4}He(^{8}He,^{8}Be) [12]. A ^{8}He beam was directed at a liquid ^{4}He target to produce four-neutron systems together with ^{8}Be that decays into two alpha particles. As it is difficult to detect the four-neutron system directly, RIKEN's high resolution SHARAQ spectrometer was used to measure the momenta of the two alpha particles. Combining this information with the measured momentum of ^{8}He allows one to deduce the missing energy ("missing mass") of the four neutrons. The reaction studied is advantageous in two ways. First, almost no recoil momentum is transferred to the four neutrons, which avoids an immediate disintegration of the system. Second, the signal of the two alpha particles provides a characteristic signature of the ^{8}Be very distinct from the experimental background. Due to the relatively low beam intensity and the small cross section of the process only four events corresponding to possible tetraneutron resonance states could be observed as shown in Fig. 1.6.

Nevertheless, the authors were able to perform a statistical analysis such that the statistical significance of the extraced tetraneutron resonance energy of $(0.83 \pm 0.65 \pm 1.25)$ MeV was quoted as 5σ. However, this analysis was based on certain assumptions such as the form of the continuum. Other experiments are currently underway to verify this result [13–15]. While further experimental data will appear in the near future, the initial result has already revived theoretical interest in a possible tetraneutron resonance. Today refined realistic nuclear potentials exist, among which there are potentials derived from effective field theory approaches discussed in Sec. 1.2. In particu-

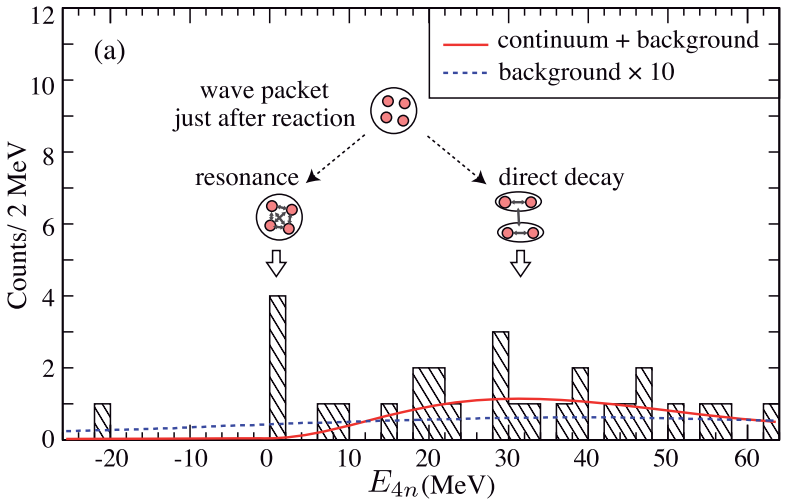

Figure 1.6: Missing mass spectrum of the tetraneutron system. The red curve represents the sum of the direct decay of two-neutron pairs and the estimated background. The dashed blue curve represents the estimates background multiplied by a factor of 10. Figure taken from Ref. [12].

lar the importance of many-body forces for neutron-rich systems has been revealed [8]. Therefore, recent studies focused on the role of three- and four-body forces. The authors of Refs. [18, 22] applied their CSM method to the AV8' potential plus a toy three-nucleon force in the total isospin $T = 3/2$ channel to bind the system [19]. It was found that in order to allow for a tetraneutron resonance, the $T = 3/2$ three-nucleon force needs to be attractive to an extent inconsistent with other properties of light nuclei and low-energy scattering data.

A range of alternative few-body methods was used in Ref. [16] to extract resonance parameters. Performing calculations in the No-Core Gamow Shell Model and in addition in a modified version of the No-Core Shell Model using the Single-State Harmonic Oscillator Representation of Scattering equations a low-lying $4n$ resonance was obtained at $E_R = 0.8\,\text{MeV}$ with a relatively large width of $\Gamma = 1.4\,\text{MeV}$, based on the realistic JISP16 NN interaction. A different study using the No-Core Gamow Shell Model, which includes bound, resonant, and non-resonant basis states, finds a resonance in agreement with the experimental observation, however, with a significantly larger width based on chiral NN forces [17]. However, due to the very large width the authors suggest that the experimental observation is a reaction process too short to form a nucleus. For a possible three-neutron resonance the situation is similar, as several, both old and recent, publications judge the existence of such a state to be unlikely [21–23].

What still remains missing is an *ab initio* investigation based on two- and three-neutron interactions derived from chiral effective field theory (EFT). Motivated by the initial hint for a possible tetraneutron resonance in Ref. [11], we investigate in Chapter 3 the properties of 2, 3, and 4 neutrons confined in an external potential well. Extrapolating to vanishing external potential strength, we extract possible resonance energies of three- and four-neutron systems interacting via nuclear Hamiltonians constructed within chiral EFT. The results obtained have been published in Ref. [100].

In addition, we propose and assess here a new approach that is based on studying the energy spectrum of the system of interest as it is enclosed in finite volume with periodic boundary conditions. As discussed in Sec. 1.3.1, it has been shown for two-body systems that the infinite-volume properties of interacting particles are encoded in the volume dependence of their (discrete) energy levels in the box. In particular, it has been shown that a resonant state shows up as an avoided crossing of energy levels as the size L of the box is varied [24]. In Chapter 4, we establish this method as a tool for identifying few-body resonance states and postpone studies of few-neutron systems using EFT-based interactions to future work.

1.3.3 Chiral EFT for dark matter direct detection

One of the greatest unsolved questions in modern physics is the origin of the large majority of matter in the universe. Surprisingly, the ordinary baryonic matter that surrounds us accounts for only roughly 20% of the total matter. Due to its nonluminous nature the remaining 80% are referred to as dark matter. As its existence is inferred only through gravitational effects on luminous matter, a wide range of experimental efforts are underway trying to observe possible particle candidates of dark matter in the laboratory. One possible approach consists of so-called direct detection experiments searching for signals of dark matter particles scattering off atomic nuclei. The scattering cross section of these processes depends strongly on nuclear matrix elements describing the coupling of the dark matter particle to the collectivity of nucleons in the nucleus. On the one hand, input from nuclear physics is required for the description of the nuclear wave functions. On the other hand, the question arises how operators describing the interaction of the dark matter particles with nucleons should be constructed. Even though the interaction type is in principle unknown, the underlying theory of the strong interaction, i.e., QCD, determines how the coupling of dark matter particles to the fundamental particles of quarks and gluons translates into couplings to composite structures like nucleons and pions. Such effects can be studied within the framework of chiral EFT (see Sec. 1.2). Before we discuss in Chapters 5, 6, and 7 the applications of chiral EFT in the context of direct detection of dark matter, we will provide an overview of the diverse evidence for dark matter, possible candidates of dark matter particles and current experimental detection methods. We will focus mainly on the aspects relevant for our study, i.e., direct detection of weakly interacting massive particles, however, also discussing some aspects of alternative approaches. Most of this introductory section is based on the reviews in Refs. [30, 31, 101] to which we refer for more details.

Early evidence for dark matter

The first indications for the existence of a new type of matter range back to the 1930s. As astronomy almost solely relied on the observation of light in the visible spectrum, masses of stellar objects such as stars or galaxies were inferred via their luminosity. Taking the mass to luminosity ratio of the Sun as reference allowed for a rough estimate of the mass. The Swiss astronomer Zwicky observed Doppler shifts in the galactic spectra of the Coma cluster, a large accumulation of galaxies [102, 103]. Based on the Doppler shifts, he calculated the velocity dispersion of the individual galaxies. Using the virial theorem, he was then able to infer the total mass of the cluster. By comparing to the estimate obtained from the mass to luminosity ratio, it was evident that the

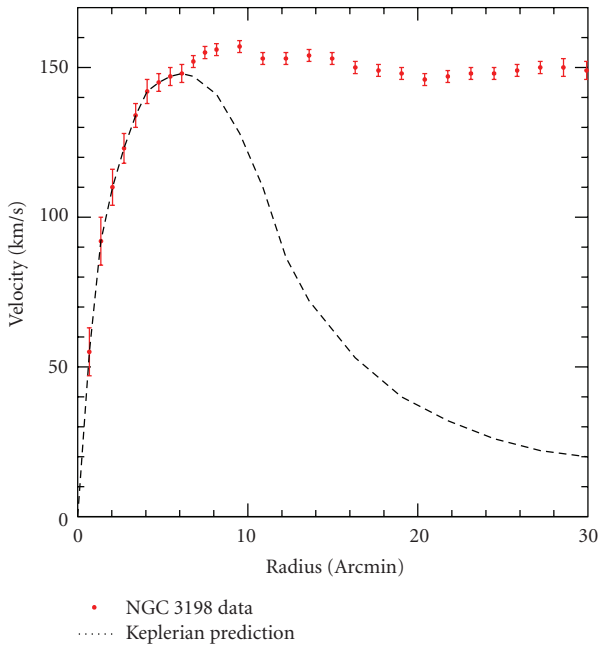

Figure 1.7: Comparison of the measured rotational velocities of in the galaxy NGC 3198 and the prediction based on the luminous matter only [104]. Figure taken from Ref. [101].

vast majority of the mass had to be nonluminous. Zwicky referred to this new form of matter as dark matter.

Later in the 1970s Rubin and collaborators found further evidence for the existence of dark matter [105]. The rotation curve of a galaxy shows the rotation velocity of the stars as a function of their distance r to the center of the galaxy. Based on the fundamental laws of Newtonian gravity the velocities $v(r)$ of the stars on their orbits around the galactic center are given by

$$v(r) = \sqrt{G\frac{m(r)}{r}}, \tag{1.33}$$

where G is the gravitational constant and $m(r)$ is the mass enclosed by the radius r. For our solar system the total mass is essentially given by the Sun's mass at the center of the planets' orbits. Therefore, one expects the velocities of the planets to behave as $v(r) \propto 1/\sqrt{r}$ which matches observations. For the rotation velocities of galaxies a similar behavior is expected as the majority of luminous matter is observed at the center of a galaxy. Rubin's observations of the rotation curves of 60 galaxies, however, showed a very different behavior. While at small radii the rotation velocity would rise in agreement with the expectations, it was found that at large radii, instead of decreasing, the rotation curves would remain flat. An example is shown in Fig. 1.7. If Newtonian laws should not be violated, this observation leads to the conclusion that the mass in a galaxy cannot be dominated by the accumulation of luminous matter at the center. Instead, a more homogeneous distribution of matter is required to account for the flat rotation curves. Thus, again there has to be a nonluminous kind of matter that is spread throughout the galaxy.

Also during the 1970s another method to probe the density distribution of dark matter was established. Einstein predicted that the spacetime curvature caused by the gravity of large stellar objects affects light in a similar way as it governs how planets move around their star. A massive object bends the paths of photons effectively changing their direction. This effect is termed gravitational lensing and can be observed by following a distant, bright object, such as a single galaxy, passing behind a closer, very massive object, like a cluster of galaxies. When the distant object is behind the closer object its visible shape gets distorted through the effect of gravitational lensing. The distortion can be used to estimate the mass of the lensing cluster. Again it was found that the total mass of the observed clusters must exceed the mass expected based on the observed luminous matter [106].

Up to this point it was not clear how dark matter is distributed on the scale of individual stars as the different observations only pointed to missing mass distributed throughout a whole galaxy. It was suggested that large astrophysical objects that consist of baryonic matter but that are nevertheless dark in the sense that they do not contribute to the luminosity of a galaxy, account for the effects attributed to dark matter. The search for these massive compact halo objects (MACHOs) was performed by investigating the sky for microlensing effects. Similar to the gravitational lensing effect discussed earlier a small change in brightness of a distant object is expected when passing behind a MACHO. Several extensive studies showed that the number of such objects, such as brown dwarfs, neutron stars or black holes, is significantly too low to account for dark matter on its own [107, 108]. These observations already pointed to the conclusion that dark matter had to be nonbaryonic.

Cosmological evidence

During the very early stages of the universe, more precisely from a few seconds to a few minutes after the Big Bang, protons and neutrons combined to form deuterium, helium and very low amounts of lithium. This phase is therefore called Big Bang Nucleosynthesis (BBN). Theoretical simulations of the processes that occurred during the BBN allow for a calculation of the relative abundances of the produced light elements with respect to hydrogen. In later stages of the universe deuterium and the other light elements are fused together with hydrogen in stars to form heavier elements. Observations of very distant regions of the universe where there are no traces of elements heavier than lithium allows effectively looking back in time. Measurements of the spectral lines from these regions determine the relative abundances of the light elements produced during BBN. Remarkably, the result from the BBN calculations very precisely agree with the measured data. In particular, the ratio of deuterium to hydrogen depends heavily on the overall density of baryons in the universe, which effectively constrains the baryon density. It was found that the derived baryon density accounts for only 20% of the total matter density in the universe [109]. The latter was extracted from observations of the cosmic microwave background (CMB), which will be discussed next.

Immediately after the Big Bang the universe underwent a phase of rapid expansion. For about 370,000 years the expansion continued at decreasing speed, hence, the universe cooled and finally reached the epoch of recombination. At this time, the initially hot plasma, in which photons were continuously scattered from free charged particles, converted into neutral atoms. As a result, the universe became transparent for electromagnetic radiation and the mean free path of photons be-

came so large that photons produced at that point in time could travel the universe until today. The afterglow of the final scattering after the recombination epoch still exists as an omnidirectional signal in the microwave spectrum. Due to the following expansion of the universe the signal got redshifted and today corresponds to a temperature of 2.73 K. After having been predicted in 1948 by Alpher and Herman [110], it was only detected rather accidentally in 1964 in the famous experiment by Penzias and Wilson [111]. More precise measurements were later performed when the cosmic background explorer (COBE) was launched into space. COBE was able to measure fluctuation within the CMB and found an extremely small variation of only $30 \pm 5\,\mu$K. This observation was very surprising at the time as it did not allow for structure formation in the early universe. The large scale structures we see in the universe today such as galaxy clusters have been formed from initial seeds forming gravitational wells. Starting from the small impurities of the CMB, representing the state of the universe after the phase of recombination, the universe would not have been able to reach its present structure within the age of the universe [112]. This showed that an additional form of matter, which does not or only weakly couple to photons, initiated the formation of structure prior to the epoch of recombination.

Successive missions like the Wilkinson microwave anisotropy probe (WMAP) [113] or the Planck probe [114] refined the picture obtained by COBE. Simulations of the anisotropies determine the total and baryonic matter densities. The latest Planck data from 2015 [114] lead to cold dark matter/baryonic mass densities $\Omega_{c/b}$ of

$$\Omega_c h^2 = 0.1198 \pm 0.0015\,, \qquad \Omega_b h^2 = 0.02225 \pm 0.00016\,, \tag{1.34}$$

where Ω is the density relative to a reference density ρ_c and h is the reduced Hubble constant. Based on the Planck data, the total energy density of the universe consists of 4.9% ordinary matter, 26.8% dark matter and 68.3% dark energy. The latter is an unknown form of energy necessary to explain the accelerated expansion of the universe.

Recent evidence and alternative explanations

Less complex evidence for the existence of dark matter is found in collisions of two clusters of galaxies. A famous example is the collision of the Bullet cluster with a larger galaxy cluster [115]. The individual galaxies part of the two clusters were mostly not affected by the collision as they were unlikely to interact due to the large distances separating them. The majority of the baryonic mass in the two clusters, however, exists in the form of hot gas, which got compressed during the collision. The resulting X-ray radiation could be observed from earth and compared to results from weak gravitational lensing pointing to the location of the majority of the mass of the two clusters. A superposition of the different images is shown in Fig. 1.8. The results showed that the location of the majority of the mass did not coincide with the areas of strong X-ray emission. This leads to the conclusion that the halos of dark matter, in which the two clusters sit, pass almost unaffected through each other while only the interacting baryonic matter got slowed down. This remarkable observation presents one of the most compelling evidences of dark matter today.

Only very recently, a galaxy was found that seems to lack dark matter almost entirely as the rotation velocities of stars in the galaxy were significantly smaller than in galaxies of similar size [118]. Through an estimate of the mass of the galaxy, it became evident that there seems to be almost

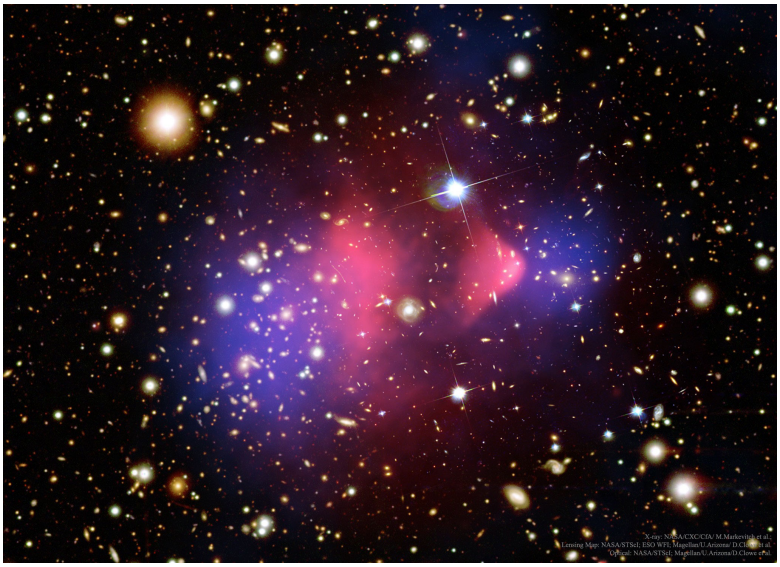

Figure 1.8: The matter of the bullet cluster observed via X-ray image (pink) and matter distribution calculated from gravitational lensing (blue) superimposed over a visible light image (galaxies) [116, 117].

no dark matter present in this particular galaxy. While this poses new questions concerning the formation of galaxies, which is expected to rely on the presence of dark matter, it presents evidence for the existence of dark matter as a separate form of matter different from ordinary matter.

These two observations are of particular relevance as they contradict alternative theories that account for the gravitational effects attributed to dark matter as a consequence of modified laws of motion on cosmic scales. These theories are known as modified Newtonian dynamics (MOND) and rely on the assumption that Newton's second law has to be modified on very large galactic scales [119]. However, evidence for dark matter is found on all scales as we discussed above. Furthermore, dark matter is required to explain observations such as the Bullet cluster or the galaxy without dark matter, which cannot be accounted for by MOND theories.

Particle candidates

While the range of hints for dark matter constrains the overall density and distribution of dark matter on galactic scales, the exact nature of it is still not clear. As large massive object, i.e., MACHOs, have been ruled out, dark matter is thought to consist of new elementary particles. Such dark matter particles would have to be non-baryonic, i.e., without color charge, and nonluminous, thus without electric charge. The self-interaction of dark matter particles can be inferred from events like the collision of the Bullet cluster and is found to be rather weak. Finally, the particles would have to be stable or very long lived to account for their existence right from the very early moments of the universe until today. The obvious candidate within the Standard Model (SM) is the neutrino. However, as neutrinos are very light and relativistic they would contribute to so-called hot dark matter. Simulations of the formation of galaxies show that in a universe with hot dark matter large superclusters would form first, which later fragment to galaxies. Observations of small scale structures such as the distribution of individual galaxies are in disagreement with this

scenario. Rather dark matter needs to be cold to allow for the formation of small galaxies starting from the initial conditions measured in the CMB.

Other than the neutrino the SM does not offer a viable candidate. Despite its great success the SM has some problems on the conceptional level such as the hierarchy problem and the fine-tuning problem [30]. Therefore, extensions have been suggested, which might account for both the flaws on the theoretical side and the lack of a dark matter particle. One possibility is supersymmetry (SUSY). SUSY theories propose an additional symmetry between fermions and bosons which would allow for the interconversion of the two particle species. Every fermion member of the SM is associated with a supersymmetric boson, likewise every boson with a supersymmetric fermion. As we do not see the superpartners of the SM partner in nature SUSY must be broken at the typical energies of the universe today. Due to this symmetry breaking the superpartners become extremely massive, which would explain why they have evaded detection so far. Most importantly, some of the predicted additional particles indeed represent viable candidates for dark matter [120]. Without going into detail, we mention here the most promising candidates, the neutralino, which is the superpartner of the Higgs and the other gauge bosons, the sneutrino, the superpartner of the neutrino and the gravitino, the superpartner of the graviton. In particular, the neutralino is considered the lightest supersymmetric particle and therefore stable. The most appealing feature of neutralinos is, however, that their predicted abundance would account naturally for the observed dark matter density. The recent years, however, have significantly reduced the possible parameter space of possible SUSY particles as various searches at the LHC were not successful at discovering beyond Standard Model (BSM) physics [121, 122]. A different type of extension of the SM adds extra spatial dimensions to the universe. This gives rise to new particles among which the lightest Kaluza-Klein particle represents another viable dark matter candidate [123, 124].

The neutralinos and similar supersymmetric particles as well as the Kaluza-Klein particle are classified as weakly interacting massive particles (WIMPs), which is one class of dark matter candidates. We want to emphasize that the term weakly interacting refers to the strength of the interaction and not the weak interaction, which is described within the SM. The possibilities for the WIMP-SM-particle interaction are vast and only experimental constraints can provide further insights into the exact mechanism.

There are many more exotic candidates for dark matter particles predicted by various theories. Among the different possibilities axion like particles (ALPs) are especially appealing. Axions arise from solutions of the so-called strong CP problem [125] and are expected to be very light. Latest constraints from laboratory searches and astrophysical observation yield $m \sim 1\,\mu\text{eV}-3\,\text{meV}$ [122]. Despite ongoing efforts the axion has not been detected.

In the following, we will focus on experimental searches for WIMPs as they are expected to interact with atomic nuclei.

WIMP detection

In view of the evidence coming from astrophysical and cosmological observations one could claim that dark matter has already been detected. However, the term “dark matter detection” usually refers to the detection of individual dark matter particles in the laboratory. The hunt for WIMPs relies on three different experimental approaches, which are complementary to each other and together cover WIMP masses from a few GeV to more than 10 TeV [126].

The large hadron collider (LHC) at CERN has been used very successfully for the production and detection of a wide range of new particles. The latest and most prominent discovery is the Higgs boson which was produced in collisions between protons [1, 2]. In a similar approach, collider searches for dark matter try to produce BSM particles in collisions of SM particles. As the dark matter particles do not interact with the detector material they can only be detected indirectly via the missing energy they extract from the collision. The production of a dark matter particle in a collider experiment would be advantageous as the boundary conditions can be controlled easily allowing for a repetition of the experiment. On the other hand, given an observation of a BSM particle in a collision it is not clear if the produced particle is identical to the dark matter particle. Up to today no evidence for possible dark matter particles has been found at the LHC.

Indirect searches aim at the detection of SM particles produced when dark matter particles annihilate or decay. Natural places to search for dark matter self-annihilation or decays are regions of high expected dark matter densities as the annihilation rate is proportional to the square of the density while the decay rate is still proportional to the density. Thus, typical regions considered in indirect searches are the Sun, Earth, and the galactic center. The annihilation products are expected to be pairs of SM particles which consequently lead to high-energy gamma-rays, neutrinos or antimatter. The expected rates furthermore depend on the WIMP mass as well as astrophysical inputs such as the dark matter distribution in the Milky Way. So far results are ambiguous. The rise in the measurements of positron fractions $e^+/(e^+ + e^-)$ in the PAMELA [127] and AMS-02 [128] experiments points to a new source of positrons of either astrophysical nature or from dark matter annihilation. Another observation comes from an excess of the antiproton-to-proton ratio observed by AMS-02 or measurements of Gamma rays originating from the galactic center observed by the Fermi-LAT collaboration [129–132]. In addition, limits of WIMP-annihilation cross section can be inferred from measurements of high-energy neutrinos from the sun in the neutrino detectors IceCube [133, 134] and Super-Kamiokande [135, 136]. However, it is difficult to control all astrophysical backgrounds. So far, evidence obtained in indirect searches draws an inconsistent picture as extracted WIMP masses would range from a few keV to several TeV.

Direct detection approaches aim at the detection of signatures of WIMPs scattering off atomic nuclei. Large amounts of target material are placed deep underground which, in addition to a wide range of sophisticated techniques, reduces background radiation to a minimum.

First, we start with some general considerations on the order of the deposited energy and the expected total rate. Predicted WIMP masses range from a few GeV to the order of 10 TeV. The maximum WIMP velocity is given by the escape velocity $v_{\text{esc}} = 544\,\text{km/s}$ in the galactic rest frame [137, 138]. Faster WIMPs escape the gravitational well of the galaxy.

The energy transferred to the nucleus of mass m_A in an elastic scattering process is the nuclear recoil energy

$$E_r = \frac{\mu^2 v^2}{m_A}(1-\cos\theta), \tag{1.35}$$

where μ is the reduced mass of the WIMP-nucleus system, $\mathbf{v}$ the WIMP velocity and θ the scattering angle. It follows that for a dark matter particle with a mass in the GeV - TeV range the recoil energy $E_r < 50\,\text{keV}$. Events caused by the natural background radiation are of the order of MeV. Therefore, measuring an excess of only a few keV is extremely challenging and detectors need to be shielded while the amount of radioactive isotopes in the detector has to be constrained.

The local dark matter density is expected to be around $\rho \sim 7 \times 10^{-25}\,\mathrm{g/cm^3}$ ($0.4\,\mathrm{GeV/cm^{-3}}$). Assuming a WIMP mass of $m_\chi = 100\,\mathrm{GeV}$ this implies a flux on the Earth of about $10^5\,\mathrm{cm^{-2}s^{-1}}$ (assuming $v = 250\,\mathrm{km/s}$). The differential rate for elastic WIMP-nucleus scattering in a detector of N_T target nuclei is given by [139]

$$\frac{\mathrm{d}R}{\mathrm{d}E_r} = N_T \frac{\rho}{m_\chi} \int_{v_{\mathrm{min}}}^{v_{\mathrm{esc}}} \mathrm{d}^3 v\, |\mathbf{v}| f(\mathbf{v}) \frac{\mathrm{d}\sigma_{\chi\mathcal{N}}}{\mathrm{d}E_R}\,, \tag{1.36}$$

where $f(\mathbf{v})$ is the velocity distribution in the Earth rest frame, and $\mathrm{d}\sigma_{\chi\mathcal{N}}/\mathrm{d}E_r$ the WIMP-nucleus differential cross section. The velocity distribution is derived in astrophysical models of the galaxy. The minimal velocity $v_{\mathrm{min}} = \sqrt{m_A E_{\mathrm{th}}/2\mu^2}$ depends on the detector threshold E_{th}, which is in current experiments of the order of 1 keV [140] and thus similar to expected recoil energies.

The WIMP scattering elastically off an atomic nucleus causes a nuclear recoil, which leaves three different signatures in a detector:

- In a solid state detector the nuclear recoil causes vibration of the crystal lattice. Such vibrations, or phonons, correspond to extremely small temperature variations, which can be measured via sensitive thermometers on the surface of the detector material.

- Incident radiation can ionize a nucleus by knocking out a bound electron. A global electric field in the detector is used to accelerate the free electron towards one side. On its way the electron knocks out additional electrons. The resulting free charges are detected at the detector wall.

- Similarly, an electron can absorb enough energy to get excited to a higher orbital. The scintillation light produced when the electron deexcites travels through the detector and induces an electric signal in photomultiplier detectors placed around the target material.

In order to distinguish events induced by a WIMP scattering off a target nucleus from background events, direct detection searches rely on the measurement of two of these different signals. The relation between the two channels is characteristic for the particle that induced the signal allowing a distinction on an event-by-event basis.

Elastic scattering is the standard scenario considered in current direct detection experiments. However, inelastic excitation of the nucleus to low-lying excited states are appealing as in addition to the nuclear recoil the deexcitation gamma could be observed. Provided a measurement of a WIMP signal, this could help to distinguish between spin-independent and spin-dependent interactions [141, 142].

The background consists of various types of radiation. For large-scale detectors the active target material is purified and shielded against most background sources. However, it is impossible to shield against neutrinos coming mainly from the Sun. While the analysis of the different signals in the detector allows for a distinction between neutrino-electron scattering and nuclear recoils, the final limitation of direct searches is the background from neutrino-nucleus interactions. The coherent scattering from ^{8}Be solar neutrinos limits achievable sensitivities to $\sim 4 \times 10^{-45}\,\mathrm{cm^2}$ for WIMP masses of 6 GeV. For larger masses the reachable sensitivities will be limited by atmospheric and diffuse neutrinos to $\sim 10^{-49}\,\mathrm{cm^2}$ [143–145] as shown in Fig. 1.9.

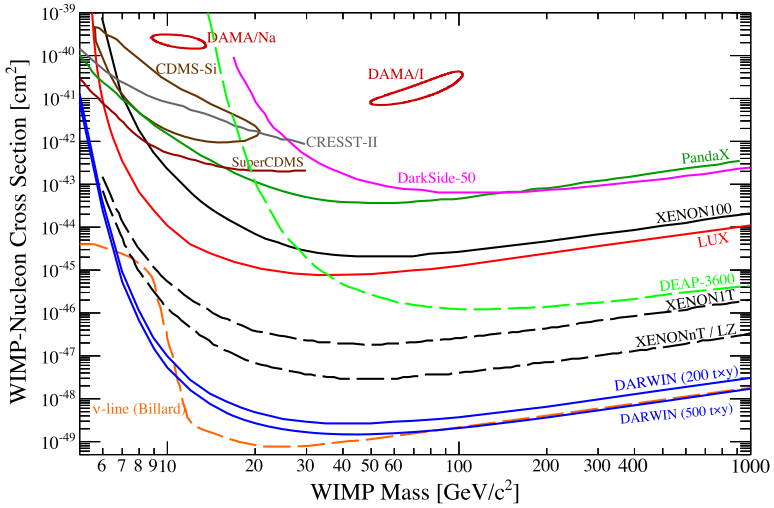

Figure 1.9: Upper limits on the WIMP-nucleon cross section for the spin-independent interaction obtained in various direct detection experiments as of 2016. Latest results of the XENON1T, LUX, and PandaX-II experiments are not shown. The limits for the planned DARWIN experiment are extrapolations. The line label ν-line represents the neutrino background from coherent neutrino-nucleus scattering in the detector. Figure taken from Ref. [101].

Figure 1.9 shows a summary of various upper limits obtained by different experimental collaborations on the spin-independent WIMP-nucleon cross section as a function of the WIMP mass. Even though there have been claims of signal detections, that one could interpret as originating from dark matter particles, there is no convincing evidence for WIMP dark matter from direct detection experiments. The most promising, however controversial, results were found by the DAMA/LIBRA collaboration, which found an excess signal by studying the annual modulation of scattering events [146]. The data was found to be in agreement with expected modulations in WIMP signal due to the Earth's relative motion to the Milky Way's dark matter halo. However, several more sensitive searches have excluded the claim (see Fig. 1.9).

For very light WIMP masses the most sensitive upper limits are obtained by DarkSide-50 [147], CDMSlite [148], and CRESST [149, 150], which use argon, germanium, and $CaWO_4$, respectively, as target material. The most stringent constraints to the WIMP parameter space above $m_\chi = 6\,\text{GeV}$ come from the results of XENON1T [151], LUX [152], and PandaX-II [153] experiments. All of these experiments use xenon-filled time-projection chambers. Only very recently, updated results from the XENON1T collaboration set the most stringent limit on the WIMP-nucleus cross section of 4.1×10^{-47} at $m_\chi = 30\,\text{GeV}$ [32]. Figure 1.9 also shows projected sensitivities of future experiments XENONnT [140], LZ [154] and DARWIN [33]. The latter, also referred to as "ultimate WIMP detector", will feature a multi-ton xenon target and push sensitivity to the boundaries of the experimentally accessible region until neutrino scattering dominates.

Nuclear physics contributes to direct detection searches via the WIMP-nucleus differential cross section $\mathrm{d}\sigma_{\chi\mathcal{N}}/\mathrm{d}E_r$ in Eq. (1.36). First, the nuclear wave functions of the inital and final nuclear states need to be calculated. This is challenging as it requires the solution of the nuclear many-body problem. In Sec. 1.4.3 we outline shell-model calculations that allow for the calculation of wave functions even for very heavy nuclei such as xenon.

The second aspect is the description of the WIMP-nucleus interaction. As WIMPs are cold dark matter they are non-relativistic. The operators describing the WIMP-hadron coupling are therefore usually derived in non-relativistic effective field theories, e.g., constrained to WIMP-nucleon interactions in Refs. [155–157] and including the coupling to pions in Refs. [158, 159].

These are then evaluated between initial and final nuclear states in order to provide nuclear structure factors. The particular choice of the effective operators is of great importance as it affects the analysis of direct detection experiments. In addition, provided a signal detection, additional information about the interaction type can be extracted by comparing data from different target nuclei as well as from studying inelastic scattering [141] and probing the q-dependence (see Sec. 7.2). Traditionally, only the coherent scalar, called spin-independent, and the axial-vector, labeled as spin-dependent, interactions are taken into account. For those interaction channels limits on the WIMP-nucleon couplings are extracted in experimental searches. Even though it is unknown how WIMPs interact with SM particles, the coupling to composite particles such as nucleons and pions is constrained via the strong interaction, that describes how the SM fields, quarks and gluons, combine into nucleons and pions. It is therefore necessary to include these constraints. Momentum transfers in the WIMP-nucleus scattering process are expected to be of the order of the pion mass. A natural choice is therefore to use chiral EFT to derive these effective operators, automatically incorporating QCD physics. In addition, chiral EFT describes the strong interaction among the nucleons within the nucleus thus predicting the interaction of WIMPs to two and more nucleons. For spin-dependent interactions, contributions from chiral two-body currents have been shown to lead to significant differences in the derived response functions [67, 160].

In Chapter 5 we present effective operators for the WIMP-nucleon interaction based on the framework of chiral EFT. A minimal extension based on a study of which operators get coherently enhanced when evaluated between nuclear states is discussed in Chapter 6. Finally, we show in Chapter 7 how our formalism can be applied to improve limits on the WIMP-nucleon coupling extracted from collider searches (Sec. 7.1). We also present an analysis of how different interaction channels can be distinguished within one single experiment based on the momentum dependence of the interaction (Sec. 7.2).

1.4 Overview of methods

The nuclear chart ranges from the lightest systems of just a few nucleons to very heavy nuclei comprised of more than 200 nucleons. Properties of nuclear systems are obtained via solutions of the corresponding Schrödinger equation. In general, for such many-body systems analytic solutions are impossible to obtain, and exact numerical solutions become more expensive with increasing particle number. Therefore, there is a range of many-body methods aiming to limit the computational cost of numerical calculations by introducing additional approximations and/or assumptions about the system.

The few-neutron systems studied in this thesis can be described in a single-particle basis. A particular choice is presented in Sec. 1.4.1, where we introduce the Discrete Variable Representation (DVR). Later, in Chapter 4 we discuss a DVR based on plane waves in order to conveniently implement the periodic boundary conditions in a cubic box.

Several *ab initio* many-body methods exist to calculate light and medium-mass nuclear systems. The term *ab initio* here refers to calculations were only controlled approximations in the many-body treatment are being made. Such methods, e.g., the no-core shell model [161], the coupled cluster method [162, 163], the in-medium similarity renormalization group (SRG) [164], and the self-consistent Green's function method [165], have been able to extend their reach in the recent decades to the light to medium-mass region limited by proton and neutron numbers of roughly $Z = N = 20$ with exceptions including closed shell nuclei such as the calcium isotopes and $N = Z$ nuclei such as ^{28}Si [164] or ^{100}Sn [166]. Most relevant, however, for this thesis are quantum Monte Carlo (QMC) methods which have been successfully used to compute the properties of light nuclei [167, 168] and nuclear matter [169–171]. QMC methods rely on a statistical approach to the solution of the many-body Schrödinger equation. In Sec. 1.4.2, we will discuss the basics underlying the QMC methods applied to the few-neutron systems in Chapters 2 and 3 of this thesis.

Heavy nuclei such as the xenon isotopes used as target material in direct detection dark matter experiments are at the moment well beyond the scope of *ab initio* methods. Therefore, in Sec. 1.4.3, we outline the interacting shell model (ISM) method [172], which allows for calculations of medium-mass to heavy nuclei, discussed in Chapters 6 and 7.

1.4.1 Discrete variable representation

The most straightforward approach to find approximate eigenstates of the time-independent Schrödinger equation

$$H\Psi = E\Psi \tag{1.37}$$

is to constrain the full Hilbert space of the wave function Ψ to a finite set of orthonormal states $\{\phi_i\}_{i=1,\dots,n}$. The matrix elements of the Hamiltonian in this truncated basis are given by

$$H_{ij} = \langle\phi_i|H|\phi_j\rangle = \langle\phi_i|T|\phi_j\rangle + \langle\phi_i|V|\phi_j\rangle \ , \tag{1.38}$$

where T and V denote kinetic and potential energy operators, respectively. The eigenstates of the system,

$$\Psi = \sum_{i=1}^{n} c_i \phi_i \,, \tag{1.39}$$

are then obtained by diagonalization of H in the truncated model space. This approach is variational in the sense that the lowest energy eigenstate is an upper bound for the exact ground state of the system and it is therefore also called variational basis representation. In general, the solutions obtained this way will differ from the exact solution, which in general might not be representable in any finite basis.

For nuclear structure calculations, a natural choice for the single-particle states ϕ_i are the harmonic oscillator (HO) eigenstates as the mean field of light nuclei resembles a harmonic oscillator potential at short distances. The HO basis is therefore commonly used in shell model calculations as outlined in Sec. 1.4.3.

In Chapters 2 and 4, we study the finite-volume spectrum of particles confined in a cubic box of size L^3 with periodic boundary conditions. The natural choice for a basis adapted to the symmetries of this problem are plane wave states as used in Sec. 2.3.2.

An alternative basis representation is given by the discrete variable representation (DVR). In the DVR, overlap integrals are replaced by a sum over discrete grid points in coordinate space. The DVR states ψ are constructed such that when evaluated at the grid points x_j they yield

$$\psi_k(x_j) \propto \delta_{kj} \,. \tag{1.40}$$

As a consequence of this quasi locality, the corresponding DVR matrix representation of the potential is approximately diagonal for local potentials,

$$\langle \psi_i | V | \psi_j \rangle \approx V(x_i) \delta_{ij} \,, \tag{1.41}$$

thus reducing significantly computational expenses as no numerical evaluations of integrals are needed. In addition, the required memory to store the potential matrix elements is much smaller than for a dense matrix. The kinetic-energy matrix, on the other hand, is no longer diagonal. However, for many DVR variants analytic formulas can be derived or, as in the case of the DVR for periodic boundary conditions introduced in Chapter 4, a fast Fourier transform can be used to calculate the matrix elements. Furthermore, the kinetic energy matrix becomes relatively sparse in multi-dimensional problems as for example in three dimensions

$$\langle \psi_{i_x} \psi_{i_y} \psi_{i_z} | T | \psi_{j_x} \psi_{j_y} \psi_{j_z} \rangle = T_{i_x j_x} \delta_{i_y j_y} \delta_{i_z j_z} + T_{i_y j_y} \delta_{i_x j_x} \delta_{i_z j_z} + T_{i_z j_z} \delta_{i_x j_x} \delta_{i_y j_y} \,, \tag{1.42}$$

where we assumed that cross terms like $T_{i_x j_y}$ vanish. This might not always be the case as we will see in Chapter 4.

In conclusion, the calculation of the matrix elements of the Hamiltonian in the DVR basis is cheaper than in other basis representations as no integrals have to be evaluated. Furthermore, the diagonalization also profits from the sparse matrices as the required memory is significantly lower

than for other methods. In addition, we want to point out that there is no significant complication when including higher-body interactions such as three-body forces to the DVR framework.

1.4.2 Quantum Monte Carlo methods

Quantum Monte Carlo (QMC) methods comprise a large group of methods developed to solve the many-body Schrödinger equation. The common feature of this family is the use of stochastic sampling methods to numerically handle multidimensional integrals arising from the many-body problem. Applications of QMC methods to the nuclear problem range back to the 1960s when the ground states of three- and four-body nuclei were inferred using Green's function Monte Carlo [173]. Ever since, QMC methods have been extensively used in many different fields of physics such as condensed matter physics, few-body physics or quantum chemistry, to name just a few.

In the following, we will discuss Variation Monte Carlo, which combines the idea of Monte Carlo sampling and the variational principle. More sophisticated methods like the Green's function Monte Carlo (GFMC) and Auxiliary field diffusion Monte Carlo (AFDMC) methods project out the ground state from a given initial wave function by treating the Schrödinger equation as a diffusion equation in imaginary time. While other many-body methods used in nuclear physics introduce truncations of the basis size effectively constraining momentum and energy, the QMC solution of many systems does not suffer from these limitations. However, QMC methods are more demanding what concerns the inter-particle interactions studied as we will discuss below. The discussion provided here is based on the extensive reviews of QMC methods in Refs. [169, 174].

The calculations presented in this work were obtained using the AFDMC method (see below), which has been successfully applied to both homogeneous and inhomogeneous neutron matter in the past decade Refs. [169, 170] and more recently has shown promising progress towards generalization to nuclear matter and nuclei [171].

Variational Monte Carlo

We start with the simplest approach, Variational Monte Carlo (VMC), which basically consists of a stochastic evaluation of the integral corresponding to the quantum mechanical expectation value of a given operator for a given trial wave function Ψ_T. The variational energy E_V is given by the expectation value

$$E_V = \frac{\langle \Psi_T | H | \Psi_T \rangle}{\langle \Psi_T | \Psi_T \rangle}. \tag{1.43}$$

Due to the variational principle we have $E_V \geq E_0$, where E_0 is the exact ground state energy of the system. In coordinate space, the wave function depends on A particle coordinates $\mathbf{R} = \{\mathbf{r}_1, \mathbf{r}_2, \cdots, \mathbf{r}_A\}$ (we neglect additional degrees of freedom such as spin and isospin for the moment).

The energy E_V is now sampled by creating sets of configurations $\{\mathbf{R}_i\}_{i=1,\ldots,N}$ distributed according to the probability density function

$$\mathcal{P}(\mathbf{R}) = \frac{|\Psi_T(\mathbf{R})|^2}{\int |\Psi_T(\mathbf{R})|^2 d\mathbf{R}}, \tag{1.44}$$

and evaluating the local energy

$$E_L(\mathbf{R}) = \frac{H\Psi_T(\mathbf{R})}{\Psi_T(\mathbf{R})}. \tag{1.45}$$

In practice, the samples are created from the distribution $\mathcal{P}(\mathbf{R})$ using the Metropolis algorithm [175]. An estimator for the variational energy is then obtained by averaging over the samples.

The accuracy of results obtained in VMC depends entirely on the accuracy of the trial wave function. Improvement can be achieved by optimizing parameters in the trial wave function, however, the result will always be constrained by the functional form of the latter. Those limitations can be overcome by diffusion Monte Carlo (DMC) methods. The latter are not constrained by the initial guess of the wave function. Nevertheless, trial wave functions optimized in VMC can serve as starting point for DMC calculations significantly reducing the number of iterations needed to reach convergence.

Green's function Monte Carlo

The Green's function Monte Carlo method [167] is very similar to the DMC method, which has been used intensively in solid state physics [174]. Differences are minor, so we will treat both as equivalent in the following. The DMC method solves the time-dependent many-body Schrödinger equation by stochastically projecting out the lowest-energy state from a given initial wave function.

The time dependent Schrödinger equation of A particles can be written as

$$-\partial_\tau \psi(\mathbf{R}, \tau) = (H - E_T)\psi(\mathbf{R}, \tau), \tag{1.46}$$

where $\tau = it$ is the imaginary-time and E_T is a constant energy offset, the purpose of which will be explained later. Equation (1.46) is equivalent to

$$\psi(\mathbf{R}, \tau + \Delta\tau) = \int G(\mathbf{R}, \mathbf{R}'; \Delta\tau)\psi(\mathbf{R}', \tau)\mathrm{d}\mathbf{R}', \tag{1.47}$$

with the Green's function

$$G(\mathbf{R}, \mathbf{R}'; \Delta\tau) = \left\langle \mathbf{R} \middle| e^{-(H-E_T)\Delta\tau} \middle| \mathbf{R}' \right\rangle. \tag{1.48}$$

Equation (1.47) describes the propagation of the wave function by a time step $\Delta\tau$ in imaginary time. We assume now that there is set of eigenstates $\{\phi_i\}$ with eigenvalues $\{E_i\}$ of the Hamiltonian H. It is now possible to express the Green's function in terms of a spectral representation

$$G(\mathbf{R},\mathbf{R}';\Delta\tau) = \sum_i \phi_i(\mathbf{R}) e^{-(E_i-E_T)\Delta\tau} \phi_i^*(\mathbf{R}') . \tag{1.49}$$

The GFMC method starts from a trial wave function $|\psi_T\rangle$ often obtained through an optimization in VMC. It is now straightforward to show that applying $\exp[-(H-E_T)\tau]$ to $|\psi_T\rangle$ in the limit of $\tau\to\infty$ projects out the lowest eigenstate ϕ_0 that has nonzero overlap with the trial state:

$$\begin{aligned}\lim_{\tau\to\infty} \langle\mathbf{R}|\exp[-(H-E_T)\tau]\,|\psi_T\rangle &= \lim_{\tau\to\infty} \int G(\mathbf{R},\mathbf{R}';\tau)\psi_T(\mathbf{R}')\mathrm{d}\mathbf{R}' \\ &= \lim_{\tau\to\infty} \sum_i \phi_i(\mathbf{R}) \exp[-(E_i-E_T)\tau]\,\langle\phi_i|\psi_T\rangle \\ &= \lim_{\tau\to\infty} \phi_0(\mathbf{R}) \exp[-(E_0-E_T)\tau]\,\langle\phi_0|\psi_T\rangle\ . \end{aligned} \tag{1.50}$$

For $E_T = E_0$, the exponential is equal to one and the limit in the last line is exactly proportional to $\phi_0(\mathbf{R})$. Calculating the limit in Eq. (1.50) is the basis of all DMC methods.

For strongly interacting many-body systems it is not possible to calculate directly the Green's function. One resorts to an approximation in the small imaginary-time limit based on the Trotter-Suzuki formula for the exponential sum of two operators [176], in this case kinetic energy T and potential V,

$$G(\mathbf{R},\mathbf{R}';\Delta\tau) \approx \left\langle \mathbf{R}\middle|\exp[-(V-E_T)\Delta\tau/2]\exp[-T\Delta\tau]\exp[-(V-E_T)\Delta\tau/2]\middle|\mathbf{R}'\right\rangle . \tag{1.51}$$

The exponentials containing the potential V can be directly evaluated if the potential is local (see also Sec. 1.2.3). For local potentials we have $\langle\mathbf{R}|\exp[-V\Delta\tau]\,|\mathbf{R}\rangle = \exp[-V(\mathbf{R})\Delta\tau]$ and the Green's function of the kinetic energy reads

$$\begin{aligned} G^0(\mathbf{R},\mathbf{R}';\Delta\tau) &= \langle\mathbf{R}|\exp[-T\Delta\tau]\,|\mathbf{R}'\rangle \\ &= \left[\frac{1}{\lambda^3\pi^{3/2}}\right]^A \exp\left[-(\mathbf{R}-\mathbf{R}')^2/\lambda^2\right], \end{aligned} \tag{1.52}$$

where $\lambda^2 = 4(\hbar^2/2m)\Delta\tau$. In the small-time-step approximation the Green's function can thus be written as

$$G(\mathbf{R},\mathbf{R}';\Delta\tau) \approx \exp\left[-\frac{V(\mathbf{R})+V(\mathbf{R}')}{2}\Delta\tau\right] G^0(\mathbf{R},\mathbf{R}';\Delta\tau) . \tag{1.53}$$

The propagation in imaginary time is now performed as a sequence of N small-time evolutions,

$$\psi(\mathbf{R}_N,\tau) = \int G(\mathbf{R}_N,\mathbf{R}_{N-1},\Delta\tau)\cdots\times G(\mathbf{R}_1,\mathbf{R}_0,\Delta\tau)\psi_T(\mathbf{R}_0,0)\,\mathrm{d}\mathbf{R}_{n-1}\cdots\mathrm{d}\mathbf{R}_0\ . \tag{1.54}$$

In practice, the trial wave function is represented by a set of discrete sampling points or random walkers

$$\psi_T(\mathbf{R},\tau) = \sum_n \delta(\mathbf{R}-\mathbf{R}_n)\,, \tag{1.55}$$

which are propagated according to the diffusion term $G^0(\mathbf{R},\mathbf{R}';\Delta\tau)$. The exponential in Eq. (1.53),

$$P = \exp\left[-\frac{V(\mathbf{R})+V(\mathbf{R}')}{2}\Delta\tau\right], \tag{1.56}$$

represents a weight term usually implemented by a branching algorithm that allows walkers with a large weight to multiply. If the weight $P<1$, the corresponding walker continues its evolution with probability P, while for $P\geq 1$ the walker continues and in addition a new walker at the same position is created with probability $P-1$. For more details on these Markov chain Monte Carlo techniques we refer to Refs. [169, 174, 177].

Finally, in order to extract the energy of the system, the mixed estimator for the energy of the ground state,

$$E(\tau) = \frac{\langle\psi_T|H|\psi(\tau)\rangle}{\langle\psi_T|\psi(\tau)\rangle}\,, \tag{1.57}$$

is calculated and the average over all walkers is taken. During the propagation of the walkers the energy estimator decreases rapidly before eventually converging to the ground state energy E_0.

Up to this point, we have omitted the spin and isospin degrees of freedom of the wave function. In GFMC, the sums over these quantum numbers are performed explicitly. As a result, the computational cost scales exponentially with the number of particles limiting calculations to light nuclei up to ^{12}C and pure neutron matter of 16 neutrons.

Auxiliary field diffusion Monte Carlo

In order to overcome the limitations of GFMC, methods have been developed which exhibit an improved scaling behavior, however, at the cost of accuracy. The AFDMC method [177, 178] takes as basis states the tensor products of the $3A$ coordinates of the A nucleons and the tensor product of the four complex amplitudes for each nucleon to be in a state $|s\rangle = |p\uparrow, p\downarrow, n\uparrow, n\downarrow\rangle$. That is,

$$|\mathbf{R}S\rangle = |\mathbf{r}_1 s_1\rangle \otimes |\mathbf{r}_2 s_2\rangle \otimes \cdots \otimes |\mathbf{r}_A s_A\rangle\ . \tag{1.58}$$

As a consequence of the choice of basis, the propagator must contain, at most, linear operators in spin-isospin space. Since for an operator quadratic in either spin and/or isospin acting on such a state, the result will be a linear combination of two states instead of just one single state. As an example, we consider a state of two particles

$$\psi = \chi_{\alpha_1}(s_1)\chi_{\alpha_2}(s_2)\,, \tag{1.59}$$

where χ_α with $\alpha = s, m_s$ denotes a spin eigenstate. When the quadratic spin operator $\boldsymbol{\sigma}_1 \cdot \boldsymbol{\sigma}_2 = 2P_{12}^\sigma - 1$, where P_{12}^σ exchanges spins, acts on this state we obtain

$$\boldsymbol{\sigma}_1 \cdot \boldsymbol{\sigma}_2 \psi = 2\chi_{\alpha_1}(s_2)\chi_{\alpha_2}(s_1) - \chi_{\alpha_1}(s_1)\chi_{\alpha_2}(s_2)\,. \tag{1.60}$$

If this operator is part of the potential, it is necessary to sum over all single-particle spin states in each step of the propagation, usually done in GFMC. On the other hand, if only a single spin operator acts on ψ, the result will still be just a single state of the same form as ψ. Therefore, the Hubbard-Stratonovich transformation is used to linearize quadratic operators in the Hamiltonian

$$e^{O^2/2} = \frac{1}{\sqrt{2\pi}} \int_{-\infty}^{\infty} \mathrm{d}x\, e^{-x^2/2} e^{xO}\,, \tag{1.61}$$

where O denotes an operator acting on spin or isospin states, introducing the auxiliary fields x, which are Monte Carlo sampled to perform the integrals. The Green's function used in AFDMC can now be written as

$$\begin{aligned} G(\mathbf{R}, \mathbf{R}'; \Delta\tau) \approx \exp\left[-\frac{V_{\mathrm{SI}}(\mathbf{R}) + V_{\mathrm{SI}}(\mathbf{R}')}{2} \Delta\tau \right] G^0(\mathbf{R}, \mathbf{R}'; \Delta\tau) \\ \times \prod_n \frac{1}{\sqrt{2\pi}} \int_{-\infty}^{\infty} \mathrm{d}x_n\, e^{-x_n^2/2} e^{\sqrt{-\lambda_n \Delta\tau} x_n O_n}\,, \end{aligned} \tag{1.62}$$

where V_{SI} is the spin-isospin independent part of the potential and the product runs over the different spin-isospin operator structures in the potential. The AFDMC algorithm exhibits a polynomial scaling with nucleon number, allowing for simulations of larger systems than those accessible via GFMC.

Trial wave function

The trial wave function affects any QMC simulation not only through the initial configuration of the system. More importantly, the trial wave function guides the propagation of walkers through importance sampling (see Ref. [174]). Therefore, the quality of the trial wave function determines both efficiency of the simulation and the accuracy of the final result. Throughout the propagation process the trial wave function and its derivatives are repeatedly evaluated. It is therefore crucial to construct a trial wave function that is both accurate and easy to evaluate.

As we are studying systems of fermions in this thesis, the trial wave function must be antisymmetric under permutation of the particles. Therefore, the trial wave function used throughout this work is of Jastrow type, which is a product of central correlations acting on a Slater determinant of single-particle orbitals [169],

$$|\psi_J\rangle = \Big[\prod_{i<j} f^c(r_{ij}) \Big] |\Phi\rangle\,, \tag{1.63}$$

with $\langle \mathbf{R}S|\Phi\rangle = \mathcal{A}[\langle \mathbf{r}_1 s_1|\phi_1\rangle \cdots \langle \mathbf{r}_2 s_2|\phi_2\rangle \cdots \langle \mathbf{r}_A s_A|\phi_A\rangle]$, where $\mathcal{A}$ is the antisymmetrization operator. The single particle states $|\phi_i\rangle$ are chosen according to the symmetries of the system studied. In Secs. 2.2 and 3.2, more details on particular choices for these single-particle states are provided. The Jastrow correlation function $f^c(r_{ij})$ is symmetric and incorporates the dominant short-range central correlations into the wave function. It is obtained by a solving the radial Schrödinger equation in the given spin-isospin channel of the Hamiltonian.

A significant complication of QMC simulations stems from the fact that it is implicitly required that the sign of the wave function does not change as it is interpreted as a probability distribution. However, for fermionic systems the wave function cannot be positive everywhere. The fixed-node approximation defines a fixed nodal surface on which the wave function vanishes. Usually, this is implemented via the trial wave function. The QMC algorithm then produces the lowest-energy eigenstate in agreement with the given nodal surface. It can be shown that this solution is always an upper bound for the exact solution. The main difficulty is to model the nodal surface, which for most systems is not known exactly. In Sec. 2.3.2, we deal with the problem of determining the nodal surface for the excited state of two neutrons in a finite volume.

An approach which can be used for configurations with complex trial wave functions is the constrained path approximation [179]. The latter limits the path of a walker to regions where the real part of the overlap with the trial wave function is positive.

1.4.3 Interacting shell model

This short summary of the shell-model method is based on Refs. [172, 180], to which we refer the reader for an extensive discussion of the subject.

The shell model as a method to quantitatively describe nuclei has been established already in the late 1940s [181, 182]. The spectrum of nuclei exhibits an obvious shell structure with the appearance of magic numbers which mostly coincide with closed-shell states of the harmonic oscillator orbitals. It was realized that the closed-shell nuclei could be modeled by independent nucleons interacting via a mean-field interaction including an attractive spin-orbit term, which accounts for nuclear pairing. The wave function of the nucleus is then the product of only two Slater determinants, one for neutrons, the other for protons. This very simplistic picture fails when the number of protons and neutrons differs from the magic numbers and the two-body interaction between nucleons beyond the mean field needs to be taken into account. More accurate solutions can be obtained by increasing the number of basis states, i.e., Slater determinants.

It is natural to resort to a description of the many-body states in second quantization where the antisymmetry of states is incorporated via the commutation relations of creation and annihilation operators $a^\dagger$ and a, respectively. The nuclear states will now consist of a superposition of Slater determinants $|\phi\rangle = \prod_i a_i^\dagger |0\rangle$ interacting via

$$H = \sum_{ij} T_{ij} a_i^\dagger a_j + \sum_{i\le j,k\le l} V_{ijkl} a_i^\dagger a_j^\dagger a_k a_l \,, \tag{1.64}$$

where i, j, k, l denote the quantum number of the orbitals, T_{ij} is the kinetic energy matrix and V_{ijkl} the potential energy matrix. The number of Slater determinants taken into account is limited in order to allow for a computational solution such that the basis states are represented by the

finite sum $|\Phi\rangle = \sum_i^N c_i |\phi\rangle$. The diagonalization of H is usually performed using fast numerical algorithms such as Lanczos, which is especially well suited for the solution of the lowest-energy states.

The energy of the harmonic oscillator orbitals nlj is solely determined by the principle quantum number n since $E = \hbar\omega(n+3/2)$. The basis of Slater determinants is then usually labeled according to the number of additional excitation quanta $\hbar\omega$ compared to the state where the lowest orbitals compatible with the Pauli principle are occupied. As an example, we consider ^{6}Li. The $0\hbar\omega$ space consists of the Slater determinants which can be constructed from the four single particle states in the s shell and two states in the p shell. The $2\hbar\omega$ space in addition includes configurations that have an harmonic oscillator energy larger by two units compared to the $0\hbar\omega$ space, i.e., the Slater determinants which consist of four particles in the s shell, one in p and one in the pf, or three in the s shell, two in the p shell and one in the sd shell, or four s shell particles plus two sd shell particles. The energy converges to the ground state energy with increasing $N\hbar\omega$. The method described above is referred to as no-core shell model (NCSM) in the literature [161]. The interactions used for NCSM calculations are nucleon-nucleon interactions obtained either through phenomenological approaches or taken from effective theories such as chiral EFT (see Sec. 1.2). With increasing nucleon number A, the number of basis states becomes too large to allow for a numerical diagonalization. As a result, NCSM calculations are constrained to very light nuclei up to mass numbers of $A = 16$ [183].

Heavier systems become accessible when the full configuration space of the nucleons is separated in a core of completely filled major shells and an additional valence space on top of this core. This approach is referred to as interacting shell model. As an example, we mention here the sd shell nuclei such as, for example, flourine, sodium or silcon. The latter can be calculated based upon a core consisting of ^{16}O, which corresponds to the completely filled orbitals of the s and p shells, and the $0\hbar\omega$ valence space, i.e., the sd shell. In this valence space the particles interact with each other and with the core. Therefore, the main challenge of the interacting shell model is a transformation of the nucleon-nucleon interaction in Eq. (1.64) into effective potentials which act on a given valence space and still describe the nuclear states accurately [184, 185].

For light nuclei, it is possible to start from a Hamiltonian in the full space and decouple parts acting on the valence space from the rest. A very successful method that has been applied to this problem is the in-medium SRG [164]. Very recently this method has been applied to study electromagnetic transitions [186]. For heavy elements, however, the standard approach still consists of constructing phenomenological interactions that are fitted to some nuclei in a particular mass region. There have been recent efforts to construct the operator structure for the valence-space interactions based on chiral EFT [187].

Interacting shell model calculations based on phenomenological potentials are used in Chapters 6 and 7 to calculate the nuclear wave functions of the isotopes currently used in direct Dark Matter detection experiments.

2 Quantum Monte Carlo calculations of two neutrons in finite volume

In this chapter, we discuss quantum Monte Carlo calculations in a finite volume for ground and excited states, both for a contact potential as well as chiral EFT interactions. The motivation for these studies is twofold:

As discussed in Sec. 1.3.1, calculating nuclear observables directly from QCD remains a challenging problem as presently solving QCD on a lattice of discretized space-time constitutes the only available ab-initio technique to approach this problem. In order to make numerical calculations feasible it is necessary to work with small lattices. Lüscher [4, 5] established a direct connection between phase-shifts and finite-volume calculations for $2 \to 2$ scattering. As a result it is possible to obtain scattering parameters such as the scattering length and effective range directly from lattice QCD calculations. However, as the Lüscher result corresponds to an EFT in which particles interact only via contact interactions, it is not applicable to the regime of nuclear physics where pion exchange becomes important. Therefore, other approaches are necessary. We verify that QMC finite-volume calculations, by means of the Lüscher formalism, reproduce the low-energy effective-range parameters corresponding to a given neutron-neutron (nn) potential. We thereby demonstrate that such QMC calculations provide a reliable tool to establish a bridge between lattice QCD calculations and chiral EFT, in particular in kinematic configurations where the consideration of pion-exchange effects becomes mandatory and the Lüscher formula cannot be applied straightforwardly. As future work might aim at matching higher-body systems, a numerical method is required which is scalable to many particles and is well suited to study systems in a cubic box with periodic boundary conditions. We choose the auxiliary field diffusion Monte Carlo (AFDMC) method introduced in Sec. 1.4.2 as it meets these requirements. Finite-volume calculations are straightforward in QMC calculations as coordinate space is intrinsically constrained.

The second motivation concerns the study of parameters of few-particle resonances which can also be inferred from finite-volume calculations, as discussed in Sec. 1.3.1. For QMC methods to contribute in this direction, especially for channels where resonances may occur, it is crucial that excited states can also be accessed, in order to be able to identify the expected avoided level crossing [24]. This presents a challenge. Quantum Monte Carlo methods were developed to solve the many-body Schrödinger equation of a given system and find the lowest-energy state. As this particular state is given by the bosonic solution, nodal surfaces in the many-body wave function have to be introduced, something which can only be done approximately [169, 174, 188]. While an exact solution to this problem is therefore not available at the moment, we propose a strategy to obtain an approximate numerical solution for the excited state. Although the nn system strictly speaking does not exhibit a resonance, but only a virtual state, the nn calculations presented in this paper can be considered a first step towards this application.

We start in Sec. 2.1 with a derivation of the Lüscher formula in pionless EFT. In Sec. 2.2 we present the AFDMC method for ground and excited states of particles in a cubic box with periodic

boundary conditions. Special emphasis is put on the construction of trial wave functions that become important for the calculation of excited states. In Sec. 2.3, we present AFDMC results for finite-volume calculations of nn energies for a contact potential as well as chiral EFT interactions at different orders. Both ground states and excited states are compared with results from the Lüscher formula and also to exact diagonalizations. Based on this, we analyze in detail the finite-volume effects and deviations from the Lüscher prediction caused by pion exchanges. We then extract scattering parameters from the finite-volume results using the Lüscher formula. Finally, we conclude in Sec. 2.4.

This chapter presents work published in Ref. [189]. In this thesis additional details concerning the derivation of the Lüscher formula and the diagonalization method are provided. Also, we present results, which have not been published, for the chiral LO potential obtained via the diagonalization method together with an extended discussion of the final results.

2.1 Lüscher formula

In the original publications a derivation of the Lüscher formula entirely based on a quantum mechanical formalism is presented [4, 5]. Here we provide a derivation in pionless EFT based largely on Refs. [77, 190].

2.1.1 Derivation in pionless EFT

The very low-momentum properties of nucleon-nucleon (NN) interactions can be efficiently described within a pionless EFT [190–192]. Constrained to short-range interactions the effective Lagrangian becomes a series of local operators that consist of derivatives acting on nucleon fields,

$$\mathcal{L} = N^\dagger\left(\mathrm{i}\partial_t + \frac{\nabla^2}{2M}\right)N + \left(\frac{\mu}{2}\right)^{4-D}\left[-C_0(N^\dagger N)^2 + \frac{C_2}{8}\left[(NN)^\dagger(N^\dagger(\overleftrightarrow{\nabla})^2 N) + \text{h.c.}\right] + \ldots\right], \tag{2.1}$$

where $(\overleftrightarrow{\nabla})^2 = (\overleftarrow{\nabla})^2 - 2\overleftarrow{\nabla}\cdot\overrightarrow{\nabla} + (\overrightarrow{\nabla})^2$ and spin-isospin labels are omitted. The parameter μ is introduced for dimensional regularization as will become clear later. For $D = 3+1$ dimensions the Lagrangian is independent of μ. Based on this Lagrangian the tree-level amplitude is given by

$$\mathcal{A}_{\text{tree}} = -\left(\frac{\mu}{2}\right)^{4-D}\sum_{n=0}^{\infty} C_{2n}(\mu)p^{2n}\,, \tag{2.2}$$

with the relative momentum $p = |\mathbf{p}|$, $\mathbf{p} = (\mathbf{p}_1 - \mathbf{p}_2)/2$, where $\mathbf{p}_1$, $\mathbf{p}_2$ are the momenta of the two nucleons. If we include the loop diagrams shown in Fig. 2.1 the amplitude reads

$$\mathcal{A} = -\left(\frac{\mu}{2}\right)^{4-D}\left[\sum_{n=0}^{\infty} C_{2n}(\mu)p^{2n} + \left(\frac{\mu}{2}\right)^{4-D}\sum_{n,m} C_{2n}(\mu)C_{2m}(\mu)\int\frac{\mathrm{d}^{D-1}q}{(2\pi)^{D-1}}\frac{q^{2n}q^{2m}}{E - \frac{|\mathbf{q}|^2}{M} + \mathrm{i}\epsilon} + \ldots\right], \tag{2.3}$$

where the first term is the tree-level amplitude and the … stand for diagrams with more than one loop. As a result we need to evaluate integrals of the form

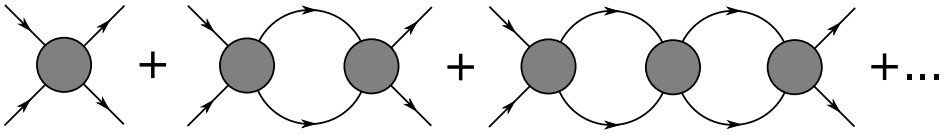

Figure 2.1: Loop diagrams arising from the contact interactions.

$$I_n = \left(\frac{\mu}{2}\right)^{4-D} \int \frac{\mathrm{d}^{D-1}q}{(2\pi)^{D-1}} \frac{q^{2n}}{E - \frac{|\mathbf{q}|^2}{M} + \mathrm{i}\epsilon}, \tag{2.4}$$

where $E = p^2/M$. The integrals are divergent but using dimensional regularization one obtains

$$I_n = -M(ME)^n(-ME - \mathrm{i}\epsilon)^{(D-3)/2}\Gamma\left(\frac{3-D}{2}\right)\frac{(\mu/2)^{4-D}}{(4\pi)^{(D-1)/2}} \tag{2.5}$$

$$= (ME)^n\left(\frac{M}{4\pi}\right)\sqrt{-ME - \mathrm{i}\epsilon} = -\mathrm{i}\left(\frac{M}{4\pi}\right)p^{2n+1}. \tag{2.6}$$

The expression in the first line does not contain any poles for $D = 4$, which would correspond to logarithmic divergences that could be subtracted in the minimal subtraction scheme (MS). Therefore, in MS the equation can be evaluated without any alterations. For large scattering lengths, however, the sum in Eq. (2.3) does not converge as every term gets larger than the previous when using the minimal subtraction scheme. Hence, one needs to apply a different regularization scheme (see Ref. [190]). We apply here the power subtraction scheme which removes the pole in $D = 3$ in Eq. (2.5) (in the Gamma function) by adding

$$\delta I_n = -\frac{M(ME)^n\mu}{4\pi(D-3)}. \tag{2.7}$$

In $D = 4$ dimensions we obtain

$$I_n^{(\mathrm{PDS})} = I_n + \delta I_n = -(ME)^n\left(\frac{M}{4\pi}\right)(\mu + \mathrm{i}p), \tag{2.8}$$

and the scattering amplitude can be rewritten as

$$\begin{aligned}\mathcal{A} &= -\left[\sum_{n=0}^{\infty} C_{2n}(\mu)p^{2n} + \sum_{n,m}^{\infty} C_{2n}(\mu)C_{2m}(\mu)(-1)p^{2(n+m)}\left(\frac{M}{4\pi}\right)(\mu + \mathrm{i}p) + \ldots\right] \\ &= -\sum_{n=0}^{\infty} C_{2n}(\mu)p^{2n}\sum_{i=0}^{\infty}\left[I_0^{(\mathrm{PDS})}\sum_{n}^{\infty} C_{2n}(\mu)p^{2n}\right]^i,\end{aligned} \tag{2.9}$$

where $I_0^{(\mathrm{PDS})} = -\frac{M}{4\pi}(\mu + \mathrm{i}p)$. Solving the geometric series the full amplitude can be written as

$$\mathcal{A} = \frac{-\sum C_{2n}(\mu)p^{2n}}{1 - I_0^{(\mathrm{PDS})}\sum C_{2n}(\mu)p^{2n}}. \tag{2.10}$$

The amplitude $\mathcal{A}$ has to be independent of the subtraction point μ. This sets the μ dependence of the couplings $C_{2n}(\mu)$.

In a box of size L^3 with periodic boundary conditions (PBC) the loop integral is replaced by a discrete sum over the momentum states allowed on the lattice,

$$I_0(L) = \frac{1}{L^3} \sum_{\mathbf{k}} \frac{1}{E - \frac{|\mathbf{k}|^2}{M}} \,. \tag{2.11}$$

In order to get rid of the divergence of the sum we add and subtract the infinite-volume integrals evaluated at $E = 0$. Since the divergence comes from the contribution of large momenta $\mathbf{k}$ in the sum it is sufficient to subtract the divergent part for one single value for the energy E. Then $E = 0$ is chosen for convenience. The integral that is added will be evaluated with PDS while the subtracted one is evaluated with a momentum cutoff, which is equal to the mode cutoff introduced to regulate the discrete sum. As a result, only the divergent part is subtracted from the discrete sum:

$$\begin{aligned} I_0^{(\mathrm{PDS})}(L) &= \frac{1}{L^3} \sum_{\mathbf{k}}^{\Lambda} \frac{1}{E - \frac{|\mathbf{k}|^2}{M}} - I_0^{\Lambda}(E=0) + I_0^{(\mathrm{PDS})}(E=0) \\ &= \frac{1}{L^3} \sum_{\mathbf{k}}^{\Lambda} \frac{1}{E - \frac{|\mathbf{k}|^2}{M}} + M \int^{\Lambda} \frac{\mathrm{d}^3 k}{(2\pi)^3} \frac{1}{|\mathbf{k}|^2} - \frac{M}{4\pi}\mu \\ &= \frac{1}{L^3} \sum_{\mathbf{k}}^{\Lambda} \frac{1}{E - \frac{|\mathbf{k}|^2}{M}} + M \frac{\Lambda}{2\pi^2} - \frac{M}{4\pi}\mu \\ &= -\frac{M}{4\pi}\left[\frac{1}{\pi L} S\left(\left(\frac{Lp}{2\pi} \right)^2 \right) + \mu \right], \end{aligned} \tag{2.12}$$

where the limit $\Lambda \to \infty$ is taken implicitly. $S(\eta)$ can be defined as a regularized sum

$$S(\eta) = \lim_{\Lambda \to \infty} \left(\sum_{|\mathbf{j}|<\Lambda} \frac{1}{\mathbf{j}^2 - \eta} - 4\pi\Lambda \right), \tag{2.13}$$

which runs over all three-vectors of integers $\mathbf{j}$ with $|\mathbf{j}| < \Lambda$. A more detailed discussion of $S(\eta)$ as well as its practical implementation for a numerical evaluation are summarized in Appendix A.1; a plot is shown in Fig. 2.2.

In the box both bound and scattering states are discrete and correspond to poles in the scattering amplitude

$$\mathcal{A}(k) = \frac{1}{k \cot(\delta_0(k)) - \mathrm{i}k} \,, \tag{2.14}$$

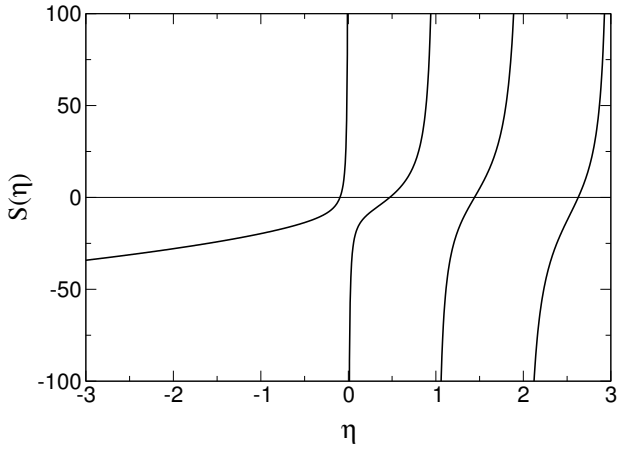

Figure 2.2: $S(\eta)$ from Eq. (2.13).

where δ_0 denotes the S-wave phase shift. Therefore, the energy eigenvalues of the NN system in a box can be found by requiring the real part of the inverse scattering amplitude to vanish,

$$\frac{1}{\sum C_{2n}(\mu)p^{2n}} - \mathrm{Re}\Big(I_0^{(\mathrm{PDS})}(L)\Big) = 0\,. \tag{2.15}$$

Now it is possible to relate the infinite-volume scattering data to the finite volume results: With Eqs. (2.14), (2.10) and (2.15) we find

$$-\frac{M}{4\pi}(p\cot\delta_0 - \mathrm{i}p) = \frac{1}{\sum C_{2n}(\mu)p^{2n}} - I_0^{(\mathrm{PDS})} = \mathrm{Re}\Big(I_0^{(\mathrm{PDS})}(L)\Big) - I_0^{(\mathrm{PDS})}\,, \tag{2.16}$$

which leads with Eqs. (2.8) and (2.12) to the final result

$$p\cot\delta_0(p) = \frac{1}{\pi L}S\left(\left(\frac{Lp}{2\pi}\right)^2\right). \tag{2.17}$$

Eq. (2.17) relates the finite volume eigenvalues for the energy $E = p^2/M$, with relative momentum p and particle mass M, with the infinite volume S-wave phase shift δ_0. This result is known as Lüscher formula [4, 5]. This version only holds for an S-wave projected potential. However, the cubic symmetry of the box (see also Appendix C) implies that the next partial wave that contributes in the box is the G-wave. A generalized version of the Lüscher formula including G-wave admixtures is given in Appendix A.2. We found the changes to the S-wave Lüscher formula to be negligible for all except very small box sizes. For small box size of the order of $L \sim 5$ fm the corrections are very small and depend on the G-wave phase shift. Due to the large suppression of the physical G-wave phase shift in nucleon-nucleon scattering we found the corrections to be negligible.

In this derivation, Eq. (2.17) strictly holds as long as a description in pionless EFT is justified. Due to the t-channel cut in the one-pion exchange, this restricts its range of validity to $|p| < m_\pi/2$ in the complex p plane. However, as shown in Refs. [4, 5], corrections to Eq. (2.17) for momenta

below the first inelastic threshold $|p| < \sqrt{m_\pi M}$ are suppressed by $e^{-m_\pi L}$, so that in practice the relation can be used as long as $m_\pi L$ is sufficiently large. In Ref. [78], the size of these corrections in the two-nucleon system was estimated for EFT-inspired potentials with pion exchange and contact interactions.

2.1.2 Finite volume energies from the effective range expansion

For low-energy NN scattering the first two parameters of the effective-range expansion, the scattering length a and the effective range r_e, are sufficient for an accurate description of the phase shift:

$$p \cot \delta_0(p) = -\frac{1}{a} + \frac{1}{2} r_\mathrm{e} p^2 + \mathcal{O}(p^4) \,. \tag{2.18}$$

Therefore, it is possible for a given scattering length and effective range to predict the energies of ground and excited states in a finite volume. Vice versa, given a set of data points $\{E_i, \Delta E_i\}$ for the energy eigenvalues for different box sizes L_i one can determine the scattering parameters a and r_e that best fulfill Eq. (2.17), where the left-hand side has been replaced by Eq. (2.18). In fact, whenever energy levels become negative, Eq. (2.17) provides a constraint in the unphysical region that cannot immediately be translated into a corresponding value for the phase shift. In such cases, the effective-range expansion (2.18), in addition to providing a convenient parametrization of the phase shift, serves another purpose, namely that of stabilizing the analytic continuation towards the physical region, which can only be performed if the functional form is known. This situation is realized for the ground-state energy of the two-neutron system.

Although Eq. (2.17) could still be used for $m_\pi/2 < |p| < \sqrt{m_\pi M}$ provided the volume is sufficiently large, the validity of the analytic continuation based on the effective-range expansion (2.18) is limited by the t-channel pion exchange, which in the partial-wave projection generates cuts on the imaginary momentum axis starting at $p = \pm i m_\pi/2$. Therefore, if points with $|p| > m_\pi/2$ were to be included, these cuts would have to be accounted for explicitly in the functional form used in the analytic continuation. For this reason we restrict all fits in this paper to points within the strict radius of convergence of pionless EFT $|p| < m_\pi/2$.

Since $S(\eta)$ is not invertible, it is not possible to directly define a function $E = E(L, a, r_\mathrm{e})$ which could be used in a standard χ^2 fit, so that we minimize instead

$$\chi^2 = \sum_{i=1}^{N} \frac{\left(\frac{1}{a} - \frac{1}{2} r_\mathrm{e} M E_i + \frac{1}{\pi L_i} S\Big(\big(\frac{L_i}{2\pi}\big)^2 M E_i \Big) \right)^2}{\sigma_i^2} \,, \tag{2.19}$$

with standard deviations obtained from Gaussian error propagation

$$\sigma_i^2 = \left[-\frac{1}{2} r_\mathrm{e} M + \frac{M L_i}{4\pi^3} S'\Big(\Big(\frac{L_i}{2\pi}\Big)^2 M E_i \Big) \right]^2 (\Delta E_i)^2 \,, \tag{2.20}$$

and $S'(\eta) = dS(\eta)/d\eta$. Parameter errors are estimated from the Hessian

$$H = \frac{1}{2}\begin{pmatrix} \frac{\partial^2\chi^2}{\partial a^2} & \frac{\partial^2\chi^2}{\partial a \partial r_e} \\ \frac{\partial^2\chi^2}{\partial r_e \partial a} & \frac{\partial^2\chi^2}{\partial r_e^2} \end{pmatrix}\Bigg|_{a_{\min},(r_e)_{\min}}, \tag{2.21}$$

according to

$$\Delta a = \sqrt{(H^{-1})_{11}}, \qquad \Delta r_e = \sqrt{(H^{-1})_{22}}. \tag{2.22}$$

Based on these equations we demonstrate the feasibility of an extraction of scattering parameters from finite-volume QMC calculations in Sec. 2.3, for both a contact potential as well as chiral EFT interactions.

2.2 Quantum Monte Carlo method for particles in a periodic box

In this section we show how the AFDMC method introduced in Sec. 1.4.2 is applied in the two-neutron system. We give particular attention to the calculation of excited states, which is in general a nontrivial task for QMC methods.

In Eq. (1.63) the generic trial wave function used in AFDMC simulations is provided. For neutrons in a cubic periodic box of volume L^3, the single-particle orbitals are taken as plane waves: $\phi_\alpha(\mathbf{r}_i, s_i) = e^{i\mathbf{k}_\alpha\cdot\mathbf{r}_i}\chi_{s,m_s}(s_i)$, with $\mathbf{k}_\alpha = \frac{2\pi}{L}\mathbf{n}_\alpha$ and $\mathbf{n}_\alpha$ being a vector of integers. χ_{s,m_s} denotes the spin eigenstates. For two neutrons, only the lowest two states with $\mathbf{k}_1 = \mathbf{k}_2 = \mathbf{0}$ are occupied, leaving the Slater determinant $\langle \mathbf{R}S|\Phi\rangle$ independent of spatial coordinates.

Imposing periodic boundary conditions is equivalent to identifying the endpoints of each Cartesian interval. This implies that, in coordinate space, the potential includes, in addition to the original potential $V(\mathbf{r})$, copies from the surrounding boxes

$$V(\mathbf{r}) \to \sum_{\mathbf{n}\in\mathbb{Z}^3} V(\mathbf{r} + \mathbf{n}L) \tag{2.23}$$

to preserve periodicity [4]. As long as the range of the potential, characterized by the effective range r_e for example, is small compared to the box size, $r_e \ll L$, the higher terms in the sum in Eq. (2.23) can be safely ignored. However, when the box size becomes comparable to the range of the potential $L \sim r_e$, these higher terms need to be included in both the expectation value of the Hamiltonian and in the calculation of the propagator in order to maintain the periodic boundary conditions. Below, if necessary, we consider terms corresponding up to either the nearest, second-to-nearest, or third-to-nearest boxes around the original one and thereby check for convergence of the sum in Eq. (2.23).

The calculation of excited states can be a challenging task for diffusion Monte Carlo methods. Since such methods always project, out of a trial wave function, the lowest-energy state of a given Hamiltonian, care must be taken to ensure orthogonality to, for example, the ground state (if the first-excited-state solution is sought). For nuclei, in many cases, the excited state which is desired has quantum numbers distinct from the ground state. In this case, all that is required is to construct a trial wave function with the appropriate quantum numbers [193]. However, in some

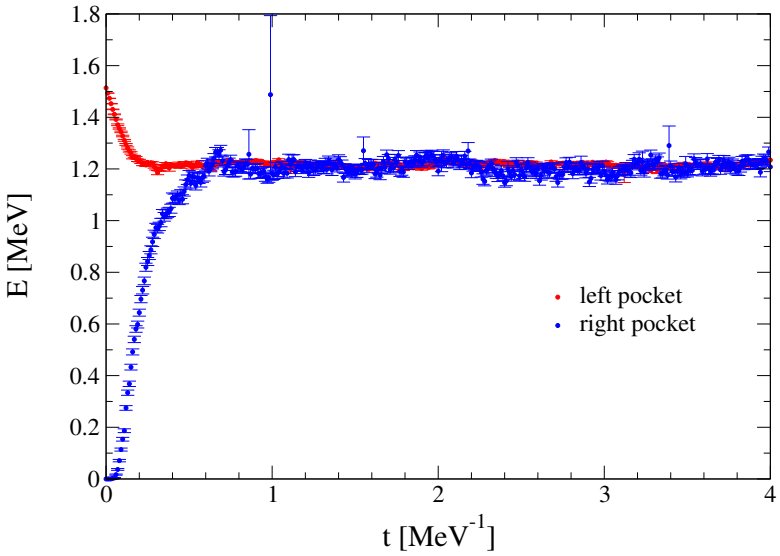

Figure 2.3: Propagation of the AFDMC energy estimator as a functions of imaginary time in the regions separated by a nodal surface of the Jastrow trial wave function (left and right pockets). The nodal position has been adjusted such that the two simulations converge to the same energy within statistical uncertainties.

cases, for example the Hoyle state of ^{12}C, the desired excited state has the same quantum numbers as the ground state, and then more care in constructing an appropriate trial wave function is required [188]. In the two-neutron system for low-energy scattering, we consider only the case where the neutrons are in a singlet spin state ($^1S_0$), which corresponds to the state described by the Lüscher formula in Sec. 2.1, and therefore the excited states possess the same quantum numbers as the ground state. Such excited scattering states have not been calculated previously using the AFDMC method.

The trial wave function for the first excited state calculated here was determined as follows. We assume a nodal surface defined by a particular relative distance r_{node} between the two particles. Since our Slater determinant is spatially independent, we introduce the node in the central correlation of the Jastrow wave function such that $\psi_J(r_{\text{node}}) = 0$. This implies that there is no angular dependence and the nodal surface is a sphere in relative coordinates. The validity of this assumption and an estimate for the related systematic error as well as an improved nodal surface will be discussed later. To determine the nodal position, we adopt the iterative approach described below.

Quantum Monte Carlo methods typically require local potentials. For an eigenstate of a local Hamiltonian, the solution of the Schrödinger equation must yield the same energy independent of the coordinates at which it is evaluated. Evaluating $[H\psi(\mathbf{R})]/\psi(\mathbf{R})$, where ψ is the exact solution of the problem, should therefore yield the same energy for a configuration of the two particles $\mathbf{R} = \{\mathbf{r}_1, \mathbf{r}_2\}$ with relative distance $r < r_{\text{node}}$ or $r > r_{\text{node}}$. As a consequence, the node position can be obtained by performing separate AFDMC simulations in the two subspaces divided by the nodal surface and adjusting the node position such that the AFDMC energies in the two subspaces agree. Each of these simulations starts from initial configurations where all walkers are placed in one of the two subspaces. For an arbitrarily chosen node position the two simulations will yield different energies. Moving the node position in the relative coordinate such that the two

independent simulations yield the same energy within statistical uncertainties leads to the results presented in Fig. 2.3. As the constrained-path approximation [194], which we use to tame the sign problem, prohibits walkers from crossing the nodal surface, this is equivalent to performing a simulation in a space which is limited to the region where the trial wave function does not change sign.

2.3 Results

We perform AFDMC simulations of two neutrons in a cubic box with periodic boundary conditions for both a simple contact potential as well as chiral EFT interactions. Both ground-state and first-excited-state energies are calculated and compared to exact solutions derived from the Lüscher formula in Eq. (2.17) with the effective range expansion in Eq. (2.18). The box size was varied from $L = 5$ fm to $L = 50$ fm.

2.3.1 Contact interaction

First, we consider a contact interaction independent of spin and isospin operators smeared out by a regulating function $V(r) = C_0\delta(r) \to C_0\delta_{R_0}(r)$ with

$$\delta_{R_0}(r) = \frac{1}{\pi\Gamma(3/4)R_0^3}\exp\left[-\left(\frac{r}{R_0}\right)^4\right], \tag{2.24}$$

where C_0 is a constant and $R_0 = 1.0$ fm determines the range of the regulator.

This potential corresponds to the smeared-out contact interaction part of the local chiral EFT interactions introduced in Sec. 1.2.3. Furthermore, up to the regulator, this potential corresponds to the interaction underlying the derivation of the Lüscher formula described in Sec. 2.1. For our calculations we take $L > R_0$ to minimize the finite-cutoff effects. Results obtained using this potential will serve as a benchmark for the AFDMC method in the two-particle system since we expect agreement with the Lüscher prediction up to statistical uncertainties.

Table 2.1 compares results of both the AFDMC and GFMC methods for representative box sizes. The GFMC calculations reproduce the AFDMC results within uncertainties, i.e., using the same number of configurations the uncertainties in the two methods are similar. Therefore, results will be shown only for the AFDMC method. Concerning the convergence of the sum in Eq. (2.23), we found for this potential that taking only the interaction in the original box into account is sufficient, which is consistent with the range of the potential.

Figure 2.4 compares the ground-state energies in terms of the dimensionless quantity $q^2 = EML^2/(4\pi^2)$ obtained from AFDMC simulations with the exact solutions from the Lüscher formula for two different sets of scattering parameters. In the first case we used $C_0 = -2.2369$ fm^2, which corresponds to the physical value for the nn scattering length of $a = -18.9$ fm and an effective range $r_e = 1.096$ fm in infinite volume. The second case shows results for a potential with $C_0 = -2.319$ fm^2 corresponding to a very large scattering length of $a = -101.7$ fm and an effective range of $r_e = 1.074$ fm. As can be seen, the agreement between the Lüscher results and the AFDMC simulations of the ground state is excellent over the full range of box sizes considered.

Potential	L (fm)	q^2 AFDMC	q^2 GFMC
C_0 physical a	5	-0.1001(3)	-0.0999(1)
	10	-0.0879(7)	-0.0875(4)
	20	-0.069(2)	-0.072(2)
LO $R_0 = 1.0$ fm	5	-0.1179(6)	-0.1178(1)
	10	-0.0931(6)	-0.0940(4)
	20	-0.079(2)	-0.077(1)

Table 2.1: Comparison of ground-state results for two different potentials with both the AFDMC and GFMC methods for several box sizes L.

It is worth pointing out the precision possible with the AFDMC method even at the extremely low densities of $2/(50\text{ fm})^3 \sim n_0/10^4$, with n_0 being the saturation density of nuclear matter.

In future applications, one could take finite-volume results from lattice QCD calculations, extract scattering parameters from them, and adjust LECs in chiral EFT interactions to match these scattering parameters. Here we demonstrate this idea by extracting the scattering parameters from the AFDMC results in several cases. We propagate the estimated uncertainties from the AFDMC simulations through the χ^2 fit discussed in Sec. 2.1 and fit the first two or three parameters of the effective range expansion. In particular, in order to see how robust the extraction of the infinite-volume scattering parameters from the AFDMC calculations is, we consider the contact potential with the very large scattering length. Here we performed a two-parameter fit to a and r_e by using the ground-state data yielding $a = -98(4)$ fm and $r_e = 1.066(7)$ fm which agree within the uncertainties with the infinite-volume parameters given above. Figure 2.4 shows the corresponding Lüscher result. The large uncertainty in the fitted scattering length of more than 4% could be reduced significantly when including more data at $L \geqslant 20$ fm where a dominates the fit.

Results for excited-state energies of two neutrons with the contact potential with physical scattering length are shown in Fig. 2.5. AFDMC results are shown for both a spherical nodal surface as described in Sec. 2.2 and a nonspherical nodal surface, as will be introduced in Sec. 2.3.2. The AFDMC results from the spherical node are systematically above the Lüscher results by $\sim$ 1%; however, the overall trend is correctly reproduced. The global deviations can be understood when taking the assumption of a spherical nodal surface into account. An analysis of the systematic error related to this assumption will be discussed in the following section. The results from the nonspherical nodal surface reproduce the Lüscher results very accurately.

Figure 2.5 also shows a fit to the combined data of all AFDMC results for ground and excited states with the improved nodal surface for the contact potential with physical scattering length. For the fit, the first three coefficients of the effective range expansion including the shape parameter were taken into account. The sensitivity to the shape parameter is largest for the states with largest momentum p, which correspond to excited states for small box sizes. As there are only a few of these contained in the data set the shape parameter cannot be determined with enough precision. The three-parameter fit yields a reduced χ^2 value of 0.74, a scattering length of $a = -19.0(1)$ fm, and an effective range of $r_e = 1.081(5)$ fm. These both agree well with the infinite-volume values

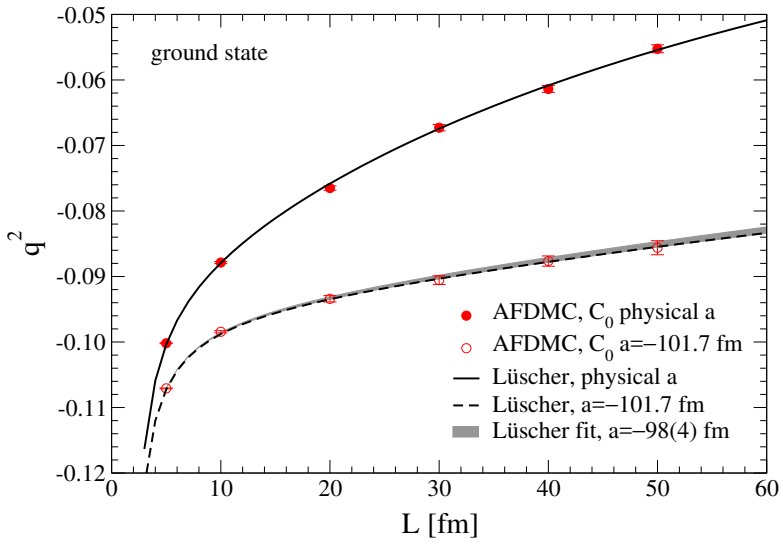

Figure 2.4: AFDMC results for the energy of two neutrons in the ground state in finite volume with the contact potential (2.24) for different box sizes L compared with the Lüscher formula [189]. C_0 is adjusted to give the physical nn scattering length $a = -18.9$ fm (closed circles and solid line) and to give a very large scattering length $a = -101.7$ fm (open circles and dashed line). The gray band shows a fit (as described in the text) to the AFDMC results for $a = -101.7$ fm. The energies are given in terms of the dimensionless quantity $q^2 = EML^2/(4\pi^2)$.

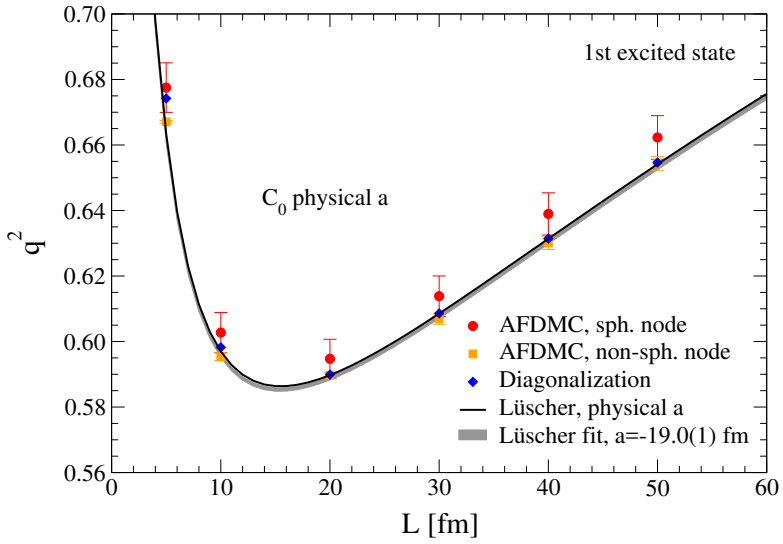

Figure 2.5: AFDMC results for the energy of two neutrons in the first excited state in finite volume with the potential (2.24) for different box sizes L (red circles) compared with the Lüscher formula (solid line) [189]. The error bars on the AFDMC results with a spherical nodal surface include both statistical uncertainties and a systematic uncertainty of 1% discussed in the text in Sec. 2.3.2. C_0 is adjusted to give the physical nn scattering length $a = -18.9$ fm. The energies are given in terms of the dimensionless quantity $q^2 = EML^2/(4\pi^2)$. Also shown are the energies calculated by exact diagonalization (blue diamonds) as discussed in Sec. 2.3.2.

given above. A more detailed discussion covering different aspects of extracting the scattering parameters from finite-volume energies of ground and excited states is given in Sec. 2.3.3.

2.3.2 Exact diagonalization and nodal surface

Diffusion Monte Carlo simulations do not provide direct access to the propagated wave function. To study the nodal structure of the wave function of two neutrons in a box we therefore directly diagonalize the Hamiltonian in an appropriate basis. The basis states are chosen to satisfy the boundary conditions of the system under study. We are interested in the zero-total-momentum eigenstates of a cubic box with periodic boundary conditions. Furthermore, since we are limiting ourselves to S-wave states we only need to take basis functions of even parity into account. A convenient set of basis functions meeting these requirements is given by

$$\begin{aligned} \psi^{\mathrm{3D}}_{nmk}(\mathbf{r}) &= \psi_n(x)\psi_m(y)\psi_k(z)\,, \\ \psi_n(x) &= \sqrt{\frac{2-\delta_{0n}}{L}}\cos\!\left(\frac{2\pi}{L}nx\right), \end{aligned} \tag{2.25}$$

where $n = 0, 1, 2, \ldots$ and $\mathbf{r} = \mathbf{r}_1 - \mathbf{r}_2$. In the cubic box the rotational symmetry group is broken down to the cubic symmetry group $\mathcal{O}$. As a result the irreducible representations of the rotational symmetry group, which are labeled by angular momentum, are mapped on the five irreducible representations Γ of the cubic symmetry group, $A_1^{\pm}$, $A_2^{\pm}$, $E^{\pm}$, $T_1^{\pm}$, and $T_1^{\pm}$. The irreducible representations of the rotational symmetry group are reducible with respect to $\mathcal{O}$. As a consequence, the angular momentum states in infinite volume contribute to several Γ. In particular, it can be shown that the S-wave states are mapped solely onto A_1^+ states (see Appendix C). The 24 members of the cubic group, i.e., the cubic rotations in Table C.1, reduce to the six permutations of the three coordinates x, y, z in the present case. Therefore, the eigenstates in the box have to remain invariant under exchange of coordinates x, y, z and the number of basis states can be reduced by defining symmetrized states for $n \leqslant m \leqslant k$:

$$\begin{aligned} \psi^{\mathrm{3D\ sym}}_{nmk}(x,y,z) &= N \sum_{\{n,m,k\}} \psi^{\mathrm{3D}}_{nmk}(x,y,z)\,, \\ N &= \begin{cases} 1/\sqrt{6} & \text{for } n \neq m \neq k \\ 1/\sqrt{12} & \text{for } n = m \neq k \\ 1/6 & \text{for } n = m = k\,, \end{cases} \end{aligned} \tag{2.26}$$

where the sum runs over all permutations of $\{n, m, k\}$. The number of basis states implicitly set by $n_{\max} > n, m, k$ has to be chosen such that the energy eigenstates are converged. As the box size L grows, $n_{\max}$ has to be increased because higher momentum states contribute to the eigenstates. The calculations for $L = 5, 10, 20, 30, 40, 50$ fm presented here were performed by using $n_{\max} = 10, 16, 32, 48, 54, 54$, respectively. Additional details concerning the numerical implementation of the diagonalization are provided in Appendices B.1 and B.2. Solving the eigensystem $H\psi = E\psi$

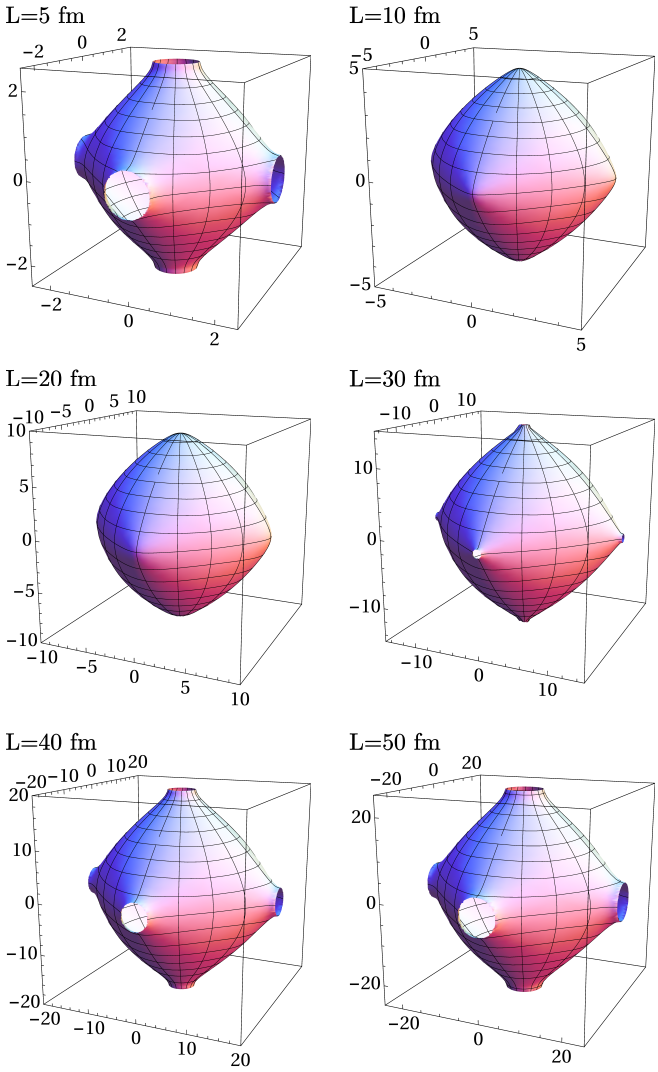

Figure 2.6: The nodal surfaces $r_{\text{node}}(\theta, \phi)$ of the first excited states of the contact potential (2.24) with the physical nn scattering length $a = -18.9$ fm for different box sizes L [189]. The wave functions from which the nodal surfaces are extracted are obtained via diagonalization. See text for details.

yields the eigenstates ψ_{gs} and ψ_{ex} corresponding to the ground- and first-excited-state energies E_0 and E_1 in terms of the basis defined in Eq. (2.26),

$$\psi_{\text{gs/ex}} = \sum_{\substack{n,m,k<n_{\max} \\ n\leqslant m\leqslant k}} c_{nmk}^{\text{gs/ex}}\, \psi_{nmk}^{\text{3D sym}}\,. \tag{2.27}$$

The excited-state energies for the contact potential (2.24) with the physical nn scattering length $a = -18.9$ fm are shown in Fig. 2.5. The results for the excited state from the diagonalization agree within 0.01% for $L = 20, 30, 40$ fm with the exact results obtained from the Lüscher formula. At $L = 5$ fm ($L = 10$ fm) a deviation of 1.6% (0.2%) from the Lüscher result can be observed. For the small boxes, especially for $L = 5$ fm, the range of the potential R_0 and the box size L are of the same order and the finite range of the contact potential (2.24) becomes relevant. Hence,

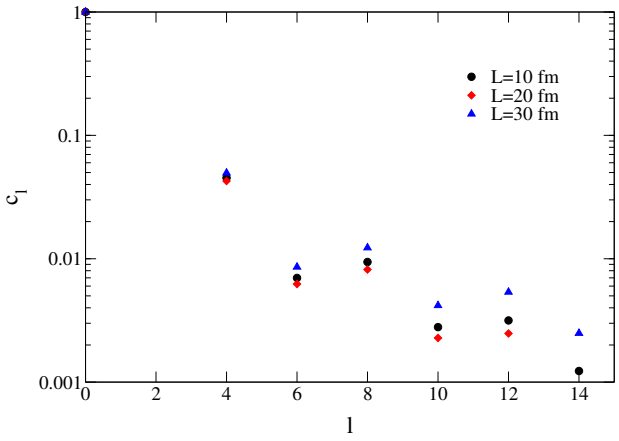

Figure 2.7: The coefficients c_l of the decomposition of the nodal surfaces in terms of cubic harmonics Y_l^c as in Eq. (2.30) as a function of l [189]. The coefficients for each box size shown are normalized such that $c_0 = 1$. The y-axis is log scaled showing the power-law suppression of the two coefficients c_4 and c_6 with comparison to c_0.

a deviation from the Lüscher prediction is expected. For $L = 50$ fm a deviation of $\sim 0.1\%$ was obtained implying that $n_{\max}$ needs to be increased in order to reach convergence.

The nodal surface $r_{\text{node}}(\theta, \varphi)$ can be extracted from the wave function of the excited state by solving $\psi_{\text{ex}}(r_{\text{node}}, \theta, \varphi) = 0$ for $\theta \in [0, \pi]$, $\varphi \in [0, 2\pi]$. Figure 2.6 shows the nodal surfaces for different box sizes. For the contact potential (2.24) with the physical nn scattering length $a = -18.9$ fm, the nodal surface is not spherical for any box size and not even closed for box sizes of 5, 30, 40, and 50 fm. To estimate the systematic error caused by assuming spherical symmetry in the nodal surface for the AFDMC simulations, we decomposed the nodal surfaces in real spherical harmonics Y_{lm}:

$$r_{\text{node}}(\theta, \phi) = \sum_{l=0}^{\infty} \sum_{m=-l}^{l} c_{lm} Y_{lm}(\theta, \phi) \,. \tag{2.28}$$

We found that the coefficients c_{lm} vanish for all l, m other than $l = 0, 4, 6, 8, \ldots$ and $m = 0, 4, 8, \ldots$, which suggests that there is a more appropriate set of functions in which one can expand the nodal surface. Indeed, as we mentioned above already, in a cubic box the rotation symmetry group is broken down to the cubic symmetry group $\mathcal{O}$. The irreducible representation of $\mathcal{O}$ is given by combinations of spherical harmonics, so-called cubic harmonics Y_l^c, with

$$Y_l^c(\theta, \phi) = \sum_{m=0,4,8,\ldots} a_{lm} Y_{lm}(\theta, \phi) \,, \tag{2.29}$$

where the coefficients a_{lm} are given in Ref. [195]. We found that for a given l the coefficients $c_l = \frac{c_{lm}}{a_{lm}}$ agree for all $|m| \leqslant l$. Hence, as expected it is possible to expand the nodal surface in terms of cubic harmonics,

$$r_{\text{node}}(\theta, \phi) = \sum_l c_l Y_l^c(\theta, \phi). \tag{2.30}$$

The corresponding coefficients c_l for box sizes where the nodal surface is closed ($L = 10, 20$ fm) and almost closed ($L = 30$ fm) are shown in Fig. 2.7. Note that the coefficients are normalized such that $c_0 = 1$. c_0 being much larger than c_l for $l \geqslant 4$ justifies the approximation of the nodal surface as a sphere used in the AFDMC simulations because the spherical contribution from Y_0^c dominates the nodal surface. We do not perform the decomposition for the other box sizes since the holes in the surfaces cause large uncertainties when decomposing into cubic harmonics.

The radial solution of the two-particle scattering problem in infinite volume can be written in terms of spherical Bessel functions $j_l(pr)$. For $pr \ll 1$, the Bessel functions behave as $j_l(pr) \sim (pr)^l$. In a cubic box the lowest-possible momentum is $p \sim 1/L$. As the excited states are completely determined by the nodal surface, which in our case is described by its radius r_{node}, naive dimensional analysis suggests that we can identify $r = r_{\text{node}}$. Hence, we expect that higher-l contributions are suppressed by $(r_{\text{node}}/L)^l$ when comparing to the leading contribution. Indeed, the coefficients c_4 and c_6, shown in Fig. 2.7, are suppressed according to a power law compared with the leading spherical contribution with $l = 0$.

Although this is no longer true for $l > 6$, the argument can still serve as an estimate of the systematic uncertainty introduced through the assumption of a spherical nodal surface in the AFDMC simulations of the first excited state. A perturbative expansion of the energy in terms of different l contributions to the wave function,

$$E = \langle \psi_{l=0} | H | \psi_{l=0} \rangle + c_4^2 \langle \psi_{l=4} | H | \psi_{l=4} \rangle + \dots, \tag{2.31}$$

implies a correction proportional to $(c_4)^2$ when assuming that $\langle \psi_l | H | \psi_l \rangle$ is of the same order for all l. Taking into account that the suppression seems to decrease with higher l we estimate $(c_4)^2$ conservatively as being of the order of 1% even though $c_4 \approx 0.045$ (see Fig. 2.7). Therefore, an additional systematic error of 1% is added to the statistical uncertainties from the QMC simulations in Figs. 2.5 and 2.9.

Furthermore, it is clear that the nodal surfaces shown in Fig. 2.6 are less spherical for box sizes where the surface is not closed. This statement is supported by Fig. 2.7 where the coefficients for $L = 30$ fm are larger than the other contributions. This matches the deviations of AFDMC results with the spherical node from the Lüscher predictions in Figs. 2.5 and 2.9, which are largest for $L = 5, 40, 50$ fm.

Our diagonalization study suggests that a large improvement in our AFDMC results can be obtained by incorporating the first nonspherical contribution into the nodal surface

$$r_{\text{node}}(\theta, \phi) = c_0 Y_0^c(\theta, \phi) + c_4 Y_4^c(\theta, \phi). \tag{2.32}$$

As discussed in Sec. 2.2 separate QMC runs were preformed on the two sides of the nodal surface in order to find an optimal set of parameters c_0 and c_4. Details on how the nonspherical nodal surface was incorporated into the Jastrow wave function can be found in Appendix B.3.

As can be seen in Fig. 2.5, the improved nodal surface yields AFDMC results much closer to the Lüscher prediction. However, one can see still some disagreement between the three methods employed (diagonalization, AFDMC, and Lüscher) at the smallest box size considered, $L = 5$ fm. The results coming from the exact diagonalization and the AFDMC results should agree well, as they do for larger box sizes. That they do not suggests that our improved nodal surface is likely missing higher-order Y_l^c contributions and the associated uncertainties might be underestimated. Since the Lüscher results are based on the effective range expansion, while the diagonalization uses the full potential, deviations at large energies (corresponding to small box sizes) are expected as soon as the effective range expansion is no longer accurate enough to describe the phase shift.

2.3.3 Chiral EFT interactions

In this section, we present results for the different local chiral EFT potentials from Ref. [55]. To avoid large statistical uncertainties, QMC simulations require interactions where all momentum dependencies up to quadratic terms can be separated. This requirement is met by local potentials [169]. However, chiral EFT interactions are usually formulated in momentum space and are typically nonlocal. Local chiral NN potentials have been developed recently up to next-to-next-to-leading order (N^2LO) in the chiral power counting as we discussed in Sec. 1.2.3.

Table 2.1 compares results for the leading chiral potential for both GFMC and AFDMC methods. As discussed before, uncertainty estimates are very similar and we limit our plots to results from the AFDMC method.

The range of the chiral potentials exceeds the range of the contact potential in Eq. (2.24). A check for convergence shows that, for box sizes up to L = 20 fm, inclusion of copies of the original box up to the second-to-nearest is required to reach truncation uncertainties comparable to the statistical errors, while beyond L = 20 fm at most the nearest copies need to be included.

In Fig. 2.8 we show results of AFDMC simulations which were performed using the chiral leading-order (LO) potential for $R_0 = 1.0$ fm and $R_0 = 1.2$ fm, corresponding (roughly) to cut-offs of 500 MeV and 400 MeV in momentum space, respectively. The scattering lengths and effective ranges were obtained by calculating phase shifts in the infinite volume. Similar to the previous cases we compare Lüscher results by using the scattering parameters to AFDMC results for different box sizes. Figure 2.8 also shows results for the chiral NLO and N^2LO potentials for $R_0 = 1.0$ fm. In all cases the overall agreement for box sizes $L \geqslant 10$ fm is excellent, while the AFDMC results for ground-state energies at $L = 5$ fm start to deviate from the Lüscher prediction. In Fig. 2.9 we show results for the excited states of the chiral LO potential for both a spherical nodal surface as described in Sec. 2.2 and a nonspherical nodal surface as introduced in Sec. 2.3.2. For the excited state we are able to solve Eq. (2.17) directly from the phase shift since no analytic continuation to imaginary momenta is necessary. The corresponding energies in finite volume are shown as well as the result when taking only the first two parameters of the effective range expansion into account. The full phase shift and its effective range expansion are compared in Fig. 2.10. As expected, the two-parameter effective range expansion fails to reproduce the phase

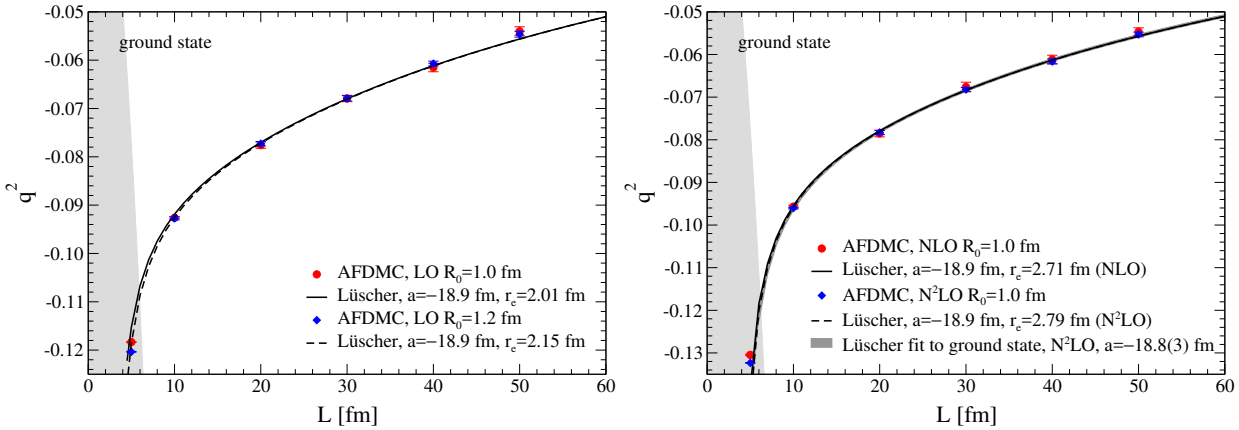

Figure 2.8: AFDMC results for the energy of two neutrons in the ground state in finite volume with the LO (left panel) and NLO and N^{2}LO (right panel) chiral EFT interaction compared with the Lüscher formula for different box sizes L [189]. The energies are given in terms of the dimensionless quantity $q^2 = EML^2/(4\pi^2)$. The region where $|p| > m_\pi/2$ is indicated by the gray band; see Sec. 2.1. Left: Results are shown for cutoffs $R_0 = 1.0$ fm (red circles and solid line) and $R_0 = 1.2$ fm (blue diamonds and dashed line). Right: The results at NLO (N^{2}LO) are given as the red circles and solid line (blue diamonds and dashed line). The dark gray band shows a fit (as described in the text) to the AFDMC results for the N^{2}LO chiral potential. Points in the region $|p| > m_\pi/2$ indicated by the gray band are not included in the fit; see Sec. 2.1.

shift at large momenta. Similarly, in Fig. 2.9 at small box sizes the Lüscher lines from the full phase shift and the effective range expansion deviate at small box sizes (large momenta).

Returning to the AFDMC results we observe that while the spherical node over-predicts at large L, the improved nodal surface yields results consistent with the Lüscher prediction in this region. However, in this context it is worth pointing out that for the chiral potentials the nodal surfaces tend to be more deformed than for the contact potential, which implies that the uncertainties for the small boxes are likely underestimated. At very small box sizes of $L = 5 - 10$ fm the results from the non-spherical nodal surface are getting closer to the Lüscher prediction obtained from the full phase shift, which is expected as the effective range expansion breaks down in this region. Furthermore, results obtained by diagonalization of the chiral LO potential projected on the S-waven channel (see Appendix B.4) are shown. The small deviation from the Lüscher result derived from the full phase shift can be perfectly accounted for when taking into account corrections to the Lüscher formula which are of the order $\exp(-m_\pi L)$ (see green band in Fig. 2.9).

As discussed in Sec. 2.1 the analytic continuation of the Lüscher formula is limited to the threshold of pionless EFT $|p| < m_\pi/2$. Figures 2.8 – 2.9 show the corresponding maximal value for q^2. The absolute values of the AFDMC and diagonalization energies for $L = 5$ fm (ground states) and $L \leq 10$ fm (excited state) for the different chiral potentials exceed the threshold of pionless EFT, and hence the (exponentially suppressed) disagreement with the Lüscher result from the full phase shift is to be expected. This effect reflects the necessity of including pions in the effective theory for the correct description of processes where momenta are of the order of the pion mass. However, we find that the size of the corrections is smaller than naively expected: for the smallest box size with $m_\pi L = 3.5$ the leading effect should scale as $c_1 e^{-m_\pi L} = 18\%$ [78], where $c_1 = 6$ denotes

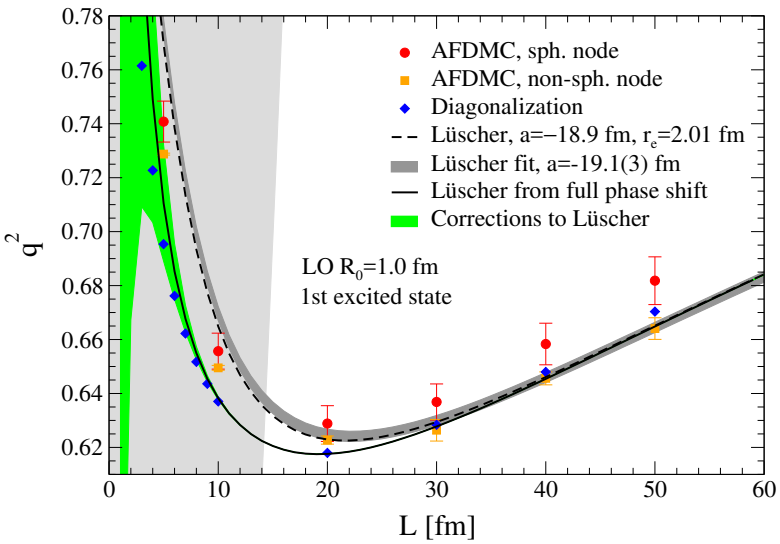

Figure 2.9: AFDMC results for the energy of two neutrons in the first excited state in finite volume with the LO chiral EFT interaction with cutoff $R_0 = 1.0$ fm (red circles) compared with the Lüscher formula derived from the full phase shift (solid line) and the first two terms of the effective range expansions (dashed line) for different box sizes L. Corrections $\exp(-m_\pi L)$ to the Lüscher result are shown as a green band. The error bars on the AFDMC results with a spherical nodal surface include both statistical uncertainties and a systematic uncertainty of 1 % discussed in the text in Sec. 2.3.2. The dark gray band shows a combined fit (as described in the text) to the ground- and first-excited-state AFDMC results for the LO chiral potential. The energies are given in terms of the dimensionless quantity $q^2 = EML^2/(4\pi^2)$. Points in the region $|p| > m_\pi/2$ indicated by the gray band are not included in the fit; see Sec. 2.1. Also shown are the energies calculated by exact diagonalization (blue diamonds) as discussed in Sec. 2.3.2.

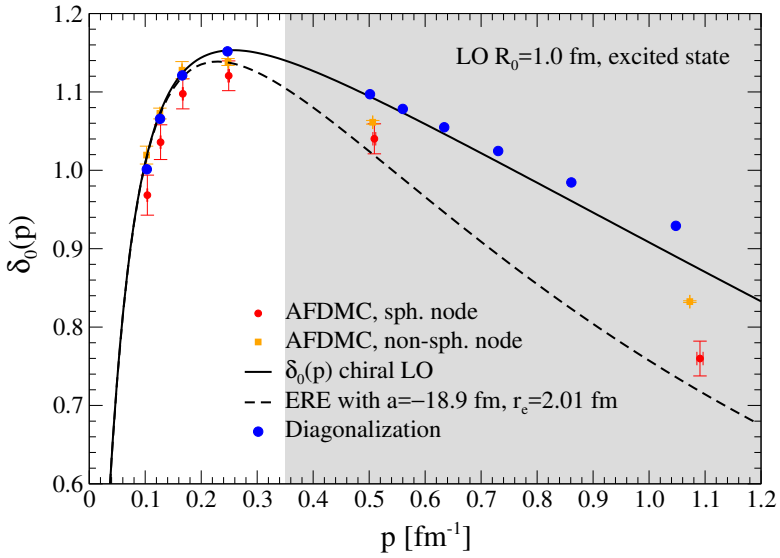

Figure 2.10: ${}^1S_0$ nn phase shift $\delta_0(p)$ from AFDMC results for the first excited state in finite volume with the LO chiral EFT interaction with cutoff $R_0 = 1.0$ fm with spherical nodal surface (red circles) and nonspherical nodal surface (orange squares) compared with the phase shift obtained from nn scattering in infinite volume (solid line). The error bars on the AFDMC results include both statistical uncertainties and a systematic uncertainty of 1 % discussed in the text in Sec. 2.3.2. The dashed line shows the phase shift obtained from the effective range expansion (ERE) with $a = -18.9$ fm and $r_\mathrm{e} = 2.01$ fm. The region where $|p| > m_\pi/2$ is indicated by the gray band; see Sec. 2.1. Also shown are phase shifts obtained through exact diagonalization of the finite volume system (blue diamonds) as discussed in Sec. 2.3.2.

the multiplicity of nearest neighbors (in Fig. 2.9 we conservatively took $c_1 = 6$ for the correction shown in the green band), but the actually observed deviation merely amounts to about 3%. This finding could be related to the observation in [78] that, for a realistic NN potential, the effective scale in the exponent can exceed the pion mass, leading to a stronger suppression than expected from one-pion exchange alone.

Figure 2.10 shows phase shifts obtained by solving Eq. (2.17) for the AFDMC results for the excited state with the LO chiral potential shown in Fig. 2.9 (red circles and orange squares). A direct extraction of phase shifts from finite-volume energies is only possible for states with $E > 0$. For $E < 0$ the phase shift can only be extracted via the effective-range expansion, which provides an analytic continuation to imaginary momenta corresponding to bound states. We compare the AFDMC results to the phase shifts obtained by solving the nn scattering problem for the same chiral LO potential in infinite volume (black line). As in Fig. 2.9, the overall trend is correctly reproduced by both the spherical and the nonspherical node results. We show again in gray the region for which momenta exceed the regime of pionless EFT, $|p| > m_\pi/2$. The AFDMC data with a spherical node underestimate the phase shift over the whole region. The improved nodal surface yields phase shifts in very good agreement with the infinite-volume phase shift at small momenta. Beyond the regime of pionless EFT the results are still too low but are significantly closer to the phase shift than the spherical node results. We also show the phase shift obtained from the effective range expansion with the first two parameters $a = -18.9$ fm and $r_\mathrm{e} = 2.01$ fm (dashed line), as used for the Lüscher result in Fig. 2.9. For momenta above the strict range of validity of the Lüscher formalism, the AFDMC results are larger than the phase shift from the truncated effective range expansion. This corresponds to Fig. 2.9 where these points lie below the Lüscher result. Also similar to Fig. 2.9, results obtained by converting the energies from diagonalizing the Hamiltonian (blue dots) agree very well with the phase shift.

2.4 Conclusions

In this chapter, we presented first results for the two-neutron finite-volume ground and first-excited states using AFDMC, both for a contact potential and chiral EFT interactions. To extract the excited-state energy we used an approximate method based on an iterative determination of the nodal surface of the excited-state wave function, with systematic uncertainties estimated by direct diagonalization of the contact-potential Hamiltonian. Having obtained the exact nodal surfaces through the diagonalization, we incorporated nonspherical nodal surfaces in the AFDMC method, which significantly improves results for the excited states. Using Lüscher's method to extract the scattering length and effective range from fits to the finite-volume energy levels of the ground and excited state, we found good agreement with the scattering parameters determined directly in infinite volume, which demonstrates the viability of the AFDMC approach for the calculation of the finite-volume two-particle spectrum.

However, we note that the computational effort necessary for the AFDMC calculations of the excited states exceeds significantly the expenses required for the diagonalization of the two-neutron system. For the two-particle systems this is expected since QMC methods become numerically favorable only for larger particle numbers. QMC methods have been successfully used to extract excited state properties in light nuclei where the quantum numbers of the excited state differs from those of the ground state [193] and for narrow excited states of the same quantum num-

bers [188]. Neither of the two is the case for the two-neutron system studied here. Progress in extracting excited states for such cases involving more than two particles would likely require a generalization of our iterative method to determine the nodal surface. This would be a challenging but interesting avenue for further research. In Chapter 4 we calculate finite-volume ground and excited states of few-particle systems by diagonalizing the Hamiltonian using the discrete variable representation basis.

By equating the finite-volume energy levels one can directly determine the LECs in the chiral potential without the necessity of first extracting the infinite-volume phase shift. Advantages of this procedure concern the fact that it evades limitations of the Lüscher formula for small volumes and should generalize straightforwardly to the multi-body system, to avoid the complexity typically inherent in the extension of Lüscher's approach beyond the two-body sector. For the extraction of resonance properties along these lines, we anticipate control over excited states to be essential. In this regard, the recovery of the virtual state in the two-neutron system as reflected by the large scattering length, both in the ground and first excited state, can be considered a successful proof of principle.

3 Quantum Monte Carlo calculations of three and four neutron resonances

Few-neutron resonances have enjoyed increasing attention in recent years due to an experimental claim for a possible tetraneutron resonance [12]. Within a short time, a range of different theoretical methods combined with different nucleon potentials have been applied to the problem [16–20] (see also Sec. 1.3.2).

More than ten years before the renewed interest in tetraneutron resonances arose, Pieper [11] conducted extensive Green's function Monte Carlo (see Sec. 1.4.2) calculations with the Argonne v_{18} NN potential (AV18) [92] plus $3N$ forces from the Illinois models [93] to answer the question if such realistic potentials would support a bound tetraneutron. It was found that this is only possible if the potential is significantly modified, leading to severely perturbed properties of light nuclei. By construction QMC methods are best suited for the calculation of bound states. Therefore, Pieper added an attractive external potential well to bind the otherwise unbound four-neutron system. The external well was chosen as a Woods-Saxon potential

$$V_{\mathrm{WS}}(r) = -\frac{V_0}{1+e^{(r-R_{\mathrm{WS}})/a}}\,, \tag{3.1}$$

with depth V_0, radius R_{WS}, and diffuseness $a = 0.65$ fm [196]. Similar configuration are used in studies of so-called "neutron drops" [58, 197]. The strength of the confining potential is then varied until the system becomes unbound. As shown in Fig. 1.5, it was found that the system became unbound before the well depth was reduced to zero. An extrapolation from the bound state energies to the realistic case of no external potential led to an energy of $E = 2\,\mathrm{MeV}$, independent of the radius R_{WS} of the well. Pieper interpreted this result as a possible tetraneutron resonance.

In this chapter we revisit this method using the Quantum Monte Carlo method now together with nuclear interactions derived in chiral EFT (see Sec. 1.2). While there is no strict proof that the extracted energy indeed corresponds to the resonance energy of the system, we provide evidence that this is the case by studying a two-body test case where it is possible to extract the resonance energy independently. The results presented in this chapter point to the conclusion that the chiral EFT interaction supports both three- and four-neutron resonances, independent of details of both the three- and higher-body interactions and regulator variations. Furthermore, we find that the three-neutron resonance is possibly lower in energy than the four-neutron resonance. These results open up the possibility for new experimental searches of a trineutron resonance.

The chapter is organized as follows. First, we discuss in Sec. 3.1 a two-particle test case that motivates the method of extracting the resonance energy by extrapolating from bound state configurations. In Sec. 3.2, details of the QMC method used for the calculation of the trapped multi-neutron systems are presented. The discussion is based upon Sec. 1.4.2, which provides more details on the QMC – and in particular – the AFDMC method. Results for the three- and four-neutron resonance energies are provided in Sec. 3.3. To rule out that the ordering of the extracted resonance

energies is just an effect of the external trapping potential, in Sec. 3.4 a similar configuration, few neutrons trapped in an external trap, is used to calculate the energies of the Helium isotopes. For the three- and four-neutron systems we find the one-body densities to be extremely low. Based on this observation we point in Sec. 3.5 to interesting analogies with systems made of ultra-cold fermions. Similar systems might be simulated using ultra-cold Fermi gases.

This chapter is based on Ref. [100]. Additional details not part of the publication are provided throughout the discussion.

3.1 Two-particle test case

Our results rely on the assumption that the extrapolation of the energy to the zero-depth external potential may be interpreted as a resonance energy, as suggested in Ref. [11]. To provide support for this interpretation, we have designed a simple S-wave potential consisting of two Gaussians:

$$V(r) = V_1 \, \mathrm{e}^{-\left(\frac{r}{R_1}\right)^2} + V_2 \, \mathrm{e}^{-\left(\frac{r-r_2}{R_2}\right)^2}, \tag{3.2}$$

with parameters $V_1 = -1000\,\mathrm{MeV}$, $V_2 = 865\,\mathrm{MeV}$, $R_1 = 0.4981\,\mathrm{fm}$, $R_2 = 0.2877\,\mathrm{fm}$, and $r_2 = 0.9972\,\mathrm{fm}$, such that we have an attractive well at the origin and a repulsive barrier at $\sim 1.0\,\mathrm{fm}$. Figure 3.1 shows the S-wave phase shift for two particles interacting via the two-Gaussian potential obtained through solving numerically the radial two-particle Schrödinger equation. From the phase shift the resonance energy E_R and width are extracted via the inflection point [198]

$$\left[\frac{\mathrm{d}^2\delta(E)}{\mathrm{d}E^2}\right]_{E=E_R} = 0\,. \tag{3.3}$$

This assumes a resonance of Breit-Wigner type with a background phase shift that varies only slowly around the location of the resonance. The width Γ of the resonance can now be extracted via

$$\left[\frac{\mathrm{d}\delta(E)}{\mathrm{d}E}\right]_{E=E_R} = \frac{2}{\Gamma}\,. \tag{3.4}$$

In Fig. 3.1 we show the extracted resonance energy of $E_R = 1.84$ MeV with a width of $\Gamma = 0.282$ MeV. Note that the phase shift is very sensitive to small changes in the parameters of the potential. In order to obtain a resonance energy well above zero, the parameters needed to be fine-tuned to the number of digits shown above.

In the next step, we added the external Woods-Saxon potential as in Eq. (3.1) to the two-particle Hamiltonian and adjusted the strength such that the system becomes bound. The two-particle Schrödinger equation was again solved numerically to obtain the S-wave bound states. In Fig. 3.2, we show results for various widths and depths of the Woods-Saxon well. The two particle system becomes unbound at around $V_0 = -1.0\,\mathrm{MeV}$. From the bound-state energies we extrapolate to zero well depth using a linear fit function. Remarkably, the different curves, which correspond to different radii R_{WS}, intersect at approximately the same energy of $E_R = 1.83(5)$ MeV. The uncertainty is extracted from the spread of the intersection points of the different curves.

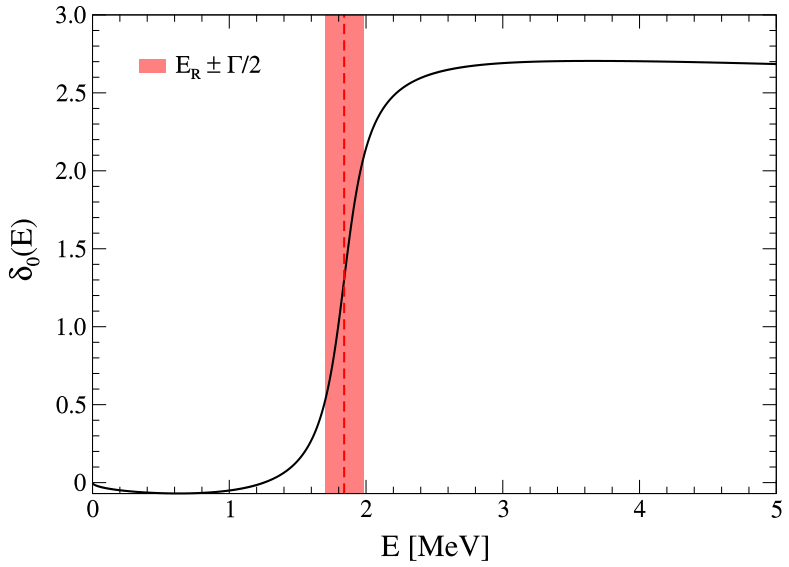

Figure 3.1: S-wave phase shift δ_0 as a function of relative energy E of two neutrons interacting via the model potential in Eq. (3.2). The resonance energy $E_R = 1.84\,\text{MeV}$ and width $\Gamma = 0.282\,\text{MeV}$ are highlighted in red.

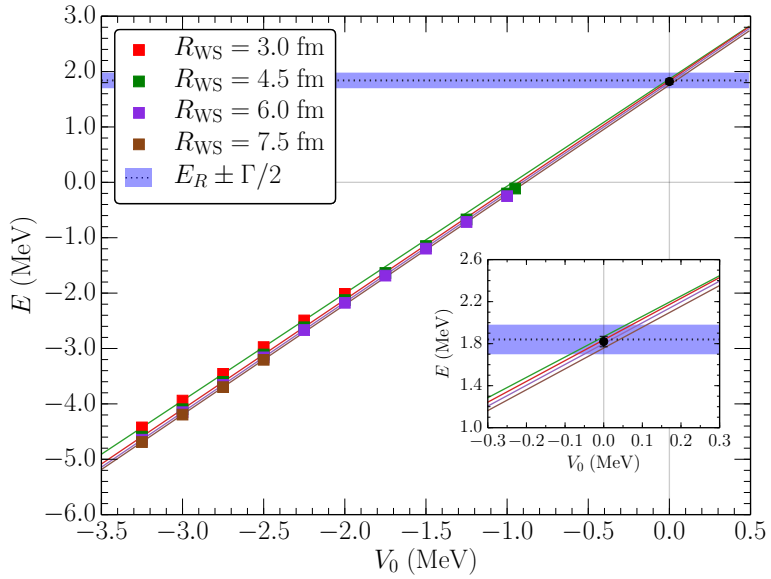

Figure 3.2: Energy of two neutrons trapped in various Woods-Saxon wells interacting via a simple model potential as in Eq. (3.2) designed to give a low-lying resonance [100]. Also shown are the linear extrapolations to zero well depth and the resonance energy E_R and width Γ extracted from the continuum. The black point at $V_0 = 0$ MeV is the average and standard deviation of the extrapolations evaluated at zero well depth.

Similarly, we have calculated the eigenstates of a purely attractive Gaussian potential that does not have any resonance and found that the Woods-Saxon depth required to bind the system is unnaturally large. Extrapolating to vanishing external potential strength for different widths the different curves did not converge to the same energy. In addition, we have calculated the energy of two neutrons interacting via the chiral N^{2}LO interactions in a Woods-Saxon well and found an extrapolation compatible with the virtual state energy of ~ 0.1 MeV.

These findings support the conclusion that this extrapolation method indeed leads to meaningful resonance energies. Nevertheless, it should be emphasized that our results provide evidence, however, not a formal proof, which should be kept in mind.

3.2 Quantum Monte Carlo calculations for trapped neutrons

In Sec. 1.4.2 we have discussed the auxiliary-field diffusion Monte Carlo (AFDMC) method. The AFDMC method projects out the ground-state energy from a trial wave function usually chosen to be a Slater determinant of single particle states (see Eq. (1.63) and discussion below). In the present case, the system is effectively confined by the external trap potential, which preserves rotational symmetry. Therefore, we resort to a single particle basis adapted to this symmetry. We start from a variational trial wave function whose form is

$$\langle \mathbf{R}S|\Psi_V\rangle = \langle \mathbf{R}S|\Big[\prod_{i<j} f^c(r_{ij})\Big]\Big[1+\sum_{i<j}F_{ij}+\sum_{i<j<k}F_{ijk}\Big]|\Phi_{JM}\rangle\,, \tag{3.5}$$

where $|\mathbf{R}S\rangle$ represent a collection of sampled $3A$ spatial coordinates and the $2A$ spinors of the A neutrons with an amplitude for the $\uparrow$ and $\downarrow$ spin, see Eq. (1.58). The physics of short-range correlations among the nucleons are incorporated in the trial wave functions through $f^c(r_{ij})$, which accounts for spin-isospin independent correlations, while F_{ij}, and F_{ijk} are two- and three-body spin-dependent functions, respectively. The trial wave function above is a modification of Eq. (1.63). The latter does not include effects of tensor interactions, which have been shown to be very important [169]. Therefore, by using Eq. (3.5) we expect an improved result already for variational QMC calculations.

The state $|\Phi\rangle$ is an antisymmetric uncorrelated mean-field part that describes the correct quantum numbers and asymptotic behavior of the system, i.e., in the present case total angular momentum J and its projection M. The QMC algorithm will then project onto the lowest-energy eigenstate with the same quantum numbers. In our case, Φ_{JM} is given by

$$\langle \mathbf{R}S|\Phi_{JM}\rangle = \sum_n k_n\Big[\det\{\phi_\alpha(\mathbf{r}_i,s_i)\}\Big]_{JM}\Big|_{\{\alpha\}_n}\,, \tag{3.6}$$

where $[\dots]_{JM}$ means a linear combination of Slater determinants $\det\{\phi_\alpha(\mathbf{r}_i,s_i)\}$ coupled with Clebsch-Gordan coefficients to have the quantum numbers JM. The sum over n runs over different sets of single particle quantum numbers $\{\alpha\}_n$, which can be coupled to JM. The single particle states

$$\phi_\alpha(\mathbf{r}_i,s_i) = R_{nlj}(r_i)\big[Y_{lm_l}(\hat{\mathbf{r}}_i)\xi_{sm_s}(s_i)\big]_{jm_j}\,, \tag{3.7}$$

are similar to the orbitals commonly used in the shell model, where $\alpha = (nljm_j)$, Y_{lm_l} are spherical harmonics, and ξ_{sm_s} are spinors in the usual up-down basis that are coupled to j, m_j,

$$\left[Y_{lm_l}(\hat{\mathbf{r}}_i)\xi_{sm_s}(s_i)\right]_{jm_j} = \sum_{m_l,m_s} \mathcal{C}^{jm_j}_{lm_lsm_s} Y_{lm_l}(\hat{\mathbf{r}}_i)\xi_{sm_s}(s_i)\,, \tag{3.8}$$

where $\mathcal{C}^{jm_j}_{lm_lsm_s}$ denote Clebsch-Gordon coefficients. The sum over n in Eq. (3.6) takes into account sets of A states out of the $\alpha = 1S_{1/2}$, $1P_{3/2}$, $1P_{1/2}$, $1D_{5/2}$, $2S_{1/2}$, and $1D_{3/2}$ orbitals. The radial components R_{nlj} are obtained by solving the Hartree-Fock equations with the Skyrme force SKM [199], which yield relatively accurate results for the densities of small nuclei. Since the Hartree-Fock solution for pure neutron systems is unbound, we tuned the depth of an external trap (imposed on the orbitals, which is distinct from the external Woods-Saxon potential) to generate the orbitals in such a way that they are bound. In a second step, an additional variational parameter a was included to vary their width, i.e., $R_{nlj}(r) \to R_{nlj}(ar)$.

The variational wave function Ψ_V is used as input for variational QMC calculations (see Sec. 1.4.2). Through a Lanczos algorithm, the free parameters in the two- and three-body correlations as well as the coefficients k_n are obtained by minimizing the variational energy [200]. Using these parameters we perform AFDMC calculations to project out the ground state of the system. One important point worth emphasizing is that the AFDMC method does not rely on a basis-set expansion. Therefore, in the infinite-volume limit, continuum states are automatically included.

Since we are simulating a system that is naturally unbound, we enforce the center of mass to have no motion in order to calculate internal energies only, as is commonly done in quantum Monte Carlo calculations for nuclei; i.e., given the translationally invariant Hamiltonian, the Monte Carlo evolution is performed so that the center of mass of the system does not move.

3.3 Three and four neutrons in a trap

We perform AFDMC calculations of three and four neutrons interacting via the many-body Hamiltonian that includes two- and three-nucleon interactions obtained within the framework of chiral EFT at next-to-next-to-leading order ($\mathrm{N^2LO}$) as discussed in Sec. 1.2.3. The Hamiltonian of the system is given by

$$H = -\sum_i \frac{\hbar^2}{2m}\nabla_i^2 + \sum_i V_{\mathrm{WS}}(r_i) + \sum_{i<j} V_{ij} + \sum_{i<j<k} V_{ijk}\,, \tag{3.9}$$

where V_{ij} and V_{ijk} are two-body [54, 55] and three-body [56] interactions, respectively, constructed at $\mathrm{N^2LO}$, with a cutoff of $R_0 = 1.0$ fm. V_{WS} is the Woods-Saxon potential as in Eq. (3.1). We have checked that our results are insensitive to the precise value of the diffuseness parameter a. Changing a by 20% in either direction changes the energy by less than 1% in the two-neutron case. Therefore, the results presented in this section were obtained with $a = 0.65$ fm. In addition, we vary the well depths V_0 and radii R_{WS}.

Figure 3.3 shows the energy as a function of V_0 for three (squares) and four (circles) neutrons. The blue (upper curves for various neutron numbers), green (middle curves), and

red (lower curves) are the results obtained for different radii R_{WS} as indicated in the figure. As for the two-particle test case we extrapolate to vanishing well depths via quadratic fits

$$E(V_0) = c_0 + c_1 V_0 + c_2 V_0^2 , \tag{3.10}$$

where c_i are the fitted coefficients, to the energies of four (solid lines) and three (dashed lines) neutrons. The extrapolations to $V_0 \to 0$ obtained for the different values of R_{WS} converge to the same point, indicating that the results at zero well depth are independent of the geometry of the external potential (provided that it goes to zero at large distances and its range is larger than the nucleon-nucleon effective range).

In order to study variations of the cutoff R_0 in the nucleon-nucleon interaction, and the importance of three-body forces, we have repeated the calculation using $R_0 = 1.2$ fm and turning off the three-neutron interaction. The results are indistinguishable from the cases shown in Fig. 3.3, within statistical errors (which are smaller than the points). Given the density of the system, this is not totally unexpected, as we discuss below. Another source of systematic uncertainty comes from the truncation of the chiral expansion at N^{2}LO. To estimate this uncertainty, we have considered the case of four neutrons in the Woods-Saxon well with $R_{WS} = 6.0$ fm and repeated our calculations at leading order (LO) and next-to-leading order (NLO). We estimate the uncertainty coming from the truncation of the chiral expansion at N^{2}LO following Ref. [201] by calculating

$$\Delta E^{\mathrm{N^2LO}} = \max(Q^3|E^{\mathrm{LO}}|, Q^2|E^{\mathrm{LO}} - E^{\mathrm{NLO}}|, Q|E^{\mathrm{NLO}} - E^{\mathrm{N^2LO}}|) , \tag{3.11}$$

where

$$Q = \max\left(\frac{p}{\Lambda_b}, \frac{m_\pi}{\Lambda_b}\right), \tag{3.12}$$

with the breakdown scale $\Lambda_b = 500\,\mathrm{MeV}$ (see Sec. 1.2) and the typical momentum scale $p \leq m_\pi$. We add these in quadrature to the quantum Monte Carlo statistical uncertainties. These are displayed as the error bars in Fig. 3.3 for the case with $R_{WS} = 6.0\,\mathrm{fm}$. They are still smaller than the points and, within the uncertainties we have quoted, do not affect the extrapolated energy of the four-neutron system. The inset in Fig. 3.3 also shows the LO, NLO, and N^{2}LO results with uncertainties as described above. One can see that, especially near the limit where the system becomes unbound, the results are not very sensitive to the chiral order. The fits in Fig. 3.3 evaluated at $V_0 = 0$ give an energy of $1.1(2)\,\mathrm{MeV}$ for three neutrons and $2.1(2)\,\mathrm{MeV}$ for four neutrons. This suggests that there could be a trineutron resonance in nature at a lower energy than the four-neutron resonance. The energy for four neutrons is in agreement with the result found in the initial study by Pieper [11] and compatible with the experimental result of $(0.83 \pm 0.65 \pm 1.25)\,\mathrm{MeV}$ [12].

In Ref. [17] resonance parameters of the tetraneutron were calculated using the no-core Gamow shell model and density matrix renormalization group method together with chiral NN interactions at N^{3}LO. Part of the study was to scale the potential such that the system becomes bound. In a similar approach, we have multiplied the N^{2}LO interaction by an overall scale factor α and tuned α until the four neutrons were bound as shown in Fig. 3.4. We find a scale factor of $\alpha \sim 1.3$ is sufficient to bind the four neutrons. We have varied α and performed an extrapolation to the original potential ($\alpha = 1$) by fitting a quadratic fit to the last four data points as shown in the right

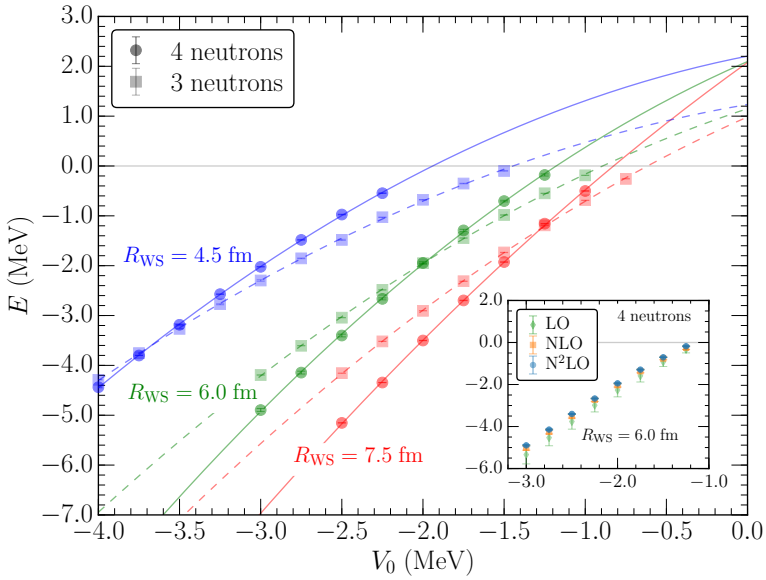

Figure 3.3: The energy of three (squares) and four (circles) neutrons in external Woods-Saxon potentials for varying radius $R_{\rm WS}$ as a function of the well depth V_0 [100]. The blue (upper) lines correspond to $R_{\rm WS} = 5$ fm, the green (middle) lines to $R_{\rm WS} = 6$ fm, and the red (lower) lines to $R_{\rm WS} = 7.5$ fm. In each case, a quadratic fit to the AFDMC results was obtained and used to extrapolate to the zero-well-depth limit. The inset shows calculations of four neutrons at LO (green diamonds), NLO (orange squares), and N^{2}LO (blue circles) with uncertainties coming both from the quantum Monte Carlo statistical uncertainty and from the truncation of the chiral expansion for the Woods-Saxon radius $R_{\rm WS} = 6.0$ fm.

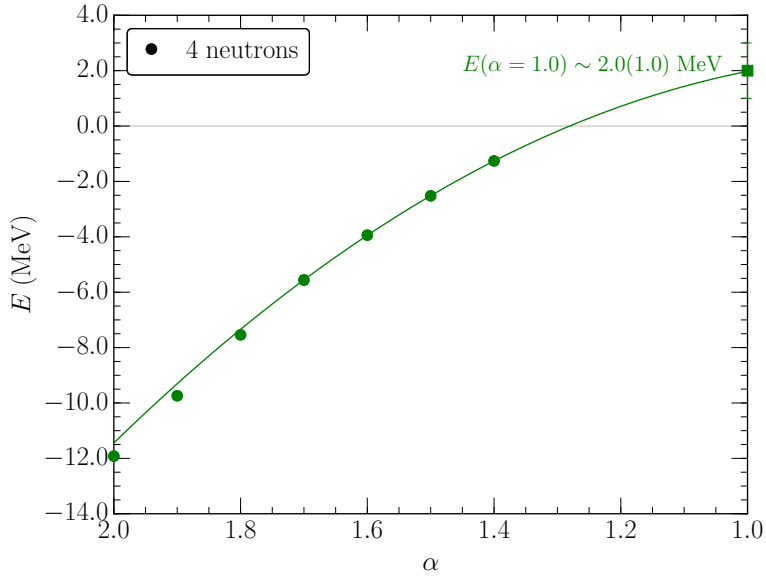

Figure 3.4: The energy of four neutrons as a function of the scaling factor α with which the NN and $3N$ potentials were scaled. A quadratic fit to the last four data points from the AFDMC calculation was obtained and used to extrapolate to the $\alpha = 1$ limit.

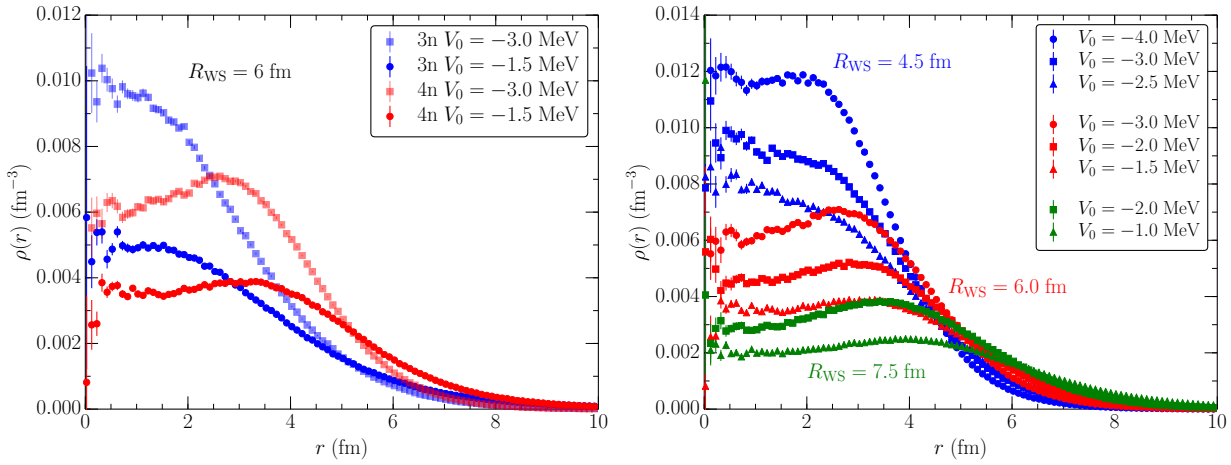

Figure 3.5: Left: One-body densities for three (blue) and four (red) neutrons in two different Woods-Saxon wells with depths 3 MeV (squares) and 1.5 MeV (circles) with a fixed $R_{WS} = 6.0$ fm. Right: One-body densities for four neutrons in Woods-Saxon wells with various depths and widths [100].

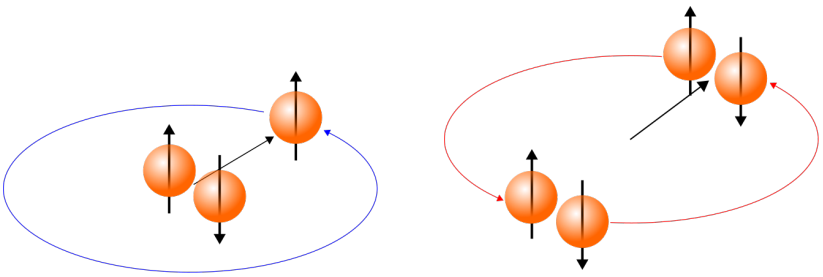

Figure 3.6: One neutron orbiting a cluster of two neutrons (left) and two two-neutron cluster orbiting each other (right) as suggested by the one-body densities distribution in Fig. 3.5. Figure courtesy of Joel E. Lynn.

panel in Fig. 3.3. The extracted energy for the unbound system at $\alpha = 1$ is $E = 2.0(1.0)$ MeV, where the relatively large uncertainty is due to the low number of data points considered in the fit. This energy is consistent with our results coming from the trapped four neutrons. This highlights the universal character of the extrapolated resonance energy obtained via confinement in the external trap and the scaling of the interaction potential.

In addition to the calculation of estimators for the energy of a system of particles, the QMC method also allows one to extract particle densities from the simulation. The expectation value of the one-body density is given by [169]

$$\rho_N(r) = \frac{1}{4\pi r^2} \langle \Psi | \sum_i \delta(r - |\mathbf{r}_i - \mathbf{R}_{\rm cm}|) | \Psi \rangle \,, \tag{3.13}$$

where $\mathbf{R}_{\rm cm}$ is the center-of-mass coordinate. In the left panel of Fig. 3.5, we show the neutron distribution inside the trap for three and four neutrons in different Woods-Saxon wells with $R_{WS} =$ 6 fm, normalized such that their integral is equal to the number of neutrons. We find that the

system is extremely dilute as the density of the systems never exceeds the value of $\sim 0.01\,\mathrm{fm}^{-3}$. For infinite neutron matter [55, 56, 58] it was found that at such low densities the energy per neutron is totally dominated by the S-wave part of the neutron-neutron interaction, and the results are almost independent of the two-body cutoff R_0 and the three-neutron interaction. This explains why we found the energies of three- and four neutrons to be independent of both the cutoff value R_0 and three-body forces.

Furthermore, it is interesting to note that in the same well the three-neutron system is always denser near the center than the four-neutron system, and the latter shows a distribution with a peak around 3 fm, suggesting that the system is arranged on a "shell". Notably, this difference in shape between the three- and four-neutron systems persists as the geometry of the trap is changed. One possible interpretation is that in the case of three neutrons one pair (up-down) of neutrons is sitting in the center of the trap, and one extra neutron is orbiting around in a P state. In the case of four neutrons, instead, the two pairs are orbiting around the center, making the system less dense in the center as illustrated in Fig. 3.6. As we discuss below, it might be possible to create similar systems with cold atoms. It would be very interesting to measure the shapes of such systems by tracking the position of the individual particles.

In additon, in the right panel of Fig. 3.5 we show one-body densities of four neutrons for different depths V_0 and radii R_{WS}. For a smaller radius of $R_{\mathrm{WS}} = 4.5$ fm the density becomes larger at smaller distances and the peak at finite particle distances is less pronounced. A larger radius of $R_{\mathrm{WS}} = 7.5$ fm leads to a broader distribution. However, the distributions are still peaked now at a slightly larger distance. For all cases the system remains very dilute.

3.4 Helium chain

The ordering of the extracted resonance energies (with the possible three-neutron resonance being lower in energy than the extracted four-neutron resonance) might seem unnatural, as one would naively expect the four-neutron system to have a lower energy due to pairing effects. However, this behavior seems to be reversed at deeper well depths as can be seen in Fig. 3.3. For small enough V_0 the four-neutron system becomes lower in energy than the three-neutron system, independent of the radius of the trap. In order to rule out that the external trap alters significantly the properties of few-particle systems beyond a relatively simple shift in energy, we perform additional calculations of two to six neutrons in different wells to reproduce qualitatively the helium isotopes. This model of a few neutrons confined in a trapping potential has been successfully applied to describe the oxygen isotopic chain [202].

The helium isotopic chain shows odd-even pairing effects (see Fig. 3.7); i.e., the systems with odd numbers of neutrons always have higher energies than the neighboring systems with an even number of neutrons. We try to recover this behavior by replacing the two protons in the Helium nucleus by a Woods-Saxon potential as in Eq. (3.1), the depth and radius of which are adjusted such that the binding energies of the different isotopes are of the same order as the experimental value. The resulting well depths V_0 are significantly deeper than the traps used for our study of the three- and four-neutron systems in Fig. 3.3 and hence at least the ^{6}He (four neutrons) energy should be smaller than the ^{5}He (three neutrons) energy. We calculate the energy of the neutrons in such a well, interacting with the local N^{2}LO interaction as used before. Fig. 3.7 show results normalized to the ^{4}He energy, which corresponds to the energy of only two neutrons in the

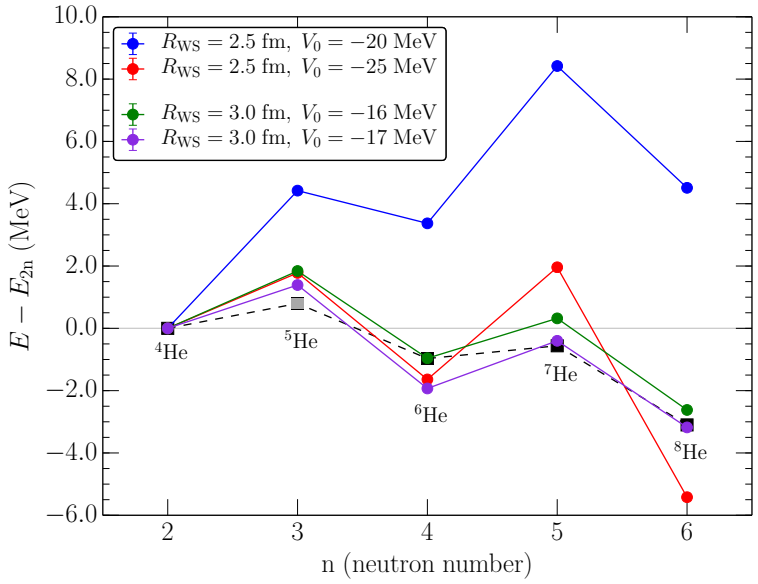

Figure 3.7: Energy of two to six neutrons trapped in various Woods-Saxon wells (circles) [100]. The wells are designed to approximately reproduce the binding pattern of the helium chain. For each well, the two-neutron energy is taken as the reference point to which the other energies for that well are compared. The black squares are the experimental values compared to the ^{4}He energy. For ^{5}He, we take the value of the $P_{3/2}$ resonance, the width of which is shown in gray.

Woods-Saxon well. Again, we keep the center of mass of the system fixed. Indeed, we find that the ordering of three versus four neutron energies for the Helium chain is reversed compared to the extrapolated resonance energies found above. Also we find for the different Woods-Saxon potentials the expected odd-even staggering qualitatively in agreement with experiment. For the helium isotopes, we attribute this to the additional pairing attraction generated among the neutrons in the well. Apparently the pairing attraction breaks down in the region of small V_0 where densities are much lower than for the helium isotopes causing the trineutron to be lower in energy than the tetraneutron.

3.5 Connections to ultra-cold atoms

Very dilute systems of particles can often be approximated by a Fermi gas that interacts only via S-wave interactions. Our results shown in Fig. 3.5 suggest that the three- and four-neutron systems are very dilute. In addition, we observe that the extrapolated resonance energies of three- and four-neutron states in Fig. 3.3 scale with the number of pairs, which is $N(N-1)/2$ (see Table 3.1). For large particle numbers a scaling with N^2 was found for the mean-field (MF) interaction energy of a dilute gas of spin-1/2 fermions [203],

$$E_{\mathrm{MF}} = \frac{\pi a}{m}\frac{N^2}{V}, \tag{3.14}$$

N	$N(N-1)/2$	E_R (MeV)
3	3	1.2(2)
4	6	2.1(2)

Table 3.1: Number of neutrons N, number of pairs $N(N-1)/2$, and the resonance energies E_R as extracted from Fig. 3.3. The resonance energies scale as the number of pairs.

where a is the two-body scattering length and V is the volume. As for large N, $N(N-1) \to N^2$, this suggests that those few-neutron systems can effectively be described by a dilute Fermi gas despite the low number of particles. Dilute Fermi gases can also be engineered in experiments with ultracold atoms [204]. The mean-field energy of a two-component Fermi gas in a harmonic trap was measured for both signs of the scattering length using radio-frequency spectroscopy [205]. Reducing the number of particles, it might be possible to simulate few-fermion systems in such experiments with ultracold atoms. This would allow for the study of the transition from few- to many-body physics. Similar experiments have already been carried out for quasi-one-dimensional systems with an impurity, where it was found that systems with $N \geq 4$ majority atoms already develop a Fermi sea [206]. Moreover, experiments with ultracold atoms could be used to investigate whether the properties of the density distributions in Fig. 3.5 are governed by universal large-scattering length physics or details of nuclear forces.

3.6 Conclusions

In this study, we have calculated ground state energies of three- and four-neutron systems artificially bound via an external Woods-Saxon potential. This allowed us to extract possible three- and four-neutron resonance energies by extrapolating to vanishing external potential strength. While there is no formal proof that the extrapolated energy is identical to the resonance energy, we provided empirical evidence that this is the case by studying two fermions interacting via a simple S-wave potential. We find the extrapolated energies to be independent of the trap geometry, since different Woods-Saxon widths converge to the same energy at zero well depth. The calculated energy of a possible tetraneutron resonance $E = 2.1(2)\,\mathrm{MeV}$ is compatible with the potential resonance energy $(0.83 \pm 0.65 \pm 1.25)\,\mathrm{MeV}$, found in the measurement of Ref. [12]. In addition, our study provides evidence that a three-neutron resonance might exist as well, and even be lower in energy than a tetraneutron resonance. However, the method used in this study does not allow for the determination of the width of the resonance. Also, it could be that the extrapolated energies correspond to virtual states.

We also conclude that the effects of three-neutron interactions are very small in these systems due to their low densities. In addition, the diluteness of these systems offers the exciting possibility to shed more light on the properties of few-neutron systems with experiments with ultracold atomic Fermi gases. Finally, in Chapter 4 we investigate an alternative method based on finite volume calculations, which in the future might allow for an independent investigation of the few-neutron-resonance problem.

4 Signatures of few-body resonances in finite volume

In the two-particle sector, Wiese [24] showed that a resonance leads to remarkable features in the finite volume spectrum. When plotted as a function of the box size the discrete energy levels in a cubic box with periodic boundary conditions show patters referred to as avoided level crossings (see also Sec. 1.3.1).

In this chapter, we study the extension of this method to few-body resonances. In particular, we are interested in resonances that couple only to asymptotic three- or higher-body channels. The properties of such systems, which one could refer to as "genuine" few-body resonances, cannot be obtained by calculating a standard two-body scattering phase shift. Since to date there are no formal derivations for the case of genuine resonances of more than two particles, we explore here whether such states again show up as avoided crossings in the finite-volume, few-body energy spectrum, and how the properties of the resonance state can be inferred from the position and shape of these avoided crossings. Beyond establishing this method as a tool for identifying resonance states, our results are relevant to test and help extend the ongoing formal work, in particular regarding the derivation of three-body finite-volume quantization conditions [26–29].

Our studies require the calculation of several few-body energy levels in the finite box. An important consequence of the finite volume is that for any given box size L the spectrum is discrete, but it is still possible to identify few-body bound states, which have an exponential volume dependence [74, 207]. In contrast, levels corresponding to continuum scattering states have a power-law volume dependence in finite volume. Resonances are then identified as avoided crossings between these discrete "scattering" states as L is varied (although we emphasize already here that in general this signature is expected to be necessary, but not sufficient, for the existence of resonance states).

Naturally, such calculations are numerically challenging, in particular when the number of particles, the number of desired energy levels, or the size of the volume increases. As numerical method we use a discrete variable representation (DVR) based on an underlying basis of plane-wave eigenstates of the box. The latter allow for a convenient implementation of periodic boundary conditions and naturally describe scattering states, and the use of the DVR promises significant advantages in computational efficiency over other methods [208, 209]. We have developed a DVR framework that solves the finite-volume problem for both few-fermion and few-boson systems, supporting both small-scale (running on standard computers) as well as efficient large-scale (running on high-performance computing clusters) calculations. An important challenge is to extend the reach of our method to the very large box sizes that are required to unambiguously identify the existence of proposed three- and four-neutron resonances at very low energies. Postponing studies of few-neutron systems using EFT-based interactions to future work, we investigate here systems of three and four bosons and fermions using different model interactions.

This chapter is organized as follows. In Sec. 4.1 we present the DVR method applied to finite periodic boxes for both bosons and fermions, discussing in some detail our numerical implementation. This also addresses the fact that in the periodic box one has to account for the breaking of rotational symmetry to the cubic group, some details of which are given in Appendix C. After discussing signatures of two-body resonances in Sec. 4.2, we proceed to the multi-body case in Sec. 4.3, establishing first the validity of our approach using a known three-body test case before we study bosonic and fermionic multi-body resonances using shifted Gaussian potentials. We conclude in Sec. 4.4 with a brief summary and outlook. This chapter follows our publication in Ref. [210].

4.1 Discrete variable representation for particles in a periodic box

In order to avoid contributions from the center-of-mass motion to the energy of the system, we consider the n-body system in $n-1$ relative coordinates, $\mathbf{x}_i = \mathbf{r}_n - \mathbf{r}_i$ for $i = 1,\ldots,n-1$, where $\mathbf{r}_i$ denotes the position of the ith particle. These are not Jacobi coordinates, so the kinetic energy operator T_{rel} contains mixed derivatives in the position representation. Since such terms are straightforward to deal with in the DVR representation, our choice of coordinates is convenient because it keeps the boundary conditions simple. While the three-dimensional case is physically the most relevant one, the construction here is completely general. In d spatial dimensions, the only difference is that all vectors have d components.

One-dimensional case

The basic discussion of the DVR method given here follows that of Ref. [208], to which we also refer for more details. To explain the DVR method, we first consider two particles (with equal mass m and reduced mass $\mu = m/2$) in one spatial dimension, setting $x = \mathbf{x}_1$. Confined to an interval of length L, periodic boundary conditions are imposed by choosing a basis of plane waves,

$$\phi_i(x) = \langle x|\phi_i\rangle = \frac{1}{\sqrt{L}}\exp(\mathrm{i}p_i x)\,, \quad \text{with} \quad p_i = \frac{2\pi}{L}i\,, \tag{4.1}$$

and $i = -N/2,\ldots,N/2-1$ with a truncation parameter N (even) determining the basis size. It is clear that any periodic solution of the Schrödinger equation,

$$[T_{\mathrm{rel}} + V]\,|\psi\rangle = E\,|\psi\rangle\,, \tag{4.2}$$

can be expanded in the basis (4.1), and this representation becomes exact for $N \to \infty$.

Following the DVR construction laid out in Ref. [208], we consider now pairs (x_k, w_k) of grid points x_k and associated weights w_k such that

$$\sum_{k=-N/2}^{N/2-1} w_k\,\phi_i^*(x_k)\phi_j(x_k) = \delta_{ij}\,. \tag{4.3}$$

For the plane-wave basis (4.1), this is obviously satisfied by

$$x_k = \frac{L}{N} k \quad \text{and} \quad w_k = \frac{L}{N} \,. \tag{4.4}$$

If we now define matrices

$$\mathcal{U}_{ki} = \sqrt{w_k}\phi_i(x_k) \,, \tag{4.5}$$

then these are unitary according to Eq. (4.3), and we obtain the DVR basis functions $\psi_k(x)$ by rotating the original plane-wave states:

$$\psi_k(x) = \sum_{i=-N/2}^{N/2-1} \mathcal{U}^*_{ki} \phi_i(x) \tag{4.6}$$

for $k = -N/2, \ldots, N/2-1$. The range of indices is the same as for the original plane-wave states, but whereas in Eq. (4.1) they specify a momentum mode, $\psi_k(x)$ is peaked at position $x_k \in [-L/2, L/2)$.

It follows directly from Eqs. (4.4) and (4.5) and the transpose $\mathcal{U}^T$ also being unitary that the DVR states have the property

$$\psi_k(x_j) = \frac{1}{\sqrt{w_k}} \delta_{kj} \,. \tag{4.7}$$

This greatly simplifies the evaluation of the potential matrix elements:

$$\begin{aligned} \langle \psi_k | V | \psi_l \rangle &= \int \mathrm{d}x \, \psi^*_k(x) V(x) \psi_l(x) \,, \\ &\approx \sum_{m=-N/2}^{N/2-1} w_m \, \psi^*_k(x_m) V(x_m) \psi_l(x_m) \,, \\ &= V(x_k) \delta_{kl} \,, \end{aligned} \tag{4.8}$$

so that the potential operator is (approximately) diagonal in the DVR representation. The approximation here lies in the second step in Eq. (4.8), replacing the integral by a sum, which is possible because the (x_k, w_k) defined in Eq. (4.4) constitute the mesh points and weights of a trapezoidal quadrature rule. Note that for this identification it is important that the points $-L/2$ and $L/2$ are identified through the periodic boundary condition because otherwise the weight $w_{-N/2}$ would be incorrect.

The kinetic energy, given in configuration space by the differential operator (note that we set here $\hbar = 1$)

$$T_{\mathrm{rel}} = -\frac{1}{2\mu} \frac{\mathrm{d}^2}{\mathrm{d}x^2} \,, \tag{4.9}$$

is not diagonal in the DVR representation:

$$\langle\psi_k|T_{\text{rel}}|\psi_l\rangle = \int \mathrm{d}x\, \psi_k^*(x) T_{\text{rel}} \psi_l(x) = \sum_{i,j=-N/2}^{N/2-1} \mathcal{U}_{ki} \langle\phi_i|T_{\text{rel}}|\phi_j\rangle \mathcal{U}_{lj}^*\,, \tag{4.10}$$

where

$$\langle\phi_i|T_{\text{rel}}|\phi_j\rangle = \int \mathrm{d}x\, \phi_i^*(x) T_{\text{rel}} \phi_j(x)\,. \tag{4.11}$$

Note that this expression is exact. As the plane waves ϕ_i are eigenstates of the kinetic energy operator, i.e., $T_{\text{rel}}\,|\phi_i\rangle = \frac{p_i^2}{2\mu}\,|\phi_i\rangle$, we find

$$T_{kl} \equiv \langle\psi_k|T_{\text{rel}}|\psi_l\rangle = \sum_{i=-N/2}^{N/2-1} \left(\frac{p_i^2}{2\mu}\right) e^{-\mathrm{i}p_i x_k} e^{\mathrm{i}p_i x_l}\,, \tag{4.12}$$

which can be evaluated analytically [209]:

$$\langle\psi_k|T_{\text{rel}}|\psi_l\rangle = \begin{cases} \dfrac{\pi^2 N^2}{6\mu L^2}\left(1+\dfrac{2}{N^2}\right), & \text{for} \quad k=l\,, \\ \dfrac{(-1)^{k-l}\pi^2}{\mu L^2 \sin^2\left(\pi(k-l)/N\right)}, & \text{otherwise}\,. \end{cases} \tag{4.13}$$

While this matrix is dense here, we will see below that it becomes sparse for $d > 1$. Alternatively, as pointed out in Ref. [209], one can use a discrete fast Fourier transform to evaluate the kinetic energy in momentum space. This operation switches from the DVR to the original plane-wave basis (4.1) and back. This can be understood by multiplying T_{kl} in Eq. (4.12) by an N-dimensional vector v. We write symbolically

$$\sum_l T_{kl}\, v_l = \sum_i \left(\frac{p_i^2}{2\mu}\right) e^{-\mathrm{i}p_i x_k} \sum_l v_l\, e^{\mathrm{i}p_i x_l}\,, \tag{4.14}$$

which is equivalent to two discrete Fourier transformations (DFT) which can be implemented efficiently using the fast Fourier transform algorithm. This matrix-vector multiplication can then be used in the Lanczos algorithm to find the eigenvectors.

General construction

The construction is straightforward to generalize to the case of an arbitrary number of particles n and spatial dimensions d: The starting point simply becomes a product of $(n-1)\times d$ plane waves, one for each relative-coordinate component. The transformation matrices and DVR basis functions are defined via tensor products. Eventually, while a single index suffices to label the

one-dimensional DVR states, a collection of $(n-1)\times d$ indices defines the general case. For these states, we introduce the notation (generalizing the 1D short-hand form $|\psi_k\rangle = |k\rangle$)

$$|s\rangle = |(k_{1,1},\cdots,k_{1,d}),\cdots,(k_{n-1,1},\cdots);(\sigma_1,\cdots,\sigma_n)\rangle\ . \tag{4.15}$$

Here we have also included additional indices to account for spin degrees of freedom. If the particles have spin S, then each σ_i, labeling the projections, takes values from $-S$ to S. Additional internal degrees of freedom, such as isospin, can be included in the same way. The collection of all these states $|s\rangle$ is denoted by B, which is our DVR basis with dimension $\dim B = (2S+1)^n \times N^{(n-1)d}$.

We take the interaction V in Eq. (4.2) to be a sum of central, local A-body potentials (with $A = 2,\ldots,n$ for an n-body system). Each contribution to this sum depends only on the relative distances between pairs of particles, so that evaluated between n-particle states V depends on $n-1$ relative coordinates. For each of these one has a delta function in the matrix element,

$$\langle \mathbf{x}_1,\cdots,\mathbf{x}_{n-1}|V|\mathbf{x}'_1,\cdots,\mathbf{x}'_{n-1}\rangle = V(\{|\mathbf{x}_i|\},\{|\mathbf{x}_i-\mathbf{x}_j|\}_{i<j})\prod_i \delta^{(d)}(\mathbf{x}'_i-\mathbf{x}_i)\,, \tag{4.16}$$

and the interaction thus remains diagonal in the general DVR basis. For the evaluation between DVR states $|s\rangle$, each modulus $|\mathbf{x}_i|$ in Eq. (4.16) gets replaced with

$$|s_i| \equiv \frac{L}{N}\left(\sum_{c=1}^{d} k_{i,c}^2\right)^{1/2}\ . \tag{4.17}$$

If the potential depends on the spin degrees of freedom, the potential matrix in our DVR representation acquires nondiagonal terms, but these are determined solely by overlaps in the spin sector, and overall this matrix remains very sparse.

As already pointed out, the kinetic energy matrix is also sparse in $d > 1$. To see this, first note that the 1D matrix elements Eq. (4.13) enter for each component $k_{i,c}$, multiplied by Kronecker deltas for each $c' \neq c$ and summed for all relative coordinates $i = 1,\ldots,n-1$. The only additional complication, stemming from our choice of simple relative coordinates, is that the general kinetic energy operator,

$$T_{\text{rel}}^{n\text{-body}} = -\frac{1}{2\mu}\sum_{i=1}^{n-1}\sum_{j=1}^{i}\frac{\partial}{\partial x_i}\frac{\partial}{\partial x_j}\,, \tag{4.18}$$

contains mixed (non-diagonal) terms. As an example to illustrate this, consider the kinetic-energy operator for three particles in one dimension,

$$T_{\text{rel}}^{3\text{-body}} = -\frac{1}{2\mu}\left(\frac{\partial^2}{\partial x_1^2}+\frac{\partial^2}{\partial x_2^2}+\frac{\partial}{\partial x_1}\frac{\partial}{\partial x_2}\right). \tag{4.19}$$

For this the kinetic-energy matrix elements are given by

$$\langle k_1 k_2|T_{\text{rel}}^{3\text{-body}}|l_1 l_2\rangle = \langle k_1|T_{\text{rel};1}|l_1\rangle\delta_{k_2 l_2} + \langle k_2|T_{\text{rel};2}|l_2\rangle\delta_{k_1 l_1} + \langle k_1 k_2|T_{\text{rel};12}|l_1 l_2\rangle\,, \tag{4.20}$$

where the first two matrix elements on the right-hand side are given in Eq. (4.13) and the last term is a special case of the general mixed-derivative operator

$$T_{\mathrm{rel};ij} = -\frac{1}{2\mu}\frac{\partial}{\partial x_i}\frac{\partial}{\partial x_j}\,. \tag{4.21}$$

The DVR matrix elements for this are given by

$$\langle k_i k_j | T_{\mathrm{rel};ij} | l_i l_j \rangle = -\frac{1}{2\mu}\Big[\langle k_i|\partial_i|l_i\rangle\langle k_j|\partial_j|l_j\rangle\Big] \tag{4.22}$$

with [211]

$$\langle k|\partial|l\rangle = \begin{cases} -\mathrm{i}\dfrac{\pi}{L}\,, & \text{for} \quad k = l\,, \\ \dfrac{\pi}{L}\dfrac{(-1)^{k-l}\exp\left(-\mathrm{i}\dfrac{\pi(k-l)}{N}\right)}{\sin\left(\dfrac{\pi(k-l)}{N}\right)}\,, & \text{otherwise}\,. \end{cases} \tag{4.23}$$

As for the diagonal terms, for a general state $|s\rangle$ these terms are summed over for all pairs of relative coordinates and spatial compenents c, including Kronecker deltas for $c' \neq c$.

Analogous to the one-dimensional case the kinetic energy can alternatively be implemented by switching to momentum space with a fast Fourier transform, applying a diagonal matrix with entries

$$T_{\mathrm{rel}}^{n\text{-body}}\,|s\rangle = \frac{1}{2\mu L^2}\sum_{i=1}^{n-1}\sum_{j=1}^{i}\sum_{c=1}^{d} k_{i,c}k_{j,c}\,|s\rangle\,, \tag{4.24}$$

and then transforming back with the inverse transform.

(Anti-)symmetrization and parity

To study systems of identical bosons (fermions), we want to consider (anti-)symmetrized DVR states. The construction of these can be achieved with the method described, e.g., in Ref. [212] (for the stochastic variational model in Jacobi coordinates):

1. The transformation from single-particle to relative coordinates is written in matrix form as

$$\mathbf{x}_i = \sum_{j=1}^{n} U_{ij}\mathbf{r}_j\,, \tag{4.25}$$

where

$$U_{ij} = \begin{cases} \delta_{ij}\,, & \text{for} \quad i,j < n\,, \\ -1\,, & \text{for} \quad i < n,\, j = n\,, \\ 1/n\,, & \text{for} \quad i = n\,. \end{cases} \tag{4.26}$$

Note that for $i = n$ this definition includes the center-of-mass coordinate.

2. For the n-particle system there are $n!$ permutations, constituting the symmetric group S_n. A permutation $p \in S_n$ can be represented as a matrix $C(p)$ with

$$C(p)_{ij} = \begin{cases} 1\,, & \text{for} \quad j = p(i)\,, \\ 0\,, & \text{otherwise}\,, \end{cases} \tag{4.27}$$

acting on the single-particle coordinates $\mathbf{r}_i$.

3. The operation of $p \in S_n$ on the relative coordinates is then given by the matrix

$$C_{\text{rel}}(p) = U\, C(p)\, U^{-1}\,, \tag{4.28}$$

with the row and column of the left-hand side discarded, so that $C_{\text{rel}}(p)$ is an $(n-1) \times (n-1)$ matrix.

Since the indices $k_{i,c}$ correspond directly to positions on the spatial grid via Eq. (4.7), acting with $C_{\text{rel}}(p)$ on a state $|s\rangle$ is now straightforward: The $k_{i,c}$ are transformed according to the entries $C_{\text{rel}}(p)_{ij}$, where for each i one considers all $c = 1, \ldots, d$ at once. In other words, $C_{\text{rel}}(p)$ is expanded (by replication for each c) to a matrix acting in the space of individual coordinate components. As a final step, to maintain periodic boundary conditions, any transformed indices that may fall outside the original range $-N/2, \ldots, N/2-1$ are wrapped back into this interval by adding appropriate multiples of N. Applying the permutation to the spin indices $(\sigma_1, \ldots, \sigma_n)$ is trivial because they are given directly as an n-tuple. The final result of this process for a given state $|s\rangle \in B$ and permutation p is a transformed state

$$|s'\rangle = \mathcal{C}(p)\,|s\rangle \in B\,, \tag{4.29}$$

where

$$\mathcal{C}(p) = C_{\text{rel}}(p)\, C_{\text{spin}}(p) \tag{4.30}$$

denotes the total permutation operator in the space of DVR states. The statement of Eq. (4.29) is that each $p \in S_n$ acts on B as a whole by permuting the order of elements.

With this, we can now define the symmetrization and antisymmetrization operators as

$$\mathcal{S} = \frac{1}{n!} \sum_{p \in S_n} \mathcal{C}(p) \quad \text{and} \quad \mathcal{A} = \frac{1}{n!} \sum_{p \in S_n} \operatorname{sgn}(p)\, \mathcal{C}(p)\,, \tag{4.31}$$

where $\operatorname{sgn}(p) = \pm 1$ denotes the parity of the permutation p. Since both of these operators are projections ($\mathcal{S}^2 = \mathcal{S}$, $\mathcal{A}^2 = \mathcal{A}$), they map our original basis B onto bases $B_{\mathcal{S}/\mathcal{A}}$ of, respectively, symmetrized or antisymmetrized states, each consisting of linear combinations of states in B. An important feature of these mappings is that each $|s\rangle \in B$ appears in at most one state in $B_{\mathcal{S}}$ (for symmetrization) or $B_{\mathcal{A}}$ (for antisymmetrization). Thus, in order to determine $B_{\mathcal{S}}$ we can simply apply $\mathcal{S}$ to all $|s\rangle \in B$, dropping duplicates, and analogously for the construction of $B_{\mathcal{A}}$. Moreover, for

the practical numerical implementation of this procedure (discussed in more detail below) it suffices to store a single term for each linear combination because the full state can be reconstructed from that through an application of the (anti-)symmetrization operator.

Parity can be dealt with in much the same way: The parity operator $\mathcal{P}$ merely changes the sign of each relative coordinate, so it can be applied to the DVR states defined in Eq. (4.15) by mapping $k_{i,c} \to -k_{i,c}$ for all i, c, and, if necessary, wrapping the result back into the range $-N/2, \ldots, N/2-1$. The spin part remains unaffected by this operation. Projectors onto positive and negative parity states are given as

$$\mathcal{P}_\pm = \mathbb{1} \pm \mathcal{P} \,. \tag{4.32}$$

They have the same properties as $\mathcal{S}$ and $\mathcal{A}$ (each $|s\rangle \in B$ appears in at most one linear combination forming a state with definite parity), and, importantly, the same is true for the combined operations $\mathcal{P}_\pm\mathcal{S}$ and $\mathcal{P}_\pm\mathcal{A}$. In practice this means that it is possible to efficiently construct bases of (anti-)symmetrized states with definite parity, where for each element it suffices to know a single generating element $|s\rangle \in B$.

Cubic symmetry projection

While permutation symmetry and parity remain unaffected by the finite periodic geometry, rotational symmetry is lost. In particular, in $d = 3$ dimensions (to which the remaining discussion in this subsection will be limited), angular momentum l is no longer a good quantum number for the n-body system in the periodic cubic box. Specifically, the spherical $SO(3)$ symmetry of the infinite-volume system is broken down to a cubic subgroup $\mathcal{O} \subset SO(3)$.

This group has 24 elements and five irreducible representations Γ, conventionally labeled A_1, A_2, E, T_1 and T_2. Their dimensionalities are 1, 1, 2, 3 and 3, respectively, and irreducible representations D^l of $SO(3)$, determining angular-momentum multiplets in the infinite volume, are reducible with respect to $\mathcal{O}$. As a result, a given (infinite-volume) angular momentum state can contribute to several Γ. In the cubic finite volume, one finds the spectrum decomposed into multiplets with definite Γ, where an index $\alpha = 1, \ldots, \dim\Gamma$ further labels the states within a given multiplet.

For our calculations, it is desirable to select spectra by their cubic transformation properties. To that end, we construct projection operators [213]

$$\mathcal{P}_\Gamma = \frac{\dim\Gamma}{24} \sum_{R\in\mathcal{O}} \chi_\Gamma(R) D_n(R) \,, \tag{4.33}$$

where $\chi_\Gamma(R)$ denotes the character, tabulated in Table C.2 of the cubic rotation R for the irreducible representation Γ and $D_n(R)$ is the realization of the cubic rotation in our DVR space of periodic n-body states. For example, for the one-dimensional representation $\Gamma = A_1$, $\chi_{A_1}(R) = 1$ for all cubic rotations R, so in this case Eq. (4.33) reduces to an average over all rotated states. In Appendix C we provide some further discussion of the cubic group and the construction of the $D_n(R)$.

We use a numerical implementation of the method described above written predominantly in C++, with some smaller parts (dealing with permutations) conveniently implemented in Haskell. For optimal performance, parallelism via threading is used wherever possible. Our design choice to use modern C++11 allows us to achieve this by means of the TBB library [214], which provides high-level constructs for nested parallelism as well as convenient concurrent data structures. To support large-scale applications, we also split calculations across multiple nodes using MPI, so that overall we have a hybrid parallel framework.

For a fixed setup (given physical system, box size L, DVR truncation parameter N), the calculation is divided into three phases:

1. Basis setup
2. Hamiltonian setup
3. Diagonalization

The last step is the simplest one conceptually, so we start the discussion from that end. In order to calculate a given number of lowest energy eigenvalues we use the parallel ARPACK package [215], implementing Arnoldi/Lanczos iterations distributed via MPI. This method requires the calculation of a number of matrix-vector products,

$$\psi_{\text{out}} = H\psi_{\text{in}}\,, \tag{4.34}$$

applying the DVR Hamiltonian H to state vectors ψ_{in} (provided by the algorithm) until convergence is reached. These are potentially very large (see Sec. 4.1) and thus are distributed across multiple nodes. Explicit synchronization is only required for ψ_{in} in order to evaluate the right-hand side of Eq. (4.34). Each node only calculates its local contribution to ψ_{out}.

We note here that while (anti-)symmetrization and parity are directly realized by considering appropriate basis states, the simplifications discussed in Sec. 4.1 are not possible for the cubic-symmetry projectors $\mathcal{P}_\Gamma$. Instead, the latter are accounted for via the substitution

$$H \to H + \lambda(\mathbb{1} - \mathcal{P}_\Gamma)\,, \tag{4.35}$$

where λ is an energy scale chosen much larger than the energy of the states of interest. This construction applies a shift to all states which do not possess the desired symmetry, leaving only those of interest in the low-energy spectrum obtained with the Lanczos algorithm.

The operator $\mathcal{P}_\Gamma$ is constructed as a large sparse matrix, which we implement using Intel MKL [216], if available, and via `librsb` [217] otherwise. The same holds for the kinetic-energy matrix when operating in a mode where this matrix is constructed explicitly (as described in Sec. 4.1) in step 2.

While this mode of operation has good scaling properties with increasing number of compute nodes, we find it to be overall more efficient (in particular with respect to the amount of required memory) to use the Fourier-transform based kinetic-energy application, which we implement using

FFTW [218]. Since the transform is defined for the full (not symmetry-reduced) basis, this method involves transforming the vectors ψ_{in} to the large space, and transforming back after applying the kinetic-energy operator. These transformations are again implemented via sparse-matrix multiplications, where the matrix X that expands from the reduced space to the full space has entries given by eigenvectors of (appropriate combinations of) the operators $\mathcal{S}$, $\mathcal{A}$, and $\mathcal{P}_\pm$ described in Sec. 4.1. Reducing back at the end is performed with the transpose matrix X^T. For calculations on multiple nodes using MPI, individual ranks need only calculate local slices of these matrices.

In Fourier-transform mode, step 2 consists only of calculating diagonal matrices for the kinetic energy and the potential parts of the Hamiltonian, and possibly of setting up the sparse cubic projection matrix $\mathcal{P}_\Gamma$. These calculations are based on determining the symmetry-reduced basis states in step 1, which can be efficiently parallelized across multiple nodes. In addition, this requires calculating X and X^T.

4.2 Resonance signatures

In the two-particle sector it has been shown that a resonance state manifests itself as avoided level crossings when studying the volume dependence of the discrete energy levels in a periodic box [24]. Before we move on to establish the same kind of signature for more than two particles in the following section, we compare here the finite-volume resonance determination to other methods. As a test case, we consider two particles interacting via a shifted Gaussian potential,

$$V(r) = V_0 \exp\left(-\left(\frac{r-a}{R_0}\right)^2\right). \tag{4.36}$$

This kind of repulsive barrier is very well suited to produce narrow resonance features without much need for fine tuning. To illustrate this we show in Fig. 4.1 S-wave scattering phase shifts for $a = 3$, $R_0 = 1.5$ and two different values of V_0 (all in natural units, which besides using $\hbar = c = 1$ also set $m = 1$). For $V_0 = 6.0$ the phase shift exhibits a very sharp jump of approximately 180°. From the location of the inflection point of the phase shift we extract the resonance energy E_R, while the width Γ is given by the value of the derivative at the resonance energy

$$\left[\frac{\mathrm{d}\delta(E)}{\mathrm{d}E}\right]_{E=E_R} = \frac{2}{\Gamma}. \tag{4.37}$$

We find a very narrow two-body resonance with energy $E_R = 2.983$ and width $\Gamma = 0.001$. When the height of the barrier is lowered to $V_0 = 2.0$, the jump is much less pronounced, implying that the width of this resonance is broadened. Indeed, we find resonance parameters of $E_R = 1.606$, $\Gamma = 0.097$ for this case.

To further check these parameters, we consider Eq. (4.36) Fourier transformed to momentum space and look for poles in the S-wave projected S-matrix on the second energy sheet, using the technique described in Ref. [219]. For $V_0 = 6.0$ we find a resonance pole at $E_R - \mathrm{i}\Gamma/2 = 2.9821(3) - \mathrm{i}0.00035(5)$, where the uncertainty is estimated by comparing calculations with 300 and 256 points for a discretized momentum grid with cutoff 8 (in natural inverse length units). In the same way, we extract $E_R - \mathrm{i}\Gamma/2 = 1.606(1) - \mathrm{i}0.047(2)$ for $V_0 = 2.0$. Noting that there is

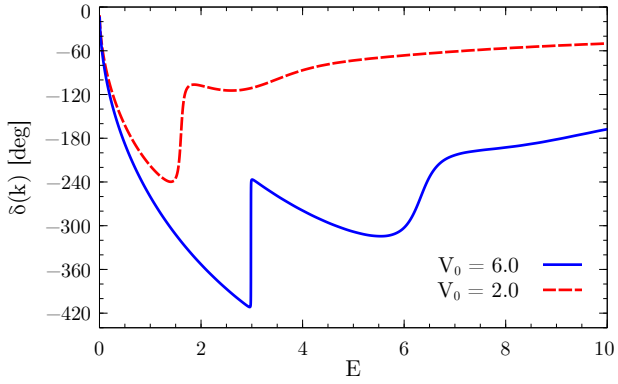

Figure 4.1: S-wave phase shift of two particles interacting via the potential given in Eq. (4.36) as a function of the (dimensionless) relative kinetic energy E for $V_0 = 6.0$ (blue solid curve) and $V_0 = 2.0$ (red dashed curve) [210].

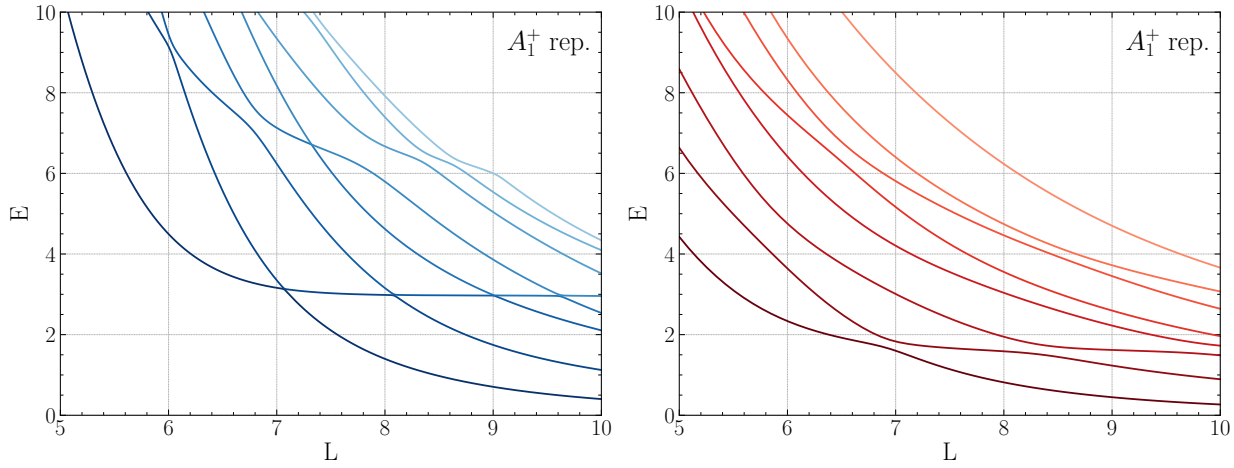

Figure 4.2: Energy spectrum of two particles interacting via the potential given in Eq. (4.36) in finite volume for different box sizes L [210]. The left panel shows results for $V_0 = 6.0$ in the A_1^+ representation, whereas for the right panel a weaker barrier $V_0 = 2.0$ was used.

no completely unambiguous way to relate the parameters extracted from the phase shifts (except in the limit of vanishing background and poles infinitesimally close to the real axis), we conclude that these pole positions are in very good agreement with the behavior seen in the phase shifts.

We now perform finite-volume calculations of two particles in a three-dimensional box with periodic boundary conditions using the DVR method discussed in Sec. 4.1. As avoided level crossings corresponding to a resonance are only expected for states with the same quantum numbers, we project onto states that belong to a single irreducible representation Γ of the cubic group and definite parity. Specifically, we consider here only A_1^+ states, which to a good approximation correspond to S-wave states in the infinite volume. As shown in Table C.3, the next higher angular momentum contributing to A_1^+ is $l = 4$, which can be safely neglected for low-energy states.

Our results are shown in Fig. 4.2. In the spectrum for $V_0 = 6.0$ (left panel of Fig. 4.2), a series of extremely sharp avoided level crossings, forming an essentially horizontal plateau, is observed at approximately $E \approx 3.0$. According to Ref. [24] the width of the resonance is related to the spacing of the different levels at the avoided crossing. Therefore, we conclude that the resonance is very

narrow, and find good qualitative agreement with the parameters extracted from the phase shift. For the weaker potential ($V_0 = 2.0$, right panel of Fig. 4.2), on the other hand, the avoided level crossings are less sharp, pointing to a larger resonance width. Along with the observed sequence of plateaus at approximately $E = 1.6$, we again find good qualitative agreement with the phase-shift calculation.

For a more quantitative analysis, we extract the resonance energies from the finite volume spectra by fitting the coefficients $\{c_i\}$ of a polynomial,

$$E(L) = \sum_{i=0}^{i_{\max}} c_i L^i \,, \tag{4.38}$$

to the plateau region of each curve in Fig. 4.2 and taking the position of the plateau inflection point as the resonance energy. We vary the number of data points taken into account for the fit by adjusting the lower and upper boundary of the fit interval. Furthermore, we vary $i_{\max}$ in Eq. (4.38) until we find the extracted resonance energy to be independent of the order of polynomial. For $V_0 = 6.0$ and $V_0 = 2.0$ we obtain, respectively, $E_R = 2.98(3)$ and $E_R = 1.63(3)$, where the quoted errors correspond to the spread of the extracted inflection points from different plateau curves. This means that with the inflection-point method we obtain very good agreement with the resonance positions from the phase-shift determination.

At higher energies the spectra for both $V_0 = 6.0$ and $V_0 = 2.0$ exhibit less pronounced avoided level crossings. These structures, however, do not show clear plateaus, instead varying strongly as a function of the box size. Most likely these finite-volume features correspond to the resonance-like jumps of the phase shift at $E \sim 6-10$ for $V_0 = 6.0$ and $E \sim 3-7$ for $V_0 = 2.0$, respectively, which may correspond to broader resonances.

Altogether, we have demonstrated here that the positions of narrow two-body resonances can be extracted from finite-volume calculations with very good quantitative agreement compared to other methods.

4.3 Applications to three and four particles

We now proceed to explore the method in the three- and four-body sector, starting with bosonic (spin-0) particles. Because these lack a spin degree of freedom, we can quite easily achieve large DVR basis dimensions for these systems, whereas fermionic systems are more computationally demanding.

4.3.1 Three-body benchmark

In order to verify our hypothesis that, analogously to the two-body case, three-particle resonances appear as avoided level crossings in finite-volume spectra, we start with three identical spin-0 bosons with mass $m = 939.0$ MeV (mimicking nucleons) interacting via the two-body potential

$$V(r) = V_0 \exp\left(-\left(\frac{r}{R_0}\right)^2\right) + V_1 \exp\left(-\left(\frac{r-a}{R_1}\right)^2\right), \tag{4.39}$$

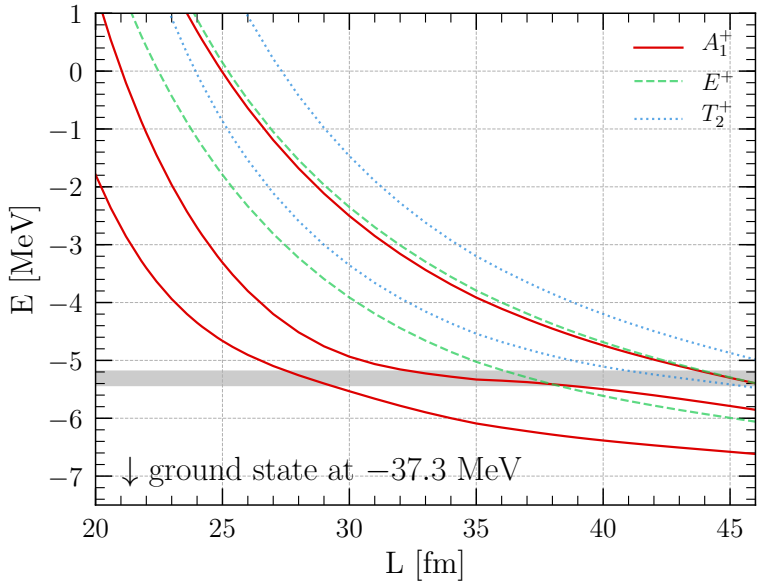

Figure 4.3: Energy spectrum of three bosons in finite volume for different box sizes L interacting via the potential given in Eq. (4.39) [210]. States corresponding to the irreducible representation A_1 of the cubic symmetry group are shown as solid lines, whereas E^+ and T_2^+ states are indicated as dashed and dotted lines, respectively. The shaded area indicates the resonance position and width as calculated in Ref. [221].

where $V_0 = -55\,\text{MeV}$, $V_1 = 1.5\,\text{MeV}$, $R_0 = \sqrt{5}\,\text{fm}$, $R_1 = 10\,\text{fm}$, and $a = 5$ fm. This setup was studied in Ref. [220], where Faddeev equations with complex scaling were used to calculate resonances, as well as in Ref. [221], which used slow-variable discretization to extract three-body resonance parameters. The potential given in Eq. (4.39) supports a two-body bound state (dimer) at $E = -6.76$ MeV [220] and a three-boson bound state at $E = -37.35$ MeV [221] (Ref. [220] obtained $E = -37.22$ MeV for this state). In addition, it was found that there is a three-boson resonance at $E_R = -5.31$ MeV with a half width of 0.12 MeV [221] ($E_R = -5.96$ MeV and $\Gamma/2 = 0.40$ MeV according to Ref. [220]), which decays into a dimer-particle state that is overall lower in energy.

Using Eq. (4.39) with our DVR method, we find $E = -6.756(1)$ and $E = -37.30(5)$ for two and three bosons, respectively, in good agreement with the results of Refs. [220, 221] as shown in Table 4.1. Note that bound-state energies converge exponentially to the physical infinite-volume values as we increase the box size L (see, e.g., Refs. [74, 207]). To look for the three-boson resonance, we study the positive-parity three-body spectrum as a function of L. For small box sizes around $L \sim 20$ fm, we find that $N = 26$ DVR points is sufficient to obtain converged results. For large box size ($L \sim 40$ fm), on the other hand, we performed calculations using $N = 30$. The terms “small” and “large” here refer to the scale set by the range of the interaction, which is quite sizable for the parameters given below Eq. (4.39).

Our combined results are shown in Fig. 4.3, where we also indicate the irreducible representations of the energy levels shown. These assignments were determined by running a set of cubic-projected calculations at small volumes. The levels corresponding to A_1^+ clearly show an avoided crossing at around the expected resonance energy from Ref. [221], which is indicated

	E_2	E_3	E_R	$\Gamma/2$
This work	$-6.756(1)$	$-37.30(5)$	$-5.32(1)$	—
[221]	—	-37.35	-5.31	0.12
[220]	-6.76	-37.22	-5.96	0.40

Table 4.1: Energies of the bound states of two (E_2) and three (E_3) bosons as well as the three-boson resonance energy E_R and half widths $\Gamma/2$, all in MeV, for particles interacting via the potential given in Eq. (4.39) compared to previous calculations in Refs. [220, 221].

in Fig. 4.3 as a shaded horizontal band, the width of which corresponds to $E_R \pm \Gamma/2$. For the other states (with quantum numbers E^+ and T_2^+) shown in the figure we do not observe avoided crossings or plateaus. At $L \sim 38$ fm there is an actual crossing between A_1^+ and an E^+ levels. This is not a very sharp avoided crossing because the participating levels belong to different cubic representations.

In order to extract the resonance energy from the spectrum shown in Fig. 4.3 we proceed as described in Sec. 4.2 and extract the inflection points of the curves corresponding to the A_1^+ states by fitting polynomials. For the first excited state we find the fit to be quite sensitive to the number of data points included in the fit, which reflects the fact that this level does not exhibit a pronounced plateau. For the second excited state, however, there is a clearly visible plateau. Applying our fit method to this state, we extract a resonance energy $E_R = -5.32(1)$ MeV. This means that within the quoted uncertainty, determined by varying the number of data points included in the fit as well as the order of the fit polynomial, we obtain good agreement with the resonance energy obtained in Ref. [221] (see Table 4.1). While a determination of the resonance width is left for future work, we conclude from this result that indeed finite-volume spectra can be used to reliably determine the existence and energy of few-body resonances.

4.3.2 Shifted Gaussian potentials

Three bosons

Having established the validity of the finite-volume method to extract three-body resonances, we now go back to the shifted Gaussian potential given in Eq. (4.36) which was used in Sec. 4.2 to study two-body resonances. Starting again with the stronger barrier, ($V_0 = 6.0$), we consider the A_1^+ spectrum for three bosons, calculated with $N = 10$ DVR points and shown in Fig. 4.4 as solid lines. We observe a large number of avoided crossings at $E \sim 7.4$ as the box size L is varied, producing together an almost horizontal plateau region. Using the same inflection-point method as discussed above, we extract $E = 7.42(6)$ as a potential resonance energy. In addition to this, there are several avoided crossings at lower energies which have a significant slope with respect to changes in the box size, which we interpret as two-body resonances (known from Sec. 4.2 to exist at $E_R \sim 3.0$ for this potential) embedded into the three-body spectrum. In order to test this hypothesis we repeat the calculation with an added short-range three-body force,

$$V_3(x_1, x_2, x_{12}) = V_0^{(3)} \exp\left(-\left(\frac{x_1}{R_0}\right)^2\right) \exp\left(-\left(\frac{x_2}{R_0}\right)^2\right) \exp\left(-\left(\frac{x_{12}}{R_0}\right)^2\right), \tag{4.40}$$

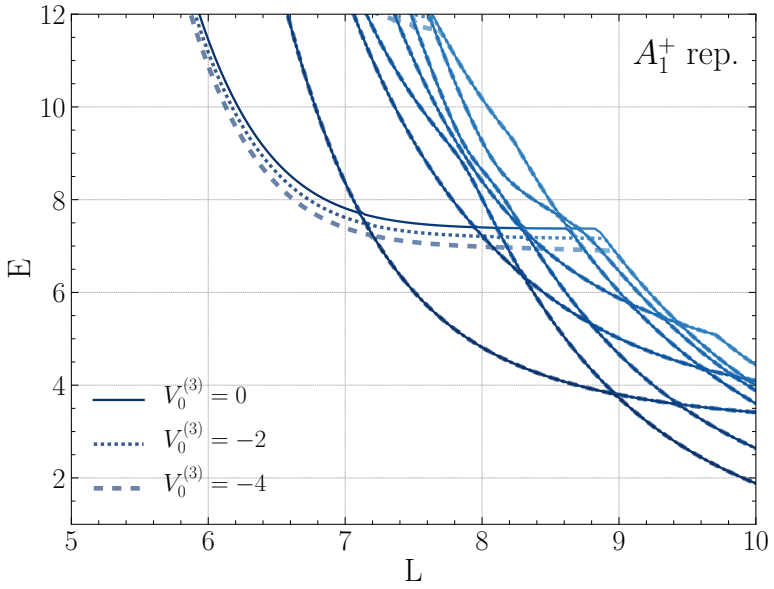

Figure 4.4: Energy spectrum of three bosons in finite volume for different box sizes L [210]. The solid lines shows the spectrum for three bosons interacting purely via the shifted Gaussian potential given in Eq. (4.36) with $V_0 = 6.0$ while the dashed and dotted lines show results with an additional attractive three-body force as in Eq. (4.40). With increasing three-body force, the avoided level crossing is shifted to lower energy, while the rest of the spectrum remains unaffected.

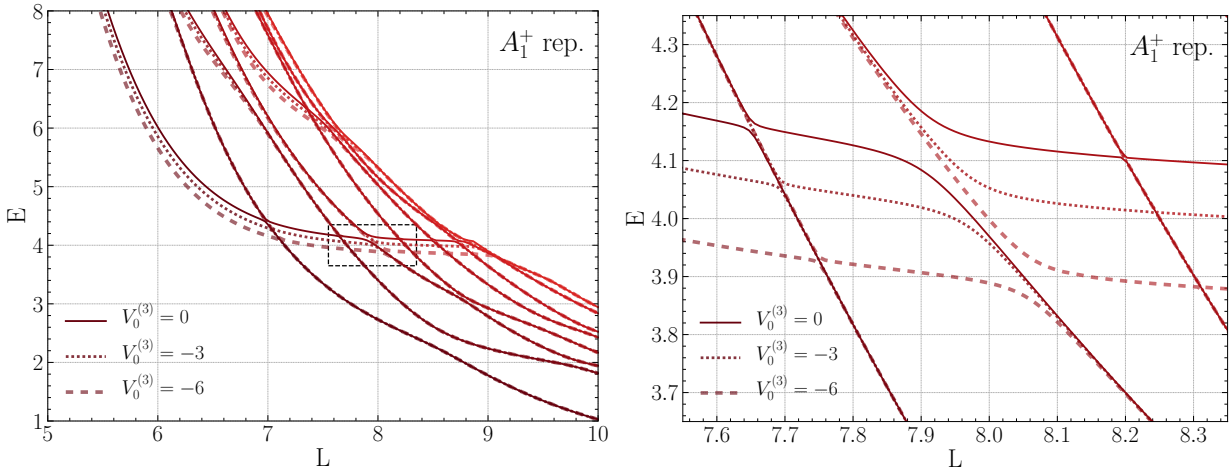

Figure 4.5: Energy spectrum of three bosons in finite volume for different box sizes L [210]. The solid line shows the spectrum for three bosons interacting purely via the shifted Gaussian potential given in Eq. (4.36) with $V_0 = 2.0$ while the dashed and dotted lines show results with an additional attractive three-body force as in Eq. (4.40). With increasing three-body force the avoided level crossing is shifted to lower energy, while the rest of the spectrum remains unaffected. The dashed rectangle in the left panel indicates the zoomed region shown in the right panel.

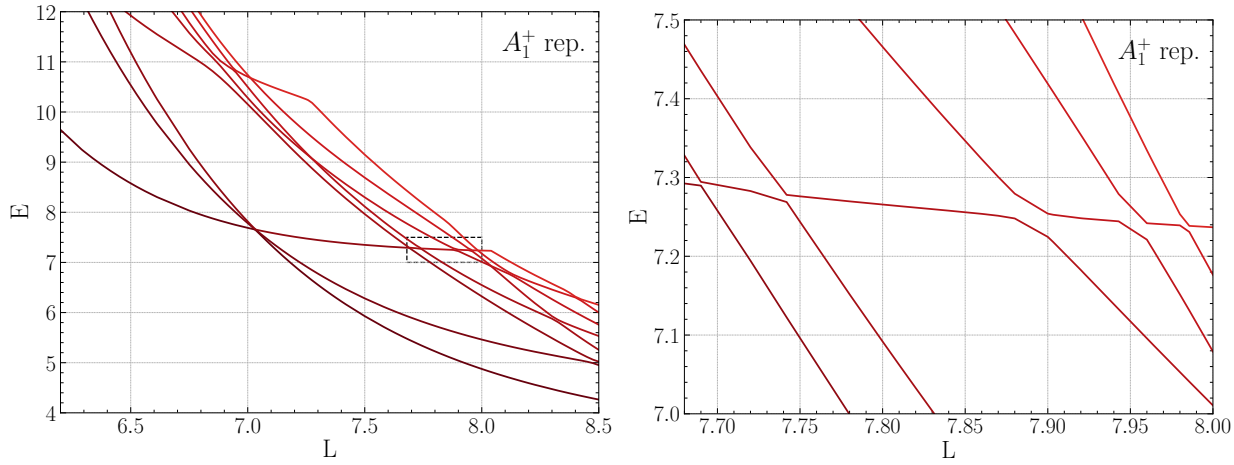

Figure 4.6: Energy spectrum of four bosons in finite volume for different box sizes L interacting via the shifted Gaussian potential given in Eq. (4.36) with $V_0 = 2.0$ [210]. The dashed rectangle in the left panel indicates the zoomed region shown in the right panel.

with $R_0 = 1.0$ and varying strength $V_0^{(3)}$. Choosing a set of negative values for $V_0^{(3)}$ we find in Fig. 4.4 that the lower avoided crossings (and in fact most of the L-dependent spectrum) remain unaffected, whereas the upper plateau set is moved downwards as $V_0^{(3)}$ is made more negative.

Since the range of $R_0 = 1.0$ was chosen small (compared to the box sizes considered), we expect it to primarily affect states, which are localized in the sense that their wave function is confined to a relatively small region in the finite volume. Interpreting a resonance as a nearly bound state, its wave function should satisfy this criterion in the finite volume. On the other hand, scattering states or states where only two particles are bound or resonant are expected to have a large spatial extent. Based on this intuitive picture, we interpret the action of the three-body force as confirmation that indeed we have a genuine (since the potential we used does not support any bound states) three-boson resonance state at $E = 7.42(6)$.

Similar to the two-body spectrum shown in the left panel of Fig. 4.2 we find that Eq. (4.36) with $V_0 = 6.0$ generates very sharp features in the three-boson spectrum so that even though we used a fine L grid to generate Fig. 4.4 it is difficult to exclude that some crossings might not actually be avoided crossings. However, we observe the exact same qualitative behavior for the potential given in Eq. (4.36) but with $V_0 = 2.0$, only that in this case the avoided crossings are broader and easily identified. From the spectrum, shown in Fig. 4.5, we extract $E = 4.17(8)$ as the three-boson resonance energy for this case.

Four bosons

Looking next at four bosons, we find a very similar picture. As shown in Fig. 4.6 for the shifted Gaussian potential given in Eq. (4.36) with $V_0 = 2.0$, the L-dependent A_1^+ four-boson spectrum (calculated with $N = 8$ DVR points in this case) shows a large number of avoided level crossings that give rise to plateaus with different slopes. Interpreting the nearly horizontal set of avoided crossings as a possible four-boson resonance, we extract its energy as $E = 7.31(8)$ with the inflection-point method. The more tilted sets of avoided crossings at lower energies most likely correspond to two- and three-boson resonance states embedded in the four-boson spectrum.

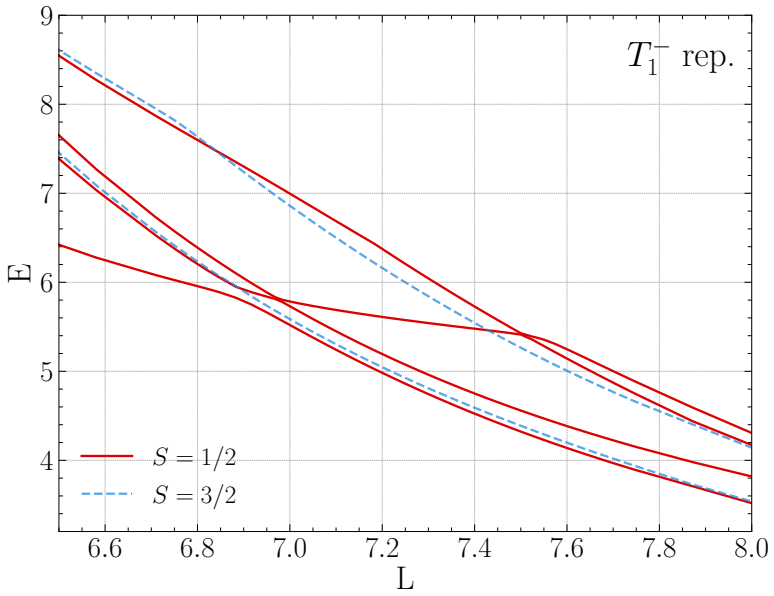

Figure 4.7: Negative-parity energy spectrum of three fermions in finite volume for different box sizes L interacting via the shifted Gaussian potential given in Eq. (4.36) with $V_0 = 2.0$ [210]. All levels shown in the plot were found to belong to the T_1^- cubic representation by performing fully projected calculations at selected volumes. Results are shown in the spin $S = 1/2$ and $S = 3/2$ channels.

Three fermions

To conclude our survey, we now turn to fermionic systems. Since the additional spin degree of freedom (we consider here identical spin-1/2 particles) increases the DVR basis size (see discussion below Eq. (4.15)), these calculations are more computationally demanding, but we can still achieve well converged results for the shifted Gaussian potential given in Eq. (4.36). Before we turn to the three-body sector, we note that the results of Sec. 4.2 remain correct when we assume the two fermions to be in the channel with total spin $S = 0$. In this case, the spin part of the wave function is antisymmetric and the spatial part has to be even under exchange. Since the latter corresponds to the bosonic case with positive parity, we conclude that for two spin-1/2 fermions the two-body potential given in Eq. (4.36) has a resonance state at $E_R \sim 1.6$ for $V_0 = 2.0$.

For three fermions, on the other hand, the situation is more involved because the overall antisymmetry of the wave function can be realized via different combinations of spin and spatial parts. Indeed, we find the finite-volume spectrum to look different from the bosonic case. For negative parity, we find the six lowest levels, shown in Fig. 4.7 to all belong to the T_1^- cubic representation, which in this case we determined by running calculations with full cubic projections at selected volumes while otherwise only restricting the overall parity. Since the interaction we consider here is spin independent, total angular momentum l and spin S are separately good quantum numbers in infinite volume, and in the finite volume we likewise have Γ and S as good quantum numbers. The latter, which can be $S = 1/2$ or $S = 3/2$ for three spin-1/2 fermions, we determine by running calculations with fixed spin z-component at selected volumes, which can be realized by restricting the set of DVR basis states. Because $S = 3/2$ states show up with both $S_z = 3/2$ and $S_z = 1/2$,

whereas $S = 1/2$ states are absent for $S_z = 3/2$, we infer that four of the six levels shown in Fig. 4.7 have $S = 1/2$, whereas the other two (given by the dashed lines in Fig. 4.7) have $S = 3/2$.

For $S = 1/2$ we observe a sequence of three avoided level crossings. Within this sequence there is a drift towards lower energies as L increases, the magnitude of which is comparable to what we observe also for the three-boson spectra analyzed in Sec. 4.3.2 for the state that we concluded to correspond to an actual three-body resonance (based on varying the three-body force). We thus conclude that this effect is likely a residual volume dependence of an actual resonance state also in this case. With this interpretation, we extract a resonance energy $E_R = 5.7(2)$ from the spectrum shown in Fig. 4.7 with our inflection-point method.

4.4 Conclusions

We established the method of analyzing few-body energy spectra in finite periodic boxes in order to extract three- and four-particle resonance energies. Our approach relies on the observation of avoided level crossings and/or plateaus in the spectra considered as a function of the box size. Observing such features in few-body spectra and showing that they can be used to find and analyze resonance states, thus generalizing the method introduced in Ref. [24] for two-body systems, is the central result of this project.

In order to calculate the finite-volume spectra, which were then used for the resonance identification, we used a DVR basis based on plane-wave states in relative coordinates. Resonance features are expected for finite-volume energies corresponding to scattering states in infinite volume. Unlike bound states, the energies of which converge exponentially with the box size L, finite-volume scattering states have a power-law dependence on L (away from regions with avoided crossing). Looking at low-energy resonances therefore requires going to volumes that are sufficiently large for the relevant levels to come down to the energy range of interest. Because calculations in this regime typically require large DVR basis sizes and become computationally very demanding, we have developed a numerical framework to run the calculations on high-performance computing clusters when necessary. We have furthermore extended the formalism to include the symmetrization (antisymmetrization) to study bosonic (fermionic) systems, as well as for projecting onto the subspaces belonging to parity eigenstates and to the different irreducible representations of the cubic symmetry group. The latter allows us to determine the finite-volume quantum numbers of the resonance states that we find.

After testing our method in the two-body sector, where we verified the existence of resonances by looking at characteristic jumps in the scattering phase shifts as well as by looking for S-matrix poles on the second energy sheet, we studied three- and four-body systems with different potentials. First, we used a model potential known to generate a three-boson resonance that decays into a lower lying two-body bound state and a free particle. For this system, the resonance parameters were extracted previously based on different methods [220, 221]. Our results clearly show an avoided level crossing in the corresponding finite-volume spectrum and we find good agreement for the resonance energy, which we extracted from the inflection points of the volume-dependent energy levels.

Taking this agreement as confirmation that our method works both qualitatively and quantitatively, we used shifted Gaussian potentials (with the same parameters known to generate two-body resonances) in the three- and four-body sector. Studying the three-boson finite-volume spectrum,

we showed that an additional short-range three-body force can be used to move avoided crossings forming a plateau region whereas others avoided crossings remain unchanged. We interpret this as confirmation that the observed plateau region indeed corresponds to a three-body resonance (with a spatially localized wave function so that it "feels" the three-body forces), whereas the other levels likely correspond to two-body resonances plus a third particle. For the same shifted Gaussian potential we were also able to observe avoided crossings for three fermions and four bosons, from which we extracted resonance energies via the inflection-point method. Based on these findings, we conclude that our method can be used to search for possible three- and four-neutron resonances. Work in this direction is ongoing.

5 WIMP-nucleus interactions

Direct detection experiments search for nuclear recoils induced by WIMPs scattering off target nuclei in the detector. The scattering rate of this process depends on several quantities among which there is the momentum-tranfer dependent nuclear structure factor describing the scattering of WIMPs off the target nuclei. As already discussed in Sec. 1.2, the chiral Lagrangian gives rise not only to the nuclear forces describing the interaction among nucleons but also allows one to derive nuclear currents, which couple to external sources. For the interactions described by the Standard Model, the nature of these external fields is known. An electron, for example, couples to nucleons via the electromagnetic and weak interactions, which are described by vector and axial-vector lepton fields coupling to their equivalents in the hadronic sector. In case of WIMP-nucleus scattering, however, the situation is unknown. Due to the diversity of models describing beyond Standard Model physics, the number of possible types of WIMP-hadron interactions is very large. In the past, dark matter searches constrained their standard analysis to two channels, which are distinguished by their sensitivity to the spin of the nucleus, conveniently labeled as spin-independent and spin-dependent. This choice is based on a non-relativistic analysis, not taking into account constraints from QCD. We want to broaden this picture based on the chiral symmetry of QCD, and the hierarchy it predicts for WIMP-nucleon interactions, and discuss channels beyond the standard analysis of WIMP-nucleus scattering. Similar studies have been performed, however limited either to scalar-mediated WIMP-nucleon interactions [222, 223] or, after our work, to one-body operators [224, 225]. Here, we take into account all WIMP-nucleon operators at both the one- and two-body level up to order $\mathcal{O}((Q/\Lambda_b)^3)$ in the chiral power counting. In Chapter 6, we will then continue and include nuclear structure effects in order to find a generalization of spin-independent WIMP-nucleus scattering.

This chapter is organized as follows. In Sec. 5.1, we discuss the basic formalism describing the WIMP-nucleus scattering rate. Then, in Sec. 5.2 we will focus on the nuclear currents. An alternative approach of an operator basis discribing WIMP-nucleon interactions has been derived in Refs. [155, 156]. The matching to our formalism is discussed in Sec. 5.3.

The results of this chapter have been published in Refs. [159, 226]. The author's contribution to these publications were mainly in the derivation of the electroweak nuclear two-body currents, the evaluation of the two-body operators and the analysis of the chiral power counting.

5.1 WIMP-nucleus scattering rate

We start from a WIMP χ with initial/final momentum p/p' scattering off a target nucleus $\mathcal{N}$ with initial/final momentum k/k'

$$\mathcal{N}(p) + \chi(k) \to \mathcal{N}(p') + \chi(k'), \tag{5.1}$$

where we denote the four-vector of the transferred momentum as

$$q = k' - k = p - p', \qquad q^2 = t\,. \tag{5.2}$$

Later, we will also use

$$P = p + p', \qquad K = k + k'\,. \tag{5.3}$$

The differential rate for elastic WIMP-nucleus scattering in a detector with an active mass M reads

$$\frac{\mathrm{d}R}{\mathrm{d}\mathbf{q}^2} = \frac{\rho M}{m_A m_\chi} \int_{v_{\min}}^{v_{\mathrm{esc}}} \mathrm{d}^3 v\, |\mathbf{v}| f(|\mathbf{v}|)\, \frac{\mathrm{d}\sigma_{\chi\mathcal{N}}}{\mathrm{d}\mathbf{q}^2}\,, \tag{5.4}$$

where m_A and m_χ denote the masses of the target nucleus and the WIMP, respectively, $\sigma_{\chi\mathcal{N}}$ the WIMP–nucleus cross section in the lab frame, $f(|\mathbf{v}|)$ the normalized velocity distribution of the WIMP, and ρ the WIMP density in the solar system, which is usually taken as $\rho = 0.3\,\mathrm{GeV/cm^3}$. The upper limit of the integral is given by the escape velocity of our galaxy $v_{\mathrm{esc}} = 544^{+64}_{-46}\,\mathrm{km\,s^{-1}}$ [227], while the lower limit is given by

$$v_{\min}^2 = -t \left[\frac{\sqrt{4m_A^2 - t} + \sqrt{4m_\chi^2 - t}}{\sqrt{4m_A^2 - t}\sqrt{4m_\chi^2 - t} - t} \right]^2 = \frac{\mathbf{q}^2}{4\mu_A^2} + \mathcal{O}(\mathbf{q}^4), \qquad \mu_A = \frac{m_A m_\chi}{m_A + m_\chi}\,, \tag{5.5}$$

with $t = -\mathbf{q}^2$ up to relativistic corrections. The rate in Eq. (5.4) is sometimes provided as differential in the recoil energy $E_{\mathrm{r}} = \mathbf{q}^2/2m_A$ (see Eq. (1.36)).

The differential cross section with respect to the momentum transfer for the elastic WIMP-nucleus scattering process can be expressed as

$$\frac{\mathrm{d}\sigma_{\chi\mathcal{N}}}{\mathrm{d}\mathbf{q}^2} = \frac{\zeta^2}{8\pi \mathbf{v}^2 (2J+1)} \sum_{\mathrm{spins}} |\mathcal{M}_{\mathrm{NR}}|^2\,, \tag{5.6}$$

where J is the angular momentum of the target nucleus and $\mathcal{M}_{\mathrm{NR}}$ the non-relativistic (NR) amplitude of the WIMP-nucleon interaction. For a Dirac (Majorana) spin-1/2 WIMP we have $\zeta = 1(2)$. The sum implies summation over both WIMP states and nucleon states in the nucleus.

Traditionally, the WIMP-nucleus cross section in Eq. (5.6) is expressed in terms of so-called structure factors [228]

$$\frac{\mathrm{d}\sigma_{\chi\mathcal{N}}}{\mathrm{d}\mathbf{q}^2} = \frac{8G_F^2}{\mathbf{v}^2(2J+1)} \Big[S_S(\mathbf{q}^2) + S_A(\mathbf{q}^2) \Big], \tag{5.7}$$

where G_F denotes the Fermi constant[1] and S_S and S_A are the structure factors for spin-independent (SI) and spin-dependent (SD) scattering, respectively[2]. In the standard analysis, the SI structure factor is derived from a simple scalar-scalar (SS) interaction with an amplitude given by

$$\mathcal{M}^{SS} = \chi^{\dagger}_{r'} \chi_r \chi^{\dagger}_{s'} 2\sqrt{2} G_F (c_0 + c_1 \tau^3) \chi_s \,. \tag{5.8}$$

where $\chi_{r,s}$ ($\chi_{r',s'}$) are non-relativistic two-component spinors for the incoming (outgoing) WIMP and nucleon, respectively. The SD structure factor is derived from the axial-vector–axial-vector (AA) interaction at the one-body level. When combining the isoscalar current with the isovector one-body current as in Eq. (1.26), the amplitude reads

$$\mathcal{M}^{AA} = -\chi^{\dagger}_{r'} \boldsymbol{\sigma} \chi_r \cdot \chi^{\dagger}_{s'} \sqrt{2} G_F \left[a_0 \boldsymbol{\sigma} + a_1 \tau^3 \left(\frac{G_A^3(\mathbf{q}^2)}{g_A} \boldsymbol{\sigma} - \frac{G_P^3(\mathbf{q}^2)}{4 m_N^2 g_A} (\mathbf{q} \cdot \boldsymbol{\sigma}) \mathbf{q} \right) \right] \chi_s \,, \tag{5.9}$$

where $G_A^3(\mathbf{q}^2)$ and $G_P^3(\mathbf{q}^2)$ are axial and pseudo-scalar couplings [159] and m_N denotes the nucleon mass. The couplings a_0/c_0 and a_1/c_1 denote isoscalar and isovector coupling constants, respectively. The SI interaction basically probes the nuclear density while the SD response describes a coupling of the WIMP spin to the spin of the nucleus. In the limit of vanishing momentum transfer the structure factors can be written as

$$\begin{aligned} S_S(0) &= \frac{2J+1}{4\pi} \Big| c_0 A + c_1 (Z - N) \Big|^2 \,, \\ S_A(0) &= \frac{(2J+1)(J+1)}{4\pi J} \Big| (a_0 + a_1) \langle \mathbf{S}_p \rangle + (a_0 - a_1) \langle \mathbf{S}_n \rangle \Big|^2 \,, \end{aligned} \tag{5.10}$$

with proton and neutron numbers Z and N ($A = Z + N$) and proton/neutron spin expectation values $\langle \mathbf{S}_{p/n} \rangle$. At the fundamental level, WIMPs couple to the SM fields, which are embedded in the nucleons. The constants c_i, a_i correspond to form factors accounting for the information about particle and hadronic physics, see Ref. [226] for more details. The normalization in Eq. (5.10) yields, assuming $c_1 = 0$, that the SI structure factor at zero momentum transfer scales as A^2. In this case, the cross section for SI scattering is often represented as [229]

$$\frac{\mathrm{d}\sigma^{\mathrm{SI}}_{\chi\mathcal{N}}}{\mathrm{d}\mathbf{q}^2} = \frac{\sigma^{\mathrm{SI}}_{\chi N}}{4 \mathbf{v}^2 \mu_N^2} \mathcal{F}^2_{\mathrm{SI}}(\mathbf{q}^2), \qquad \mu_N = \frac{m_N m_\chi}{m_N + m_\chi}, \tag{5.11}$$

[1] Note that G_F is only included to set the scale and does not imply that WIMPs and nucleons interact via the weak interaction.

[2] This assumes that the WIMP is a Dirac particle, i.e., $\zeta = 1$.

with the single-nucleon cross section $\sigma^{\rm SI}_{\chi N}$. The nuclear-physics quantity $\mathcal{F}_{\rm SI}(\mathbf{q}^2)$ is the only remnant of the structure factor, and is frequently approximated by [139]

$$\begin{aligned}\mathcal{F}^{\rm Helm}_{\rm SI}(\mathbf{q}^2) &= A\frac{3j_1(|\mathbf{q}|r_n)}{|\mathbf{q}|r_n}e^{-\frac{1}{2}\mathbf{q}^2s^2}, \\ r_n^2 &= c^2+\frac{7}{3}\pi^2a^2-5s^2, \qquad s=1\,\text{fm}, \\ c &= (1.23A^{1/3}-0.60)\,\text{fm}, \qquad a=0.52\,\text{fm},\end{aligned} \tag{5.12}$$

whose square is known as Helm form factor. This approximation is very accurate [230] as the SI interaction couples to the nuclear density that can be easily modeled.

At the one-body level, the SD structure factor S_A at vanishing momentum transfer is a simple function of either the spin expectation values of the two species in the nucleus, which is convenient as in odd-mass nuclei either $\langle \mathbf{S}_p\rangle = 0, \langle \mathbf{S}_n\rangle \neq 0$ or $\langle \mathbf{S}_p\rangle \neq 0, \langle \mathbf{S}_n\rangle = 0$. Traditionally, the combinations $a_0 = a_1 = 1$ ("proton-only") and $a_0 = -a_1 = 1$ ("neutron-only") are chosen. We want to remark that this clear distinction between the coupling of the WIMP to either only protons or only neutrons breaks down when two-body currents are included [67, 160].

5.2 Nuclear currents from chiral EFT

On the most fundamental level, WIMPs interact with quark and gluon degrees of freedom. The coupling strengths of the WIMP-quark and WIMP-gluon couplings are commonly referred to as Wilson coefficients [231]. Hence, in order to construct a formalism based on nucleons and pions as degrees of freedom, nucleon and pion form factors have to be calculated for the different interaction channels. This requires a convolution of Wilson coefficients and nucleon matrix elements. The discussion provided here focuses on the currents at the nucleon/pion level. For details on the nucleon form factors we refer to Ref. [159].

In this section, we want to provide an overview of the nuclear currents in the context of WIMP-nucleus scattering. We will focus on the currents in the scalar and pseudoscalar channels as the vector and axial–vector channels are summarized in Ref. [66] including a detailed explanation of the derivation of these currents from the chiral EFT Lagrangian. Detailed discussions concerning nuclear currents for spin-dependent interactions can be found in our Refs. [67, 141, 160]. For a comprehensive summary of all expressions of the currents relevant for WIMP-nucleus scattering we refer to Ref. [159].

5.2.1 One-body currents

One-body currents describe the coupling of a WIMP χ to a single nucleon N as shown in Fig. 5.1. The coupling of WIMP current to the nucleon can be either direct or via exchange pions. The chiral counting determines the order at which a particular diagram contributes to the scattering amplitude. We constrain ourselves to contributions up to $\mathcal{O}(Q^3)$ (here and in the following we omit $\Lambda_{\rm b}$) in the chiral power counting as discussed in Sec. 1.2.3.

The amplitude $\mathcal{M}_{\rm NR}$ in Eq. (5.6) incorporates the operators acting on both nucleon and WIMP fields. For the WIMPs we only have to consider one-body currents as they are assumed to be

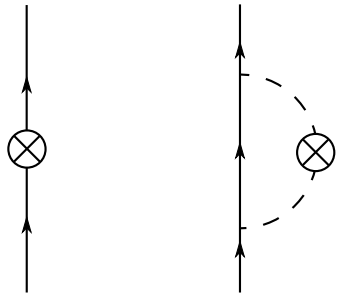

Figure 5.1: One-body currents describing the coupling of a nucleon (solid line) to a WIMP current (crossed circle) via contact (a) or pion-loop (b) (dashed line) terms. The latter is referred to as radius correction.

elementary particles. There are four structures that can be formed from the Dirac spinors u of the WIMP, namely a scalar $\bar{u}u$, pseudo-scalar $\bar{u}\gamma_5 u$, vector $\bar{u}\gamma^\mu u$, and axial-vector $\bar{u}\gamma^\mu\gamma_5 u$, which can couple to the nuclear currents. Since the WIMPs are non-relativistic we use the non-relativistic expansion of the Dirac spinor bilinears [66]. Relativistic corrections that are suppressed by the nucleon mass m_N are counted as two orders, i.e., $p/m_N = \mathcal{O}(Q^2)$. We assume the same counting as for nucleons implying that we count terms suppressed by the WIMP mass m_χ as order $\mathcal{O}(Q^2)$. If, however, $m_\chi > m_N$, the suppression will of course be stronger while in the case $m_\pi \lesssim m_\chi \lesssim m_N$ the counting should be adapted. If $m_\chi < m_\pi$, this naive counting breaks down.

Now, given this counting scheme, we can derive the chiral order of any amplitude $\mathcal{M}_{\rm NR}$. The chiral orders for all diagrams considered are summarized in Table 5.1. We start with the amplitude of the scalar-scalar channel,

$$\mathcal{M}^{SS}_{1,\rm NR} = \chi^\dagger_{r'}\chi_r\chi^\dagger_{s'}f_N(t)\chi_s\,, \tag{5.13}$$

where $\chi_{r,s}$ ($\chi_{r',s'}$) are non-relativistic spinors for the incoming (outgoing) WIMP and nucleon, respectively. Here and in the following, we label the amplitudes according to the nature of the WIMP current (first letter in the superscript) and the nature of the nuclear current (second letter in the superscript). The WIMP-nucleon coupling $f_N(t)$ depends on the Wilson coefficients, which parameterize the effect of new physics and the light and heavy quark couplings (see Ref. [159] for more details). When taking into account not only the contact interaction shown in Fig. 5.1 (a) but also the contribution from the pion-coupling in Fig. 5.1 (b) the coupling becomes momentum-transfer dependent [159]

$$f_N(t) = f_N + t\dot{f}_N\,, \tag{5.14}$$

where the first and second terms correspond to diagrams (a) and (b), respectively. When identifying $f_N(0) = 2\sqrt{2}G_F c_0$, we recover the same coupling as in Eq. (5.10) [228]. Since to first order in the chiral expansion we have $f_N(t) \sim m_\pi^2$, we find that the scalar one-body current is of order $\mathcal{O}(Q^2)$ (see Table 5.1).

The nucleon spinors in Eq. (5.13) include isospin indices according to

$$\chi^\dagger_{s'}f_N(t)\chi_s \equiv \frac{1}{2}\chi^\dagger_{s'}\Big[\big(f_p(t)+f_n(t)\big)\mathbb{1} + \big(f_p(t)-f_n(t)\big)\tau^3\Big]\chi_s\,. \tag{5.15}$$

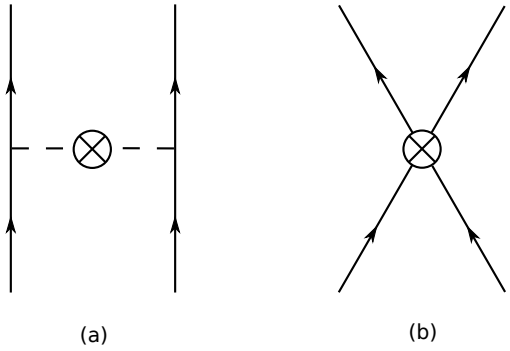

Figure 5.2: Two-body current describing the coupling of a WIMP to two nucleons. Solid/dashed lines refer to nucleons/pions, the crosses to the coupling of the external current, i.e., the WIMP.

This means that depending on the individual values of the f_i one can construct an isoscalar ($f_p = f_n$) and an isovector coupling ($f_p = -f_n$). For the isoscalar case this interaction corresponds to the coupling associated with the standard Helm form factor in Eq. (5.12).

The pseudoscalar-scalar amplitude $\mathcal{M}^{PS}_{1,\mathrm{NR}}$ is of higher chiral order than $\mathcal{M}^{SS}_{1,\mathrm{NR}}$ as the non-relativistic reduction of the pseudoscalar WIMP current $\bar{u}\gamma_5 u$ produces a term $-\boldsymbol{\sigma}\cdot\mathbf{q}/(2m_\chi)$, which, as discussed above, we count as $\mathcal{O}(Q^2)$ for $m_\chi \gtrsim m_N$.

From the pseudoscalar nucleon current at one-body level we obtain the scalar-pseudoscalar and pseudoscalar-pseudoscalar amplitudes:

$$\begin{aligned}\mathcal{M}^{SP}_{1,\mathrm{NR}} &= \chi^\dagger_{r'}\chi_r \frac{i}{2}\chi^\dagger_{s'}\boldsymbol{\sigma}\cdot\mathbf{q}\, g_5^N(t)\chi_s\,,\\ \mathcal{M}^{PP}_{1,\mathrm{NR}} &= \frac{1}{2m_\chi}\chi^\dagger_{r'}\boldsymbol{\sigma}\cdot\mathbf{q}\chi_r \frac{1}{2}\chi^\dagger_{s'}\boldsymbol{\sigma}\cdot\mathbf{q}\, h_5^N(t)\chi_s\,,\end{aligned} \tag{5.16}$$

with nucleon couplings $g_5^N(t)$ and $h_5^N(t)$ [159]. The $\mathbf{q}$-dependence leaves these amplitudes at order $\mathcal{O}(Q^1)$ while there is an additional suppression of two orders for $\mathcal{M}^{PP}_{1,\mathrm{NR}}$ from the WIMP mass as for $\mathcal{M}^{PS}_{1,\mathrm{NR}}$ (see Table 5.1).

For the expressions for the vector and axial-vector one-body amplitudes, we refer to Refs. [66, 159], the corresponding chiral orders are shown in Table 5.1.

5.2.2 Two-body currents

At higher chiral order two-body currents, which couple two nucleons to an external particle, become relevant. For vector and axial-vector two-body currents, we again refer to Refs. [66, 159] and we will focus on the scalar and pseudoscalar two-nucleon currents in the following. Figure 5.2 shows the corresponding diagrams. Diagram (a) shows a coupling to the so-called "pion in flight" meaning that the external field depicted by the cross is coupling to the exchange pion between the two nucleons. A contact interaction is shown in diagram (b). The WIMP could couple either directly to the nucleon contact or via pion exchange.

WIMP	Nucleon	V		A	
		t	$\mathbf{x}$	t	$\mathbf{x}$
V	1b	0	$1+2$	2	$0+2$
	2b	4	$2+2$	2	$4+2$
	2b NLO	–	–	5	$3+2$
A	1b	$0+2$	1	$2+2$	0
	2b	$4+2$	2	$2+2$	4
	2b NLO	–	–	$5+2$	3

WIMP	Nucleon	S	P
S	1b	2	1
	2b	3	5
	2b NLO	–	4
P	1b	$2+2$	$1+2$
	2b	$3+2$	$5+2$
	2b NLO	–	$4+2$

Table 5.1: Left: leading chiral order of time (t) and space ($\mathbf{x}$) components of the WIMP and nucleon currents for vector and axial-vector interactions, for one-body (1b) and two-body (2b) operators. For the axial-vector nucleon operator, terms involving vertices from the NLO chiral Lagrangian (indicated by "2b NLO") need to be included at chiral order $\mathcal{O}(Q^3)$ [66]. The second number ("+2") refers to the additional suppression originating from the NR expansion of the WIMP spinors, if momentum over WIMP mass is counted in the same way as for the nucleon mass. Right: leading chiral order of the WIMP and nucleon currents for scalar and pseudoscalar interactions.

The scalar-scalar nonrelativistic amplitudes take the form [159, 222, 223, 226, 232]

$$\mathcal{M}^{SS}_{2,\mathrm{NR}} = -\left(\frac{g_A}{2F_\pi}\right)^2 f_\pi M_\pi \frac{\boldsymbol{\tau}_1\cdot\boldsymbol{\tau}_2\,\boldsymbol{\sigma}_1\cdot\mathbf{q}_1\,\boldsymbol{\sigma}_2\cdot\mathbf{q}_2}{\left(\mathbf{q}_1^2+M_\pi^2\right)\left(\mathbf{q}_2^2+M_\pi^2\right)}, \tag{5.17}$$

$$\mathcal{M}^{\theta}_{2,\mathrm{NR}} = \frac{4M_\pi^2-2\mathbf{q}_1\cdot\mathbf{q}_2}{M_\pi^2}\frac{f_\pi^\theta}{f_\pi}\mathcal{M}^{SS}_{2,\mathrm{NR}} - \frac{f_\pi^\theta}{M_\pi}2(C_S+C_T\boldsymbol{\sigma}_1\cdot\boldsymbol{\sigma}_2), \tag{5.18}$$

$$\mathcal{M}^{(2)}_{2,\mathrm{NR}} = -\frac{\mathbf{q}_1\cdot\mathbf{q}_2}{2M_\pi^2}\frac{f_\pi^{(2)}}{f_\pi}\mathcal{M}^{SS}_{2,\mathrm{NR}} - \frac{f_\pi^{(2)}}{2M_\pi}(C_S+C_T\boldsymbol{\sigma}_1\cdot\boldsymbol{\sigma}_2), \tag{5.19}$$

where the couplings to the pion are denoted f_π, f_π^θ, and $f_\pi^{(2)}$. The operators $\boldsymbol{\sigma}_i$ and $\boldsymbol{\tau}_i$ denote the spin and isospin Pauli matrices of nucleon i, respectively, and $\mathbf{q}_i = \mathbf{p}_i' - \mathbf{p}_i$. The momentum transfer to the WIMP is hence given by $\mathbf{q} = -\mathbf{q}_1 - \mathbf{q}_2$. Diagrammatically, these amplitudes represent the coupling of the WIMP to the pion in flight (Fig. 5.2 (a)) via a scalar current and by means of the QCD trace anomaly θ^μ_μ and the spin-2 term[3]. The latter two also obtain a contribution corresponding to the contact diagram (b) in Fig. 5.2 that yields the second terms in Eq. (5.18) and (5.19). The second term in Eq. (5.18) and the full spin-2 two-body current were not included in Ref. [159].

In contrast to the situation for the spin-dependent interaction, it is not possible for the scalar case to write the two-body current contribution as a correction to the one-body coupling f_N of Eq. (5.13). This is because the scalar couplings of pions, f_π, f_π^θ, and $f_\pi^{(2)}$ probe a different combination of Wilson coefficients [223]. As a result, the scalar two-body currents cannot be parameterized in terms of a single coupling c_0 as conventionally done for the one-body currents [228].

In Table 5.1, we summarize the leading chiral order of all one- and two-body currents. We find that the two-body currents are in some cases of the same order as their one-body correspondents.

[3] The spin-2 term describes a WIMP-SM-particle interaction via a $S = 2$ mediator.

5.3 Matching to NREFT

An alternative approach to the description of the interaction of possible dark matter particles with nucleons was pursued by the authors of Refs. [155, 156]. Instead of directly starting from chiral EFT, the authors developed an effective field theory of non-relativistic nucleon and WIMP fields. We will refer to this approach in the following as "NREFT". Scales related to the spontaneous chiral symmetry breaking of QCD are integrated out. This approach corresponds to a pionless EFT commonly used for few-particle nuclear physics with the exception that the "NREFT" scheme does not include two-body currents present in pionless EFT. In order to derive limits on the WIMP parameter space, information from QCD would have to be included in a second step. This represents a disadvantage compared to our approach that is directly based upon the WIMP-quark couplings, i.e., Wilson coefficients. However, as the multipole operators necessary for the evaluation of nuclear matrix elements (see Sec. 6.2.1) have been derived for the NREFT operators [156], it is useful to express our results in terms of the NREFT operator basis, which is given by

$$\begin{aligned}
&\mathcal{O}_1 = 1\,, && \mathcal{O}_2 = \left(\mathbf{v}^\perp\right)^2, && \mathcal{O}_3 = i\mathbf{S}_N \cdot (\mathbf{q} \times \mathbf{v}^\perp),\\
&\mathcal{O}_4 = \mathbf{S}_\chi \cdot \mathbf{S}_N\,, && \mathcal{O}_5 = i\mathbf{S}_\chi \cdot \left(\mathbf{q} \times \mathbf{v}^\perp\right), && \mathcal{O}_6 = \mathbf{S}_\chi \cdot \mathbf{q}\, \mathbf{S}_N \cdot \mathbf{q},\\
&\mathcal{O}_7 = \mathbf{S}_N \cdot \mathbf{v}^\perp\,, && \mathcal{O}_8 = \mathbf{S}_\chi \cdot \mathbf{v}^\perp\,, && \mathcal{O}_9 = i\mathbf{S}_\chi \cdot \left(\mathbf{S}_N \times \mathbf{q}\right),\\
&\mathcal{O}_{10} = i\mathbf{S}_N \cdot \mathbf{q}, && \mathcal{O}_{11} = i\mathbf{S}_\chi \cdot \mathbf{q}, &&
\end{aligned} \tag{5.20}$$

where $\mathbf{S} = \boldsymbol{\sigma}/2$ and the velocity is defined as

$$\mathbf{v}^\perp = \frac{\mathbf{K}}{2m_\chi} - \frac{\mathbf{P}}{2m_N}\,, \tag{5.21}$$

with $\mathbf{K}$ and $\mathbf{P}$ as defined in Eq. (5.3). Including vector and axial-vector currents, we find the relations

$$\begin{aligned}
\mathcal{M}^{SS}_{1,\mathrm{NR}} &= \chi^\dagger_{r'}\chi^\dagger_{s'}\mathcal{O}_1 f_N(t)\chi_r\chi_s\,,\\
\mathcal{M}^{SP}_{1,\mathrm{NR}} &= \chi^\dagger_{r'}\chi^\dagger_{s'}\mathcal{O}_{10} g_5^N(t)\chi_r\chi_s\,,\\
\mathcal{M}^{PP}_{1,\mathrm{NR}} &= \frac{1}{m_\chi}\chi^\dagger_{r'}\chi^\dagger_{s'}\mathcal{O}_6 h_5^N(t)\chi_r\chi_s\,,\\
\mathcal{M}^{VV}_{1,\mathrm{NR}} &= \chi^\dagger_{r'}\chi^\dagger_{s'}\Bigg[\mathcal{O}_1\Big(f_1^{V,N}(t) + \frac{t}{4m_N^2}f_2^{V,N}(t)\Big) + \frac{1}{m_N}\mathcal{O}_3 f_2^{V,N}(t)\\
&\qquad + \frac{1}{m_N m_\chi}\Big(t\mathcal{O}_4 + \mathcal{O}_6\Big)f_2^{V,N}(t)\Bigg]\chi_r\chi_s\,,\\
\mathcal{M}^{AV}_{1,\mathrm{NR}} &= \chi^\dagger_{r'}\chi^\dagger_{s'}\Bigg[2\mathcal{O}_8 f_1^{A,N}(t) + \frac{2}{m_N}\mathcal{O}_9\Big(f_1^{A,N}(t) + f_2^{A,N}(t)\Big)\Bigg]\chi_r\chi_s\,,\\
\mathcal{M}^{AA}_{1,\mathrm{NR}} &= \chi^\dagger_{r'}\chi^\dagger_{s'}\Bigg[-4\mathcal{O}_4 g_A^N(t) + \frac{1}{m_N^2}\mathcal{O}_6 g_P^N(t)\Bigg]\chi_r\chi_s\,,\\
\mathcal{M}^{VA}_{1,\mathrm{NR}} &= \chi^\dagger_{r'}\chi^\dagger_{s'}\Bigg[-2\mathcal{O}_7 + \frac{2}{m_\chi}\mathcal{O}_9\Bigg]h_A^N(t)\chi_r\chi_s\,,
\end{aligned} \tag{5.22}$$

where the f_i, g_i and h_i denote the respective nucleon couplings for the different interaction types [159]. If we include subleading corrections in the non-relativistic expansion of the spinors, we find the missing operators. We only show the contributions of $\mathcal{O}_5$ and $\mathcal{O}_{11}$ as we will refer to these in the next chapter:

$$\begin{aligned}\mathcal{M}^{VV}_{1,\mathrm{NR}}(\mathcal{O}_5) &= f_1^{V,N}(t)\frac{\mu_N}{m_N}\frac{1}{m_\chi}\mathcal{O}_5\,,\\ \mathcal{M}^{PS}_{1,\mathrm{NR}}(\mathcal{O}_{11}) &= -f_N(t)\frac{1}{m_\chi}\mathcal{O}_{11}\,.\end{aligned} \tag{5.23}$$

We conclude this chapter by noting that due to QCD effects the WIMP-nucleon couplings of the individual NREFT operators are not independent. For example, as shown in Eq. (5.22), the nuclear matrix element $\mathcal{M}^{AA}_{1,\mathrm{NR}}$ combines both axial $\mathcal{O}_4$ and pseudoscalar $\mathcal{O}_6$ operators. The results in Eq. (5.22) show the amplitudes up to the chiral order $\mathcal{O}(Q^3)$. It turns out that while there are only 7 amplitudes present at this order, there are 8 of the 11 NREFT operators involved. Hence, the relation cannot be inverted as $\mathcal{M}^{AV}_{1,\mathrm{NR}}$ and $\mathcal{M}^{VA}_{1,\mathrm{NR}}$ involve the three operators $\mathcal{O}_{7-9}$. Therefore, not all of the NREFT operators can be isolated by choosing a particular configuration of the WIMP-quark and WIMP-gluon couplings.

In addition, the two-body currents we presented in Sec. 5.2.2 cannot be matched to the NREFT basis since the NREFT scheme only includes one-body operators. This highlights again the need for a derivation of WIMP-nucleon interactions based on QCD.

For WIMP masses m_χ significantly larger than the nucleon mass the pseudoscalar–pseudoscalar amplitude $\mathcal{M}^{PP}_{1,\mathrm{NR}}$ gets pushed to higher orders. The same is true for the terms suppressed by $1/m_\chi$ in $\mathcal{M}^{VV}_{1,\mathrm{NR}}$ and $\mathcal{M}^{VA}_{1,\mathrm{NR}}$. On the other hand, the two-body currents in the SS, AV, AA, and VA channels up to $\mathcal{O}(Q^3)$ are independent of m_χ.

6 General spin-independent responses

Having presented a common chiral power-counting scheme for the different chiral currents in the previous section, we now turn to the analysis of nuclear structure effects in the context of WIMP-nucleus scattering. In particular, we study which of the amplitudes derived in the previous chapter are coherently enhanced when evaluated between nuclear states.

This chapter is based upon work published in Ref. [226]. The author of this thesis contributed mainly to the evaluation of the two-body operators in the "naive" shell model discussed in Sec. 6.3.2 and to the discussion of all results.

6.1 Standard responses and coherence

Direct detection experiments usually distinguish in their analysis between spin-independent (SI) and spin-dependent (SD) channels, which refer to the nature of the WIMP-nucleon interaction. In this very simple picture the SI interaction corresponds to the scalar–scalar amplitude of Eq. (5.8), while the SD interaction is defined as the axial-vector–axial-vector channel in Eq. (5.9) [228]. The labels of SI and SD refer to the fact that the nuclear axial-vector current depends on the nucleon spin operator while the scalar current couples to the particle number. As a result, the nuclear responses of these two operators are very different. The standard SI response is enhanced by the coherent contribution of all nucleons in the nucleus. For an isoscalar coupling ($c_0 = 1$, $c_1 = 0$) the WIMPs couple to the nuclear density, which at vanishing momentum transfer leads to

$$\left\langle \mathcal{N} \middle| \sum_i^A \mathbb{1}_i \middle| \mathcal{N} \right\rangle = A, \tag{6.1}$$

where $\mathcal{N}$ denotes the wave function of the target nucleus, and we obtain the scaling with the mass number A (see also discussion below Eq. (5.10)). On the other hand, for SD interactions the scale is set by a single-nucleon matrix element since due to the nucleon spin pairing, the individual contributions of all nucleons cancel and the WIMP effectively couples to a single unpaired nucleon for an odd number of either protons or neutrons, i.e., (at zero momentum transfer)

$$\left\langle \mathcal{N} \middle| \sum_i^A \mathbf{S}_i \middle| \mathcal{N} \right\rangle = \langle \mathbf{S}_n \rangle \text{ or } \langle \mathbf{S}_p \rangle, \tag{6.2}$$

where $\langle \mathbf{S}_n \rangle, \langle \mathbf{S}_p \rangle$ denote the spin expectation values of the odd numbered species of nucleons, either neutrons n or protons p for an odd-mass nucleus (see also discussion below Eq. (5.12)).

The standard SI and SD interactions are just two out of all the different possible interaction types summarized in Table 5.1. When other contributions are considered, the classification in SI and SD responses becomes less useful as there are other operators that are coherently enhanced even though they involve a WIMP or even a nucleon spin operator. The experimental signature of

these responses would be closer to the standard SI response meaning that they exhibit a similar enhancement with respect to the coupling to a single nucleon. In this chapter, we want to extend the standard SI analysis to a more general picture, where also subleading responses that contribute coherently will be taken into account. In this sense, SI responses will be defined by their coherent enhancement rather than by their operator structure which means that we will allow for spin operators in these interactions.

This chapter is organized as follows. In Sec. 6.2, we provide the necessary translation of the chiral EFT amplitudes of Chapter 5 in nuclear operators, which will allow us to find the coherently enhanced responses. In Sec. 6.3, we discuss the nuclear structure aspects of the evaluation of the one-body operators in the interacting shell model and the implementation of two-body currents in a simplified shell-model. In Sec. 6.4, we collect the coherent responses to construct the generalized SI cross section thus extending the standard SI response.

6.2 Nuclear responses

The amplitudes $\mathcal{M}_{\text{NR}}$ have to be evaluated between nuclear many-body states. An efficient description of the relatively heavy nuclei, which make up the target material of most direct detection experiments, is given by the interacting shell model introduced in Sec. 1.4.3. Therefore, it is convenient to find a representation of the nucleon operators in terms of multipole operators, which act on harmonic oscillator basis states. In Sec. 6.2.1, we present such a representation, however, only for one-body operators. A simplified evaluation of the two-body operators is discussed in Sec. 6.3.2.

6.2.1 One-body currents

When evaluating the nuclear matrix elements

$$\left\langle \mathcal{N} \middle| \sum^{A} \mathcal{O}_i \middle| \mathcal{N} \right\rangle, \tag{6.3}$$

it was found that the 11 NREFT operators $\mathcal{O}_i$ in Eq. (5.20) lead to only five multipole operators [156, 157]:

$$\begin{aligned}
M_{JM}(q\mathbf{x}) &= j_J(qx) Y_{JM}(\Omega_x)\,, \\
\Delta_{JM}(q\mathbf{x}) &= \mathbf{M}^M_{JJ}(q\mathbf{x}) \cdot \frac{1}{q}\nabla\,, \\
\Sigma'_{JM}(q\mathbf{x}) &= -i\left(\frac{1}{q}\nabla \times \mathbf{M}^M_{JJ}(q\mathbf{x})\right) \cdot \boldsymbol{\sigma}\,, \\
\Sigma''_{JM}(q\mathbf{x}) &= \left(\frac{1}{q}\nabla M_{JM}(q\mathbf{x})\right) \cdot \boldsymbol{\sigma}\,, \\
\Phi''_{JM}(q\mathbf{x}) &= i\left(\frac{1}{q}\nabla M_{JM}(q\mathbf{x})\right) \cdot \left(\boldsymbol{\sigma} \times \frac{1}{q}\nabla\right),
\end{aligned} \tag{6.4}$$

where $M_{JM}(q\mathbf{x}) = j_J(qx)Y_{JM}(\Omega_x)$ and $\mathbf{M}^M_{JL}(q\mathbf{x}) = j_L(qx)\mathbf{Y}_{JM}(\Omega_x)$, with the vector spherical harmonics $\mathbf{Y}_{JM}$. The position of a nucleon is denoted as $\mathbf{x}$ and the transferred momentum as $q = |\mathbf{q}|$. For a general discussion of multipole operators we refer to Ref. [233]. The M operator corresponds to the standard SI response while Σ' and Σ'' are the transverse electric and longitudinal multipoles of the standard SD response [66, 233]. Fitzpatrick et al. [156] found the following matching between multipole operators and NREFT operators:

$$\begin{aligned} M: &\quad \mathcal{O}_1, \mathcal{O}_5, \mathcal{O}_8, \mathcal{O}_{11} \\ \Sigma': &\quad \mathcal{O}_3, \mathcal{O}_4, \mathcal{O}_7, \mathcal{O}_9 \\ \Sigma'': &\quad \mathcal{O}_4, \mathcal{O}_6, \mathcal{O}_{10} \\ \Delta: &\quad \mathcal{O}_5, \mathcal{O}_8 \\ \Phi'': &\quad \mathcal{O}_3 \end{aligned} \tag{6.5}$$

Hence, e.g., the multipole operator M gets contributions from to the matrix elements of $\mathcal{O}_1$, $\mathcal{O}_5$, $\mathcal{O}_8$, and $\mathcal{O}_{11}$. For the exact relation we refer again to Ref. [156].

This together with the matching of our chiral responses to the NREFT operators in Eq. (5.20) allows us to find a direct matching between the multipole operators and the chiral amplitudes of the previous section:

$$\begin{aligned} M: &\quad \mathcal{M}^{VV}, \mathcal{M}^{SS}, \mathcal{M}^{AV}, \mathcal{M}^{PS} \\ \Sigma': &\quad \mathcal{M}^{AA}, \mathcal{M}^{AV}, \mathcal{M}^{VV} \\ \Sigma'': &\quad \mathcal{M}^{AA}, \mathcal{M}^{SP}, \mathcal{M}^{VV}, \mathcal{M}^{PP} \\ \Delta: &\quad \mathcal{M}^{AV} \\ \Phi'': &\quad \mathcal{M}^{VV} \end{aligned} \tag{6.6}$$

We now discuss the response functions of the five multipole operators, symbolically defined by the reduced matrix element

$$\mathcal{F}^{\tilde{\mathcal{O}}} \simeq \left\langle \mathcal{N} \middle\| \sum_J \tilde{\mathcal{O}}_J \middle\| \mathcal{N} \right\rangle, \tag{6.7}$$

with $\tilde{\mathcal{O}} \in \{M, \Sigma', \Sigma'', \Delta, \Phi''\}$. The sum runs over J that connect the angular momenta of initial and final nuclear states via the triangular relation. The structure factors of Eq. (5.7) are equivalent to the square of the corresponding response functions. It was found that only the M operator exhibits a coherent enhancement, which is proportional to the mass number A of the nucleus at low exchanged momenta when evaluated between nuclear states. Furthermore, for the Φ'' response there is a weaker enhancement, called "quasi-coherence" by the authors of Ref. [157], which is especially relevant for heavy nuclei. Assuming a naive filling of the shell-model orbitals, the quasi-coherent responses scale approximately as $0.3 \times A$.

A different aspect is the possibility of interferences between the different operators. If the interaction between WIMPs and nucleons is not described by only one out of the six multipole operators,

products of the response functions have to be taken into account since the cross section is given by the square of the sum over the different response functions, symbolically written as

$$\frac{\mathrm{d}\sigma^{\mathrm{SI}}_{\chi\mathcal{N}}}{\mathrm{d}\mathbf{q}^2} \simeq \left|\sum_i \mathcal{F}^{\tilde{\mathcal{O}}_i}\right|^2 . \tag{6.8}$$

Some of the NREFT operators in Eq. (5.20) depend on the velocity $\mathbf{v}^\perp$ defined in Eq. (5.21). When evaluated between many-nucleon states these operators can be decomposed into two parts [156, 157]. The first part is proportional to the relative WIMP velocity with respect to the center of mass of the nucleus

$$\mathbf{v}_T^\perp = \frac{\mathbf{K}}{2m_\chi} - \frac{1}{A}\sum_{i=1}^{A}\frac{\mathbf{P}_i}{2m_N}, \tag{6.9}$$

where $\mathbf{P}_i = \mathbf{p}_i + \mathbf{p}_i'$ and $\mathbf{K} = \mathbf{k} + \mathbf{k}'$ are the sums of initial and final nucleon and WIMP momenta. Operators involving this term are effectively suppressed by the WIMP velocity with respect to the target $|\mathbf{v}_T^\perp| \approx 10^{-3}$ and will hence be neglected in the following. On the other hand, there are parts of $\mathbf{v}^\perp$ involving the relative velocities of the nucleons with respect to the center of mass of the nucleus that is part of the Δ and Φ'' responses. These terms suffer only from a weaker suppression of $|\mathbf{q}|/m_N$, which is the case for the $\mathcal{O}_3$ operator.

As shown in Eq. (5.15), the Wilson coefficients allow for both isoscalar and isovector couplings of the WIMP to the nucleon. This holds for all one-body interactions. Therefore, we will distinguish in the following between isoscalar and isovector couplings for each response.

According to the previous discussion, when including all one-body operators expected to exhibit a coherent enhancement, we need to take into account the NREFT operators $\mathcal{O}_1$, $\mathcal{O}_3$, $\mathcal{O}_5$, $\mathcal{O}_8$, and $\mathcal{O}_{11}$. The generalized cross section only including one-body operators then reads

$$\begin{aligned}\frac{\mathrm{d}\sigma^{\mathrm{SI}}_{\chi\mathcal{N}}}{\mathrm{d}\mathbf{q}^2} = \frac{\zeta^2}{4\pi\mathbf{v}^2}\Bigg(&\left|\sum_{I=\pm}\left[\xi_{\mathcal{O}_1} f_I^{\mathcal{O}_1}(\mathbf{q}^2)\mathcal{F}_I^M(\mathbf{q}^2) + \xi_{\mathcal{O}_3} f_I^{\mathcal{O}_3}(\mathbf{q}^2)\mathcal{F}_I^{\Phi''}(\mathbf{q}^2)\right]\right|^2 \\ &+ \sum_{i=5,8,11}\left|\sum_{I=\pm}\xi_{\mathcal{O}_i} f_I^{\mathcal{O}_i}\mathcal{F}_I^M(\mathbf{q}^2)\right|^2\Bigg),\end{aligned} \tag{6.10}$$

where $f_\pm^{\mathcal{O}_i}$ denote nucleon form factors [226]

$$\begin{aligned} f_\pm^{\mathcal{O}_1}(\mathbf{q}^2) &= \frac{1}{2}\left[f_p \pm f_n - \mathbf{q}^2\left(\dot{f}_p \pm \dot{f}_n\right) + f_1^{V,p} \pm f_1^{V,n} - \mathbf{q}^2\left(\dot{f}_1^{V,p} \pm \dot{f}_1^{V,n}\right) - \frac{\mathbf{q}^2}{4m_N^2}\left(f_2^{V,p} \pm f_2^{V,n}\right)\right], \\ f_\pm^{\mathcal{O}_3}(\mathbf{q}^2) &= \frac{1}{2}\left(f_2^{V,p} \pm f_2^{V,n}\right), \\ f_\pm^{\mathcal{O}_5} = f_\pm^{\mathcal{O}_8} &= \frac{1}{2}\left[f_1^{V,p} \pm f_1^{V,n}\right], \\ f_\pm^{\mathcal{O}_{11}} &= \frac{1}{2}\left[f_p \pm f_n\right], \end{aligned} \tag{6.11}$$

expressed as superpositions of the isoscalar and isovector nucleon couplings in Eqs. (5.15) and (5.22). For a Dirac (Majorana) spin-1/2 WIMP we have $\zeta = 1(2)$. The kinematic prefactors $\xi_{\mathcal{O}_i}$ are derived from the chiral operators as shown in Eqs. (5.22) and (5.23) (scalar–scalar, vector–vector, axial-vector–vector, and pseudoscalar–scalar channels) and the operator multipole decomposition shown in Refs. [156, 157]. We find [226]

$$\begin{aligned} \xi_{\mathcal{O}_1} &= 1\,, & \xi_{\mathcal{O}_3} &= \frac{\mathbf{q}^2}{2m_N^2}\,, \\ \xi_{\mathcal{O}_5} &= \frac{\mu_N |\mathbf{q}| |\mathbf{v}_T^\perp|}{2m_\chi m_N}\,, & \xi_{\mathcal{O}_8} &= |\mathbf{v}_T^\perp|\,, \\ \xi_{\mathcal{O}_{11}} &= -\frac{|\mathbf{q}|}{2m_\chi}\,. \end{aligned} \tag{6.12}$$

In Eq. (6.10), the operators $\mathcal{O}_5$, $\mathcal{O}_8$, and $\mathcal{O}_{11}$ do not interfere with $\mathcal{O}_1$ and $\mathcal{O}_3$ as the former are linear in the WIMP spin $\mathbf{S}_\chi$ and therefore, the corresponding interference terms vanish after averaging over WIMP spin projections. Also, the kinematical factors of $\mathcal{O}_5$, $\mathcal{O}_8$, and $\mathcal{O}_{11}$ are suppressed by $|\mathbf{v}_T^\perp|$ or $1/m_\chi$. As a result, the $\mathcal{O}_3$ operator can be expected to be the main correction to the standard SI operator $\mathcal{O}_1$ when constraining the analysis to the NREFT basis.

Also, we point out that Eq. (6.10) only shows interference terms that arise from $J = 0$ multipoles as derived in Refs. [156, 157]. As we are studying elastic scattering, only multipoles with even parity contribute, which translates to J being even. Multipoles with $J \geq 2$ will only be relevant for isotopes with total angular momentum of one or larger. As even-even nuclei have $J = 0$ ground states, and odd-odd nuclei heavier than ^{14}N are not stable[1] (both properties are driven by the attractive nuclear pairing interaction), for the targets of direct detection experiments $J \geq 2$ multipoles only contribute in odd-even isotopes. For the xenon isotopes we consider, only ^{131}Xe has a ground state of $3/2^+$, and the $J = 2$ contribution of the M operator was shown to be very small and not coherent [230]. Higher multipoles are therefore neglected in our study.

6.2.2 Two-body currents

Beyond the one-body currents discussed above, we take into account the two-body currents of Sec. 5.2.2. Out of the two-body operators summarized in Table 5.1, only the scalar amplitudes in Eqs. (5.17), (5.18), and (5.19) need to be taken into account. The other two-body currents (vector, axial-vector, ...) involve isospin structures as $[\boldsymbol{\tau}_1 \times \boldsymbol{\tau}_2]^3$ as well as spin structures that when summed over spin and isospin states will mostly vanish and not yield coherent contributions. There is only one contribution from the axial-vector–vector channel remaining, namely the exchange diagram which comes with an isospin structure of $\tau_1^3 - \tau_2^3$. This leads to an isovector coherent enhancement, which is suppressed by $(N - Z)/A$ compared to the scalar two-body current. Also, this current does not interfere with the dominant operator $\mathcal{O}_1$. On the other hand, the vector-vector two-body current is also isovector coherent, however, its chiral order is even more suppressed.

The two-body terms of the three scalar channels, scalar-scalar SS, trace anomaly θ, and spin-2 (2), in Eqs. (5.17), (5.18), and (5.19), respectively, can be written in form of only two indepen-

[1] With the odd-odd nuclear isomer ^{180m}Ta being an exception.

dent amplitudes when some subleading one-body contributions are included. In Appendix D, we provide a brief derivation showing that the response functions of the three physical responses can be written as

$$\mathcal{F}_\pi^\theta(\mathbf{q}^2) = 2\mathcal{F}_\pi(\mathbf{q}^2) + \mathcal{F}_\mathrm{b}(\mathbf{q}^2), \tag{6.13}$$

$$\mathcal{F}_\pi^{(2)}(\mathbf{q}^2) = -\frac{1}{2}\mathcal{F}_\pi(\mathbf{q}^2) + \frac{1}{4}\mathcal{F}_\mathrm{b}(\mathbf{q}^2), \tag{6.14}$$

where $\mathcal{F}_\pi$ is the response function of the scalar-scalar amplitude in Eqs. (5.17) and $\mathcal{F}_\mathrm{b}$ is defined in Appendix D.

For the two-body operators, there is no matching to the NREFT operators possible. The evaluation of the two-body operators will be performed in a simplified shell model, discussed in Sec. 6.3.2. Hence, no kinematic factors are necessary and the contributions of the two-body operators to the cross section can be written as

$$\frac{\mathrm{d}\sigma_{\chi\mathcal{N}}^\mathrm{SI}}{\mathrm{d}\mathbf{q}^2} = \frac{1}{4\pi\mathbf{v}^2}\left|c_\pi\mathcal{F}_\pi(\mathbf{q}^2) + c_\mathrm{b}\mathcal{F}_\mathrm{b}(\mathbf{q}^2)\right|^2, \tag{6.15}$$

where the c_i denote the pion form factors in terms of the three pion couplings f_π, f_π^θ, and $f_\pi^{(2)}$,

$$\begin{aligned} c_\pi &= \zeta\left(f_\pi + 2f_\pi^\theta - \frac{1}{2}f_\pi^{(2)}\right), \\ c_\mathrm{b} &= \zeta\left(f_\pi^\theta + \frac{1}{4}f_\pi^{(2)}\right). \end{aligned} \tag{6.16}$$

Note that the full cross section would allow for interferences between the response functions of both one- and two-body operators. However, the two-body responses do not interfere with $\mathcal{O}_5$, $\mathcal{O}_8$, and $\mathcal{O}_{11}$ for the same reason as discussed for the one-body responses. In the next section, we will perform nuclear structure calculations of the different response functions in order to explicitly determine the hierarchy among the different channels.

6.3 Nuclear structure calculations

The evaluation of the response functions requires the nuclear many-body states $|\mathcal{N}\rangle$ that describe the nuclei used as detector material. As most of these isotopes are in the medium and heavy mass region of the isotopic chart, there are only a few computational methods available to solve the many-body Hamiltonian describing the interaction of nucleons. We perform calculations using the interacting shell model for the one-body terms and apply a simplified version of the shell model for the evaluation of the two-body response functions.

6.3.1 One-body currents

We calculate the nuclear matrix elements of Eq. (6.7) using the interacting-shell-model method introduced in Sec. 1.4.3. The full configuration space of nucleons is separated in a core consisting

of orbitals that are assumed to be completely occupied and the valence space of orbitals that are only partially filled. For the xenon isotopes the valence space consists of the $0g_{7/2}$, $1d_{5/2}$, $1d_{3/2}$, $2s_{1/2}$, and $0h_{11/2}$ (nlj) orbitals for both neutrons and protons, with n the radial quantum number, l the orbital angular momentum in spectroscopic notation, and j the total angular momentum. The core of our calculations for the xenon isotopes is given by ^{100}Sn. The particles in the valence space interact via a phenomenological interaction, which has been fit to excitation spectra of nuclei in the corresponding mass region. For xenon we use the GCN5082 [234, 235] interaction, which we also used in previous work [67, 160, 230]. Depending on the number of particles in the valence space, the size of the latter had to be constrained in order to limit the required basis size. This had to be done for ^{128}Xe, ^{129}Xe, ^{130}Xe, and ^{131}Xe, while for ^{132}Xe, ^{134}Xe, and ^{136}Xe the full space was taken into account. For both the calculation of the nuclear states and the evaluation of the one-body nuclear responses, the shell-model code ANTOINE [172, 180] was used.

Similarly, we performed calculations for a range of other isotopes currently used in direct detection experiments. The ground state wave functions of ^{19}F and the stable isotopes of silicon, ^{28,29,30}Si, were calculated using the USDB effective interaction, which acts on the $0d_{5/2}$, $1s_{1/2}$, and $0d_{3/2}$ orbitals. The configuration space of ^{40}Ar comprises the same sd-shell orbitals and in addition the pf-shell orbitals $0f_{7/2}$, $1p_{3/2}$, $0f_{5/2}$, and $1p_{1/2}$. We use the SDPF.SM effective interaction [236]. As for some of the xenon isotopes, we had to truncate the many-body calculation by keeping the $0d_{5/2}$ orbital filled with nucleons, and restricting the number of excitations from sd-shell to pf-shell orbitals to 8. For the stable isotopes of germanium, ^{70,72,73,74,76}Ge, we use the RG effective interaction in a configuration space consisting of the $1p_{3/2}$, $0f_{5/2}$, $1p_{1/2}$, and $0g_{9/2}$ single-particle orbitals as in Ref. [67].

The qualitative behavior of the response functions is similar for all isotopes mentioned above. Therefore, we constrain the following discussion to the results for the most abundant isotope ^{132}Xe. In the figures, we show the square of the response functions $|\mathcal{F}|^2$ as a function of the momentum transfer $q = |\mathbf{q}|$.

As already mentioned above, the isoscalar nuclear M operator leads to a coherent contribution from all nucleons. Therefore, this was the only operator considered in SI analyses of the past. The quasi-coherence of the Φ'' operator comes from the fact that at vanishing momentum transfer the operator corresponds to a sum over all nucleons of the single-nucleon spin-orbit $(\mathbf{l}\cdot\mathbf{s})$ [156, 157]. Therefore, nucleons in an orbital with spin parallel to the angular momentum, $j = l + 1/2$, contribute coherently. On the other hand, nucleons in an orbital with spin antiparallel to the angular momentum, $j = l - 1/2$ will also contribute coherently. So when both spin-orbit partners are filled, their contributions cancel each other. In heavy nuclei, however, the spin-orbit splitting is important which results in the $j = l + 1/2$ orbitals having significantly lower energies than their spin-orbit partners. For xenon this means that the proton $0g_{9/2}$ and the neutron $0h_{11/2}$ orbitals are mostly filled, especially for the neutron-rich isotopes, while the orbitals of spin-orbit partners $0g_{7/2}$ and $0h_{9/2}$ are mostly empty. This is the origin of the quasicoherence in Φ'' leading to the coherent contribution of about 20 nucleons in the isoscalar case. Neutrons contribute the most to the total response as they occupy the $0h_{11/2}$ $(l = 5)$ orbital which has space for 12 nucleons while the protons are mostly in the $0g_{9/2}$ $(l = 4)$ orbital and the expectation value of the single-particle spin-orbit operator is proportional to l for $j = l + 1/2$. Hence, the nuclear response functions of Φ'' are larger for the most neutron-rich isotopes with more neutrons in the $0h_{11/2}$ orbital. For lower

mass isotopes, e.g., fluorine, the spin-orbit splitting is less pronounced and, as a result, the Φ'' response is more suppressed.

The other responses do not show any coherent behavior. In Fig. 6.1, we show the response functions for the contributions to the coherent response M associated to the NREFT operators $\mathcal{O}_1$, $\mathcal{O}_{11}$, $\mathcal{O}_8$, and $\mathcal{O}_5$ and Φ'', which arises from the $\mathcal{O}_3$ term (see Eq. (6.5)). Figure 6.1 shows isoscalar and isovector couplings. We also show the interference term between $\mathcal{O}_1$ and $\mathcal{O}_3$, which is, as discussed, the only interference involving $\mathcal{O}_1$. As a result, out of the NREFT operators, the $\mathcal{O}_3$ is the most important correction to the $\mathcal{O}_1$ operator. One has to keep in mind that here the associated nucleon form factors in Eq. (6.11) are assumed to be equal $f_{\pm}^{\mathcal{O}_i} = 1$. The main features should, however, still be valid once the corresponding couplings and form factors are included.

The standard SI response, which is equivalent to the $\mathcal{O}_1$ operator, is (for an isoscalar coupling) proportional to A^2 and hence the dominant response as can be observed in Fig. 6.1. In both the isoscalar and isovector cases in Fig. 6.1 the leading correction is given by the interference term with $\mathcal{F}^{\Phi''}$ due to $\mathcal{O}_3$. The kinematic factor of this response is $\xi_{\mathcal{O}_3} = \mathbf{q}^2/2m_N^2$ leading to a suppression of roughly a factor 10^3 compared to the leading term. Furthermore, due to the $\mathbf{q}$-dependence, the interference response vanishes at $|\mathbf{q}| = 0$. Next, there is the response corresponding to $\mathcal{O}_{11}$, which comes with a kinematical factor of $\xi_{\mathcal{O}_{11}} = -|\mathbf{q}|/2m_\chi$. The results in Fig. 6.1 were generated assuming a WIMP mass of $m_\chi = 2$ GeV, roughly the smallest WIMP mass probed by direct-detection experiments using xenon as target. Due to the inverse relation to the WIMP mass, this response will suffer from an additional suppression for heavier WIMPs. For $m_\chi = 50$ GeV, it becomes comparable to the response corresponding to the $\mathcal{O}_3$ operator, which is the next response in the hierarchy.

The responses corresponding to $\mathcal{O}_8$ and $\mathcal{O}_5$ are even more suppressed as their kinematical factors carry the extremely small WIMP velocity $|\mathbf{v}_T^\perp| \approx 10^{-3}$. Note that even though the kinematic factor of $\mathcal{O}_3$ also depends on $\mathbf{v}^\perp$, it suffers from a weaker suppression as it does not involve the WIMP velocity with respect to the center of mass $\mathbf{v}_T^\perp$, but the nucleon's velocity operator that translates into a factor of $|\mathbf{q}|/m_N$.

6.3.2 Two-body currents

In the previous section, the response function of the one-body operators were evaluated using the interacting shell model code ANTOINE. In general, the two-body response functions should be evaluated using the same framework for consistency. However, as this would require deriving a representation of the two-body operators in the basis representation of single-particle harmonic-oscillator states, we postpone this to future work. Here, we want to show that for the scalar two-body currents of Eqs. (5.17), (5.18), and (5.19), it is sufficient to calculate the responses using a "naive" shell model, which allows for relatively simple and computationally not demanding calculations of the response functions of the two-body currents.

In contrast to SD interactions, for SI scattering (nuclear M response) all nucleons contribute coherently. As a result, the largest part of the nuclear response is generated by the inert core, which is assumed to be completely filled. Therefore, the configuration of the particles in the valence space plays a minor role for these responses. We start from showing that our naive picture reproduces the exact result for the standard SI channel remarkably well.

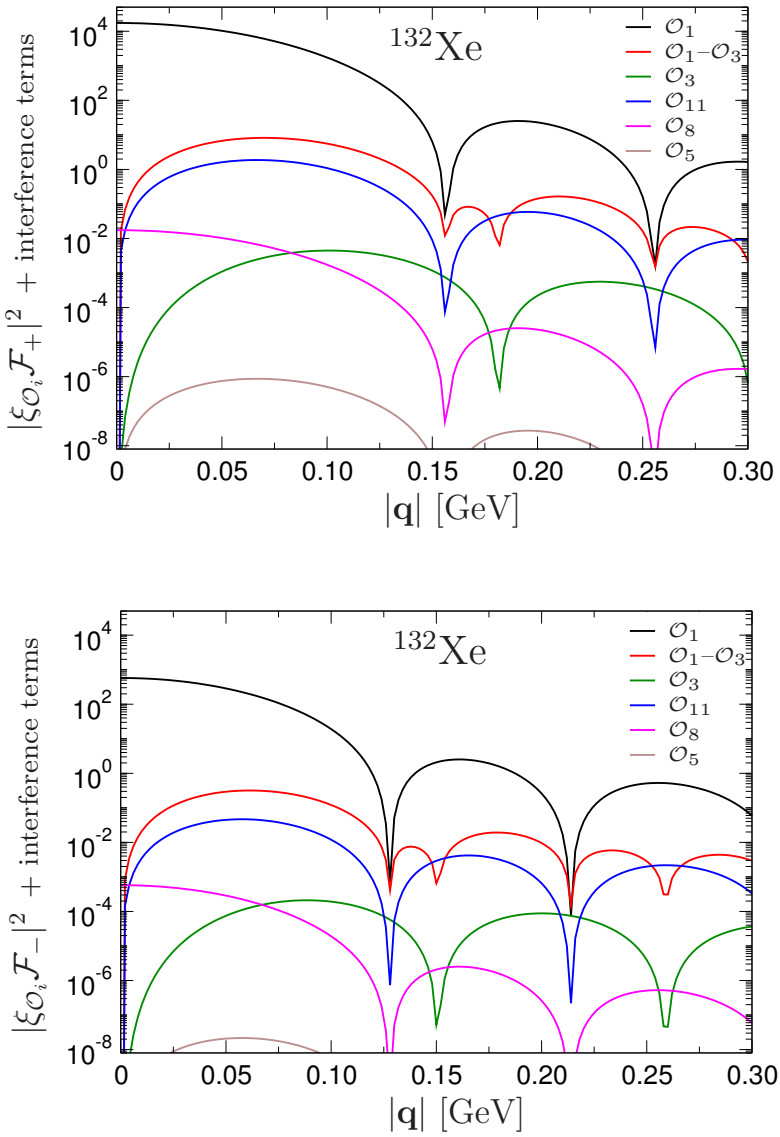

Figure 6.1: Comparison of the isoscalar (top) and isovector (bottom) structure factors associated with the coherent and quasi-coherent nuclear M and Φ'' responses. The individual contributions corresponding to the $\mathcal{O}_1$, $\mathcal{O}_3$, $\mathcal{O}_{11}$, $\mathcal{O}_8$, and $\mathcal{O}_5$ operators, $|\xi_{\mathcal{O}_i}\mathcal{F}_\pm^{M/\Phi''}(\mathbf{q}^2)|^2$, and the absolute value of the $\mathcal{O}_1$–$\mathcal{O}_3$ interference term, $|2\xi_{\mathcal{O}_1}\xi_{\mathcal{O}_3}\mathcal{F}_\pm^{M}(\mathbf{q}^2)\mathcal{F}_\pm^{\Phi''}(\mathbf{q}^2)|$, are shown. For the evaluation of the structure factors associated with $\mathcal{O}_{11}$, $\mathcal{O}_8$, and $\mathcal{O}_5$, we take the relative WIMP velocity $|\mathbf{v}_T^\perp| = 10^{-3}$ and WIMP mass $m_\chi = 2\,\text{GeV}$, roughly the minimal mass probed in xenon direct-detection experiments. The results, representative for all stable xenon isotopes, are shown for the most abundant ^{132}Xe.

n	l	maximum occupation	n^p_{nl}	n^n_{nl}
0	0	2	1	1
0	1	6	1	1
0	2	10	1	1
1	0	2	1	1
0	3	14	1	1
1	1	6	1	1
0	4	18	0.68	0.99
1	2	10	0.16	0.79
2	0	2	0.06	0.58
0	5	22	0.01	0.37

Table 6.1: Relative occupation numbers n^τ_{nl} for the nl orbitals in ^{129}Xe and maximum occupation including spin degeneracy. For orbitals in the valence space, the results of the shell-model diagonalization are used.

We construct a non-interacting shell-model picture where the wave function will be approximated by just one single Slater determinant. The latter corresponds to a state where only the lowest-lying single-particle states N_i are occupied,

$$|\mathcal{N}\rangle = \prod_i^A a^\dagger_{N_i}|0\rangle\,. \tag{6.17}$$

For a one-body operator $\mathcal{O}_{1b}$ only the single-particle matrix elements survive that connect the same single-particle states since

$$\langle\mathcal{N}|\, a^\dagger_{N_i} a_{N_j}\,|\mathcal{N}\rangle = 0 \quad \text{for} \quad i \neq j\,. \tag{6.18}$$

Note that this is only true in our naive assumption of a single Slater determinant. The operator acting on the nucleus is a sum over single-particle operators acting on each nucleon in the nucleus,

$$\mathcal{O}_\mathcal{N} = \sum_{i=1}^A \mathcal{O}_{1b,i}\,. \tag{6.19}$$

The individual operators are of course identical, i.e., $\mathcal{O}_{1b,i} = \mathcal{O}_{1b}$ for all i. As a result, the full matrix element for identical initial and final states is just the sum over the diagonal single-particle matrix elements:

$$\langle\mathcal{N}|\mathcal{O}_\mathcal{N}|\mathcal{N}\rangle = \sum_{i=1}^A \langle N_i|\,\mathcal{O}_{1b}\,|N_i\rangle\,. \tag{6.20}$$

We assume states without j-coupling such that $|N_i\rangle = |nlm\sigma\tau\rangle$, where the m, σ, and τ denote projections of angular momentum, spin, and isospin, respectively. Hence,

$$\begin{aligned}\mathcal{F}_+^M(\mathbf{q}^2) &= \sum_{nlm\sigma\tau} \langle nlm_l m_s m_\tau | \mathbb{1} | nlm_l m_s m_\tau \rangle \\ &= \sum_{nlm\tau} 2 \int \frac{\mathrm{d}^3p \mathrm{d}^3p'}{(2\pi)^3} R_{nl}(|\mathbf{p}'|) R_{nl}(|\mathbf{p}|) Y^*_{lm}(\hat{\mathbf{p}}') Y_{lm}(\hat{\mathbf{p}}) (2\pi)^3 \delta^{(3)}(\mathbf{p}-\mathbf{p}'-\mathbf{q}) \\ &= \sum_{nl\tau} 2 \int \mathrm{d}^3p \mathrm{d}^3p' R_{nl}(|\mathbf{p}'|) R_{nl}(|\mathbf{p}|) \frac{2l+1}{4\pi} P_l(\hat{\mathbf{p}}\cdot\hat{\mathbf{p}}') \delta^{(3)}(\mathbf{p}-\mathbf{p}'-\mathbf{q}), \end{aligned} \tag{6.21}$$

where the sum in the first line is over occupied orbitals. We assume an equal filling of all orbitals with different m projections. Thus, the sum over m gives rise to the Legendre polynomial P_l using the addition theorem for the spherical harmonics. The radial wave functions are given by

$$R_{nl}(k) = b^{3/2} \sqrt{\frac{2\,n!}{\Gamma(n+l+3/2)}} (bk)^l e^{-\frac{(bk)^2}{2}} L_n^{l+1/2}\left[(bk)^2\right], \tag{6.22}$$

where L_n^l denote generalized Laguerre polynomials and $b = \sqrt{\hbar/m_N\omega}$ is the harmonic-oscillator length with $\hbar\omega = (45A^{-1/3} - 25A^{-2/3})\,\mathrm{MeV}$. The remaining sum in the last line of Eq. (6.21) can be evaluated by summing over the relative occupation numbers for protons and neutrons n_{nl}^p and n_{nl}^n, provided in Table 6.1, such that

$$\mathcal{F}_+^M(\mathbf{q}^2) = \sum_{nl} (n_{nl}^p + n_{nl}^n) \langle nl|\mathbb{1}|nl\rangle\,, \tag{6.23}$$

where the matrix element is given by the integral in Eq. (6.21). Orbitals in the core, which are fully occupied, have a relative occupation number of 1, while for orbitals in the valence space of the shell-model calculation, the results of the full diagonalization are used. Alternatively, the single-particle states N_i can be taken as j-coupled states (nlj). Analytic results for the matrix elements of the one-body terms can be found in Refs. [237, 238].

In Fig. 6.2, we show the $\mathcal{F}_+^M(\mathbf{q}^2)$ response for ^{129}Xe for single-particle orbitals with and without j-coupling. Both results from the non-interacting shell model agree very well with the full shell-model calculation, which shows that the dependence on correlations among the valence nucleons as well as j-coupling effects are small for this response. Even for occupation numbers taken naively by filling the lowest orbitals there would be no significant difference in the figure.

Similarly, we evaluate the two-body matrix elements of Eq. (5.17) in the non-interacting shell model by

$$\begin{aligned}\mathcal{F}_\pi(\mathbf{q}^2) &= \frac{1}{2} \sum_{\mathrm{occ}} \langle N_1 N_2 | (1 - P_{12}) | \frac{1}{f_\pi} \mathcal{M}^{SS}_{2,\mathrm{NR}} | N_1 N_2 \rangle, \\ |N_1 N_2\rangle &= |n_1 l_1 m_1 \sigma_1 \tau_1 n_2 l_2 m_2 \sigma_2 \tau_2\rangle\,, \end{aligned} \tag{6.24}$$

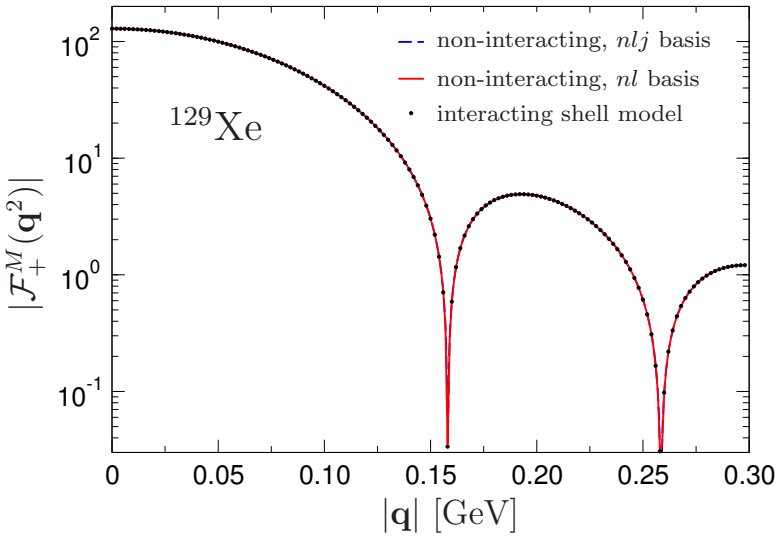

Figure 6.2: $\mathcal{F}_+^M(\mathbf{q}^2)$ for ^{129}Xe obtained from three different approximations: shell-model calculation from [230] (black dots), non-interacting shell model with j-coupling (red solid line), and in nl basis (blue dashed line).

where the sum runs over occupied states (e.g., for ^{129}Xe according to Table 6.1) and $P_{12} = P_k P_\sigma P_\tau$ is the exchange operator with

$$P_\sigma = \frac{1}{2}\big(\mathbb{1} + \boldsymbol{\sigma}_1 \cdot \boldsymbol{\sigma}_2\big), \qquad P_\tau = \frac{1}{2}\big(\mathbb{1} + \boldsymbol{\tau}_1 \cdot \boldsymbol{\tau}_2\big), \tag{6.25}$$

and P_k exchanges the momenta. Summing over spins σ_i and evaluating the matrix element in Eq. (6.24) in the harmonic-oscillator basis, we obtain

$$\begin{aligned}\mathcal{F}_\pi(\mathbf{q}^2) = \frac{M_\pi}{2}\left(\frac{g_A}{2F_\pi}\right)^2 \sum_{n_1 l_1 n_2 l_2} \sum_{\tau_1 \tau_2} \int \frac{\mathrm{d}^3 p_1 \mathrm{d}^3 p_2 \mathrm{d}^3 p_1' \mathrm{d}^3 p_2'}{(2\pi)^6} R_{n_1 l_1}(|\mathbf{p}_1'|) R_{n_2 l_2}(|\mathbf{p}_2'|) R_{n_1 l_1}(|\mathbf{p}_1|) R_{n_2 l_2}(|\mathbf{p}_2|) \\ \times \frac{(2l_1+1)(2l_2+1)}{16\pi^2} P_{l_1}\big(\hat{\mathbf{p}}_1' \cdot \hat{\mathbf{p}}_1\big) P_{l_2}\big(\hat{\mathbf{p}}_2' \cdot \hat{\mathbf{p}}_2\big) (2\pi)^3 \delta^{(3)}\big(\mathbf{p}_1 + \mathbf{p}_2 - \mathbf{p}_1' - \mathbf{p}_2' - \mathbf{q}\big) \\ \times \big(3 - \boldsymbol{\tau}_1 \cdot \boldsymbol{\tau}_2\big) \frac{\mathbf{q}_1^{\mathrm{ex}} \cdot \mathbf{q}_2^{\mathrm{ex}}}{\big((\mathbf{q}_1^{\mathrm{ex}})^2 + M_\pi^2\big)\big((\mathbf{q}_2^{\mathrm{ex}})^2 + M_\pi^2\big)},\end{aligned} \tag{6.26}$$

with

$$\mathbf{q}_1^{\mathrm{ex}} = \mathbf{p}_2' - \mathbf{p}_1, \quad \mathbf{q}_2^{\mathrm{ex}} = \mathbf{p}_1' - \mathbf{p}_2, \quad \mathbf{q} = -\mathbf{q}_1^{\mathrm{ex}} - \mathbf{q}_2^{\mathrm{ex}}. \tag{6.27}$$

As before, the sum over m_1, m_2 gives rise to the Legendre polynomials P_l using the addition theorem for the spherical harmonics, assuming an equal filling of all orbitals with different m projections. The isospin part of Eq. (6.26) can be evaluated using the occupation numbers taken from the interacting-shell-model calculation:

$$\sum_{n_1 l_1 n_2 l_2} \sum_{\tau_1 \tau_2} \big(3 - \boldsymbol{\tau}_1 \cdot \boldsymbol{\tau}_2\big) = 2 \sum_{n_1 l_1 n_2 l_2} \Big[n^p_{n_1 l_1} n^p_{n_2 l_2} + n^n_{n_1 l_1} n^n_{n_2 l_2} + 4 n^p_{n_1 l_1} n^n_{n_2 l_2}\Big], \tag{6.28}$$

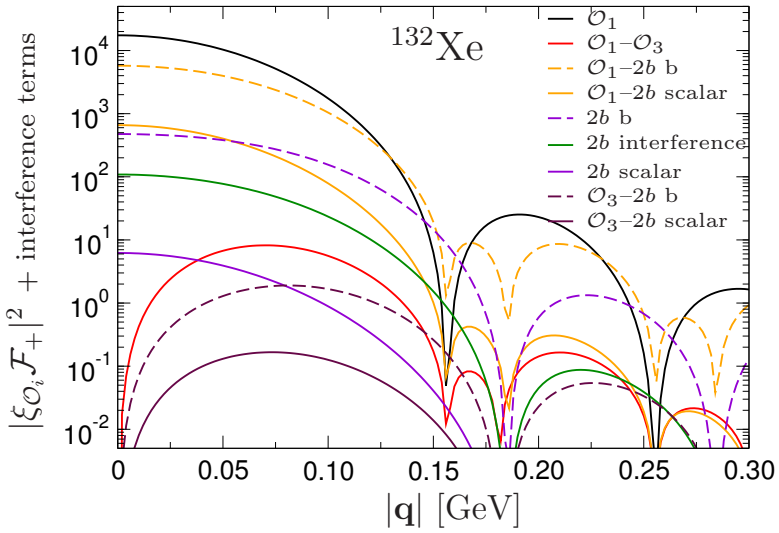

Figure 6.3: Same as the isoscalar responses in Fig. 6.1, but including the two-body-current contributions $|\mathcal{F}_{\rm b}(\mathbf{q}^2)|^2$ and $|\mathcal{F}_\pi(\mathbf{q}^2)|^2$ as well as the interference terms $|2\xi_{\mathcal{O}_1}\mathcal{F}_+^M(\mathbf{q}^2)\mathcal{F}_{{\rm b}/\pi}(\mathbf{q}^2)|$ and $|2\xi_{\mathcal{O}_3}\mathcal{F}_+^{\Phi''}(\mathbf{q}^2)\mathcal{F}_{{\rm b}/\pi}(\mathbf{q}^2)|$. Solid (dashed) lines refer to $\mathcal{F}_\pi$ ($\mathcal{F}_{\rm b}$). The green line indicates the interference $|2\mathcal{F}_\pi(\mathbf{q}^2)\mathcal{F}_{\rm b}(\mathbf{q}^2)|$ of the two-body terms. The responses associated with $\mathcal{O}_3$, $\mathcal{O}_5$, $\mathcal{O}_8$, and $\mathcal{O}_{11}$ have been omitted for clarity.

where the n_{nl}^τ denote the relative occupation numbers given in Table 6.1. The momentum integrals in Eq. (6.26) are performed numerically for given $\{n_1 l_1 n_2 l_2\}$.

Assuming an equal filling of the orbitals with different m projections picks out the $L = 0$ part of the response. This matches the choice of responses in Eq. (6.10) that only includes $L = 0$ multipoles. The contribution from $L = 2$ multipoles, which would only be relevant for ^{131}Xe, as its ground state is $J = 3/2$, is a correction to the strongly suppressed one-body $L = 2$ structure factor. The latter enters below the $\mathcal{O}_{11}$ curve in Fig. 6.1 and can hence be safely neglected. Following the same steps, the expression for $\mathcal{F}_{\rm b}(\mathbf{q}^2)$ (see Appendix D) is evaluated.

In Refs. [222, 223, 239] the $\mathcal{F}_\pi(0)$ response has been calculated for closed-shell nuclei. Converted to our normalization, the results for $A = 132$ are given by $\mathcal{F}_\pi(0) = -2.4(0.8)$ [222], $\mathcal{F}_\pi(0) = -1.4$ [223], and $\mathcal{F}_\pi(0) = -1.9$ [239], which is in good agreement with our value of $\mathcal{F}_\pi(0) = -2.49$. The differences can be traced back to our improved nuclear structure calculation. Furthermore, Refs. [222, 223, 239] used additional corrections from modeling nuclear short-range correlations [240], which are not dictated by chiral EFT in this form, and are thus not present in our calculation. This procedure is justified by studies of neutrinoless double-beta decay [241, 242] where the effect of short-range correlations was found to be small after the momentum dependence of the one-body currents is included.

In Fig. 6.3, we show an extension of Fig. 6.1 now including the responses of $\mathcal{F}_\pi(\mathbf{q}^2)$ and $\mathcal{F}_{\rm b}(\mathbf{q}^2)$ and interferences of the two-body operators with the isoscalar one-body operators. It can be observed that the two-body contributions constitute the leading correction to the $\mathcal{O}_1$ structure factor. At vanishing momentum transfer, $\mathcal{F}_{\rm b}(0)$ is similar to the isovector one-body response in Fig. 6.1 and one order of magnitude larger than $\mathcal{F}_\pi(0)$. In contrast to the responses of $\mathcal{O}_3$ and its interference with $\mathcal{O}_1$, the two-body structure factors do not vanish at $|\mathbf{q}| = 0$. In addition, the physical combinations of $\mathcal{F}_\pi$ and $\mathcal{F}_{\rm b}$ as in Eq. (6.13) and (6.14) are shown in Fig. 6.4. The two-

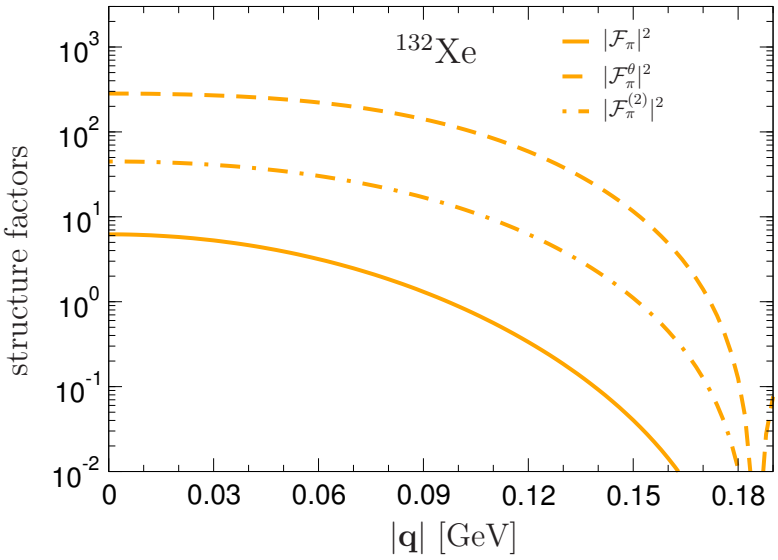

Figure 6.4: Structure factors for ^{132}Xe, physical combinations of the response functions $\mathcal{F}_\pi$ and $\mathcal{F}_b$ corresponding to the SS, θ, and spin-2 channels as in Eqs. (6.13) and (6.14).

body response from the trace anomaly term dominates by one order of magnitude over the spin-2 contribution. The scalar two-body response is suppressed by another order of magnitude.

We want to conclude this section with some final remarks concerning the hierarchy of the different responses presented in Fig. 6.3. While the ordering should be relatively general, we want to point out as before that this comparison assumes that the nucleon form factors $f_\pm^{\mathcal{O}_i}$ in Eqs. (6.10) and (6.15) are all of roughly the same size. The most striking feature is that the dominant corrections to the leading SI response come from two-body responses. These are not included in the NREFT scheme and cannot be expressed in this operator basis.

6.3.3 Chiral corrections to $\mathcal{O}_1$

Finally, we discuss the correction to the $\mathcal{O}_1$ operator that come from the momentum dependent nucleon couplings in the scalar and vector channels as well as the NR correction part of the vector–vector amplitude $\mathcal{M}_{1,\mathrm{NR}}^{VV}$, all included in $f_\pm^{\mathcal{O}_1}(\mathbf{q}^2)$ in Eq. (6.11). All of the above add a factor of $\mathbf{q}^2$ to $\mathcal{O}_1$ making it vanish at zero momentum transfer. The chiral counting implies that these so-called radius corrections appear at the same order as the other one-body responses. In Fig. 6.5, we show the response of the interference term of $\mathcal{O}_1$ and $\mathbf{q}^2/m_N^2\mathcal{O}_1$, labeled as radius, compared to the previously considered responses. We find that this response is inferior to the responses of $\mathcal{O}_1$, its interferences with the two-body operators, and $\mathcal{F}_b(0)$. Also, it is inferior to the isoscalar-isovector interference of $\mathcal{O}_1$, not shown in the figure. In particular, Fig. 6.5 shows that the correction to $\mathcal{O}_1$ are expected to be more important than the interference of $\mathcal{O}_1$ with $\mathcal{O}_3$. This highlights that the QCD corrections should indeed be taken into account.

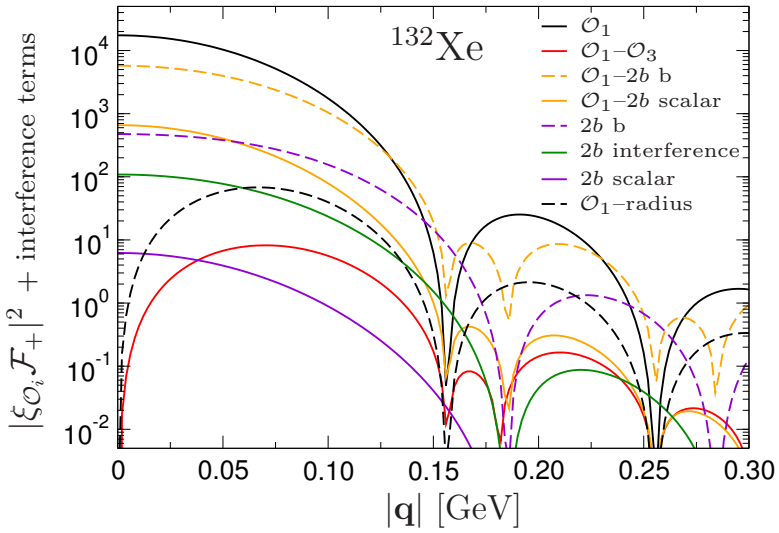

Figure 6.5: Same as Fig. 6.3, but including the radius correction term $\mathbf{q}^2/m_N^2\mathcal{O}_1$ (black dashed line). Note that the $\mathcal{O}_3$–2b interference terms have been dropped.

6.4 Generalized cross section

Collecting all the responses discussed in the previous sections, we are now able to construct a more manageable decomposition of the spin-independent WIMP-nucleus cross section in Eqs. (6.10) and (6.15). We take into account the terms that exhibit the strongest coherent enhancement as shown in our nuclear structure calculation. These terms are:

- The one-body isoscalar and isovector M responses, which exhibit the strongest coherent enhancement of all responses when excluding interference effects. The response functions of M are normalized to

$$\mathcal{F}_+^M(0) = A, \qquad \mathcal{F}_-^M(0) = Z - N\,, \tag{6.29}$$

  which means that $\mathcal{F}_+^M(\mathbf{q}^2)$ coincides with the standard SI response $\mathcal{F}_{\text{SI}}(\mathbf{q}^2)$ in Eq. (5.11). We include the M response functions of $\mathcal{O}_1$, which come from the scalar–scalar and vector–vector amplitudes in Eq. (5.22). Without the scalar nucleon coupling f_N both contributions appear at leading order in the chiral power counting. We also include the subleading contribution of the $\mathcal{O}_{11}$ term from pseudoscalar–scalar amplitude in Eq. (5.23), which appears at $\mathcal{O}(Q^4)$ in the chiral power counting of Tab. 5.1.

- The one-body isoscalar and isovector Φ'' responses, which are generated by the $\mathcal{O}_3$ operator in the vector channel, see Eq. (5.22). The Φ'' response exhibits the pseudo-coherence as discussed before. In our interacting-shell-model calculations we find a scaling of roughly

$$\mathcal{F}_+^{\Phi''}(0) \approx 0.2A, \qquad \mathcal{F}_-^{\Phi''}(0) \approx 0.2(Z-N)\,. \tag{6.30}$$

  In addition, the $\mathcal{O}_3$ contribution to the vector–vector amplitude is suppressed by $(Q/\Lambda_{\text{b}})^3$ due to the chiral power counting.

- The scalar two-body responses $\mathcal{F}_\pi(\mathbf{q}^2)$ and $\mathcal{F}_{\rm b}(\mathbf{q}^2)$. While the scaling with the nucleon number is in general similar to the M response, there is an additional suppression of $(Q/\Lambda_{\rm b})^3$ in the chiral counting.

When looking back at our matching of the different responses to the chiral amplitudes and the NREFT operators in Eqs. (5.22) and (6.5), we find that there are different chiral channels contributing to the responses listed above. As a result, the six responses do not come with only six couplings as one might have expected naively. For example, we keep the contribution of the $\mathcal{F}_+^M$ response to the $\mathcal{M}_{1,\rm NR}^{SS}$, $\mathcal{M}_{1,\rm NR}^{VV}$ and $\mathcal{M}_{1,\rm NR}^{PS}$ amplitudes. Therefore, the coupling of $\mathcal{F}_+^M$ receives contributions from the scalar nucleon couplings f_N, $\dot{f}_N$, and the vector couplings f^V, $\dot{f}^V$ (see Eq. (6.11)). We define combined couplings c_i summarizing all the couplings that come with the same $\mathbf{q}$-dependence. The final result is that we end up with ten independent parameters that can be extracted from the dependence of the cross section on Z, N, and the momentum transfer $|\mathbf{q}|$ in a direct detection experiment. We summarize these parameters:

- Isoscalar and isovector coefficients of the M response

$$c_\pm^M = \frac{\zeta}{2}\Big[f_p \pm f_n + f_1^{V,p} \pm f_1^{V,n}\Big] \tag{6.31}$$

- Coefficients of the scalar two-body responses c_π, $c_{\rm b}$ (see Eq. (6.16))
- Coefficients of the isoscalar and isovector radius corrections to the M response

$$\dot{c}_\pm^M = \frac{\zeta m_N^2}{2}\left[\dot{f}_p \pm \dot{f}_n + \dot{f}_1^{V,p} \pm \dot{f}_1^{V,n} + \frac{1}{4m_N^2}\Big(f_2^{V,p} \pm f_2^{V,n}\Big)\right] \tag{6.32}$$

- Isoscalar and isovector coefficients of the Φ'' response

$$c_\pm^{\Phi''} = \frac{\zeta}{2}\Big(f_2^{V,p} \pm f_2^{V,n}\Big) \tag{6.33}$$

- Isoscalar and isovector coefficients of the $\mathcal{O}_{11}$ response

$$\tilde{c}_\pm^M = \frac{\zeta}{2}\Big[f_p \pm f_n\Big] \tag{6.34}$$

These ten parameters are not all independent, since they map onto seven Wilson coefficients [226]. Collecting all terms, the generalized spin-independent WIMP-nucleus cross section reads

$$\begin{aligned}\frac{\mathrm{d}\sigma_{\chi\mathcal{N}}^{\rm SI}}{\mathrm{d}\mathbf{q}^2} =& \frac{1}{4\pi\mathbf{v}^2}\left|\sum_{I=\pm}\Big(c_I^M - \frac{\mathbf{q}^2}{m_N^2}\,\dot{c}_I^M\Big)\mathcal{F}_I^M(\mathbf{q}^2) + c_\pi\mathcal{F}_\pi(\mathbf{q}^2) + c_{\rm b}\mathcal{F}_{\rm b}(\mathbf{q}^2)\right.\\ &\left. + \frac{\mathbf{q}^2}{2m_N^2}\Big[c_+^{\Phi''}\mathcal{F}_+^{\Phi''}(\mathbf{q}^2) + c_-^{\Phi''}\mathcal{F}_-^{\Phi''}(\mathbf{q}^2)\Big]\right|^2 + \frac{1}{4\pi\mathbf{v}^2}\left|\sum_{I=\pm}\frac{|\mathbf{q}|}{2m_\chi}\tilde{c}_I^M\mathcal{F}_I^M(\mathbf{q}^2)\right|^2 .\end{aligned} \tag{6.35}$$

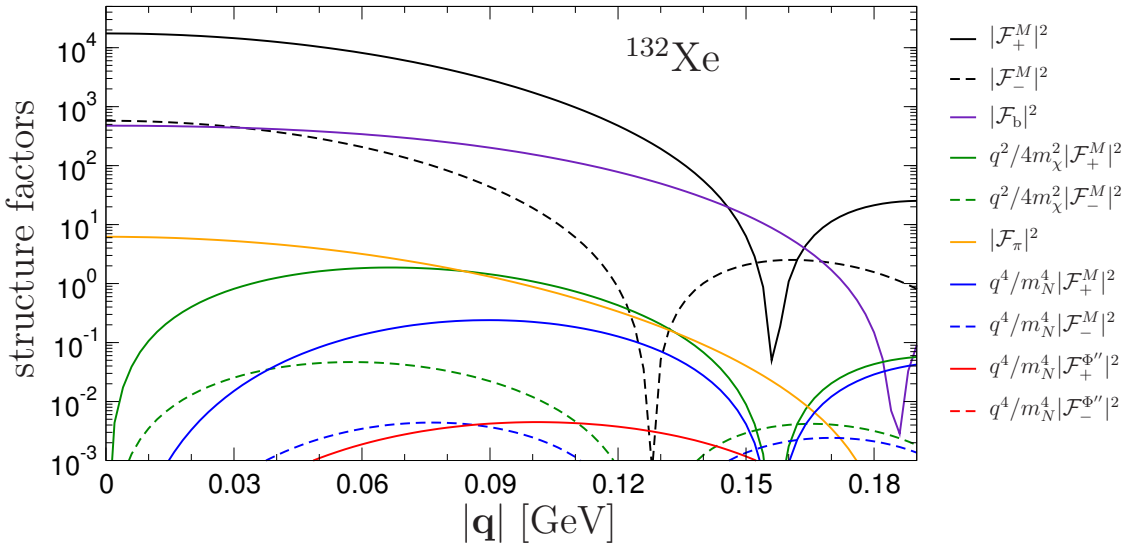

Figure 6.6: Structure factors for ^{132}Xe, 1b and 2b contributions without interference terms. 1b $\mathcal{O}_1$ (black), $\mathcal{O}_{11}$ (green), radius corrections (blue) and $\mathcal{O}_3$ (red) contributions are shown together with 2b $\mathcal{F}_\mathrm{b}$ (violet) and $\mathcal{F}_\pi$ (orange) structure factors. Solid lines show isoscalar and 2b contributions, while dashed lines correspond to isovector couplings. $m_\chi = 2$ GeV is used.

Hence, we conclude that it is sufficient for SI coherent scattering to only include interactions which involve nuclear scalar and vector currents, i.e., $\mathcal{M}^{SS}$, $\mathcal{M}^{PS}$, and $\mathcal{M}^{VV}$. The fact that the Φ'' response is only part of the vector operator (see Eq. (6.6)) might – given a discovery of a WIMP-nucleus signal – allow one to discriminate between the (pseudo)scalar and the vector channel.

Figure 6.6 shows the structure factors (square of the response functions) for all channels in Eq. (6.35) separately, i.e., setting all but one of the c_i to zero. This figure lacks the response functions that arise when interferences between the different channels are included. At $|q| = 0$, the M response dominates due to the scaling with $A^2 \approx 1.7 \times 10^4$ (for an isoscalar coupling). Next, we expect the two-body contributions that scale as $(Q/\Lambda_\mathrm{b})^6 A^2$. While for $Q = M_\pi$ and $\Lambda_\mathrm{b} = 500\,\mathrm{MeV}$ the scalar two-body structure factor agrees well with this expectation ($|\mathcal{F}_\pi(0)|^2 = 6.2$), we find that $|\mathcal{F}_b(0)|^2$ is significantly larger. This is also the case for the physical channels of $|\mathcal{F}_\pi^\theta(0)|^2$ and $|\mathcal{F}_\pi^{(2)}(0)|^2$ in Fig. 6.4.

In Fig. 6.7, the interference terms are included. Comparing the different contributions, we finally reach a hierarchy among the different channels. In Fig. 6.8, we collect the dominant response functions including interferences. The leading three corrections at low momenta to the standard spin-independent channel $\mathcal{F}_+^M$ arise from its interference with the two-body responses $\mathcal{F}_\mathrm{b}$ and $\mathcal{F}_\pi$ and the isovector $\mathcal{F}_-^M$. The single-channel responses of the two-body contributions and the isovector channel as well as the interference of $\mathcal{F}_+^M$ with the radius correction follow. The contribution from the interference of the M and Φ'' responses is more than four orders of magnitude suppressed compared to the dominant SI response. This is the first subdominant contribution that arises from an operator in the NREFT scheme different to $\mathcal{O}_1$ as all other responses are modifications of the $\mathcal{O}_1$ operator or two-body responses, which are not covered in NREFT. This highlights the importance of taking into account subleading corrections that arise from QCD via the operators derived in the

framework of chiral EFT. In addition, we want to emphasize the importance of coherence effects induced when the different operators are evaluated between nuclear states. Only at the level of response functions the hierarchy between the different channels is revealed.

Once again, we stress that the individual strengths of the different terms in an actual experiment will depend on a given new-physics model, which, together with the nucleon couplings, fixes the coefficients c_i. Nevertheless, Fig. 6.8 shows that there is a strong hierarchy among the different channels when all coefficients c_i are set to one.

In addition, in Fig. 6.9, we show the structure factors for the isotopes ^{74}Ge, ^{40}Ar, and ^{19}F, which are the most abundant isotopes of the nuclear targets currently used in direct detection experiments. The qualitative discussion concerning the hierarchy of the different responses remains unaffected.

In the next chapter, we will show different applications of our formalism both for the extension of analyses of direct detection experiments as well as in the context of extracting limits on WIMP-nucleon couplings from collider searches.

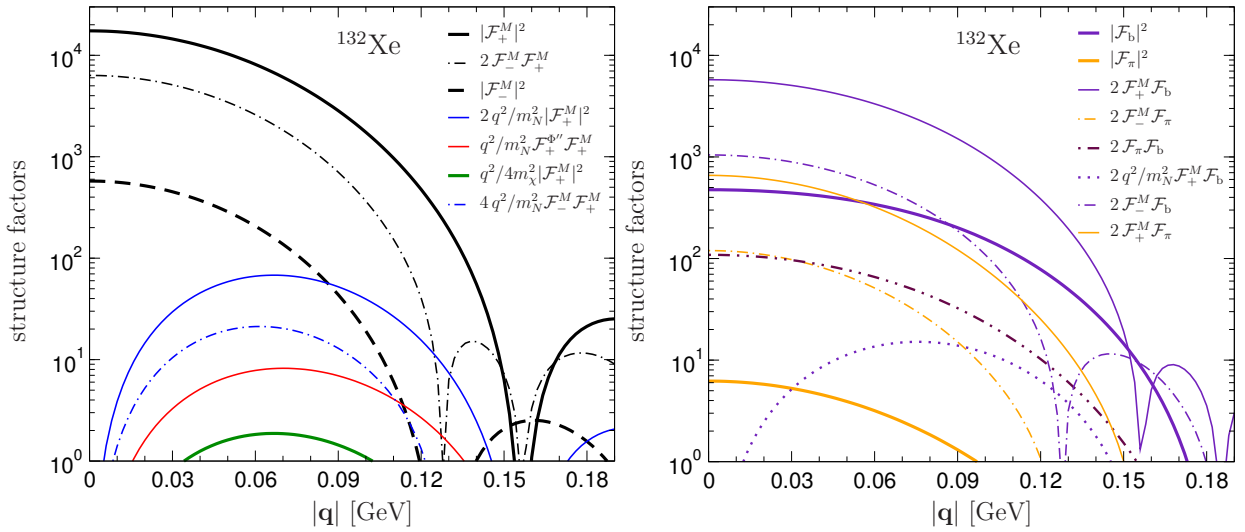

Figure 6.7: Structure factors for ^{132}Xe for 1b contributions only (left) and 2b contributions and 1b-2b interferences (right). Thick lines correspond to individual terms in Eq. (6.35), while interference terms are shown as thin lines. Left: Description as in Fig. 6.6, with dotted-dashed lines representing interference terms involving isovector couplings. Right: Structure factors involving $\mathcal{F}_\mathrm{b}$ ($\mathcal{F}_\pi$) structure factors in violet (orange), except for the $\mathcal{F}_\mathrm{b}$–$\mathcal{F}_\pi$ interference, represented by the brown dotted-dashed line.

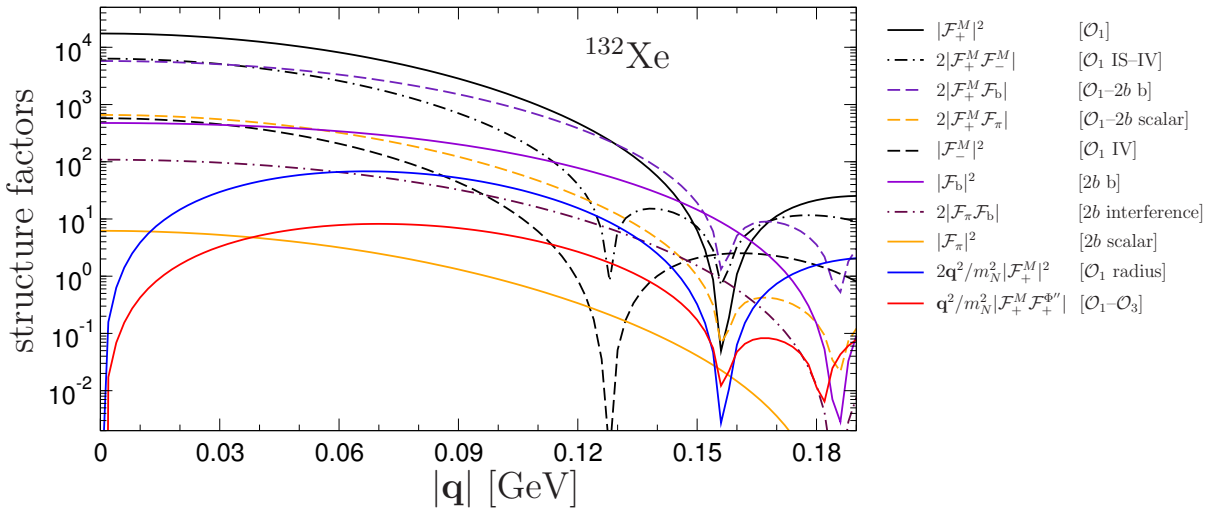

Figure 6.8: Comparison of the leading structure factors associated with the coherent and quasi-coherent one-body $\mathcal{F}^M$ and $\mathcal{F}^{\Phi''}$ nuclear responses, the two-body nuclear responses $\mathcal{F}_\pi$ and $\mathcal{F}_\mathrm{b}$, and the radius corrections to the structure factors. The individual contributions are ordered in the legend according to their size at $|\mathbf{q}| = 0$ (from top to bottom): the standard SI response $\mathcal{F}_+^M$ corresponding to the isoscalar one-body $\mathcal{O}_1$ operator (black), its interference with an $\mathcal{O}_1$ isovector contribution (black dotted-dashed) and with the two-body responses $\mathcal{F}_\mathrm{b}$ and $\mathcal{F}_\pi$ (violet/orange dashed), the purely isovector contribution $\mathcal{F}_-^M$ (black dashed) and the structure factor generated solely by the two-body currents (violet/orange) and their interference (brown dotted-dashed), the interference of $\mathcal{O}_1$ with the radius correction (blue), and the interference of the standard SI response with the quasi-coherent one-body $\mathcal{F}^{\Phi''}$ structure factor (red).

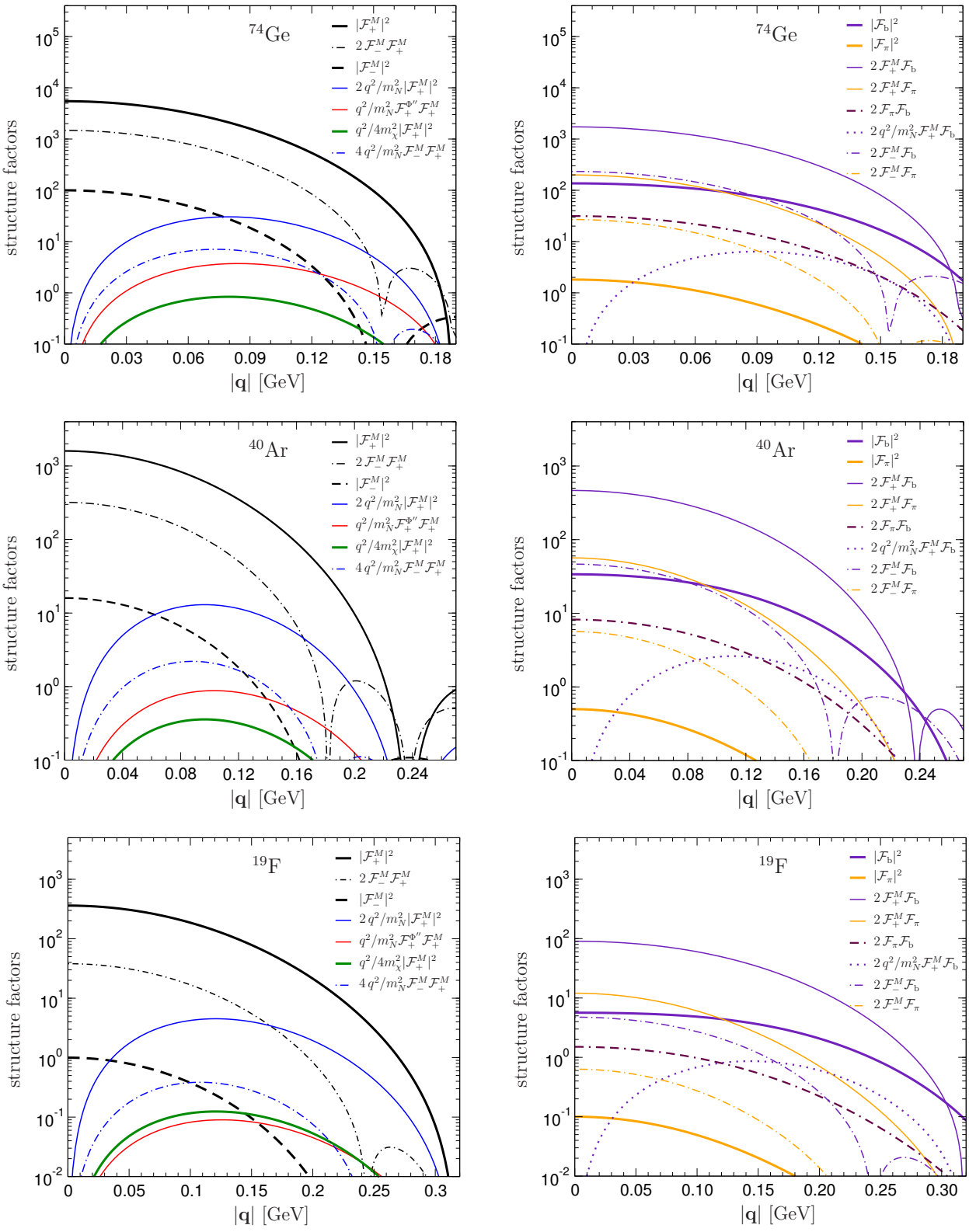

Figure 6.9: Structure factors for ^{74}Ge, ^{40}Ar, and ^{19}F. Description as in Fig. 6.7.

7 Applications

In this chapter, we present two applications of the WIMP-nucleus response functions derived in Chapter 6. First, we discuss how the scalar two-body operators contribute to the analysis of collider searches for dark matter particles in Sec. 7.1. The results discussed have been published in Ref. [243]. Here, the emphasis is put on the application of the nuclear two-body currents as this is where the author of this thesis contributed to the publication in addition to the discussion of the results.

Second, in Sec. 7.2, we study how the different operator structures can be distinguished in direct detection experiments. The results presented have been obtained in a collaboration with members of the XENON1T collaboration, Alexander Fieguth and Christian Weinheimer, who simulated the signal and background models and performed the likelihood-ratio analysis. The author of this thesis contributed to the choice and discussion of the different nuclear responses taken into account and to the discussion of the results. The discussion provided here will therefore focus on these aspects while for experimental details we refer to the original publication in Ref. [244].

7.1 Improved limits for Higgs-portal dark matter from LHC searches

There are many different possibilities for the mediator of the interaction between WIMPs and Standard Model (SM) particles. A range of so-called Higgs-portal models suggests the Higgs particle as mediator (see Fig. 7.1) [245–248]. This hypothesis can be tested by studying invisible Higgs decays in the Large Hadron Collider (LHC). If the Higgs decays into long-lived non-SM particles that do not leave a signature in the detector, events with large missing transverse momentum are expected. Up to the present day, there has been no measurement of any invisible Higgs decay [249–255]. A major constraint of these analyses is that due to energy conservation, only WIMP masses up to half of the Higgs mass $m_\chi < m_h/2$ can be probed. Up to this threshold, limits on the invisible decay width of the Higgs can be translated to limits on the WIMP-nucleon coupling derived from direct detection experiments. In order to do so, one needs to calculate the coupling of the Higgs to the nucleon f_N^h. When comparing to direct detection experiments, f_N^h obtains a correction from the coupling of the Higgs to two nucleons described by the two-body currents discussed in Chapter 5.

The contribution from the nuclear two-body currents to f_N^h together with the evaluation of f_N^h using recent phenomenological and lattice-QCD calculations has been published in Ref. [243].

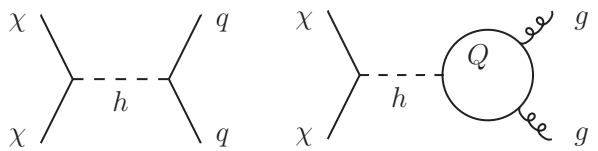

Figure 7.1: Higgs-mediated interaction of the WIMP χ with the light quarks $q = u, d, s$ (left) and the gluon field g by closing a heavy-quark loop $Q = c, b, t$ (right) [243].

7.1.1 Two-body-current contribution to the Higgs-nucleon coupling

We start from the response functions of the scalar two-body currents derived in Sec. 6.3.2. Combining the response functions $\mathcal{F}_\pi$ and $\mathcal{F}_\pi^\theta$ at $\mathbf{q} = 0$ yields the two-body currents' contribution to the Higgs-nucleon coupling (the spin-2 term does not couple to the spin-zero Higgs)

$$f_N^{h\,2\mathrm{b}} = \frac{1}{A}\frac{\Lambda^3}{m_N}\Big[f_\pi \mathcal{F}_\pi(0) + f_\pi^\theta \mathcal{F}_\pi^\theta(0)\Big]. \tag{7.1}$$

For Higgs-mediated scattering the couplings are given by [256]

$$f_\pi = \frac{7}{9}\frac{m_\pi}{\Lambda^3}, \qquad f_\pi^\theta = \frac{2}{9}\frac{m_\pi}{\Lambda^3}, \tag{7.2}$$

and thus, together with Eq. (6.13) and $\mathcal{F}_\mathrm{b}(0) = -\frac{2}{M_\pi}E_\mathrm{b}$, where E_b is the binding energy of the nucleus calculated from the LO chiral NN potential (see Appendix D), we find

$$f_N^{h\,2\mathrm{b}} = \frac{1}{A}\frac{m_\pi}{m_N}\frac{11}{9}\mathcal{F}_\pi(0) - \frac{4}{9}\frac{E_b}{Am_N}. \tag{7.3}$$

The scalar two-body response $\mathcal{F}_\pi(0)$ has been evaluated in the simplified shell model in Sec. 6.3.2. We average over a range of nuclei currently used in direct detection experiments, i.e., the stable isotopes of xenon, argon, germanium, and silicon. For the binding energy E_b, we take experimental data, corrected for the Coulomb contribution following Ref. [257]. By doing so, we effectively include higher order terms of the nuclear potential, e.g., $3N$ interactions. We obtain

$$\begin{aligned} f_N^{h\,2\mathrm{b}} &= [-3.2(0.2)(2.1) + 5.0(0.4)] \times 10^{-3} \\ &= 1.8(2.1) \times 10^{-3}, \end{aligned} \tag{7.4}$$

where the sum is over the two terms in Eq. (7.3). The first uncertainties for both terms come from the variation over the different isotopes. The second error of the first term is a result of the truncation in the chiral expansion and from the use of the harmonic-oscillator model to evaluate $\mathcal{F}_\pi(0)$. This uncertainty has been taken significantly larger than naively estimated in chiral EFT. The uncertainty in the many-body calculation has been estimated by using occupation numbers from two-different effective interactions in the valence space. We find a variation of less than 1%.

Combining the contribution from the two-body currents with updated results for the Higgs coupling to one single nucleon [243], we obtain the final result of

$$f_N^h = f_N^{h\,1\mathrm{b}} + f_N^{h\,2\mathrm{b}} = 0.308(18). \tag{7.5}$$

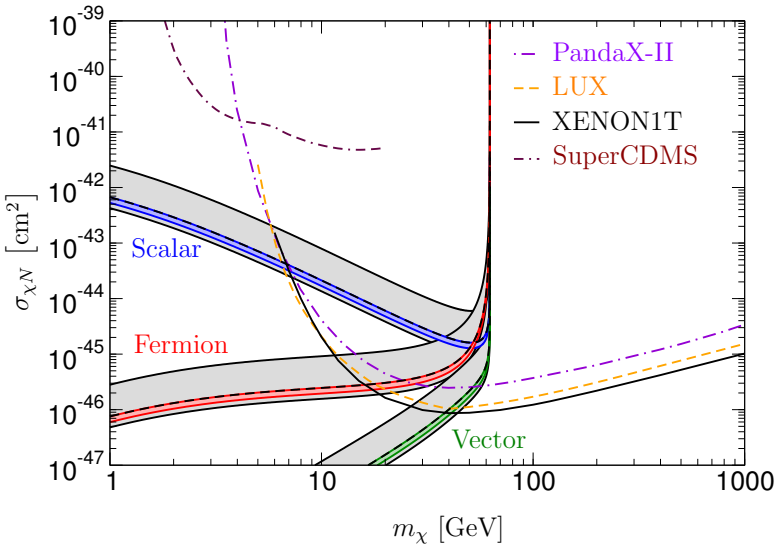

Figure 7.2: Exclusion limits for scalar (blue), fermion (red), and vector (green) Higgs-portal WIMPs [243]. The gray-shaded bands refer to the range $f_N^h = 0.260 \ldots 0.629$ from the most recent ATLAS [254] and CMS [255] analyses, the dashed lines to the central value $f_N^h = 0.326$ considered therein, and the colored bands to our improved limits using Eq. (7.5). For comparison, we show the direct-detection limits from SuperCDMS [259], PandaX-II [260], LUX [152], and XENON1T [151].

7.1.2 Impact on LHC Higgs-portal limits

We take into account three different channels for the Higgs-SM coupling: scalar $H^\dagger H S^2$, vector $H^\dagger H V_\mu V^\mu$, and fermion $H^\dagger H \bar{f} f$, with the Higgs doublet H and scalar, vector, and fermions field S, V^μ, f. The cross section is then given by

$$\sigma_{\chi N} = \Gamma_{\text{inv}} \frac{8 m_N^4 (f_N^h)^2}{v^2 \beta m_h^3 (m_\chi + m_N)^2} g_\chi \left(\frac{m_h}{m_\chi} \right), \tag{7.6}$$

where $g_S(x) = 1$, $g_V(x) = 4/(12 - 4x^2 + x^4)$, and $g_f(x) = 2/(x^2 - 4)$, $\beta = \sqrt{1 - 4m_\chi^2/m_h^2}$, $v = 246$ GeV is the Higgs vacuum expectation value, and the branching ratio $\text{BR}_{\text{inv}} = \Gamma_{\text{inv}}/(\Gamma_{\text{inv}} + \Gamma_{\text{SM}})$, with $\Gamma_{\text{SM}} = 4.07$ MeV [258]. For details we refer to [246].

In Fig. 7.2, we show the exclusion limits for the three different channels derived from the CMS limit $\text{BR}_{\text{inv}} < 0.20$ (at 90% confidence level) [255] using our result for f_N in Eq. (7.5), which has a significantly smaller uncertainty than previous results. As a consequence, in Fig. 7.2, only a narrow band remains. This presents a significant improvement of the limits from the LHC data.

7.2 Discriminating WIMP–nucleus response functions in present and future XENON-like direct detection experiments

In a scenario where the standard spin-independent (SI) response, which can be approximated by the Helm form factor (see Eq. (5.12)), is suppressed, e.g., in the vicinity of so-called blind spots of supersymmetric models [261–263], other channels such as the ones discussed in Chapter 5 might become dominant. The standard approach only considers the case of spin-dependent scattering as an alternative to the standard SI scattering. However, as was discussed in Chapter 6, there are other responses that exhibit a coherent enhancement similar to the standard SI channel. The question arises if, in the event of a WIMP detection, it is possible to distinguish between the different responses. The potential discrimination power of direct detection experiments has been studied in Ref. [264], however, based on the NREFT operators in Eq. (5.20). In this chapter, we exploit the different momentum dependencies of the response functions that we found to exhibit coherent enhancement in Chapter 6. We answer the question to what extend a distinction is possible in both present and future direct detection experiments using xenon as target material.

The leading nuclear responses of Chapter 6 are considered individually by taking into account only one at a time to investigate if a distinction from the standard SI interaction based upon the q-dependence is possible. The signal and background distributions are obtained from toy-Monte Carlo (toy-MC) simulations based on the parameters of the XENON100 detector [265, 266], with settings based on the results of Ref. [267] and standard astrophysical assumptions [139]. For the signal and background rates, we extrapolate the values of XENON100 to its successors XENON1T [151] and XENONnT [140] and the proposed DARWIN experiment [33]. The results for XENONnT are also representative for future effort like the LZ detector [154] and the PandaX-xT experiment [268] as the properties of these experiments resemble those taken into account here. A likelihood-ratio analysis then allows us to judge on the discrimination power of each of the considered experimental configurations as well as for different WIMP masses and WIMP-nucleon coupling strengths.

7.2.1 Nuclear responses

In Sec. 6.4, we presented an extension of the standard SI analysis by adding the leading contributions that are coherently enhanced. The choice of responses in Eq. (6.35) was based on an analysis of both single-channel responses, which correspond to only one single interaction type, and interference terms, which can appear when there is more than just one single interaction type present. For practical reasons, in this study we constrain ourselves to models where there is only one operator present at a time, i.e., all but one of the coefficients c_i in Eq. (6.35) vanish. In such a "one-operator-at-a-time" approach no interferences are taken into account. The remaining coherent operators of $\mathcal{O}_5$ and $\mathcal{O}_8$ not part of Eq. (6.35) lead to response functions very similar to the ones corresponding to M and $\mathcal{O}_{11}$, respectively, while being even stronger suppressed. Thus, we will not take them into account. Furthermore, we do not take into account $\mathcal{F}_{\mathrm{b}}$ for simplicity and since its momentum dependence is similar to $\mathcal{F}_{\pi}$.

Figure 7.3 shows the square of the response functions, also called nuclear structure factors, of the different channels we take into account. Note that for the response corresponding to $\mathcal{O}_{11}$ we

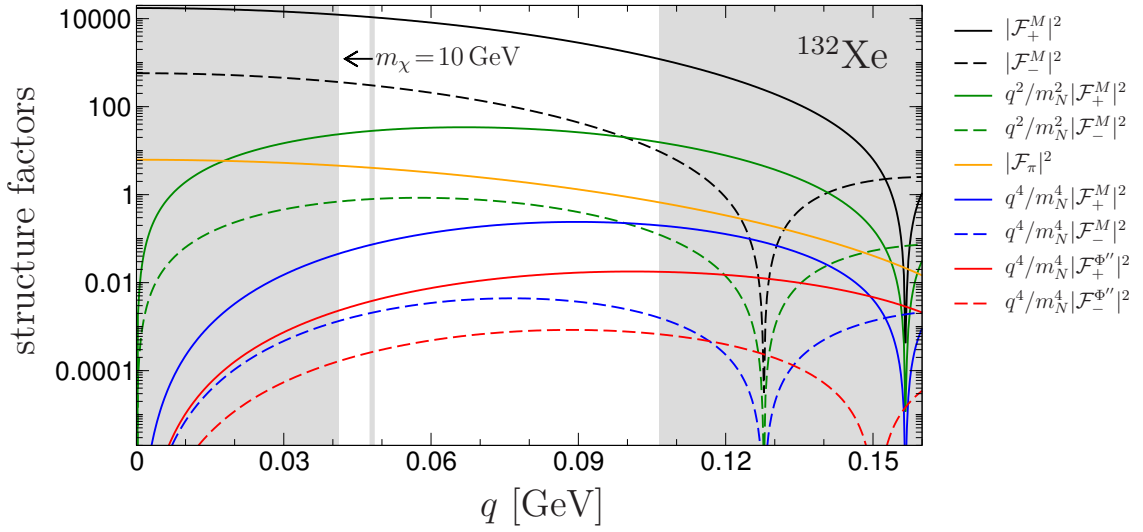

Figure 7.3: Nuclear structure factors for ^{132}Xe as in Fig. 6.6 but without $\mathcal{F}_\mathrm{b}$ and replacing $2m_\chi \to m_N$ [244]. Solid/dashed lines refer to isoscalar/isovector nucleon couplings. The energy thresholds at 6.6 keV–43.3 keV, from the search window of the XENON100 detector, translate into the solid gray bands indicating the momentum transfers below the lower (above the upper) detector threshold at $q_\mathrm{thr}^\mathrm{low} = 0.0412\,\mathrm{GeV}$ ($q_\mathrm{thr}^\mathrm{up} = 0.1065\,\mathrm{GeV}$). The vertical gray line shows the estimated maximum momentum transfer for a WIMP mass $m_\chi = 10\,\mathrm{GeV}$. For $m_\chi = 100\,\mathrm{GeV}$ and $m_\chi = 1\,\mathrm{TeV}$ the maximum momentum transfer exceeds $q_\mathrm{thr}^\mathrm{up}$. The ordering of the solid lines in the legend follows the ordering of the structure factors in the search window of the detector.

replaced $2m_\chi$ by m_N as only the functional form of the different responses will be relevant for our study.

While in general it is challenging to estimate the uncertainties associated to the nuclear structure calculations, Refs. [230, 269] found that the coherent structure factors are not very sensitive to the nuclear structure details of the nuclei involved. Therefore, in agreement with Ref. [270], we assume that these uncertainties are significantly smaller than the ones that enter this study via the astrophysical parameters in the scattering rate in Eq. (5.4).

The couplings c_i in Eq. (6.35) account for the coupling of the WIMP to the underlying structure of quarks and gluons. As their exact value is of course unknown, the c_i will be adjusted in such a way that the overall WIMP scattering rate is consistent with the published SI limits on $\sigma_{\chi\mathcal{N}}^\mathrm{SI}$ (see Eq. (5.11)).

The q-dependence ($q = |\mathbf{q}|$) of the different responses differs either due to the different nuclear structure factors or due to additional kinematical factors that add additional suppression in q. In particular, responses suppressed by a power of q vanish at $q = 0$, which leads to the most pronounced differences when comparing to the standard SI response.

7.2.2 Experimental assumptions

The experimental setups upon which our study is based are dual-phase time projection chambers (TPC) filled with xenon, designed to observe the nuclear recoil (NR) induced by a WIMP scattering

off a nucleus [33, 140, 151, 265, 266]. Signatures in the detector arise either from NRs or electronic recoils (ER) induced by background radiation such as γ-rays or β-particles. A dual-phase TPC allows us to distinguish between the two signatures based on the ratio of two signals: First, there is the direct scintillation light caused by the scattering process, which is usually labeled as S1 signal. Second, an external electric field prohibits recombination of the free electrons produced by the initial ionization, which then drift to the top of the liquid phase. Entering the gaseous phase the electrons accelerate and produce a delayed signal of electroluminescence, referred to as the S2 signal. Correcting for several detector effects the true deposited energy can be reconstructed. The corrected signals are referred to as cS1 and cS2. The energy deposited is measured in terms of the number of produced photoelectrons (PE). However, the number of PEs per unit energy is distributed according to a Poissonian distribution. Therefore, the q-dependence of any signal distribution will be smeared out in an experiment.

The sensitivity to the q-dependence is further constrained by the energy threshold of the detector. As the lowest-energy NRs are not detected, the experiments are not able to collect signals from events around $q = 0$, which is where the standard SI response is maximal. On the other hand, for responses that vanish at $q = 0$, the information loss is not as pronounced. In Fig. 7.3, we show the detector thresholds for the XENON100 experiment, 6.6 keV – 43.3 keV for NR, translated into limits on the transferred momentum. The following analysis is based on this search window.

For the active mass M of the detectors, we take the parameters for the present configuration of the XENON1T and future experiments XENONnT and DARWIN, respectively. As for the search window, we assume for the background composition the properties of the XENON100 detector (see Ref. [267]) for all detectors considered here. Furthermore, we adjust the background rate to each experiment by taking the measured values for XENON100 and XENON1T, which are $b_{\text{XENON100}} = 5.3 \times 10^{-3} \frac{\text{evts}}{\text{kg}\times\text{keV}\times\text{day}}$ [267] and $b_{\text{XENON1T}} = 0.036\, b_{\text{XENON100}}$ [151], respectively. For XENONnT we assume $b_{\text{XENONnT}} = 0.0036\, b_{\text{XENON100}}$, while for DARWIN we use the published value of $b_{\text{DARWIN}} = 0.0011\, b_{\text{XENON100}}$ [33]. These choices of background composition and rates are rather conservative as they neglect future improvements, which, if taken into account, would increase sensitivity. Therefore, the results of our study may underestimate the ability to discriminate between the different responses. A more detailed discussion of the assumptions going into the background rates can be found in Ref. [244].

7.2.3 Monte Carlo and likelihood analysis

For our study we model both the signal rate, based on the different responses in Fig. 7.3, and the background rate using toy-MC simulations. For the signal rate we fix m_χ and $\sigma^{\text{SI}}_{\chi\mathcal{N}}$, which in turn set the number of expected WIMP events $\langle N_{\text{sig}}\rangle$ for a given exposure $M \times t$, where t is the time. Hence, $\langle N_{\text{sig}}\rangle$ is kept constant when investigating the different nuclear responses one-at-a-time. The shape of the signal model depends on the q-dependence of the underlying response reflected in different signals in the cS1-cS2 plane as showcased in Fig. 7.4 for the $q^2/4m_\chi^2|\mathcal{F}^M_+|^2$ response.

The background rate b sets the number of expected background events $\langle N_{\text{bkg}}\rangle$ when assuming a particular exposure $M \times t$. Based on our initial assumptions, we obtain the probability density functions (pdf) for the signal distribution according to the standard SI response (Helm form factor) f_{Hs}, the non-Helm form factor (f_{nHs}), and the background model f_{b}. Using the expected number of events $\langle N_{\text{sig}}\rangle$ and $\langle N_{\text{bkg}}\rangle$ as weights, we derive the pdfs for the background model f in combination

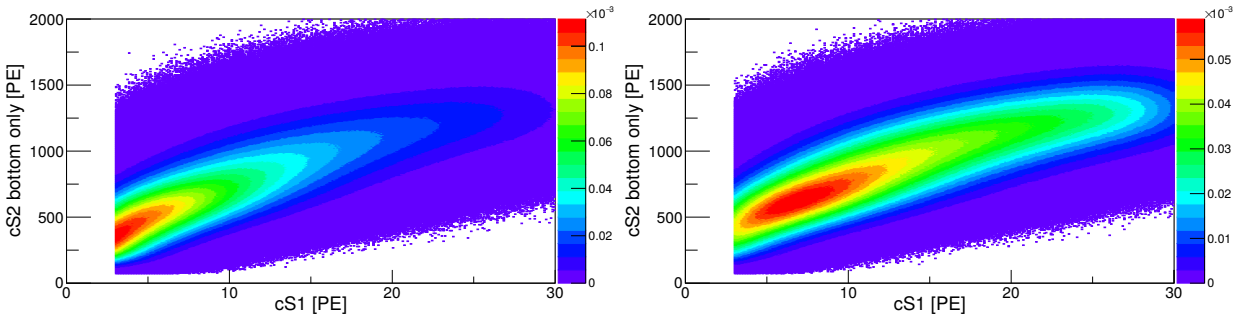

Figure 7.4: Left panel: Probability density function based on the signal model using the standard isoscalar structure factor $|\mathcal{F}_+^M|^2$, corresponding to the Helm form factor. The parameter space shows the scintillation signal (cS1) vs. the part of the ionization signal (cS2) that is seen in the bottom of the detector. The color code denotes a probability for each bin and the function is normalized to 1 in the given parameter space. Right panel: Probability density function for the signal with the underlying structure factor $q^2/4m_\chi^2|\mathcal{F}_+^M|^2$ as well normalized to 1 in the given parameter space [244].

with the signal model using either the Helm form factor ($f_{\mathrm{Hs+b}}$) or the non-Helm form factor ($f_{\mathrm{nHs+b}}$):

$$f_{\mathrm{Hs+b/nHs+b}} = \frac{\langle N_{\mathrm{sig}}\rangle \times f_{\mathrm{Hs/nHs}} + \langle N_{\mathrm{bkg}}\rangle \times f_{\mathrm{b}}}{N_{\mathrm{tot}}}, \tag{7.7}$$

where $N_{\mathrm{tot}} = \langle N_{\mathrm{sig}}\rangle + \langle N_{\mathrm{bkg}}\rangle$. These pdfs model the distribution of the experimental signal stemming from both background events and WIMP signals. In the next step, we perform an unbinned likelihood ratio test to judge on the ability of a particular experiment to distinguish between a signal stemming from the standard Helm form factor and a different response.

Using the toy-MC method, we create experimental sample data distributed according to the pdf $f_{\mathrm{Hs+b}}$. One single sample $\{x_i\}_{i=1,\ldots,N_{\mathrm{tot}}}$ consists of N_{tot} events detected in a particular experiment with a particular exposure. The hypothesis of a distribution according to the standard Helm form factor acts as the null model (H_0) of our likelihood-ratio test. The distribution of H_0 is obtained by calculating the likelihood ratio

$$Q_{N_{\mathrm{Hs}}} = \prod_{i=1}^{N_{\mathrm{tot}}} \frac{p(x_i|f_{\mathrm{nHs+b}})}{p(x_i|f_{\mathrm{Hs+b}})}, \tag{7.8}$$

for a large number of samples $\{\{x_i\}_{i=1,\ldots,N_{\mathrm{tot}}}\}$, where p is the probability of the event given the respective pdf f. The resulting histogram is shown by the green curve in Fig. 7.5 where the x-axis shows the logarithm of the likelihood ratio. Following the same steps, we create a set of samples $\{\{y_i\}_{i=1,\ldots,N_{\mathrm{tot}}}\}$ distributed according to $f_{\mathrm{nHs+b}}$ and calculate the likelihood ratio for each sample $\{y_i\}_{i=1,\ldots,N_{\mathrm{tot}}}$,

$$Q_{N_{\mathrm{nHs}}} = \prod_{i=1}^{N_{\mathrm{tot}}} \frac{p(y_i|f_{\mathrm{nHs+b}})}{p(y_i|f_{\mathrm{Hs+b}})}. \tag{7.9}$$

We obtain the distribution of the alternative hypothesis H_1 shown by the blue histogram in Fig. 7.5. We determine the 1.28σ value of the $Q_{N_{\mathrm{Hs}}}$ distribution that corresponds to the one-sided 90%

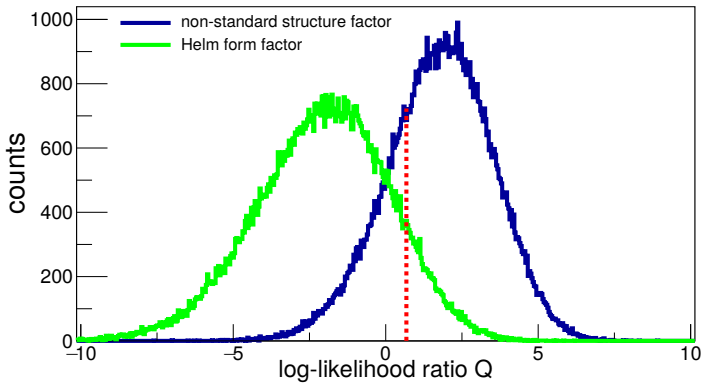

Figure 7.5: Log-likelihood ratio distributions for the null distribution (green, based on the Helm form factor) and the alternative distribution (blue, based on a non-standard structure factor) [244]. Marked in red is the $1.28\,\sigma$ line for the null distribution. The discriminating power is given by integrating the alternative distribution from the reference red line towards infinity. In this case this yields a discrimination power of 74%.

quantile, see Fig. 7.5. Now we calculate the probability with which an experiment will be able to conclude correctly that the measured signals stem from a non-Helm distribution by integrating the distribution of $Q_{N_{\mathrm{nHs}}}$ starting from the 1.28σ line of the null distribution. In the example shown in Fig. 7.5 we find 74% of the entries of the histogram of $Q_{N_{\mathrm{nHs}}}$ above the 1.28σ limit of the H_0 hypothesis. Hence, in 74% of the cases it would be possible to distinguish the non-Helm response from the Helm response in this example. In the following, we will refer to this probability as "discrimination power".

Similarly, we analyse if the non-standard response can also be distinguished from pure background. In this case, the null hypothesis H_0 would be a background-only model while the H_1 hypothesis is again given by the respective non-Helm form factors.

7.2.4 Results

We determine the discrimination power for three different experimental setups, i.e., XENON1T, XENONnT, and the most sensitive case, the planned DARWIN detector, which will cover the full experimentally accessible parameter space. For the WIMP mass we take $m_\chi = 10\,\mathrm{GeV}$, $m_\chi = 100\,\mathrm{GeV}$, and $m_\chi = 1\,\mathrm{TeV}$ into account. Furthermore, for the SI cross section $\sigma^{\mathrm{SI}}_{\chi\mathcal{N}}$ we take values that are in agreement with current experimental limits. If we find that a discrimination is possible, we continue to lower the value of $\sigma^{\mathrm{SI}}_{\chi\mathcal{N}}$ until a discrimination is no longer possible. As starting values we took $\sigma_0 = 10^{-46}\,\mathrm{cm}^2$ for $m_\chi = 100\,\mathrm{GeV}$ and $\sigma_0 = 10^{-45}\,\mathrm{cm}^2$ for $m_\chi = 1\,\mathrm{TeV}$. In addition, we varied the exposure for a XENON1T-like experiment up to 10 ton years, for a XENONnT-like experiment up to 30 ton years, and for a DARWIN-like experiment up to 200 ton years.

We find that for very light WIMPs of $m_\chi = 10\,\mathrm{GeV}$ for no combination of experiment, cross section $\sigma^{\mathrm{SI}}_{\chi\mathcal{N}}$ and exposure it is possible to discriminate between the non-Helm responses and the standard SI response. This is because for $m_\chi = 10\,\mathrm{GeV}$ the search window is extremely small as shown in Fig. 7.3.

m_χ	100 GeV		1 TeV	
$\sigma_0\,[\mathrm{cm}^2]$	10^{-46}	10^{-47}	10^{-45}	10^{-46}
$\lvert\mathcal{F}_-^M\rvert^2$	17	10	21	11
$q^2/4m_\chi^2\lvert\mathcal{F}_+^M\rvert^2$	94	19	98	20
$q^2/4m_\chi^2\lvert\mathcal{F}_-^M\rvert^2$	74	16	90	17
$q^4/m_N^4\lvert\mathcal{F}_+^M\rvert^2$	100	25	100	28
$q^4/m_N^4\lvert\mathcal{F}_-^M\rvert^2$	100	23	100	25
$\lvert\mathcal{F}_\pi\rvert^2$	38	13	48	14
$q^4/4m_N^4\lvert\mathcal{F}_+^{\Phi''}\rvert^2$	100	26	100	30
$q^4/4m_N^4\lvert\mathcal{F}_-^{\Phi''}\rvert^2$	100	25	100	29

Table 7.1: Discrimination power (in %) of the XENON1T settings after 10 ton years of exposure.

m_χ	100 GeV			1 TeV		
$\sigma_0\,[\mathrm{cm}^2]$	10^{-46}	10^{-47}	10^{-48}	10^{-45}	10^{-46}	10^{-47}
$\lvert\mathcal{F}_-^M\rvert^2$	37	13	10	21	15	11
$q^2/4m_\chi^2\lvert\mathcal{F}_+^M\rvert^2$	100	59	14	100	71	15
$q^2/4m_\chi^2\lvert\mathcal{F}_-^M\rvert^2$	100	39	13	100	53	13
$q^4/m_N^4\lvert\mathcal{F}_+^M\rvert^2$	100	90	16	100	95	17
$q^4/m_N^4\lvert\mathcal{F}_-^M\rvert^2$	100	81	15	100	87	16
$\lvert\mathcal{F}_\pi\rvert^2$	89	23	12	98	28	12
$q^4/4m_N^4\lvert\mathcal{F}_+^{\Phi''}\rvert^2$	100	93	17	100	98	19
$q^4/4m_N^4\lvert\mathcal{F}_-^{\Phi''}\rvert^2$	100	89	17	100	96	17

Table 7.2: Discrimination power (in %) of a XENONnT-like experiment after 30 ton years of exposure.

m_χ	100 GeV			1 TeV		
$\sigma_0\,[\mathrm{cm}^2]$	10^{-46}	10^{-47}	10^{-48}	10^{-45}	10^{-46}	10^{-47}
$\lvert\mathcal{F}_-^M\rvert^2$	94	26	12	100	35	13
$q^2/4m_\chi^2\lvert\mathcal{F}_+^M\rvert^2$	100	100	34	100	100	41
$q^2/4m_\chi^2\lvert\mathcal{F}_-^M\rvert^2$	100	98	25	100	100	32
$q^4/m_N^4\lvert\mathcal{F}_+^M\rvert^2$	100	100	55	100	100	63
$q^4/m_N^4\lvert\mathcal{F}_-^M\rvert^2$	100	100	47	100	100	53
$\lvert\mathcal{F}_\pi\rvert^2$	100	66	17	100	81	20
$q^4/4m_N^4\lvert\mathcal{F}_+^{\Phi''}\rvert^2$	100	100	58	100	100	69
$q^4/4m_N^4\lvert\mathcal{F}_-^{\Phi''}\rvert^2$	100	100	55	100	100	64

Table 7.3: Discrimination power (in %) of a DARWIN-like experiment after 200 ton years of exposure.

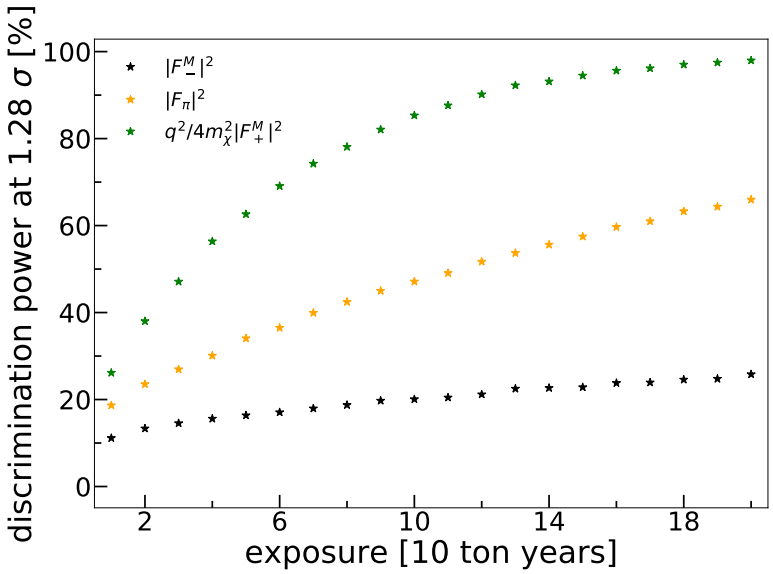

Figure 7.6: Discrimination power vs. exposure for three selected structure factors, $|\mathcal{F}_-^M|^2$ (black), $|\mathcal{F}_\pi|^2$ (orange), and $q^2/4m_\chi^2|\mathcal{F}_-^M|^2$ (green) [244]. The detector setting is DARWIN-like, with $m_\chi = 100\,\text{GeV}$ and $\sigma_0 = 10^{-47}\,\text{cm}^2$.

Figure 7.6 shows the discrimination power as a function of the exposure for $|\mathcal{F}_-^M|^2$, $|\mathcal{F}_\pi|^2$, and $q^2/4m_\chi^2|\mathcal{F}_-^M|^2$ based on the configuration of a DARWIN-like experiment using $m_\chi = 100\,\text{GeV}$ and $\sigma_{\chi\mathcal{N}}^{\text{SI}} = 10^{-47}\,\text{cm}^2$. The isovector M response is least distinguishable with only 26% even after full exposure of 200 ton years. The reason is its q-dependence similar to the standard isoscalar M response $|\mathcal{F}_+^M|^2$ as shown in Fig. 7.3. Distinction of the isoscalar and isovector M responses therefore requires most likely different target nuclei differing in their respective proton-to-neutron ratios. The latter vary between 0.6 for xenon to 1.0 for silicon. For the scalar two-body response $|\mathcal{F}_\pi|^2$, we find a higher discrimination power of up to 66% after full exposure. However, the best distinguishability of 98% is reached for $q^2/4m_\chi^2|\mathcal{F}_-^M|^2$, which can be explained by the fact that its response function vanishes at $q = 0$ leading to a shape as a function of q very different from $|\mathcal{F}_+^M|^2$ (see again Fig. 7.3). In general, the responses that vanish at $q = 0$ can be expected to be the easiest to distinguish as can be seen in Tables 7.1, 7.2, and 7.3, which summarize our results for each of the different experimental settings and WIMP masses of $m_\chi = 100\,\text{GeV}$, and $m_\chi = 1\,\text{TeV}$. A very exciting result is that if a WIMP signal is observed in the next XENON1T run that corresponds to a SI cross section slightly larger than the present limit of $\sigma_{\chi\mathcal{N}}^{\text{SI}} \sim 10^{-46}\,\text{cm}^2$ for $m_\chi = 100\,\text{GeV}$ or $\sigma_{\chi\mathcal{N}}^{\text{SI}} \sim 10^{-47}\,\text{cm}^2$ for $m_\chi = 1\,\text{TeV}$, there is a good chance to distinguish a signal that vanishes at $q = 0$ (see Table 7.1). For the same values of $\sigma_{\chi\mathcal{N}}^{\text{SI}}$ and m_χ, XENONnT would be able to discriminate $|\mathcal{F}_\pi|^2$ in addition, see Table 7.2. A full discrimination of all responses would, however, require a DARWIN-like experiment, see Table 7.3. If the cross section is lowered even further to $10^{-47}\,\text{cm}^2$ for $m_\chi = 100\,\text{GeV}$ and $10^{-46}\,\text{cm}^2$ for $m_\chi = 1\,\text{TeV}$, only the future XENONnT will have a chance to discriminate between standard SI and the responses suppressed by powers of q. A better performance is reached by a DARWIN-like experiment, which in turn is also able to distinguish the $|\mathcal{F}_\pi|^2$ with a 66% chance. When the cross section is lowered again by an order of magnitude, only the DARWIN detector retains some discrimination power.

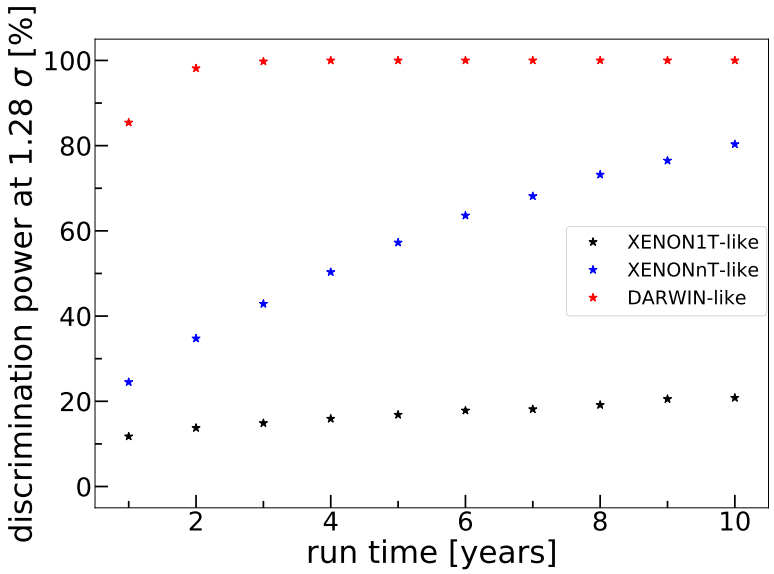

Figure 7.7: Comparison of the discrimination power during the run time of the three different experimental settings [244]. For XENON1T-like (black) a fiducial target of 1 ton is assumed, for the XENONnT-like setting (blue) a 4 ton fiducial target, and for the DARWIN-like setting (red) we assumed 30 ton fiducial volume. The signal is distributed using the structure factor $q^2/4m_\chi^2|\mathcal{F}_+^M|^2$, a WIMP mass $m_\chi = 1\,\text{TeV}$, and the mean number of events equivalent to $\sigma_0 = 10^{-46}\,\text{cm}^2$.

In Fig. 7.7, we compare the different experiments by showing their discrimination power as a function of run time for the $q^2/4m_\chi^2|\mathcal{F}_+^M|^2$ response. While even after 10 years of run time the XENON1T experiment only reaches a 20% chance of being able to distinguish the response from the standard SI assumption, we find that after the same run time XENONnT reaches 80%. For DARWIN a run time of only three years is sufficient to reach a confidence level of almost 100%.

We want to point out that the results presented in Tables 7.1, 7.2, and 7.3 do not comprise the discrimination power with respect to a pure background signal. For all responses, except the ones suppressed by q^4, the discrimination power for the non-Helm structure factors in comparison to the pure background signal hypothesis is larger than the one with respect to the background-only model. However, in case of $q^4/4m_N^4|\mathcal{F}_\pm^{\Phi''}|^2$, it turns out that the ability to discriminate is greater for H_0 being the Helm form factor plus background hypothesis than for the background only case as shown in Fig. 7.8. This observation has a huge impact on possible interpretations of direct detection limits. A true dark matter signal originating from a $q^4/4m_N^4|\mathcal{F}_\pm^{\Phi''}|^2$ interaction could be rejected based on the assumption of a standard SI WIMP-nucleon coupling. This highlights how important the study of subleading responses is not only for the extraction of WIMP properties provided a detection of a signal but even for setting limits on possible WIMP-nucleon cross sections. The worst case scenario could be that a signal is missed just due to the limitation of the analysis to the standard Helm form factor.

The study has shown that both current and future liquid xenon direct detection experiments are in principle able to discriminate the leading coherent responses from the standard SI response based on the q-dependence of their respective structure factors. While in the discussion above we

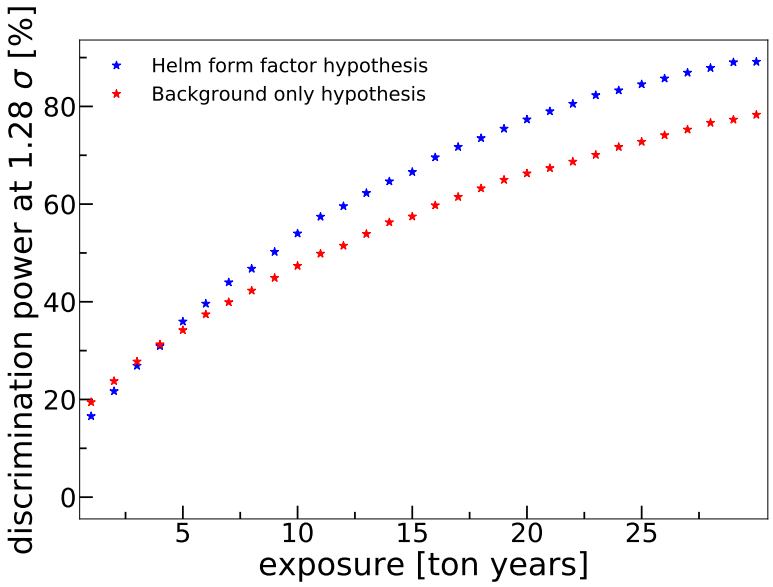

Figure 7.8: Comparison of the discrimination power of XENONnT for a signal based on the structure factor $q^4/4m_N^4|\mathcal{F}_-^{\Phi''}|^2$ vs. the Helm form factor signal (blue) and for the same signal vs. a background-only hypothesis (red) [244]. Here $\sigma_0 = 10^{-47}\text{cm}^2$ and $m_\chi = 100\,\text{GeV}$.

only mention three experiments in particular, we want to stress that the generic term "XENONnT-like" represents also other dual-phase xenon detectors with similar sensitivity.

As expected, the discrimination power depends mostly on the different shapes of the structure factors as a function of the momentum transfer q. Similarly important is the kinematically allowed range of momentum transfers q. As discussed above, for a light WIMP of $m_\chi = 10\,\text{GeV}$ the range is too small to allow for any discrimination by any of the considered experimental setups. On the other hand, for both $m_\chi = 100\,\text{GeV}$ and $m_\chi = 1\,\text{TeV}$ we found that even the present XENON1T configuration might be able to distinguish different channels from the standard SI response, provided the WIMP-nucleon cross section is just below the present limits. Both XENONnT-like and DARWIN-like experiments with their higher sensitivities exceed the discrimination power of XENON1T significantly. However, only a DARWIN-like experiment would allow a conclusive discrimination of the response functions considered if the interaction strength does lie two orders of magnitude below the current limits. It has to be kept in mind that the assumptions from which the background rate is derived are rather conservative. Therefore, the discrimination power is most likely underestimated for all experiments. In the future, when refined sensitivity and background models are available, the question could therefore be reassessed.

The most challenging response to distinguish from the standard Helm interaction was found to be the $|\mathcal{F}_-^M|^2$ response. A strategy to overcome the deficiencies concerning this interaction would be to combine experimental data from different nuclear targets with different proton-to-neutron ratios. Such an analysis could also help to identify SD interactions, which, however, require isotopes with at least one odd numbered species of either neutrons or protons. In addition, the analysis of the inelastic channel can help to distinguish between SI and SD interactions [141, 142].

Finally, it was found that in some cases the Helm form factor hypothesis is better distinguished than the background-only case from the non-Helm form factors. This is the case for all channels of our study that are suppressed by q^4. Therefore, a signal originating from such an interaction type could be missed if only the standard SI channel is considered in an analysis of the results. This motivates again the inclusion of alternative channels in the analyses of future experiments.

8 Conclusions

In the first part of this thesis, we have studied various few-neutron systems. In AFDMC calculations of two neutrons in a finite volume, we were able to extract both the ground and first excited states for a contact potential and local chiral EFT interactions. From these results, we were able to extract the scattering length and effective range by fitting the finite-volume energy levels using Lüscher's formula for scattering states in a cubic volume with periodic boundary conditions. We found good agreement with scattering data extracted directly from infinite-volume calculations, which demonstrates the viability of the AFDMC method for finite-volume calculations at very low densities. As the excited states are challenging to access in QMC calculations, we resorted to an approximate method based on an iterative determination of the nodal surface of the excited-state wave functions. In order to benchmark our approximate calculations, we performed a direct diagonalization of the system and extracted the exact nodal surfaces. This allowed us to improve the AFDMC calculations via nonspherical nodal surfaces. Generalizing this technique to higher-body systems presents a challenge that requires further research.

Our calculations of two neutrons interacting with chiral EFT forces in finite volume present first steps toward a strategy to construct nuclear forces based on QCD results. In the future, matching the finite-volume energy levels to lattice QCD results might allow for a direct determination of chiral LECs without the necessity of extracting the infinite-volume phase shifts via the Lüscher formula. As we showed in our calculations, corrections to the Lüscher results become relevant for small volumes, i.e., large momenta, where pion exchanges become relevant such that a direct matching becomes advantageous. In addition, the direct matching strategy is straightforwardly applicable to many-body systems.

Possible few-neutron resonances were studied in this thesis by performing AFDMC calculations of three and four neutrons artificially bound in an external potential well. We extrapolated to the zero well depth limit in order to extract resonance energies for these systems. For a resonant two-particle S-wave potential we found this method to yield accurate results. In a next step, we found the extracted resonance energy for the four-neutron system in agreement with recent experimental results. Furthermore, we find that there is possibly a resonant three-neutron system lower in energy than the four-neutron resonance. However, the method applied does not provide an estimate for the width of the many-body resonances. Also, in our calculations it cannot be excluded that the extracted energies correspond to virtual states. Therefore, it is not possible to judge if those states could be observed in an experiment. In addition, our study provided evidence that the few-neutron systems are very dilute. This hints at the possibility of future experiments with ultracold atomic Fermi gases that might be able to simulate analogous few-fermion systems.

In view of the large variety of theoretical results on a possible tetraneutron resonance, including the QMC-based study presented in this thesis, we investigated an alternative approach to extract many-body resonance properties based on finite-volume calculations. Similar to the two-body case, we show that many-body resonance properties can be inferred from the volume dependence of finite-volume energy spectra. We establish the DVR method as an efficient method to allow

for calculations in very large volumes where the number of basis states required in order to reach convergence becomes very large. For resonant two- and three-particle systems, we show that resonance energies extracted from the plateaus between avoided level crossings are in agreement with results obtained in infinite-volume calculations. In addition, we show for the first time that genuine three- and four-body resonances, which couple to asymptotic three- and four-particle states, appear as avoided level crossings in the corresponding finite-volume spectra. This contributes to formal work in this sector currently investigating system of more than two particles in a finite volume. Our results can serve as a benchmark once the corresponding formalism for resonant few-particle systems is derived. In the future, this method might allow for the extraction of resonance energies in few-neutron systems as well as studies of multi-body resonances in systems such as the Hoyle state in ^{12}C. Computational limitations relevant at very large box sizes can be improved by replacing periodic boundary conditions by twisted boundary conditions, which shift the discrete energy levels such that the avoided crossings might appear at smaller box sizes [211]. Calculations of light nuclei would require the implementation of isospin degrees of freedom, which is straightforward to do. However, the scaling of our DVR method would suffer.

In the second part of this thesis, we calculated nuclear structure factors for WIMP-nucleus interactions based on the framework of chiral EFT. We have studied the chiral power counting of various WIMP-nucleon interaction types in terms of scalar, pseudoscalar, vector, and axial-vector operators derived in chiral EFT at the one- and two-body level. As we have shown, only the inclusion of nuclear structure effects, such as the coherent enhancement we observed for some interaction channels, allows one to establish a hierarchy among the different responses. We have found that the dominant corrections to the standard isoscalar spin-independent response are its isovector correspondent as well as coherent contributions from different two-body currents that reflect the coupling of WIMPs to pions exchanged between interacting nucleons. Based on our results, we propose an extension of the standard spin-independent analysis by including the dominant corrections. Future analyses of direct detection experiments will be able to set limits on the WIMP couplings that correspond to these new channels. In particular, it is possible to constrain the WIMP-pion couplings using our structure factors of the scalar two-body interactions.

While we performed these calculations for the one-body operators using the interacting shell model, we evaluated the two-body operators between nuclear states obtained by naively filling the lowest orbitals of the shell model. Evaluating the two-body operators exactly between the nuclear states calculated in the interacting shell model requires the derivation of representations of the WIMP-nucleon operators that act on single-particle harmonic-oscillator states. On the other hand, the calculation of the structure factors presented in this thesis can be considered hybrid in the sense that the interaction used for the calculation of the nuclear wave functions and the framework used for the derivation of the WIMP-nucleon operators is inconsistent. A more consistent picture can be reached by using chiral EFT interactions in modern *ab initio* many-body methods such as the in-medium SRG, which has been successfully applied to calculate nuclear spectra in the medium-mass region of the nuclear chart [164]. This requires a consistent SRG evolution of the WIMP-nucleon operators. An additional advantage of such *ab initio* calculations would be that uncertainties stemming from both the many-body method and the nuclear interactions and currents can in principle be estimated.

Finally, we have presented two applications of the structure factors of the different WIMP-nucleus interactions. We have shown how nuclear physics input improves limits on the WIMP-

nucleon cross section obtained in collider searches for Higgs-portal dark matter. By including the relevant two-body currents derived in chiral EFT, we have provided improved results for those limits. In addition, we investigated to what extent the subleading coherent WIMP-nucleon interaction channels can be distinguished from the standard spin-independent interaction by their respective momentum dependence provided a signal is found in a direct detection experiment. As expected, we found the discrimination power to be correlated with the difference in shape of the structure factors as a function of the momentum transfer. Our study showed that while the XENON1T experiment would only be able to distinguish different channels when the cross section is close to current limits, future experiments like XENONnT or DARWIN will likely be able to discriminate the subleading responses from the spin-independent case for significantly smaller cross sections. Remarkably, we find that in some cases a dark matter signal could be missed when constraining the analysis to the standard spin-independent channel, motivating the inclusion of other WIMP-nucleus interaction channels in the analysis of dark matter direct detection experiments.

Acknowledgements

First, I want to thank my advisor Achim Schwenk. He has always provided excellent guidance right from my very early days in the scientific world. His knowledge of and intuition for physics have always been very impressive. I am grateful for the opportunities I have been given to participate in various conferences and meetings. Also, I would like to thank Hans-Werner Hammer for his insights and ideas that helped me in my research.

At least similarly important for my work were the group of talented postdocs I had the pleasure to work with: Sebastian König and Joel Lynn accompanied me on my adventures in the box. Martin Hoferichter and Javier Menéndez led me through the dark in our WIMP project. I want to express my sincere gratitude to all of the aforementioned for supporting me throughout my research and for giving their time so generously.

Next, I want to thank the people who I had the opportunity to work with on various different projects. Crucial for the QMC projects in my thesis were Stefano Gandolfi, Alexandros Gezerlis, and Ingo Tews. I thank Alexander Fieguth and Christian Weinheimer from the XENON1T collaboration for our successful collaboration. I also want to thank Steven Bilaj and Sebastian Dietz who contributed to my research during their B.Sc. projects. I am also grateful to Arianna Carbone and Kai Hebeler who worked with me on the endless triton project. Not forgotten should be Kyle Wendt who provided helpful ideas various times.

I would also like to thank my office mates Thomas Krüger, Stefan Schulz, Rodric Seutin, Klaus Vobig, and Lars Zurek. I enjoyed very much discussing physics as well as non-physics topics with you. In particular, I thank Stefan and Klaus and also Roland Wirth for helping out whenever I struggled with coding issues.

Also, I want to thank my colleagues Alexander Bartl, Toño Coello Pérez, Christian Drischler, Victoria Durant, Svenja Greif, Jan Hoppe, Lukas Huth, Maximilian Jacobi, Sabrina Schäfer, Marc Schönborn, Johannes Simonis, and Corbinian Wellenhofer for the pleasant atmosphere in the group.

I am also grateful for the funding received from the European Research Council by the ERC Grant No. 307986 STRONGINT.

With a special mention to the “coffee crew”, Christian Appel, Thorsten Haase, Marc Leonhardt, Martin Pospiech, and Lukas Rammelmüller, and also to Patrick Salg. This time of my life would not have been as much fun without you guys.

Finally, I want to thank my parents and my brother for all their support and the ongoing discussions about dark matter. Most importantly, I am grateful to my wife Sabrina for supporting me throughout my graduate studies and beyond, for motivating me when I was struggling and even more for being by my side every day.

Danke, Frieda, dass du da bist.

A Details concerning the Lüscher formula

A.1 Evaluation of $S(\eta)$

The definition of $S(\eta)$ that appears in Eq. (2.13) can be evaluated numerically; however, in practice it converges relatively slowly. A more efficient approach used in Ref. [4] relies on Poisson's summation formula as well as the fact that $S(\eta)$ equals the analytic continuation of

$$Z_{00}(s,\eta) = \sum_{\mathbf{j}} \frac{1}{(\mathbf{j}^2-\eta)^s}, \qquad \mathrm{Re}\, s > \frac{3}{2}, \tag{A.1}$$

for $s \to 1$, which leads to

$$\begin{aligned} S(\eta) = &\sum_{\mathbf{j}^2<\eta} \frac{1}{\mathbf{j}^2-\eta} + \int_0^1 \mathrm{d}t\, F_{00}^1(t,\eta) \\ &+ \int_1^\infty \mathrm{d}t\, F_{00}(t,\eta) + \sum_{i=0}^{1} \left(\frac{A_i}{i+1} + \frac{B_i}{i-\frac{1}{2}} \right), \end{aligned} \tag{A.2}$$

where

$$\begin{aligned} F_{00}^1(t,\eta) =& -\sum_{\mathbf{j}^2\leqslant\eta} e^{t(\eta-\mathbf{j}^2)} + \left(\frac{\pi}{t}\right)^{3/2} e^{t\eta} \sum_{\mathbf{j}} e^{-\frac{\pi^2}{t}\mathbf{j}^2} \\ &- \sum_{i=0}^{1} (A_i t^i + B_i t^{i-3/2}), \\ F_{00}(t,\eta) =& \sum_{\mathbf{j}^2>\eta} e^{-t(\mathbf{j}^2-\eta)}, \\ A_i =& -\frac{1}{i!} \sum_{\mathbf{j}^2\leqslant\eta} (\eta-\mathbf{j}^2)^i, \\ B_i =& \pi^{3/2} \frac{\eta^i}{i!}. \end{aligned} \tag{A.3}$$

This representation accelerates convergence exponentially and can be easily implemented by using standard integration routines.

A.2 Lüscher formula and G-wave admixtures

We constrain ourselves to stating only the main results relevant for the evaluation of the G-wave contributions to the energy levels in a finite volume. For S-wave scattering the Lüscher formula can also be written as [4, 5]

$$e^{2i\delta_0} = \frac{m_{00}+i}{m_{00}-i}\,, \tag{A.4}$$

where, using the Zeta function Z_{00} as in Eq. (A.1),

$$m_{00} = \frac{1}{2\pi^2 q} Z_{00}(1;q^2), \quad q = \frac{kL}{2\pi}\,. \tag{A.5}$$

The Lüscher formula including G-waves reads

$$(e^{2i\delta_0}-u_{00})(e^{2i\delta_4}-u_{44}) = u_{04}^2\,, \tag{A.6}$$

where

$$\begin{aligned} u_{00} &= [(m_{00}+i)(m_{44}-i)-m_{04}^2]/\Delta\,,\\ u_{44} &= [(m_{00}-i)(m_{44}+i)-m_{04}^2]/\Delta\,,\\ u_{04} &= u_{40} = -2im_{04}/\Delta\,,\\ \Delta &= (m_{00}-i)(m_{44}-i)-m_{04}^2\,. \end{aligned} \tag{A.7}$$

The matrix elements m_{04} and m_{44} in terms of the Zeta functions Z_{lm} [4] are given by

$$\begin{aligned} m_{04} &= \frac{3\sqrt{21}}{7}\frac{1}{\pi^2 q^5} Z_{40}(1;q^2)\,,\\ m_{44} &= \frac{1}{\pi^2}\left(\frac{1}{2}q^{-1}Z_{00} + \frac{162}{143}q^{-5}Z_{40} + \frac{40}{11}q^{-7}Z_{60} + \frac{280}{143}q^{-9}Z_{80}\right). \end{aligned} \tag{A.8}$$

Solving Eq. (A.6) yields the finite volume energies in terms of q.

B Particles in a box with periodic boundary conditions

B.1 From single-particle coordinates to relative coordinates

The dimensions of the problem of interacting particles in a box with periodic boundary conditions can be significantly reduced by rewriting the states and the potential in terms of relative coordinates. We start from the single-particle wave function for two particles in one dimension,

$$\psi_{n_1 n_2}(r_1, r_2) = N \exp\left(\mathrm{i}\frac{2\pi}{L} n_1 r_1\right) \exp\left(\mathrm{i}\frac{2\pi}{L} n_2 r_2\right). \tag{B.1}$$

Relative coordinates are given by

$$\begin{aligned} r &= r_1 - r_2\,, & r_1 &= \frac{r}{2} + R\,, \\ R &= \frac{1}{2}(r_1 + r_2)\,, & r_2 &= -\frac{r}{2} + R\,, \end{aligned} \tag{B.2}$$

and the wave function can be rewritten as

$$\psi_{n_1 n_2}(r, R) = N \exp\left(\mathrm{i}\frac{2\pi}{L}(n_1 - n_2)\frac{r}{2}\right) \exp\left(\mathrm{i}\frac{2\pi}{L}(n_1 + n_2)R\right), \tag{B.3}$$

where we can identify the center-of-mass momentum as $P = \frac{2\pi}{L}(n_1 + n_2)$. Even though the single particle wave functions obey periodic boundary conditions the relative wave function does not:

$$\psi_{n_1 n_2}(r + nL, R) = \exp\left(\mathrm{i}P\frac{nL}{2}\right)\psi_{n_1 n_2}(r, R)\,, \tag{B.4}$$

where n is an integer. Obviously, for $P = 0$ the relative wave function obeys periodic boundary conditions again.

Now for the calculation of matrix elements, especially potential matrix elements, we can make use of the formulation in relative coordinates. However, one has to keep in mind that this is only possible due to the fact that we have periodic boundary conditions and therefore the distance between two particles is always the minimum of the distance between the two particles which lays

within the box and the distance going through the wall. In order to illustrate this we start from the two particle system. The overlap integrals are of the form

$$\int_0^L \int_0^L \mathrm{d}r_1\, \mathrm{d}r_2\, f(|r_1 - r_2|_{\mathrm{pbc}}), \tag{B.5}$$

where

$$|r_1 - r_2|_{\mathrm{pbc}} = |r_1 - r_2 - L\,\mathrm{Round}((r_1 - r_2)/L)|, \tag{B.6}$$

where the function $\mathrm{Round}(x)$ gives the integer closest to a real number x. Note that the value of the integral is indeed different if we take the simple absolute value of the difference of the particles' coordinates. However, here it is possible to rewrite the integral in terms of relative coordinates

$$\iint_0^L \mathrm{d}r_1\, \mathrm{d}r_2\, f(|r_1 - r_2|_{\mathrm{pbc}}) = L \int_{-\frac{L}{2}}^{\frac{L}{2}} \mathrm{d}x\, f(x). \tag{B.7}$$

Note the change in the boundaries of the integral. To understand why the periodic boundary conditions are necessary for the identity think about it this way: For every position of r_1 it is possible to have the distance between the two particles to be in the interval $[-\frac{L}{2}, \frac{L}{2}]$, hence, it is equivalent to integral one single time over this interval and multiply the whole integral by L.

Now, for three particles the situation is more involved but performing the same steps as above we find

$$\begin{aligned} &\iiint_0^L \mathrm{d}r_1\, \mathrm{d}r_2\, \mathrm{d}r_3\, f_1(|r_1 - r_2|_{\mathrm{pbc}}) f_2(|r_2 - r_3|_{\mathrm{pbc}}) f_3(|r_1 - r_3|_{\mathrm{pbc}}) \\ &= L \iint_0^L \mathrm{d}x\, \mathrm{d}y\, f_1(|x - y|_{\mathrm{pbc}}) f_2(y) f_3(x). \end{aligned} \tag{B.8}$$

Note that for the distance of the first and second particle $r_1 - r_2 = x - y$ we still need take explicitly the distance in as in Eq. (B.6).

For a system of n particles of the same mass with coordinates $r_1, \ldots, r_n$ a set of relative coordinates is defined by

$$\begin{aligned} x_i &= r_n - r_i, \qquad i \in \{1, \ldots, n-1\}, \\ R &= \frac{1}{n} \sum_i r_i, \end{aligned} \tag{B.9}$$

where we have $n-1$ relative coordinates and the center-of-mass coordinate R. The Laplacian, which up to a constant factor defines the kinetic energy operator T, is then given by

$$\Delta = \sum_i^n \frac{\partial^2}{\partial r_i^2} = 2\sum_i^{n-1} \frac{\partial^2}{\partial x_i^2} + \frac{1}{n}\frac{\partial^2}{\partial R^2}\,. \tag{B.10}$$

As we are only interested in the energy of the system in the center-of-mass frame we will neglect the derivative with respect to R in all applications.

B.2 Diagonalization of the two-particle system

Here we show how to solve the two-particle-in-a-box problem by diagonalizing the Hamiltonian in a basis of appropriate functions as used in Sec. 2.3.2. The most general two-body wave function in a one-dimensional box of size L with periodic boundary conditions is given by plane wave states:

$$\psi_{n_1,n_2}(r_1,r_2) = N\exp\left(\mathrm{i}\frac{2\pi}{L}n_1 r_1\right)\exp\left(\mathrm{i}\frac{2\pi}{L}n_2 r_2\right). \tag{B.11}$$

We are only interested in states with total momentum equal to zero. Hence, $n_1 = -n_2$ and

$$\psi_n(r_1,r_2) = N\exp\left(\mathrm{i}\frac{2\pi}{L}n(r_1-r_2)\right), \tag{B.12}$$

which corresponds to Eq. (B.3) with $P=0$. As we are looking for S-wave states the wave function has to have even parity in coordinate space. Therefore we choose:

$$\psi_n(r_1,r_2) = \frac{\sqrt{2-\delta_{0n}}}{L}\cos\left(\frac{2\pi}{L}n(r_1-r_2)\right). \tag{B.13}$$

The matrix elements which need to be evaluated are of the form

$$\langle\psi_n|V|\psi_m\rangle = \int_{-L/2}^{L/2}\int_{-L/2}^{L/2} \mathrm{d}r_1\mathrm{d}r_2\,\psi_n(r_1,r_2)V(|r_1-r_2|_{\mathrm{pbc}})\psi_m(r_1,r_2)\,. \tag{B.14}$$

where $|r_1-r_2|_{\mathrm{pbc}}$ is defined in Eq. (B.6) and we rewrite the integral in relative coordinates (see Eq. (B.7))

$$\langle\psi_n|V|\psi_m\rangle = L\int_{-L/2}^{L/2} \mathrm{d}r\,\psi_n(r)V(r)\psi_m(r) \tag{B.15}$$

The extension of the wave function to three dimension is straight forward:

$$\psi^{\mathrm{3D}}_{nmk}(\mathbf{r}) = \psi_n(x)\psi_m(y)\psi_k(z)\,,$$
$$\psi_n(x) = \sqrt{\frac{2-\delta_{0n}}{L}}\cos\!\left(\frac{2\pi}{L}nx\right), \tag{B.16}$$

where $n = 0,1,2,\ldots$ and $\mathbf{r} = \mathbf{r}_1 - \mathbf{r}_2$. The basis size has to be constrained by setting an upper bound for the momenta in each direction, i.e., $n,m,k < N_{\max}$. Further reduction of the basis size can be reached by constraining the total kinetic energy, i.e., $n^2+m^2+k^2 < N^2_{\max}$.

For a potential which factorizes in terms which dependent solely on one direction, e.g., $V(r) \propto \exp\!\left(-r^2\right)$, the integration can be factorized, i.e., independent calculations of the integrals in x, y and z directions are possible. However, if the potential mixes the different coordinates the integration becomes more involved as one has to perform multidimensional integrals. This is the case for the potentials considered in Chapter 2 which cannot be factorized into terms which only depend on either x,y,z. Thus, calculating the matrix elements for the potential amounts to evaluating

$$\langle\psi^{\mathrm{3D}}_{n_1m_1k_1}|V|\psi^{\mathrm{3D}}_{n_2m_2k_2}\rangle = L^3\int_{-L/2}^{L/2}\int_{-L/2}^{L/2}\int_{-L/2}^{L/2}\mathrm{d}x\,\mathrm{d}y\,\mathrm{d}z\,\psi^{\mathrm{3D}}_{n_1m_1k_1}(x,y,z)V(x,y,z)\psi^{\mathrm{3D}}_{n_2m_2k_2}(x,y,z) \tag{B.17}$$

This integral can be evaluated efficiently using a fast Fourier transform (FFT). However, as the same coordinate appears in two cosine functions we introduce δ functions in order to recover the well-known form of a cosine transform,

$$\begin{aligned}\langle\psi^{\mathrm{3D}}_{n_1m_1k_1}|V|\psi^{\mathrm{3D}}_{n_2m_2k_2}\rangle = \left(\frac{2}{L}\right)^3&\int_{-L/2}^{L/2}\mathrm{d}x_1\,\mathrm{d}y_1\,\mathrm{d}z_1\,\mathrm{d}x_2\,\mathrm{d}y_2\,\mathrm{d}z_2\\
&\times\cos\!\left(\frac{2\pi}{L}n_1x_1\right)\cos\!\left(\frac{2\pi}{L}n_2x_2\right)\cos\!\left(\frac{2\pi}{L}m_1y_1\right)\cos\!\left(\frac{2\pi}{L}m_2y_2\right)\cos\!\left(\frac{2\pi}{L}k_1z_1\right)\cos\!\left(\frac{2\pi}{L}k_2z_2\right)\\
&\times V(x_1,y_1,z_1)\\
&\times\delta(x_1-x_2)\delta(y_1-y_2)\delta(z_1-z_2)\,.\end{aligned} \tag{B.18}$$

We use the library `FFTW3` [218] to perform the FFT. Since the potential is even around $x,y,z=0$ we choose the DCT-I (`FFTW_REDFT00`) option defined through

$$X_k = (x_0 + (-1)^k x_{N-1}) + 2\sum_{n=1}^{N-2} x_n\cos\!\left[\frac{\pi}{N-1}nk\right]. \tag{B.19}$$

The integral needs to be adapted to suit the FFT as defined above. We substitute $x' = \frac{2}{L}x$

$$\begin{aligned}\langle\psi^{\mathrm{3D}}_{n_1m_1k_1}|V|\psi^{\mathrm{3D}}_{n_2m_2k_2}\rangle =& 2^6\int_0^1 \mathrm{d}x_1'\,\mathrm{d}y_1'\,\mathrm{d}z_1'\,\mathrm{d}x_2'\,\mathrm{d}y_2'\,\mathrm{d}z_2' \\ &\times\cos\left(\pi n_1x_1'\right)\cos\left(\pi n_2x_2'\right)\cos\left(\pi m_1y_1'\right)\cos\left(\pi m_2y_2'\right)\cos\left(\pi k_1z_1'\right)\cos\left(\pi k_2z_2'\right) \\ &\times V\left(\frac{L}{2}x_1', \frac{L}{2}y_1', \frac{L}{2}z_1'\right) \\ &\times\delta(x_1'-x_2')\delta(y_1'-y_2')\delta(z_1'-z_2'),\end{aligned} \tag{B.20}$$

where we used $\delta(\frac{L}{2}(x_1'-x_2')) = \frac{2}{L}\delta(x_1'-x_2')$. Now we transform the integral into a discrete Fourier transform with $x_k = i_{x_k}/(N-1)$:

$$\begin{aligned}\langle\psi^{\mathrm{3D}}_{n_1m_1k_1}|V|\psi^{\mathrm{3D}}_{n_2m_2k_2}\rangle =& \frac{2^3}{(N-1)^6}\sum_{i_{x_1},i_{x_2},i_{y_1},i_{y_2},i_{z_1},i_{z_2}=0}^{N-1} \\ &\times\cos(\pi n_1x_1)\cos(\pi n_2x_2)\cos(\pi m_1y_1)\cos(\pi m_2y_2)\cos(\pi k_1z_1)\cos(\pi k_2z_2) \\ &\times V\left(\frac{L}{2}x_1, \frac{L}{2}y_1, \frac{L}{2}z_1\right) \\ &\times(N-1)^3\delta(x_1-x_2)\delta(y_1-y_2)\delta(z_1-z_2).\end{aligned} \tag{B.21}$$

Note that the integral was multiplied only by 2^3 when changing the integration boundaries since for the delta functions changing the boundaries does not change the value of the integral. Also, in the last row the delta functions were multiplied each with a factor of $N-1$ since

$$\int_{-1}^{1}\delta(x)\mathrm{d}x = 1 = \frac{1}{N}\sum_{i=1}^{N}N\delta(x_i). \tag{B.22}$$

Now we are in a position to apply the FFT in six dimensions. Note that there is an additional factor of 2 in Eq. (B.19) which needs to be canceled out:

$$\langle\psi^{\mathrm{3D}}_{n_1m_1k_1}|V|\psi^{\mathrm{3D}}_{n_2m_2k_2}\rangle = \frac{1}{(2(N-1))^3}\mathrm{FFT}\left(V\left(\frac{L}{2}x_1, \frac{L}{2}y_1, \frac{L}{2}z_1\right)\delta(x_1-x_2)\delta(y_1-y_2)\delta(z_1-z_2)\right). \tag{B.23}$$

Due to the factor of $1/2$ between the first and the second term in Eq. (B.19) when setting up the input array terms with $x, y, z = 0, L/2$ need to be multiplied with 2. This is because when the integral is transformed to the sum the delta functions are not multiplied by a factor (see Eq. (B.22)). When dividing by $N-1$ the pockets at x_0 and x_{N-1} have to be multiplied by two.

Even though the method described above allows for a fast evaluation of the necessary integrals through the FFT it requires arrays of the size $N_{\max}^6$ as in- and output for the FFT. This constrains calculations as memory is limited. Therefore, we want to rewrite the overlap intergrals in way that required less memory. We start from Eq. (B.21) and evaluate the delta functions:

$$\begin{aligned}\langle \psi^{3D}_{n_1 m_1 k_1} | V | \psi^{3D}_{n_2 m_2 k_2} \rangle =& \frac{2^3}{(N-1)^3} \sum_{i_x=0}^{N-1} \sum_{i_y=0}^{N-1} \sum_{i_z=0}^{N-1} \\ & \times \cos(\pi n_1 x) \cos(\pi n_2 x) \cos(\pi m_1 y) \cos(\pi m_2 y) \cos(\pi k_1 z) \cos(\pi k_2 z) \\ & \times V\left(\frac{L}{2}x, \frac{L}{2}y, \frac{L}{2}z\right). \end{aligned} \tag{B.24}$$

We exploit an addition theorem for the cosine as illustrated here in 1D:

$$\sum_{i_x=0}^{N-1} \cos(\pi n_1 x) \cos(\pi n_2 x) V\left(\frac{L}{2}x\right) = \frac{1}{2} \sum_{i_x=0}^{N-1} \Big[\cos(\pi x(n_1 - n_2)) + \cos(\pi x(n_1 + n_2))\Big] V\left(\frac{L}{2}x\right). \tag{B.25}$$

This results is already very similar to a discrete Fourier transform. When performing an FFT on the two terms we are constrained to $n_1 - n_2 \in \{0, \dots, N-1\}$ and $n_1 + n_2 \in \{0, \dots, N-1\}$. However, we want n_1 and n_2 to run from $0 \dots N_{\max}$ independently, which means $n_1 - n_2 \in \{-(N-1), \dots, N-1\}$ and $n_1 + n_2 \in \{0, \dots, 2(N-1)\}$. The former is easy to solve as

$$\mathrm{FFT}_{n_1 - n_2}(V) = \mathrm{FFT}_{n_2 - n_1}(V), \tag{B.26}$$

since cosine is even. For $n_1 + n_2$ the situation is more complicated. However, the missing subset $n_1 + n_2 \in \{N, \dots, 2(N-1)\}$ can be obtained by replacing $\cos(\pi x(n_1 + n_2))$ in Eq. (B.25) by

$$\begin{aligned}\cos\big(\pi x(n_1' + n_2' + N - 1)\big) &= \cos\left(\pi\left(\frac{i}{N-1}(n_1' + n_2') + i\right)\right) \\ &= \cos\big(\pi x(n_1' + n_2') + i\pi\big) \\ &= (-1)^i \cos\big(\pi x(n_1' + n_2')\big), \end{aligned} \tag{B.27}$$

with $n_1 + n_2 = n_1' + n_2' + N - 1$. Hence, the sum of the two cos can be evaluated using FFTs

$$= \frac{1}{2^2}\left[\mathrm{FFT}_{|n_1 - n_2|}(V) + \begin{cases} \mathrm{FFT}_{n_1+n_2}(V), & \text{if } n_1 + n_2 < N \\ \mathrm{FFT}_{n_1+n_2-(N-1)}((-1)^i V), & \text{if } n_1 + n_2 \geq N \end{cases}\right]. \tag{B.28}$$

Implementing this is of course a bit tedious as you have to map the FFTs results on the single particle states. However, as we will see it is not as bad as it might seem at this point. Let's look at the 3D case:

$$
\begin{aligned}
&\cos(\pi n_1 x)\cos(\pi n_2 x)\cos(\pi m_1 y)\cos(\pi m_2 y)\cos(\pi k_1 z)\cos(\pi k_2 z) \\
&= \left(\frac{1}{2}\right)^3 \Big[\cos(\pi x(n_1-n_2)) + \cos(\pi x(n_1+n_2))\Big] \\
&\qquad \times \Big[\cos(\pi y(m_1-m_2)) + \cos(\pi y(m_1+m_2))\Big] \\
&\qquad \times \Big[\cos(\pi z(k_1-k_2)) + \cos(\pi z(k_1+k_2))\Big] \\
&= \left(\frac{1}{2}\right)^3 \Big[\cos(\pi x(n_1-n_2))\cos(\pi y(m_1-m_2))\cos(\pi z(k_1-k_2)) \qquad \text{ooo} \\
&\qquad + \cos(\pi x(n_1-n_2))\cos(\pi y(m_1-m_2))\cos(\pi z(k_1+k_2)) \qquad \text{ooe} \\
&\qquad + \cos(\pi x(n_1-n_2))\cos(\pi y(m_1+m_2))\cos(\pi z(k_1-k_2)) \qquad \text{oeo} \\
&\qquad + \cos(\pi x(n_1-n_2))\cos(\pi y(m_1+m_2))\cos(\pi z(k_1+k_2)) \qquad \text{oee} \\
&\qquad + \cos(\pi x(n_1+n_2))\cos(\pi y(m_1-m_2))\cos(\pi z(k_1-k_2)) \qquad \text{eoo} \\
&\qquad + \cos(\pi x(n_1+n_2))\cos(\pi y(m_1-m_2))\cos(\pi z(k_1+k_2)) \qquad \text{eoe} \\
&\qquad + \cos(\pi x(n_1+n_2))\cos(\pi y(m_1+m_2))\cos(\pi z(k_1-k_2)) \qquad \text{eeo} \\
&\qquad + \cos(\pi x(n_1+n_2))\cos(\pi y(m_1+m_2))\cos(\pi z(k_1+k_2))\Big] \qquad \text{eee}
\end{aligned}
\tag{B.29}
$$

The labels "ooo" etc. refer to odd and even combinations of the quantum numbers n_1 and n_2 and so on. From this it becomes clear that there are only four different FFTs required: ooo, ooe, oee, and eee. For the even ones it has to be distinguished between the two regions for the sum of the two quantum numbers as in Eq. (B.28).

B.3 Jastrow wave function for nonspherical nodal surfaces

The Jastrow wave function $\psi_J(r)$ commonly used in QMC simulations is given by the solutions of the radial Schrödinger equation with the central part of the potential. The solutions are required to meet the following boundary conditions:

$$
\begin{aligned}
\psi_J(0) &= u_0\,, \\
\psi_J(L/2) &= 1\,, \\
\psi_J'(0) &= 0\,, \\
\psi_J'(L/2) &= 0\,,
\end{aligned}
\tag{B.30}
$$

where u_0 is a constant. Furthermore, for the ground-state trial wave function it is required that there be no nodes in $\psi_J(r)$.

The spherical nodal surface was implemented by constructing a Jastrow function with a single node. This was achieved by writing the Jastrow function in terms of a sum of different solutions of the radial Schrödinger equation

$$\psi_J^{\text{sph}}(r) = N(\psi_J^1(r) - c\,\psi_J^0(r)), \tag{B.31}$$

where N denotes a normalization constant and the superscript in $\psi_J^i(r)$ denotes the number of nodes. By changing the parameter c it is possible to adjust the position r_{node} of the node such that $\psi_J^{\text{sph}}(r_{\text{node}}) = 0$.

To improve the nodal surface in the QMC method we take advantage of the analysis of the nodal surface obtained from the diagonalization in Sec. 2.3.2. Usually the Jastrow function is a radial function only allowing for spherical nodal surfaces. If the nonspherical nodal surface is to be reproduced by the Jastrow function, angular dependencies have to be introduced.

Including the first nonspherical contribution in the nodal surface corresponds to adding the cubic harmonic with $l = 4$ to the spherical term:

$$r_{\text{node}}(\hat{\mathbf{r}}) = c_0 Y_0^c(\hat{\mathbf{r}}) + c_4 Y_4^c(\hat{\mathbf{r}}), \tag{B.32}$$

where Y_l^c denote cubical harmonics and $\hat{\mathbf{r}} = \mathbf{r}/r$ is the unit vector pointing in the direction of $\mathbf{r}$. c_0 and c_4 are coefficients defining the nodal surface.

The function defined by

$$f_{\text{non-sph}}(\mathbf{r}) = \psi_J^1(r) - \frac{\psi_J^1(r_{\text{node}}(\hat{\mathbf{r}}))}{\psi_J^0(r_{\text{node}}(\hat{\mathbf{r}}))}\psi_J^0(r) \tag{B.33}$$

vanishes when $r = r_{\text{node}}$ for a given direction $\hat{\mathbf{r}}$. However, this function does not meet the boundary conditions in Eq. (B.30). Furthermore it is not continuous at $r \to 0$ since for vectors $\mathbf{r}_1$ and $\mathbf{r}_2$ pointing in different directions

$$\lim_{r_1 \to 0} f_{\text{non-sph}}(\mathbf{r}_1) \neq \lim_{r_2 \to 0} f_{\text{non-sph}}(\mathbf{r}_2). \tag{B.34}$$

Therefore, the function defined in Eq. (B.33) is multiplied by a normalizing function

$$\begin{aligned}
n(\mathbf{r}) &= n_3(\hat{\mathbf{r}})r^3 + n_2(\hat{\mathbf{r}})r^2 + n_1(\hat{\mathbf{r}})r + n_0(\hat{\mathbf{r}}),\\
n_3(\hat{\mathbf{r}}) &= \frac{16}{L^3}\Big(\frac{u_0}{a(\hat{\mathbf{r}})} - \frac{1}{b(\hat{\mathbf{r}})}\Big),\\
n_2(\hat{\mathbf{r}}) &= \frac{12}{L^2}\Big(\frac{1}{b(\hat{\mathbf{r}})} - \frac{u_0}{a(\hat{\mathbf{r}})}\Big),\\
n_1(\hat{\mathbf{r}}) &= 0,\\
n_0(\hat{\mathbf{r}}) &= \frac{u_0}{a(\hat{\mathbf{r}})},
\end{aligned} \tag{B.35}$$

where

$$a(\hat{\mathbf{r}}) = f_{\text{non-sph}}(\mathbf{r})|_{r=0}\,,$$
$$b(\hat{\mathbf{r}}) = f_{\text{non-sph}}(\mathbf{r})|_{r=L/2}\,, \tag{B.36}$$

and $u_0 < 0$ defines the value of the Jastrow function at $r = 0$. The nonspherical Jastrow function is then given by

$$\psi_J^{\text{non-sph}}(\mathbf{r}) = f_{\text{non-sph}}(\mathbf{r}) n(\hat{\mathbf{r}})\,, \tag{B.37}$$

which obeys the required conditions in Eq. (B.30). Now, the excited-state energies can be found as discussed in Sec. 2.2 by adjusting the parameters c_0 and c_4.

B.4 Chiral leading-order potential for two neutrons

The chiral NN potential at LO (without isospin-breaking terms) reads [55]

$$\begin{aligned} V(r) =& \frac{1}{\pi\Gamma(3/4)R_0^3}\Big(C_S + C_T \boldsymbol{\sigma}_1\cdot\boldsymbol{\sigma}_2\Big)e^{-(r/R_0)^4} \\ &+ \frac{m_\pi^3}{12\pi}\left(\frac{g_A}{2F_\pi}\right)^2 \frac{e^{-m_\pi r}}{m_\pi r}\boldsymbol{\tau}_1\cdot\boldsymbol{\tau}_2\left[\boldsymbol{\sigma}_1\cdot\boldsymbol{\sigma}_2 + \left(1+\frac{3}{m_\pi r}+\frac{3}{(m_\pi r)^2}\right)S_{12}\right]\left(1-e^{-(r/R_0)^4}\right). \end{aligned} \tag{B.38}$$

We show how the projection of the local LO potential on a systems of two neutrons. For $T = 1$ we find $\boldsymbol{\tau}_1\cdot\boldsymbol{\tau}_2 = 1$ and thus

$$\begin{aligned} V(r) =& \frac{C_S}{\pi\Gamma(3/4)R_0^3}e^{-(r/R_0)^4} \\ &+ \left[\frac{C_T}{\pi\Gamma(3/4)R_0^3}e^{-(r/R_0)^4} - \frac{m_\pi^3}{12\pi}\left(\frac{g_A}{2F_\pi}\right)^2\frac{e^{-m_\pi r}}{m_\pi r}\left(\frac{3}{m_\pi r}+\frac{3}{(m_\pi r)^2}\right)\left(1-e^{-(r/R_0)^4}\right)\right]\boldsymbol{\sigma}_1\cdot\boldsymbol{\sigma}_2 \\ &+ \frac{m_\pi^3}{12\pi}\left(\frac{g_A}{2F_\pi}\right)^2\frac{e^{-m_\pi r}}{m_\pi r}3\left(1+\frac{3}{m_\pi r}+\frac{3}{(m_\pi r)^2}\right)\left(1-e^{-(r/R_0)^4}\right)\boldsymbol{\sigma}_1\cdot\hat{\mathbf{r}}\,\boldsymbol{\sigma}_2\cdot\hat{\mathbf{r}}\,, \end{aligned} \tag{B.39}$$

where the terms were arranged according to their spin-operator structure. So far we neglected charge-independence and charge-symmetry breaking terms. For the OPE there is only one term as only the neutral pion can be exchanged for a system which consists solely of neutrons. The corresponding contact terms are given by

$$V_{\text{cont, CIB}}(\mathbf{r}) = C_{\text{CIB}}\frac{1-\boldsymbol{\sigma}_1\cdot\boldsymbol{\sigma}_2}{4}\delta(\mathbf{r})\,, \tag{B.40}$$
$$V_{\text{cont, CSB}}(\mathbf{r}) = -C_{\text{CSB}}\frac{1-\boldsymbol{\sigma}_1\cdot\boldsymbol{\sigma}_2}{4}\delta(\mathbf{r})\,, \tag{B.41}$$

including these terms yields

$$
\begin{aligned}
V(r) = & \frac{C_S + \frac{1}{4}(C_{\mathrm{CIB}} - C_{\mathrm{CSB}})}{\pi\Gamma(3/4)R_0^3} e^{-(r/R_0)^4} \\
& + \left[\frac{C_T - \frac{1}{4}(C_{\mathrm{CIB}} - C_{\mathrm{CSB}})}{\pi\Gamma(3/4)R_0^3} e^{-(r/R_0)^4} - \frac{m_\pi^3}{12\pi}\left(\frac{g_A}{2F_\pi}\right)^2 \frac{e^{-m_\pi r}}{m_\pi r}\left(\frac{3}{m_\pi r} + \frac{3}{(m_\pi r)^2}\right)\left(1 - e^{-(r/R_0)^4}\right)\right] \boldsymbol{\sigma}_1 \cdot \boldsymbol{\sigma}_2 \\
& + \frac{m_\pi^3}{12\pi}\left(\frac{g_A}{2F_\pi}\right)^2 \frac{e^{-m_\pi r}}{m_\pi r} 3\left(1 + \frac{3}{m_\pi r} + \frac{3}{(m_\pi r)^2}\right)\left(1 - e^{-(r/R_0)^4}\right) \boldsymbol{\sigma}_1 \cdot \hat{\mathbf{r}}\, \boldsymbol{\sigma}_2 \cdot \hat{\mathbf{r}}\,. \qquad \text{(B.42)}
\end{aligned}
$$

In the ${}^1S_0$ channel of two neutrons, which we study in Chapter 2, the chiral potential can be projected on a contact interaction plus a Yukawa interaction. The chiral LO potential is then given by

$$
\begin{aligned}
V_{\mathrm{LO}}^{{}^1S_0}(r) &= \tilde{C}_S \frac{1}{\pi\Gamma(3/4)R_0^3} \exp\left[-\left(\frac{r}{R_0}\right)^4\right] - \frac{m_{\pi^0}^3}{4\pi}\left(\frac{g_A}{2F_\pi}\right)^2 \frac{e^{-m_{\pi^0} r}}{m_{\pi^0} r}\left(1 - \exp\left[-\left(\frac{r}{R_0}\right)^4\right]\right), \\
\tilde{C}_S &= C_S - 3C_T + C_{\mathrm{CIB}} - C_{\mathrm{CSB}}\,. \qquad \text{(B.43)}
\end{aligned}
$$

Numerical values for the low energy constants are provided in Ref. [55].

C Cubic symmetry group

In this section, we briefly discuss how the projector

$$\mathcal{P}_\Gamma = \frac{\dim \Gamma}{24} \sum_{R \in \mathcal{O}} \chi_\Gamma(R) D_n(R), \tag{C.1}$$

on the irreducible representations of the cubic symmetry group is constructed. There are 24 elements of the cubic group $R \in \mathcal{O}$, which can be classified according to their conjugacy classes:

- I: identity.
- $3C_2$: π rotations about 3 coordinate axes.
- $8C_3$: $\pm(2\pi/3)$ rotations about four body diagonals, e.g., $x = y = z$.
- $6C_4$: $\pm\pi/2$ rotations about 3 coordinate axes.
- $6C_2'$: π rotations about axes parallel to 6 face diagonals, e.g., $x = y$, $z = 0$.

The realization $D_n(R)$ used in Eq. (C.1) is given by a permutation and/or inversion of the components $c = 1, 2, 3$ of each relative coordinate $\mathbf{x}_i$ (simultaneously for all $i = 1, \ldots, n-1$). In Table C.1 we show these operations, where the notation gives the result of operating on a tuple $(k_{i,1}, k_{i,2}, k_{i,3})$ in a short-hand form, e.g., the rotation with index 7 transforms a tuple to $(-k_{i,2}, k_{i,3}, -k_{i,1})$. It is understood that, as discussed in Sec. 4.1, each transformed index $k_{i,c}$ is wrapped back into the interval $-N/2, \ldots, N/2-1$, if necessary. The characters $\chi_\Gamma(R)$ of the R's realizations are given in Table C.2.

Cubic symmetry commutes with parity as well as permutation symmetry, so for both bosonic and fermionic systems we end up with multiplets of the irreducible representations $\Gamma = A_1^\pm$, $A_2^\pm$, $E^\pm$, $T_1^\pm$ and $T_2^\pm$, where the superscript indicates the parity.

The irreducible representation of the full rotational group $SO(3)$ is reducible when mapped onto the cubic group. A basis for the irreducible representation of $SO(3)$ is given by the angular momentum multiplets, i.e., spherical harmonics Y_{lm}, labeled by the angular momentum quantum number l and its projection m. The numerical values in Table C.3 yield the multiplicity of the cubic irreducible representations in the decomposition of a given angular momentum multiplet. $l = 0$ and $l = 1$ contribute only to A_1^+ and T_1^-, respectively, meaning that an S-wave state is mapped solely onto the single A_1^+ state, while a P-wave state maps onto the three T_1^- states in finite volume. However, a D-wave state with its five projections $m = 0, \pm 1, \pm 2$ is decomposed into the two E^+ and three T_2^+ states.

To conclude this section, we note that in the case of spin-dependent interactions, total angular momentum J instead of l is the relevant good quantum number in the infinite volume. For example, in the case of spin-1/2 fermions, one has to consider $SU(2)$ broken down to the double cover ${}^2\mathcal{O}$ of the cubic group, giving three additional irreducible representations that receive contributions from half-integer J states. For details, see Ref. [213].

Index	Class	$D_n(R)$			Index	Class	$D_n(R)$		
1	I	1	2	3	13	$6C_4$	2	−1	3
2	$3C_2$	−1	−2	3	14		−2	1	3
3		−1	2	−3	15		3	2	−1
4		1	−2	−3	16		−3	2	1
5	$8C_3$	3	1	2	17		1	−3	2
6		2	3	1	18		1	3	−2
7		−2	3	−1	19	$6C_2'$	2	1	−3
8		−3	−1	2	20		−2	−1	−3
9		2	−3	−1	21		3	−2	1
10		−3	1	−2	22		−3	−2	−1
11		−2	−3	1	23		−1	−3	−2
12		3	−1	−2	24		−1	3	2

Table C.1: Realization of the 24 cubic rotations acting on a coordinate tuple in symbolic notation (see text). The second column indicates the conjugacy class of the rotation.

	I	$3C_2$	$8C_3$	$6C_4$	$6C_2'$
A_1	1	1	1	1	1
A_2	1	1	1	-1	-1
E	2	2	-1	0	0
T_1	3	-1	0	1	-1
T_2	3	-1	0	-1	1

Table C.2: Irreducible characters of O [213].

l	A_1^+	A_2^+	E^+	T_1^+	T_2^+	A_1^-	A_2^-	E^-	T_1^-	T_2^-
0	1									
1									1	
2			1		1					
3							1		1	1
4	1		1	1	1					
5								1	2	1
6	1	1	1	1	2					
7							1	1	2	2
8	1		2	2	2					
9						1	1	1	3	2
10	1	1	2	2	3					

Table C.3: Decomposition of the irreducible representations of the rotational symmetry group $SO(3)$ into irreducible representations of the cubic symmetry group $\mathcal{O}$; reproduced in part from Ref. [271].

D Scalar two-body response functions

The two-body terms of the three scalar channels, scalar-scalar SS, trace anomaly θ, and spin-2 (2), in Eqs. (5.17), (5.18), and (5.19) can be written in form of only two independent amplitudes when some subleading one-body contributions are included. The details will be reported in Ref. [232]. The one-body θ and spin-2 currents yield non-relativistic corrections of

$$\Delta\mathcal{M}^{\theta}_{1,\mathrm{NR}} = -\frac{f^{\theta}_{\pi}}{M_{\pi}}\frac{\mathbf{p}_1^2+\mathbf{p}_2^2+\mathbf{p}_1'^2+\mathbf{p}_2'^2}{4m_N}\big(\delta(\mathbf{p}_1-\mathbf{p}_1')+\delta(\mathbf{p}_2-\mathbf{p}_2')\big), \tag{D.1}$$

and

$$\Delta\mathcal{M}^{(2)}_{1,\mathrm{NR}} = \frac{f^{(2)}_{N}}{16m_N^2}\Big[(\mathbf{p}_2^2+\mathbf{p}_2'^2-3\mathbf{p}_1^2-3\mathbf{p}_1'^2)\delta(\mathbf{p}_1-\mathbf{p}_1')+(\mathbf{p}_1^2+\mathbf{p}_1'^2-3\mathbf{p}_2^2-3\mathbf{p}_2'^2)\delta(\mathbf{p}_2-\mathbf{p}_2')\Big], \tag{D.2}$$

which in the limit $\mathbf{q}\to 0$ reduce to

$$\Delta\mathcal{M}^{\theta}_{1,\mathrm{NR}} = -\frac{2f^{\theta}_{\pi}}{M_{\pi}}T\,, \tag{D.3}$$

$$\Delta\mathcal{M}^{(2)}_{1,\mathrm{NR}} = -\frac{f^{(2)}_{N}}{2m_N}T\,, \tag{D.4}$$

where T is the kinetic energy operator. The two-body θ and spin-2 amplitudes can be rewritten by replacing

$$2\mathbf{q}_1\cdot\mathbf{q}_2 = \mathbf{q}^2-\mathbf{q}_1^2-\mathbf{q}_2^2\,. \tag{D.5}$$

Thus, we find

$$\begin{aligned}\mathcal{M}^{\theta}_{2,\mathrm{NR}} =& -\frac{f^{\theta}_{\pi}}{M_{\pi}}\Bigg[\left(\frac{g_A}{2F_{\pi}}\right)^2\frac{\boldsymbol{\tau}_1\cdot\boldsymbol{\tau}_2\,\boldsymbol{\sigma}_1\cdot\mathbf{q}_1\,\boldsymbol{\sigma}_2\cdot\mathbf{q}_2}{\big(\mathbf{q}_1^2+M_{\pi}^2\big)\big(\mathbf{q}_2^2+M_{\pi}^2\big)}(2M_{\pi}^2-\mathbf{q}^2)\\ &+\left(\frac{g_A}{2F_{\pi}}\right)^2\boldsymbol{\tau}_1\cdot\boldsymbol{\tau}_2\,\boldsymbol{\sigma}_1\cdot\mathbf{q}_1\boldsymbol{\sigma}_2\cdot\mathbf{q}_2\left(\frac{1}{\mathbf{q}_1^2+M_{\pi}^2}+\frac{1}{\mathbf{q}_2^2+M_{\pi}^2}\right)+2(C_S+C_T\boldsymbol{\sigma}_1\cdot\boldsymbol{\sigma}_2)\Bigg],\end{aligned} \tag{D.6}$$

$$\begin{aligned}\mathcal{M}^{(2)}_{2,\mathrm{NR}} =& \frac{f^{(2)}_{\pi}}{4M_{\pi}}\Bigg[\left(\frac{g_A}{2F_{\pi}}\right)^2\frac{\boldsymbol{\tau}_1\cdot\boldsymbol{\tau}_2\,\boldsymbol{\sigma}_1\cdot\mathbf{q}_1\,\boldsymbol{\sigma}_2\cdot\mathbf{q}_2}{\big(\mathbf{q}_1^2+M_{\pi}^2\big)\big(\mathbf{q}_2^2+M_{\pi}^2\big)}(2M_{\pi}^2+\mathbf{q}^2)\\ &-\left(\frac{g_A}{2F_{\pi}}\right)^2\boldsymbol{\tau}_1\cdot\boldsymbol{\tau}_2\,\boldsymbol{\sigma}_1\cdot\mathbf{q}_1\boldsymbol{\sigma}_2\cdot\mathbf{q}_2\left(\frac{1}{\mathbf{q}_1^2+M_{\pi}^2}+\frac{1}{\mathbf{q}_2^2+M_{\pi}^2}\right)-2(C_S+C_T\boldsymbol{\sigma}_1\cdot\boldsymbol{\sigma}_2)\Bigg].\end{aligned} \tag{D.7}$$

In both cases the first lines can be related to $\mathcal{M}^{SS}_{2,\mathrm{NR}}$. The first terms in the second lines of both responses can be expressed in terms of

$$\mathcal{M}_{NN}(i) = \left(\frac{g_A}{2F_\pi}\right)^2 \boldsymbol{\tau}_1 \cdot \boldsymbol{\tau}_2 \, \frac{\boldsymbol{\sigma}_1 \cdot \mathbf{q}_1 \boldsymbol{\sigma}_2 \cdot \mathbf{q}_2}{\mathbf{q}_i^2 + M_\pi^2}, \qquad i = 1,2\,. \tag{D.8}$$

While for the θ currents in Eqs. (D.1) and (5.18) there is only one coupling f_π^θ, the spin-2 one-body contribution in Eq. (D.2) carries a coupling $f_N^{(2)}$ different from the coupling of the two-body term in Eq. (5.19), which is $f_\pi^{(2)}$. However, when all Wilson coefficients are set equal to one we have $f_N^{(2)}/m_N = f_\pi^{(2)}/M_\pi$. Summarizing all contributions, including 1b and 2b terms we obtain

$$\begin{aligned}
\mathcal{M}^\theta_{1+2,\mathrm{NR}} =& f_\pi^\theta \Bigg[\left(2 - \frac{\mathbf{q}^2}{M_\pi^2}\right) \frac{1}{f_\pi} \mathcal{M}^{SS}_{2,\mathrm{NR}} \\
&- \frac{1}{M_\pi} \big(\mathcal{M}_{NN}(1) + \mathcal{M}_{NN}(2) + 2(C_S + C_T \boldsymbol{\sigma}_1 \cdot \boldsymbol{\sigma}_2) \big) + \frac{1}{f_\pi^\theta} \Delta\mathcal{M}^\theta_{1,\mathrm{NR}} \Bigg], \qquad \text{(D.9)} \\
\mathcal{M}^{(2)}_{1+2,\mathrm{NR}} =& f_\pi^{(2)} \Bigg[-\frac{2M_\pi^2 + \mathbf{q}^2}{4M_\pi^2} \frac{1}{f_\pi} \mathcal{M}^{SS}_{2,\mathrm{NR}} \\
&- \frac{1}{4M_\pi} \big(\mathcal{M}_{NN}(1) + \mathcal{M}_{NN}(2) + 2(C_S + C_T \boldsymbol{\sigma}_1 \cdot \boldsymbol{\sigma}_2) \big) + \frac{m_N}{f_N^{(2)} M_\pi} \Delta\mathcal{M}^{(2)}_{1,\mathrm{NR}} \Bigg], \qquad \text{(D.10)}
\end{aligned}$$

In the limit $\mathbf{q} \to 0$ we have $\mathbf{q}_1 = -\mathbf{q}_2$, which is the momentum transfer between the nucleons. Hence, $\mathcal{M}_{NN}$ can be identified with the pion-exchange part $V^{(0)}_{\mathrm{OPE}}$ of the leading order chiral NN potential (see Eq. (1.13)),

$$\mathcal{M}_{NN} \to V^{(0)}_{\mathrm{OPE}}\,. \tag{D.11}$$

Together with the contact terms in the second lines of Eqs. (D.9) and (D.10) we recover two times the leading order chiral NN potential V^{LO}_{NN}.

In the limit $\mathbf{q} \to 0$ both $\Delta\mathcal{M}^\theta_{1,\mathrm{NR}}$ and $\Delta\mathcal{M}^{(2)}_{1,\mathrm{NR}}$ become proportional to T. For finite $\mathbf{q}$ the contributions of $\Delta\mathcal{M}^\theta_{1,\mathrm{NR}}$ and $\Delta\mathcal{M}^{(2)}_{1,\mathrm{NR}}$ to the full responses are small. In addition, we found results to depend very little on whether the exact expression for $\Delta\mathcal{M}^{(2)}_{1,\mathrm{NR}}$ is used and in the following we assume $\frac{M_\pi}{2f_\pi^\theta}\Delta\mathcal{M}^\theta_{1,\mathrm{NR}} \approx \frac{2m_N}{f_N^{(2)}}\Delta\mathcal{M}^{(2)}_{1,\mathrm{NR}}$. Thus we define a new amplitude

$$\mathcal{M}_{\mathrm{b}} = -\frac{1}{M_\pi} \big(\mathcal{M}_{NN}(1) + \mathcal{M}_{NN}(2) + 2(C_S + C_T \boldsymbol{\sigma}_1 \cdot \boldsymbol{\sigma}_2) \big) + \frac{1}{f_\pi^\theta} \Delta\mathcal{M}^\theta_{1,\mathrm{NR}}\,, \tag{D.12}$$

which in the limit $\mathbf{q} \to 0$ reduces to

$$\mathcal{M}_{\mathrm{b}} \to -\frac{2}{M_\pi}(T + V^{\mathrm{LO}}_{NN})\,. \tag{D.13}$$

We define response functions in the naive shell model,

$$\mathcal{F}_\pi(\mathbf{q}^2) = \frac{1}{2}\sum_{\text{occ}} \langle N_1 N_2 | (1 - P_{12}) | \frac{1}{f_\pi} \mathcal{M}^{SS}_{2,\text{NR}} | N_1 N_2 \rangle \,, \tag{D.14}$$

$$\mathcal{F}_\text{b}(\mathbf{q}^2) = \frac{1}{2}\sum_{\text{occ}} \langle N_1 N_2 | (1 - P_{12}) | \mathcal{M}_\text{b} | N_1 N_2 \rangle - \frac{q^2}{M_\pi^2} \mathcal{F}_\pi(q^2) \,, \tag{D.15}$$

where due to Eq. (D.13) we have $\mathcal{F}_\text{b}(0) = -\frac{2}{M_\pi} E_\text{b}$ with the binding energy of the nucleus $E_\text{b} < 0$. The three physical channels (SS, θ, (2)) can thus be written (approximately) in terms of two response functions (see Eqs. (6.13) and (6.14)).

Bibliography

[1] G. Aad *et al.* (ATLAS), *Observation of a new particle in the search for the Standard Model Higgs boson with the ATLAS detector at the LHC*, Phys. Lett. B **716**, 1 (2012).

[2] S. Chatrchyan *et al.* (CMS), *Observation of a new boson at a mass of 125 GeV with the CMS experiment at the LHC*, Phys. Lett. B **716**, 30 (2012).

[3] S. R. Beane, W. Detmold, K. Orginos, and M. J. Savage, *Nuclear Physics from Lattice QCD*, Prog. Part. Nucl. Phys. **66**, 1 (2011).

[4] M. Lüscher, *Volume Dependence of the Energy Spectrum in Massive Quantum Field Theories. 2. Scattering States*, Commun. Math. Phys. **105**, 153 (1986).

[5] M. Lüscher, *Two particle states on a torus and their relation to the scattering matrix*, Nucl. Phys. B **354**, 531 (1991).

[6] H. Yukawa, *On the Interaction of Elementary Particles I*, Proc. Phys. Math. Soc. Jap. **17**, 48 (1935).

[7] S. Weinberg, *Nuclear forces from chiral Lagrangians*, Phys. Lett. B **251**, 288 (1990).

[8] F. Wienholtz *et al.*, *Masses of exotic calcium isotopes pin down nuclear forces*, Nature **498**, 346 (2013).

[9] C. A. Bertulani and V. Zelevinsky, *Is the tetraneutron a bound dineutron-dineutron molecule?*, J. Phys. G **29**, 2431 (2003).

[10] N. K. Timofeyuk, *Do multineutrons exist?*, J. Phys. G **29**, L9 (2003).

[11] S. C. Pieper, *Can Modern Nuclear Hamiltonians Tolerate a Bound Tetraneutron?*, Phys. Rev. Lett. **90**, 252501 (2003).

[12] K. Kisamori *et al.*, *Candidate resonant tetraneutron state populated by the* ^{4}He(^{8}He,^{8}Be) *reaction*, Phys. Rev. Lett. **116**, 052501 (2016).

[13] S. Paschalis *et al.*, Report No. NP1406-SAMURAI19 .

[14] K. Kisamori *et al.*, Report No. NP1512-SAMURAI34 .

[15] S. Shimoura *et al.*, Report No. NP1512-SHARAQ10 .

[16] A. M. Shirokov, G. Papadimitriou, A. I. Mazur, I. A. Mazur, R. Roth, and J. P. Vary, *Prediction for a four-neutron resonance*, Phys. Rev. Lett. **117**, 182502 (2016).

[17] K. Fossez, J. Rotureau, N. Michel, and M. Płoszajczak, *Can tetraneutron be a narrow resonance?*, Phys. Rev. Lett. **119**, 032501 (2017).

[18] R. Lazauskas and J. Carbonell, *Is a physically observable tetraneutron resonance compatible with realistic nuclear interactions?*, Phys. Rev. C **72**, 034003 (2005).

[19] E. Hiyama, R. Lazauskas, J. Carbonell, and M. Kamimura, *Possibility of generating a 4-neutron resonance with a $T = 3/2$ isospin 3-neutron force*, Phys. Rev. C **93**, 044004 (2016).

[20] A. Deltuva, *Tetraneutron: Rigorous continuum calculation*, Phys. Lett. B **782**, 238 (2018).

[21] H. Witała and W. Glöckle, *Resonances in the three neutron system*, Phys. Rev. C **60**, 024002 (1999).

[22] R. Lazauskas and J. Carbonell, *Three-neutron resonance trajectories for realistic interaction models*, Phys. Rev. C **71**, 044004 (2005).

[23] A. Deltuva, *Three-neutron resonance study using transition operators*, Phys. Rev. C **97**, 034001 (2018).

[24] U. J. Wiese, *Identification of Resonance Parameters From the Finite Volume Energy Spectrum*, Nucl. Phys. Proc. Suppl. **9**, 609 (1989).

[25] R. A. Briceño, J. J. Dudek, and R. D. Young, *Scattering processes and resonances from lattice QCD*, Rev. Mod. Phys. **90**, 025001 (2018).

[26] K. Polejaeva and A. Rusetsky, *Three particles in a finite volume*, Eur. Phys. J. A **48**, 67 (2012).

[27] M. T. Hansen and S. R. Sharpe, *Expressing the three-particle finite-volume spectrum in terms of the three-to-three scattering amplitude*, Phys. Rev. D **92**, 114509 (2015).

[28] R. A. Briceño and Z. Davoudi, *Three-particle scattering amplitudes from a finite volume formalism*, Phys. Rev. D **87**, 094507 (2013).

[29] H.-W. Hammer, J.-Y. Pang, and A. Rusetsky, *Three-particle quantization condition in a finite volume: 1. The role of the three-particle force*, JHEP **09**, 109 (2017).

[30] K. Garrett and G. Duda, *Dark Matter: A Primer*, Adv. Astron. **2011**, 968283 (2011).

[31] J. L. Feng, *Dark Matter Candidates from Particle Physics and Methods of Detection*, Ann. Rev. Astron. Astrophys. **48**, 495 (2010).

[32] E. Aprile *et al.* (XENON), *Dark Matter Search Results from a One Ton-Year Exposure of XENON1T*, Phys. Rev. Lett. **121**, 111302 (2018).

[33] J. Aalbers *et al.* (DARWIN), *DARWIN: towards the ultimate dark matter detector*, JCAP **1611**, 017 (2016).

[34] D. B. Kaplan, *Five lectures on effective field theory*, in *Lectures delivered at the 17th National Nuclear Physics Summer School 2015, Berkeley, June 6-17, 2005* (2005) arXiv:nucl-th/0510023 .

[35] E. Epelbaum, *Nuclear Forces from Chiral Effective Field Theory: A Primer* (2010) arXiv:1001.3229 .

[36] R. Aaij *et al.* (LHCb Collaboration), *Observation of $J/\psi p$ Resonances Consistent with Pentaquark States in $\Lambda_b^0 \to J/\psi K^- p$ Decays*, Phys. Rev. Lett. **115**, 072001 (2015).

[37] A. Esposito, A. L. Guerrieri, F. Piccinini, A. Pilloni, and A. D. Polosa, *Four-quark hadrons: An updated review*, Int. J. Mod. Phys. A **30**, 1530002 (2015).

[38] D. J. Gross and F. Wilczek, *Ultraviolet Behavior of Non-Abelian Gauge Theories*, Phys. Rev. Lett. **30**, 1343 (1973).

[39] H. D. Politzer, *Reliable Perturbative Results for Strong Interactions?*, Phys. Rev. Lett. **30**, 1346 (1973).

[40] S. Dürr, Z. Fodor, J. Frison, C. Hoelbling, R. Hoffmann, S. D. Katz, S. Krieg, T. Kurth, L. Lellouch, T. Lippert, K. K. Szabo, and G. Vulvert, *Ab Initio Determination of Light Hadron Masses*, Science **322**, 1224 (2008).

[41] T. Yamazaki, K.-i. Ishikawa, Y. Kuramashi, and A. Ukawa, *Helium nuclei, deuteron and dineutron in 2+1 flavor lattice QCD*, Phys. Rev. D **86**, 074514 (2012).

[42] S. R. Beane, E. Chang, S. D. Cohen, W. Detmold, H. W. Lin, T. C. Luu, K. Orginos, A. Parreño, M. J. Savage, and A. Walker-Loud (NPLQCD Collaboration), *Light Nuclei and Hypernuclei from Quantum Chromodynamics in the Limit of SU(3) Flavor Symmetry*, Phys. Rev. D **87**, 034506 (2013).

[43] S. R. Beane, E. Chang, S. Cohen, W. Detmold, H. W. Lin, K. Orginos, A. Parreño, M. J. Savage, and B. C. Tiburzi (NPLQCD Collaboration), *Magnetic Moments of Light Nuclei from Lattice Quantum Chromodynamics*, Phys. Rev. Lett. **113**, 252001 (2014).

[44] J. Goldstone, A. Salam, and S. Weinberg, *Broken Symmetries*, Phys. Rev. **127**, 965 (1962).

[45] V. G. J. Stoks, R. A. M. Klomp, M. C. M. Rentmeester, and J. J. de Swart, *Partial wave analaysis of all nucleon-nucleon scattering data below 350 MeV*, Phys. Rev. C **48**, 792 (1993).

[46] P. F. Bedaque and U. van Kolck, *Nucleon-deuteron scattering from an effective field theory*, Phys. Lett. B **428**, 221 (1998).

[47] D. B. Kaplan, M. J. Savage, and M. B. Wise, *A New expansion for nucleon-nucleon interactions*, Phys. Lett. B **424**, 390 (1998).

[48] S. Weinberg, *Effective chiral Lagrangians for nucleon - pion interactions and nuclear forces*, Nucl. Phys. B **363**, 3 (1991).

[49] S. Weinberg, *Three-body interactions among nucleons and pions*, Phys. Lett. B **295**, 114 (1992).

[50] H. Krebs, A. M. Gasparyan, and E. Epelbaum, *Three-nucleon force in chiral EFT with explicit $\Delta(1232)$ degrees of freedom: Longest-range contributions at fourth order*, Phys. Rev. C **98**, 014003 (2018).

[51] E. Epelbaum, *Few-nucleon forces and systems in chiral effective field theory*, Prog. Part. Nucl. Phys. **57**, 654 (2006).

[52] E. Epelbaum, H.-W. Hammer, and U.-G. Meißner, *Modern Theory of Nuclear Forces*, Rev. Mod. Phys. **81**, 1773 (2009).

[53] E. Epelbaum, H. Krebs, and U.-G. Meißner, *Precision Nucleon-Nucleon Potential at Fifth Order in the Chiral Expansion*, Phys. Rev. Lett. **115**, 122301 (2015).

[54] A. Gezerlis, I. Tews, E. Epelbaum, S. Gandolfi, K. Hebeler, A. Nogga, and A. Schwenk, *Quantum Monte Carlo Calculations with Chiral Effective Field Theory Interactions*, Phys. Rev. Lett. **111**, 032501 (2013).

[55] A. Gezerlis, I. Tews, E. Epelbaum, M. Freunek, S. Gandolfi, K. Hebeler, A. Nogga, and A. Schwenk, *Local chiral effective field theory interactions and quantum Monte Carlo applications*, Phys. Rev. C **90**, 054323 (2014).

[56] J. E. Lynn, I. Tews, J. Carlson, S. Gandolfi, A. Gezerlis, K. E. Schmidt, and A. Schwenk, *Chiral Three-Nucleon Interactions in Light Nuclei, Neutron-α Scattering, and Neutron Matter*, Phys. Rev. Lett. **116**, 062501 (2016).

[57] J. E. Lynn, J. Carlson, E. Epelbaum, S. Gandolfi, A. Gezerlis, and A. Schwenk, *Quantum Monte Carlo Calculations of Light Nuclei Using Chiral Potentials*, Phys. Rev. Lett. **113**, 192501 (2014).

[58] I. Tews, S. Gandolfi, A. Gezerlis, and A. Schwenk, *Quantum monte carlo calculations of neutron matter with chiral three-body forces*, Phys. Rev. C **93**, 024305 (2016).

[59] E. Epelbaum, W. Glöckle, and U.-G. Meißner, *Improving the convergence of the chiral expansion for nuclear forces – I: Peripheral phases*, Eur. Phys. J. A **19**, 125 (2004).

[60] S. Pastore, R. Schiavilla, and J. L. Goity, *Electromagnetic two-body currents of one- and two-pion range*, Phys. Rev. C **78**, 064002 (2008).

[61] S. Kölling, E. Epelbaum, H. Krebs, and U.-G. Meißner, *Two-pion exchange electromagnetic current in chiral effective field theory using the method of unitary transformation*, Phys. Rev. C **80**, 045502 (2009).

[62] S. Kölling, E. Epelbaum, H. Krebs, and U.-G. Meißner, *Two-nucleon electromagnetic current in chiral effective field theory: One-pion exchange and short-range contributions*, Phys. Rev. C **84**, 054008 (2011).

[63] T. S. Park, L. E. Marcucci, R. Schiavilla, M. Viviani, A. Kievsky, S. Rosati, K. Kubodera, D. P. Min, and M. Rho, *Parameter free effective field theory calculation for the solar proton fusion and hep processes*, Phys. Rev. C **67**, 055206 (2003).

[64] A. Baroni, L. Girlanda, S. Pastore, R. Schiavilla, and M. Viviani, *Nuclear Axial Currents in Chiral Effective Field Theory*, Phys. Rev. C **93**, 015501 (2016).

[65] H. Krebs, E. Epelbaum, and U.-G. Meißner, *Nuclear axial current operators to fourth order in chiral effective field theory*, Ann. Phys. **378**, 317 (2017).

[66] P. Klos, *Electroweak currents in chiral effective field theory*, Master's thesis, Technische Universität Darmstadt (2014), (supervised by A. Schwenk and J. Menéndez).

[67] P. Klos, J. Menéndez, D. Gazit, and A. Schwenk, *Large-scale nuclear structure calculations for spin-dependent WIMP scattering with chiral effective field theory currents*, Phys. Rev. D **88**, 083516 (2013), [Erratum: Phys. Rev. D 89, 029901 (2014)].

[68] B. S. DeWitt, *Transition from discrete to continuous spectra*, Phys. Rev. **103**, 1565 (1956).

[69] K. Huang and C. N. Yang, *Quantum-mechanical many-body problem with hard-sphere interaction*, Phys. Rev. **105**, 767 (1957).

[70] M. Lüscher, *Volume Dependence of the Energy Spectrum in Massive Quantum Field Theories. 1. Stable Particle States*, Commun. Math. Phys. **104**, 177 (1986).

[71] S. König, D. Lee, and H. W. Hammer, *Volume Dependence of Bound States with Angular Momentum*, Phys. Rev. Lett. **107**, 112001 (2011).

[72] S. Bour, S. König, D. Lee, H. W. Hammer, and U.-G. Meissner, *Topological phases for bound states moving in a finite volume*, Phys. Rev. D **84**, 091503 (2011).

[73] S. König, D. Lee, and H. W. Hammer, *Non-relativistic bound states in a finite volume*, Annals Phys. **327**, 1450 (2012).

[74] S. König and D. Lee, *Volume Dependence of N-Body Bound States*, Phys. Lett. B **779**, 9 (2018).

[75] S. Kreuzer and H.-W. Hammer, *The Triton in a finite volume*, Phys. Lett. B **694**, 424 (2011).

[76] S. R. Beane, T. C. Luu, K. Orginos, A. Parreño, M. J. Savage, A. Torok, and A. Walker-Loud, *Precise Determination of the I=2 pi pi Scattering Length from Mixed-Action Lattice QCD*, Phys. Rev. D **77**, 014505 (2008).

[77] S. R. Beane, P. F. Bedaque, A. Parreño, and M. J. Savage, *Two nucleons on a lattice*, Phys. Lett. B **585**, 106 (2004).

[78] I. Sato and P. F. Bedaque, *Fitting two nucleons inside a box: Exponentially suppressed corrections to the Lüscher's formula*, Phys. Rev. D **76**, 034502 (2007).

[79] N. Barnea, L. Contessi, D. Gazit, F. Pederiva, and U. van Kolck, *Effective Field Theory for Lattice Nuclei*, Phys. Rev. Lett. **114**, 052501 (2015).

[80] J. Kirscher, N. Barnea, D. Gazit, F. Pederiva, and U. van Kolck, *Spectra and Scattering of Light Lattice Nuclei from Effective Field Theory*, Phys. Rev. C **92**, 054002 (2015).

[81] V. Huhn, L. Wätzold, C. Weber, A. Siepe, W. von Witsch, H. Witała, and W. Glöckle, *New Attempt to Determine the n-n Scattering Length with the ^2H (n, np) n Reaction*, Phys. Rev. Lett. **85**, 1190 (2000).

[82] A. Gardestig, *Extracting the neutron-neutron scattering length - recent developments*, J. Phys. G **36**, 053001 (2009).

[83] V. Bernard, U.-G. Meißner, and A. Rusetsky, *The Delta-resonance in a finite volume*, Nucl. Phys. B **788**, 1 (2008).

[84] M. Doring, J. Haidenbauer, U.-G. Meißner, and A. Rusetsky, *Dynamical coupled-channel approaches on a momentum lattice*, Eur. Phys. J. A **47**, 163 (2011).

[85] J. Schiffer and R. Vandenbosch, *Search for a particle-stable tetra neutron*, Physics Letters **5**, 292 (1963).

[86] V. Goldanskii, *The occurence of He^8 casts doubts on the stability on H^5, H^4 and tetraneutron*, Physics Letters **9**, 184 (1964).

[87] Y. C. Tang and B. F. Bayman, *Nonexistence of the tetraneutron*, Phys. Rev. Lett. **15**, 165 (1965).

[88] D. R. Tilley, H. R. Weller, and H. H. Hasan, *Energy levels of light nuclei $A = 3$*, Nucl. Phys. A **474**, 1 (1987).

[89] F. M. Marqués *et al.*, *Detection of neutron clusters*, Phys. Rev. C **65**, 044006 (2002).

[90] M. Zhukov, B. Danilin, D. Fedorov, J. Bang, I. Thompson, and J. Vaagen, *Bound state properties of Borromean halo nuclei: ^{6}He and ^{11}Li*, Physics Reports **231**, 151 (1993).

[91] M. V. Zhukov, A. A. Korsheninnikov, and M. H. Smedberg, *Simplified α+4n model for the ^{8}he nucleus*, Phys. Rev. C **50**, R1 (1994).

[92] R. B. Wiringa, V. G. J. Stoks, and R. Schiavilla, *Accurate nucleon-nucleon potential with charge independence breaking*, Phys. Rev. C **51**, 38 (1995).

[93] S. C. Pieper, V. R. Pandharipande, R. B. Wiringa, and J. Carlson, *Realistic models of pion exchange three nucleon interactions*, Phys. Rev. C **64**, 014001 (2001).

[94] S. A. Sofianos, S. A. Rakityansky, and G. P. Vermaak, *Subthreshold resonances in few neutron systems*, J. Phys. G **23**, 1619 (1997).

[95] F. M. Marqués, N. A. Orr, H. Al Falou, G. Normand, and N. M. Clarke, *On the possible detection of ^{4}n events in the breakup of ^{14}Be*, Submitted to: Phys. Rev. C (2005), arXiv:nucl-ex/0504009 .

[96] W. Glöckle, H. Witała, D. Hüber, H. Kamada, and J. Golak, *The Three nucleon continuum: Achievements, challenges and applications*, Phys. Rept. **274**, 107 (1996).

[97] N. Moiseyev, *Quantum theory of resonances: calculating energies, widths and cross-sections by complex scaling*, Physics Reports **302**, 212 (1998).

[98] Y. Ho, *The method of complex coordinate rotation and its applications to atomic collision processes*, Physics Reports **99**, 1 (1983).

[99] V. I. Kukulin and V. M. Krasnopol'sky, *Description of few-body systems via analytical continuation in coupling constant*, Journal of Physics A: Mathematical and General **10**, L33 (1977).

[100] S. Gandolfi, H.-W. Hammer, P. Klos, J. E. Lynn, and A. Schwenk, *Is a Trineutron Resonance Lower in Energy than a Tetraneutron Resonance?*, Phys. Rev. Lett. **118**, 232501 (2017).

[101] L. Baudis, *Dark matter detection*, J. Phys. G **43**, 044001 (2016).

[102] F. Zwicky, *Die Rotverschiebung von extragalaktischen Nebeln*, Helv. Phys. Acta **6**, 110 (1933).

[103] F. Zwicky, *On the Masses of Nebulae and of Clusters of Nebulae*, Astrophys. J. **86**, 217 (1937).

[104] K. G. Begeman, *H I rotation curves of spiral galaxies*, Astron. Astrophys. **223**, 47 (1989).

[105] V. C. Rubin, *Dark matter in spiral galaxies*, Scientific American **248**, 96 (1983).

[106] A. G. Bergmann, V. Petrosian, and R. Lynds, *Gravitational lens models of arcs in clusters*, The Astrophysical Journal **350**, 23 (1990).

[107] M. Moniez, *Microlensing as a probe of the galactic structure: 20 years of microlensing optical depth studies*, General Relativity and Gravitation **42**, 2047 (2010).

[108] L. E. Strigari, *Galactic Searches for Dark Matter*, Phys. Rept. **531**, 1 (2013).

[109] R. H. Cyburt, B. D. Fields, K. A. Olive, and T.-H. Yeh, *Big Bang Nucleosynthesis: 2015*, Rev. Mod. Phys. **88**, 015004 (2016).

[110] R. A. Alpher and R. Herman, *Evolution of the Universe*, Nature **162**, 774 (1948).

[111] A. A. Penzias and R. W. Wilson, *A Measurement of excess antenna temperature at 4080-Mc/s*, Astrophys. J. **142**, 419 (1965).

[112] G. F. Smoot *et al.* (COBE), *Structure in the COBE differential microwave radiometer first year maps*, Astrophys. J. **396**, L1 (1992).

[113] N. Jarosik *et al.*, *Seven-Year Wilkinson Microwave Anisotropy Probe (WMAP) Observations: Sky Maps, Systematic Errors, and Basic Results*, Astrophys. J. Suppl. **192**, 14 (2011).

[114] P. A. R. Ade *et al.* (Planck), *Planck 2015 results. XIII. Cosmological parameters*, Astron. Astrophys. **594**, A13 (2016).

[115] D. Clowe, M. Bradač, A. H. Gonzalez, M. Markevitch, S. W. Randall, C. Jones, and D. Zaritsky, *A direct empirical proof of the existence of dark matter*, The Astrophysical Journal Letters **648**, L109 (2006).

[116] M. Markevitch, *Chandra observation of the most interesting cluster in the universe*, ESA Spec. Publ. **604**, 723 (2006), arXiv:astro-ph/0511345 .

[117] D. Clowe, M. Bradac, A. H. Gonzalez, M. Markevitch, S. W. Randall, C. Jones, and D. Zaritsky, *A direct empirical proof of the existence of dark matter*, Astrophys. J. **648**, L109 (2006).

[118] P. van Dokkum *et al.*, *A galaxy lacking dark matter*, Nature **555**, 629 (2018).

[119] R. H. Sanders, *Modified gravity without dark matter*, in *The Invisible Universe: Dark Matter and Dark Energy, Lecture Notes in Physics* (Springer, New York, NY, USA, 2005) pp. 375–402.

[120] G. Jungman, M. Kamionkowski, and K. Griest, *Supersymmetric dark matter*, Phys. Rept. **267**, 195 (1996).

[121] C. Autermann, *Experimental status of supersymmetry after the LHC Run-I*, Progress in Particle and Nuclear Physics **90**, 125 (2016).

[122] K. A. Olive *et al.* (Particle Data Group), *Review of Particle Physics*, Chin. Phys. C **38**, 090001 (2014).

[123] G. Servant and T. M. P. Tait, *Is the lightest Kaluza-Klein particle a viable dark matter candidate?*, Nucl. Phys. B **650**, 391 (2003).

[124] D. Hooper and S. Profumo, *Dark matter and collider phenomenology of universal extra dimensions*, Phys. Rept. **453**, 29 (2007).

[125] R. D. Peccei and H. R. Quinn, *CP Conservation in the Presence of Instantons*, Phys. Rev. Lett. **38**, 1440 (1977).

[126] S. Arrenberg *et al.*, *Dark Matter in the Coming Decade: Complementary Paths to Discovery and Beyond*, arXiv:1310.8621 .

[127] O. Adriani *et al.* (PAMELA), *An anomalous positron abundance in cosmic rays with energies 1.5-100 GeV*, Nature **458**, 607 (2009).

[128] L. Accardo *et al.* (AMS), *High Statistics Measurement of the Positron Fraction in Primary Cosmic Rays of 0.5-500 GeV with the Alpha Magnetic Spectrometer on the International Space Station*, Phys. Rev. Lett. **113**, 121101 (2014).

[129] D. Hooper and L. Goodenough, *Dark Matter Annihilation in The Galactic Center As Seen by the Fermi Gamma Ray Space Telescope*, Phys. Lett. B **697**, 412 (2011).

[130] K. N. Abazajian, N. Canac, S. Horiuchi, and M. Kaplinghat, *Astrophysical and Dark Matter Interpretations of Extended Gamma-Ray Emission from the Galactic Center*, Phys. Rev. D **90**, 023526 (2014).

[131] F. Calore, I. Cholis, and C. Weniger, *Background model systematics for the Fermi GeV excess*, Journal of Cosmology and Astroparticle Physics **2015**, 038 (2015).

[132] T. Daylan, D. P. Finkbeiner, D. Hooper, T. Linden, S. K. N. Portillo, N. L. Rodd, and T. R. Slatyer, *The characterization of the gamma-ray signal from the central Milky Way: A case for annihilating dark matter*, Phys. Dark Univ. **12**, 1 (2016).

[133] M. G. Aartsen *et al.* (IceCube), *Search for dark matter annihilations in the Sun with the 79-string IceCube detector*, Phys. Rev. Lett. **110**, 131302 (2013).

[134] M. G. Aartsen *et al.* (IceCube), *Search for Dark Matter Annihilation in the Galactic Center with IceCube-79*, Eur. Phys. J. C **75**, 492 (2015).

[135] C. F. McKee, A. Parravano, and D. J. Hollenbach, *Stars, Gas, and Dark Matter in the Solar Neighborhood*, Astrophys. J. **814**, 13 (2015).

[136] K. Choi *et al.* (Super-Kamiokande), *Search for neutrinos from annihilation of captured low-mass dark matter particles in the Sun by Super-Kamiokande*, Phys. Rev. Lett. **114**, 141301 (2015).

[137] A. M. Green, *Astrophysical uncertainties on direct detection experiments*, Mod. Phys. Lett. A **27**, 1230004 (2012).

[138] M. C. Smith *et al.*, *The RAVE Survey: Constraining the Local Galactic Escape Speed*, Mon. Not. Roy. Astron. Soc. **379**, 755 (2007).

[139] J. D. Lewin and P. F. Smith, *Review of mathematics, numerical factors, and corrections for dark matter experiments based on elastic nuclear recoil*, Astropart. Phys. **6**, 87 (1996).

[140] E. Aprile *et al.* (XENON), *Physics reach of the XENON1T dark matter experiment*, JCAP **1604**, 027 (2016).

[141] L. Baudis, G. Kessler, P. Klos, R. F. Lang, J. Menéndez, S. Reichard, and A. Schwenk, *Signatures of Dark Matter Scattering Inelastically Off Nuclei*, Phys. Rev. D **88**, 115014 (2013).

[142] C. McCabe, *Prospects for dark matter detection with inelastic transitions of xenon*, JCAP **1605**, 033 (2016).

[143] L. E. Strigari, *Neutrino coherent scattering rates at direct dark matter detectors*, New Journal of Physics **11**, 105011 (2009).

[144] A. Gutlein *et al.*, *Solar and atmospheric neutrinos: Background sources for the direct dark matter search*, Astropart. Phys. **34**, 90 (2010).

[145] L. Baudis, A. Ferella, A. Kish, A. Manalaysay, T. M. Undagoitia, and M. Schumann, *Neutrino physics with multi-ton scale liquid xenon detectors*, Journal of Cosmology and Astroparticle Physics **2014**, 044 (2014).

[146] R. Bernabei *et al.* (DAMA, LIBRA), *New results from DAMA/LIBRA*, Eur. Phys. J. C **67**, 39 (2010).

[147] P. Agnes *et al.* (DarkSide), *Low-Mass Dark Matter Search with the DarkSide-50 Experiment*, Phys. Rev. Lett. **121**, 081307 (2018).

[148] R. Agnese *et al.* (SuperCDMS), *Low-mass dark matter search with CDMSlite*, Phys. Rev. D **97**, 022002 (2018).

[149] G. Angloher *et al.* (CRESST-II), *Results on low mass WIMPs using an upgraded CRESST-II detector*, Eur. Phys. J. C **74**, 3184 (2014).

[150] F. Petricca *et al.* (CRESST), *First results on low-mass dark matter from the CRESST-III experiment*, arXiv:1711.07692 .

[151] E. Aprile *et al.* (XENON), *First Dark Matter Search Results from the XENON1T Experiment*, Phys. Rev. Lett. **119**, 181301 (2017).

[152] D. S. Akerib *et al.* (LUX), *Results from a search for dark matter in the complete LUX exposure*, Phys. Rev. Lett. **118**, 021303 (2017).

[153] X. Cui *et al.* (PandaX-II), *Dark Matter Results From 54-Ton-Day Exposure of PandaX-II Experiment*, Phys. Rev. Lett. **119**, 181302 (2017).

[154] D. S. Akerib *et al.* (LZ), *LUX-ZEPLIN (LZ) Conceptual Design Report*, arXiv:1509.02910 .

[155] J. Fan, M. Reece, and L.-T. Wang, *Non-relativistic effective theory of dark matter direct detection*, JCAP **11**, 042 (2010).

[156] A. L. Fitzpatrick, W. Haxton, E. Katz, N. Lubbers, and Y. Xu, *The Effective Field Theory of Dark Matter Direct Detection*, JCAP **02**, 004 (2013).

[157] N. Anand, A. L. Fitzpatrick, and W. C. Haxton, *Weakly interacting massive particle-nucleus elastic scattering response*, Phys. Rev. C **89**, 065501 (2014).

[158] R. J. Hill and M. P. Solon, *Effective field theory for heavy weakly interacting massive particles scattering with nucleons*, Phys. Rev. Lett. **112**, 211602 (2014).

[159] M. Hoferichter, P. Klos, and A. Schwenk, *Chiral power counting of one- and two-body currents in direct detection of dark matter*, Phys. Lett. B **746**, 410 (2015).

[160] J. Menéndez, D. Gazit, and A. Schwenk, *Spin-dependent WIMP scattering off nuclei*, Phys. Rev. D **86**, 103511 (2012).

[161] B. R. Barrett, P. Navrátil, and J. P. Vary, *Ab initio no core shell model*, Prog. Part. Nucl. Phys. **69**, 131 (2013).

[162] G. Hagen, T. Papenbrock, M. Hjorth-Jensen, and D. J. Dean, *Coupled-cluster computations of atomic nuclei*, Rep. Prog. Phys. **77**, 096302 (2014).

[163] G. Hagen, T. Papenbrock, A. Ekström, K. Wendt, G. Baardsen, S. Gandolfi, M. Hjorth-Jensen, and C. J. Horowitz, *Coupled-cluster calculations of nucleonic matter*, Phys. Rev. C **89**, 014319 (2014).

[164] H. Hergert, S. K. Bogner, T. D. Morris, A. Schwenk, and K. Tsukiyama, *The In-Medium Similarity Renormalization Group: A Novel Ab Initio Method for Nuclei*, Phys. Rept. **621**, 165 (2016).

[165] V. Somà, T. Duguet, and C. Barbieri, *Ab initio self-consistent Gorkov-Green's function calculations of semi-magic nuclei: Formalism at second order with a two-nucleon interaction*, Phys. Rev. C **84**, 064317 (2011).

[166] T. D. Morris, J. Simonis, S. R. Stroberg, C. Stumpf, G. Hagen, J. D. Holt, G. R. Jansen, T. Papenbrock, R. Roth, and A. Schwenk, *Structure of the lightest tin isotopes*, Phys. Rev. Lett. **120**, 152503 (2018).

[167] J. Carlson, *Green's function Monte Carlo study of light nuclei*, Phys. Rev. C **36**, 2026 (1987).

[168] S. C. Pieper and R. B. Wiringa, *Quantum Monte Carlo calculations of light nuclei*, Ann. Rev. Nucl. Part. Sci. **51**, 53 (2001).

[169] J. Carlson, S. Gandolfi, F. Pederiva, S. C. Pieper, R. Schiavilla, K. E. Schmidt, and R. B. Wiringa, *Quantum Monte Carlo methods for nuclear physics*, Rev. Mod. Phys. **87**, 1067 (2015).

[170] S. Gandolfi, A. Gezerlis, and J. Carlson, *Neutron matter from low to high density*, Annu. Rev. Nucl. Part. Sci. **65**, 303 (2015).

[171] S. Gandolfi, A. Lovato, J. Carlson, and K. E. Schmidt, *From the lightest nuclei to the equation of state of asymmetric nuclear matter with realistic nuclear interactions*, Phys. Rev. C **90**, 061306 (2014).

[172] E. Caurier, G. Martínez-Pinedo, F. Nowacki, A. Poves, and A. P. Zuker, *The Shell model as unified view of nuclear structure*, Rev. Mod. Phys. **77**, 427 (2005).

[173] M. H. Kalos, *Monte Carlo Calculations of the Ground State of Three- and Four-Body Nuclei*, Phys. Rev. **128**, 1791 (1962).

[174] W. M. C. Foulkes, L. Mitas, R. J. Needs, and G. Rajagopal, *Quantum monte carlo simulations of solids*, Rev. Mod. Phys. **73**, 33 (2001).

[175] N. Metropolis, A. W. Rosenbluth, M. N. Rosenbluth, A. H. Teller, and E. Teller, *Equation of state calculations by fast computing machines*, The Journal of Chemical Physics **21**, 1087 (1953).

[176] M. Suzuki, *On the convergence of exponential operators—the Zassenhaus formula, BCH formula and systematic approximants*, Comm. Math. Phys. **57**, 193 (1977).

[177] S. Gandolfi, *The Auxiliary Field Diffusion Monte Carlo Method for Nuclear Physics and Nuclear Astrophysics*, Ph.D. thesis, Università degli Studi di Trento (2007).

[178] K. E. Schmidt and S. Fantoni, *A quantum monte carlo method for nucleon systems*, Phys. Lett. B **446**, 99 (1999).

[179] S. Zhang, J. Carlson, and J. E. Gubernatis, *Constrained Path Quantum Monte Carlo Method for Fermion Ground States*, Phys. Rev. Lett. **74**, 3652 (1995).

[180] E. Caurier and F. Nowacki, *Present status of shell model techniques*, Acta Phys. Polon. B **30**, 705 (1999).

[181] M. G. Mayer, *On closed shells in nuclei. 2*, Phys. Rev. **75**, 1969 (1949).

[182] O. Haxel, J. H. D. Jensen, and H. E. Suess, *On the "Magic Numbers" in Nuclear Structure*, Phys. Rev. **75**, 1766 (1949).

[183] P. Navrátil, S. Quaglioni, G. Hupin, C. Romero-Redondo, and A. Calci, *Unified ab initio approaches to nuclear structure and reactions*, Phys. Scripta **91**, 053002 (2016).

[184] M. Hjorth-Jensen, T. T. S. Kuo, and E. Osnes, *Realistic effective interactions for nuclear systems*, Phys. Rep. **261**, 125 (1995).

[185] A. Poves and A. P. Zuker, *Theoretical spectroscopy and the fp shell*, Phys. Rep. **70**, 235 (1981).

[186] N. M. Parzuchowski, S. R. Stroberg, P. Navrátil, H. Hergert, and S. K. Bogner, *Ab initio electromagnetic observables with the in-medium similarity renormalization group*, Phys. Rev. C **96**, 034324 (2017).

[187] L. Huth, V. Durant, J. Simonis, and A. Schwenk, *Shell-model interactions from chiral effective field theory*, Phys. Rev. C **98**, 044301 (2018).

[188] S. C. Pieper, R. B. Wiringa, and J. Carlson, *Quantum Monte Carlo calculations of excited states in A = 6 - 8 nuclei*, Phys. Rev. C **70**, 054325 (2004).

[189] P. Klos, J. E. Lynn, I. Tews, S. Gandolfi, A. Gezerlis, H. W. Hammer, M. Hoferichter, and A. Schwenk, *Quantum Monte Carlo calculations of two neutrons in finite volume*, Phys. Rev. C **94**, 054005 (2016).

[190] D. B. Kaplan, M. J. Savage, and M. B. Wise, *Two nucleon systems from effective field theory*, Nucl. Phys. B **534**, 329 (1998).

[191] U. van Kolck, *Effective field theory of short range forces*, Nucl. Phys. A **645**, 273 (1999).

[192] J.-W. Chen, G. Rupak, and M. J. Savage, *Nucleon-nucleon effective field theory without pions*, Nucl. Phys. A **653**, 386 (1999).

[193] B. S. Pudliner, V. R. Pandharipande, J. Carlson, and R. B. Wiringa, *Quantum Monte Carlo calculations of A <= 6 nuclei*, Phys. Rev. Lett. **74**, 4396 (1995).

[194] S. Zhang and H. Krakauer, *Quantum Monte Carlo method using phase-free random walks with Slater determinants*, Phys. Rev. Lett. **90**, 136401 (2003).

[195] J. Muggli, *Cubic Harmonics as Linear Combinations of Spherical Harmonics*, Z. Angew. Math. Mech. **23**, 311 (1972).

[196] A. Bohr and B. R. Mottelson, *Nuclear Structure*, Vol. I (World Scientific, Singapore, 1998).

[197] S. Gandolfi, J. Carlson, and S. C. Pieper, *Cold Neutrons Trapped in External Fields*, Phys. Rev. Lett. **106**, 012501 (2011).

[198] R. Newton, *Scattering Theory of Waves and Particles*, Dover Books on Physics (Dover Publications, 1982).

[199] C. J. Pethick, D. G. Ravenhall, and C. P. Lorenz, *The inner boundary of a neutron star crust*, Nucl. Phys. A **584**, 675 (1995).

[200] S. Sorella, *Generalized lanczos algorithm for variational quantum monte carlo*, Phys. Rev. B **64**, 024512 (2001).

[201] E. Epelbaum, H. Krebs, and U.-G. Meißner, *Improved chiral nucleon-nucleon potential up to next-to-next-to-next-to-leading order*, Eur. Phys. J. A **51**, 53 (2015).

[202] S.-Y. Chang, J. Morales, V. R. Pandharipande, D. G. Ravenhall, J. Carlson, S. C. Pieper, R. B. Wiringa, and K. E. Schmidt, *Neutron matter: a superfluid gas*, Nucl. Phys. A **746**, 215 (2004).

[203] A. L. Fetter and J. D. Walecka, *Quantum Theory of Many-Particle Systems* (McGraw-Hill, New York, 1971).

[204] B. DeMarco and D. S. Jin, *Onset of fermi degeneracy in a trapped atomic gas*, Science **285**, 1703 (1999).

[205] C. A. Regal and D. S. Jin, *Measurement of positive and negative scattering lengths in a fermi gas of atoms*, Phys. Rev. Lett. **90**, 230404 (2003).

[206] A. N. Wenz, G. Zürn, S. Murmann, I. Brouzos, T. Lompe, and S. Jochim, *From few to many: Observing the formation of a fermi sea one atom at a time*, Science **342**, 457 (2013).

[207] U.-G. Meißner, G. Ríos, and A. Rusetsky, *Spectrum of three-body bound states in a finite volume*, Phys. Rev. Lett. **114**, 091602 (2015).

[208] G. C. Groenenboom, *The Discrete Variable Represenation*, `http://www.theochem.ru.nl/cgi-bin/dbase/search.cgi?Groenenboom`.

[209] A. Bulgac and M. M. Forbes, *Use of the discrete variable representation basis in nuclear physics*, Phys. Rev. C **87**, 051301 (2013).

[210] P. Klos, S. König, H. W. Hammer, J. E. Lynn, and A. Schwenk, *Signatures of few-body resonances in finite volume*, Phys. Rev. C **98**, 034004 (2018).

[211] S. Bilaj, *Finite-Volume Calculations of Resonances using the Discrete Variable Representation*, Bachelor-Thesis, TU Darmstadt (2017).

[212] K. Varga and Y. Suzuki, *Solution of few body problems with the stochastic variational method: 1. Central forces*, Comput. Phys. Commun. **106**, 157 (1997).

[213] R. Johnson, *Angular momentum on a lattice*, Phys. Lett. B **114**, 147 (1982).

[214] Intel®, *Threading Building Blocks (TBB)*, `www.threadingbuildingblocks.org` ().

[215] K. J. Maschhoff and D. C. Sorensen, *P_ARPACK: An Efficient Portable Large Scale Eigenvalue Package for Distributed Memory Parallel Architectures*, `www.caam.rice.edu/software/ARPACK/`, `github.com/opencollab/arpack-ng`.

[216] Intel®, *Math Kernel Library (MKL)*, `software.intel.com/mkl` ().

[217] M. Martone, *librsb: A shared memory parallel sparse matrix computations library for the Recursive Sparse Blocks format*, `librsb.sourceforge.net`.

[218] M. Frigo and S. G. Johnson, *The Design and Implementation of FFTW3*, Proceedings of the IEEE **93**, 216 (2005), special issue on “Program Generation, Optimization, and Platform Adaptation”.

[219] W. Glöckle, *The Quantum Mechanical Few-Body Problem* (Springer-Verlag, 1983).

[220] D. V. Fedorov, E. Garrido, and A. S. Jensen, *Complex Scaling of the Hyper-Spheric Coordinates and Faddeev Equations*, Few-Body Syst. **33**, 153 (2003).

[221] J. Blandon, V. Kokoouline, and F. Masnou-Seeuws, *Calculation of three-body resonances using slow-variable discretization coupled with a complex absorbing potential*, Phys. Rev. A **75**, 042508 (2007).

[222] G. Prézeau, A. Kurylov, M. Kamionkowski, and P. Vogel, *New contribution to wimp-nucleus scattering*, Phys. Rev. Lett. **91**, 231301 (2003).

[223] V. Cirigliano, M. L. Graesser, and G. Ovanesyan, *WIMP-nucleus scattering in chiral effective theory*, JHEP **10**, 025 (2012).

[224] F. Bishara, J. Brod, B. Grinstein, and J. Zupan, *Chiral Effective Theory of Dark Matter Direct Detection*, JCAP **02**, 009 (2017).

[225] F. Bishara, J. Brod, B. Grinstein, and J. Zupan, *From quarks to nucleons in dark matter direct detection*, JHEP **11**, 059 (2017).

[226] M. Hoferichter, P. Klos, J. Menéndez, and A. Schwenk, *Analysis strategies for general spin-independent WIMP-nucleus scattering*, Phys. Rev. D **94**, 063505 (2016).

[227] M. C. Smith *et al.*, *The RAVE Survey: Constraining the Local Galactic Escape Speed*, Mon. Not. Roy. Astron. Soc. **379**, 755 (2007).

[228] J. Engel, S. Pittel, and P. Vogel, *Nuclear physics of dark matter detection*, Int. J. Mod. Phys. E **1**, 1 (1992).

[229] M. Schumann, *Dark Matter 2014, Proceedings, Dark Matter, Hadron Physics and Fusion Physics (DHF2014): Messina, Italy, September 24-26, 2014*, EPJ Web Conf. **96**, 01027 (2015).

[230] L. Vietze, P. Klos, J. Menéndez, W. C. Haxton, and A. Schwenk, *Nuclear structure aspects of spin-independent WIMP scattering off xenon*, Phys. Rev. D **91**, 043520 (2015).

[231] J. Goodman, M. Ibe, A. Rajaraman, W. Shepherd, T. M. P. Tait, and H.-B. Yu, *Constraints on Dark Matter from Colliders*, Phys. Rev. D **82**, 116010 (2010).

[232] M. Hoferichter, P. Klos, J. Menéndez, and A. Schwenk, *Nuclear structure factors for general spin-independent WIMP–nucleus scattering*, Manuscript in preparation.

[233] J. D. Walecka, *Theoretical Nuclear and Subnuclear Physics* (Oxford University Press, 1995).

[234] E. Caurier, J. Menéndez, F. Nowacki, and A. Poves, *The Influence of pairing on the nuclear matrix elements of the neutrinoless $\beta\beta$ decays*, Phys. Rev. Lett. **100**, 052503 (2008).

[235] J. Menéndez, A. Poves, E. Caurier, and F. Nowacki, *Disassembling the Nuclear Matrix Elements of the Neutrinoless $\beta\beta$ Decay*, Nucl. Phys. A **818**, 139 (2009).

[236] E. Caurier, J. Menéndez, F. Nowacki, and A. Poves, *Coexistence of spherical states with deformed and superdeformed bands in doubly magic Ca-40: A Shell model challenge*, Phys. Rev. C **75**, 054317 (2007), [Erratum: Phys. Rev.C76,049901(2007)].

[237] T. W. Donnelly and W. C. Haxton, *Multipole operators in semileptonic weak and electromagnetic interactions with nuclei*, Atom. Data Nucl. Data Tabl. **23**, 103 (1979).

[238] W. Haxton and C. Lunardini, *A Mathematica script for harmonic oscillator nuclear matrix elements arising in semileptonic electroweak interactions*, Comput. Phys. Commun. **179**, 345 (2008).

[239] V. Cirigliano, M. L. Graesser, G. Ovanesyan, and I. M. Shoemaker, *Shining LUX on Isospin-Violating Dark Matter Beyond Leading Order*, Phys. Lett. B **739**, 293 (2014).

[240] V. Cirigliano and M. L. Graesser, private communication, (2016).

[241] J. Menéndez, D. Gazit, and A. Schwenk, *Chiral Two-Body Currents in Nuclei: Gamow-Teller Transitions and Neutrinoless Double-Beta Decay*, Phys. Rev. Lett. **107**, 062501 (2011).

[242] J. Engel, F. Simkovic, and P. Vogel, *Chiral Two-Body Currents and Neutrinoless Double-Beta Decay in the QRPA*, Phys. Rev. C **89**, 064308 (2014).

[243] M. Hoferichter, P. Klos, J. Menéndez, and A. Schwenk, *Improved limits for Higgs-portal dark matter from LHC searches*, Phys. Rev. Lett. **119**, 181803 (2017).

[244] A. Fieguth, M. Hoferichter, P. Klos, J. Menéndez, A. Schwenk, and C. Weinheimer, *Discriminating WIMP-nucleus response functions in present and future XENON-like direct detection experiments*, Phys. Rev. D **97**, 103532 (2018).

[245] S. Kanemura, S. Matsumoto, T. Nabeshima, and N. Okada, *Can WIMP Dark Matter overcome the Nightmare Scenario?*, Phys. Rev. D **82**, 055026 (2010).

[246] A. Djouadi, O. Lebedev, Y. Mambrini, and J. Quevillon, *Implications of LHC searches for Higgs–portal dark matter*, Phys. Lett. B **709**, 65 (2012).

[247] A. Djouadi, A. Falkowski, Y. Mambrini, and J. Quevillon, *Direct Detection of Higgs-Portal Dark Matter at the LHC*, Eur. Phys. J. C **73**, 2455 (2013).

[248] A. Beniwal, F. Rajec, C. Savage, P. Scott, C. Weniger, M. White, and A. G. Williams, *Combined analysis of effective Higgs portal dark matter models*, Phys. Rev. D **93**, 115016 (2016).

[249] G. Aad *et al.* (ATLAS), *Search for Invisible Decays of a Higgs Boson Produced in Association with a Z Boson in ATLAS*, Phys. Rev. Lett. **112**, 201802 (2014).

[250] S. Chatrchyan *et al.* (CMS), *Search for invisible decays of Higgs bosons in the vector boson fusion and associated ZH production modes*, Eur. Phys. J. C **74**, 2980 (2014).

[251] G. Aad *et al.* (ATLAS), *Search for invisible particles produced in association with single-top-quarks in proton-proton collisions at $\sqrt{s} = 8$ TeV with the ATLAS detector*, Eur. Phys. J. C **75**, 79 (2015).

[252] G. Aad *et al.* (ATLAS), *Search for invisible decays of the Higgs boson produced in association with a hadronically decaying vector boson in pp collisions at $\sqrt{s} = 8$ TeV with the ATLAS detector*, Eur. Phys. J. C **75**, 337 (2015).

[253] G. Aad *et al.* (ATLAS), *Search for invisible decays of a Higgs boson using vector-boson fusion in pp collisions at $\sqrt{s} = 8$ TeV with the ATLAS detector*, JHEP **1601**, 172 (2016).

[254] G. Aad *et al.* (ATLAS), *Constraints on new phenomena via Higgs boson couplings and invisible decays with the ATLAS detector*, JHEP **11**, 206 (2015).

[255] V. Khachatryan *et al.* (CMS), *Searches for invisible decays of the Higgs boson in pp collisions at $\sqrt{s} = 7$, 8, and 13 TeV*, JHEP **02**, 135 (2017).

[256] M. A. Shifman, A. I. Vainshtein, and V. I. Zakharov, *Remarks on Higgs Boson Interactions with Nucleons*, Phys. Lett. B **78**, 443 (1978).

[257] J. Duflo and A. P. Zuker, *Microscopic mass formulae*, Phys. Rev. C **52**, R23 (1995).

[258] J. R. Andersen *et al.* (LHC Higgs Cross Section Working Group), *Handbook of LHC Higgs Cross Sections: 3. Higgs Properties*, (2013).

[259] R. Agnese *et al.* (SuperCDMS), *New Results from the Search for Low-Mass Weakly Interacting Massive Particles with the CDMS Low Ionization Threshold Experiment*, Phys. Rev. Lett. **116**, 071301 (2016).

[260] A. Tan *et al.* (PandaX-II), *Dark Matter Results from First 98.7 Days of Data from the PandaX-II Experiment*, Phys. Rev. Lett. **117**, 121303 (2016).

[261] C. Cheung, L. J. Hall, D. Pinner, and J. T. Ruderman, *Prospects and Blind Spots for Neutralino Dark Matter*, JHEP **05**, 100 (2013).

[262] P. Huang and C. E. M. Wagner, *Blind Spots for neutralino Dark Matter in the MSSM with an intermediate m_A*, Phys. Rev. D **90**, 015018 (2014).

[263] A. Crivellin, M. Hoferichter, M. Procura, and L. C. Tunstall, *Light stops, blind spots, and isospin violation in the MSSM*, JHEP **07**, 129 (2015).

[264] H. Rogers, D. G. Cerdeño, P. Cushman, F. Livet, and V. Mandic, *Multidimensional effective field theory analysis for direct detection of dark matter*, Phys. Rev. D **95**, 082003 (2017).

[265] E. Aprile *et al.* (XENON100), *Analysis of the XENON100 Dark Matter Search Data*, Astropart. Phys. **54**, 11 (2014).

[266] E. Aprile *et al.* (XENON100), *The XENON100 Dark Matter Experiment*, Astropart. Phys. **35**, 573 (2012).

[267] E. Aprile *et al.* (XENON100), *Dark Matter Results from 225 Live Days of XENON100 Data*, Phys. Rev. Lett. **109**, 181301 (2012).

[268] `https://static.pandax.sjtu.edu.cn/download/IAC-2016-pandax.pdf`.

[269] G. Co', V. De Donno, M. Anguiano, and A. M. Lallena, *Nuclear proton and neutron distributions in the detection of weak interacting massive particles*, JCAP **1211**, 010 (2012).

[270] D. G. Cerdeño, M. Fornasa, J. H. Huh, and M. Peiró, *Nuclear uncertainties in the spin-dependent structure functions for direct dark matter detection*, Phys. Rev. D **87**, 023512 (2013).

[271] M. S. Dresselhaus, *Application of Group Theory to Physics of Solids*, `http://web.mit.edu/course/6/6.734j/www/group-full02.pdf`.

Wissenschaftlicher Werdegang

Zur Person

Name	Philipp Klos
Geburtsdatum	27.12.1988
Geburtsort	Darmstadt
Nationalität	deutsch

Akademische Ausbildung

11/2014 – 10/2018	Promotion in Physik, Institut für Kernphysik, Technische Universität Darmstadt
04/2013 – 09/2014	Masterstudium in Physik, Technische Universität Darmstadt, Thesis: *Electroweak currents in chiral effective field theory*, Betreuer: Professor Achim Schwenk, Ph.D., Master of Science in Physik
08/2011 – 07/2012	Auslandsstudium im Rahmen des Erasmus Programms, École Polytechnique Fédérale de Lausanne, Schweiz
10/2009 – 02/2013	Bachelorstudium in Physik, Technische Universität Darmstadt, Thesis: *Spin-dependent WIMP scattering off nuclei*, Betreuer: Professor Achim Schwenk, Ph.D., Bachelor of Science in Physik

Preise und Auszeichnungen

06/2015	M.Sc.-Forschungspreis der Gerhard Herzberg Gesellschaft für die in der Masterarbeit gezeigten Leistungen
10/2012 – 09/2014	Deutschlandstipendium, gefördert durch die Bosch Rexroth AG
06/2011	Auslandsstarthilfe der Gerhard Herzberg Gesellschaft für den Aufenthalt and der École Polytechnique Fédérale de Lausanne

Erklärung zur Dissertation

Hiermit versichere ich, die vorliegende Dissertation ohne Hilfe Dritter nur mit den angegebenen Quellen und Hilfsmitteln angefertigt zu haben. Alle Stellen, die aus Quellen entnommen wurden, sind als solche kenntlich gemacht. Diese Arbeit hat in gleicher oder ähnlicher Form noch keiner Prüfungsbehörde vorgelegen.

Darmstadt, den 9. Juli 2018

(Philipp Klos)